Characterization of Biomass-Based Fuels and Fuel Blends for Low-Emissions, Advanced Compression Ignition Engines (The University of Alabama)

Professor Ajay K. Agrawal, Principal Investigator
The University of Alabama
Box 870279, 3047 H.M. Comer, 247 7th Ave
Tuscaloosa, Alabama 34587
Email: aagrawal@eng.ua.edu

Professor Joshua Bittle, (co-Principal Investigator)
The University of Alabama
Box 870279, 3047 H.M. Comer, 247 7th Ave
Tuscaloosa, Alabama 34587
E-mail: jbittle@eng.ua.edu

Ralph Nine, DOE Program Manager
U.S. Department of Energy
E-mail: ralph.nine@netl.doe.gov

Start Date: May 1, 2017 End Date: April 30, 2021
Project Funding: $630,493 DOE share: $567,301 Non-DOE share: $63,192

Project Overview

The goal of the Co-Optima program was to accelerate deployment of co-optimized fuels and engines that will reduce fuel consumption, and criterion pollutants and greenhouse gas (GHG) emissions for both spark and compression-ignited engines. In this project, combustion measurements from a constant pressure flow rig (CPFR) with optical access were used to assess fundamental combustion behavior of number of different candidate fuels and fuel blends. This chamber and its peripheral systems allowed stable control of ambient air pressure and temperature and fuel injection pressure and timing for hundreds of repeat injections allowing statistical interpretation of the results. The optical diagnostics enabled capturing of liquid length, vapor length, ignition timing, lift-off length as well as localized (temporal and spatially resolved) mixture refractive index, flame structure, and soot mass. The operating conditions allowed the study of combustion conditions promoting lean lifted flame combustion (LLFC), a mixing-controlled low-temperature combustion (LTC) strategy to reduce soot production in Advanced Compression Ignition (ACI) engines.

A significant part of effort was spent on developing experimental test facility, implementing optical diagnostics of rainbow schlieren deflectometry (RSD) to simultaneously measure liquid length and vapor length as well as identify first and second state ignition, and a novel two-color pyrometry (2CP) approach to obtain line-of-sight soot and temperature measurements with spatial resolution on the order of single pixel. The test chamber allowed hundreds of injections in rapid succession to collection statistically significant data. Image processing techniques were developed to accurately analyze results.

Two Co-Optima fuels were identified as candidate biofuels to blend with diesel. In experiments, n-heptane was blended with methyl decanoate (MDN) or dimethoxymethane (DMM) at 20% by volume. Both these are oxygenated fuels, and the literature presume their produce less soot because of the oxygenetion. The blends were tested at diesel-like conditions of pressure and temperature. Results show both blends suppress soot formation, but for different reasons. In case of MDN, thermophysical properties

play an important role since its Cetane number is comparable to that of n-heptane. In case of DMM, chemical effects play an important role since DMM is a less reactive fuel with Cetane number of 29 compared to that of 53.8 for n-heptane. Study makes that case that oxygenation is not the sole cause for reduced soot formation, thermophysical properties and chemical properties are equally important since they affect the mixing processes and thus, the equivalence ratio at lift-off-length. These complex dynamics must be studied further to evaluate links between known thermophysical and chemical properties to allow future fuel development to accelerate testing and validation with test volumes on the order of 100 mL per test condition prior to full-scale engine testing.

Through full or partial support from this project, more than 10 journal articles have been published focusing on development of optical diagnostics and the study of combustion behavior in relation to thermophysical and chemical properties.

Approach

The experimental results in this study are obtained using a constant-pressure flow-chamber (CPFC), designed to enable many injections in quick succession to generate a statistically useful dataset (hundreds of injections at each condition). This apparatus has optical access for multiple diagnostics to quantify liquid and vapor regions, fuel-air mixing, ignition and combustion, and soot formation of each injection. These diagnostics are Rainbow Schlieren Deflectometry (RSD), hydroxyl radical chemiluminescence (OH*CL), and two-color pyrometry (2CP). Figure 1 (left) shows the chamber and an overview of the optical diagnostics setup (right).

Rainbow Schlieren Deflectometry is an extension of the well-known schlieren technique wherein a rainbow filter is used to quantify the deflection of light rays passing through density gradients in a test media. This is done by replacing the knife-edge at the focal point of traditional schlieren with a rainbow (hue) filter, thus encoding deflection distance at the focal point as hue to be recorded by a high-speed camera. Since it was pioneered in 1995 by Greenberg et al., the project team has significantly expanded the literature regarding RSD to apply the technique to turbulent flows, fuel, and reacting environments.

Under reacting conditions, hydroxyl radicals are produced in the high temperature, main ignition stage of diesel combustion and at later times. Concentrations of this radical are routinely tracked, either by laser-excitement (as in Planar Laser Induced Fluorescence, PLIF) or by intensified, natural luminescence. This work uses natural OH*CL imaging to extend analysis of reacting jets beyond the upstream region imaged by RSD, revealing the location, timing, propagation, and intensity of combustion.

Thermal radiation from soot, which dominates flame luminosity in the visible spectrum, is captured by 2CP. Luminosity is imaged simultaneously at 550 nm and 650 nm, wavelengths known to encompass soot luminosity and no other significant spectral emissions, which enables spatially resolved measurements of soot temperature and density. This technique has been significantly improved, its known optical errors addressed by a novel design and its uncertainties rigorously quantified, by work conducted in this project.

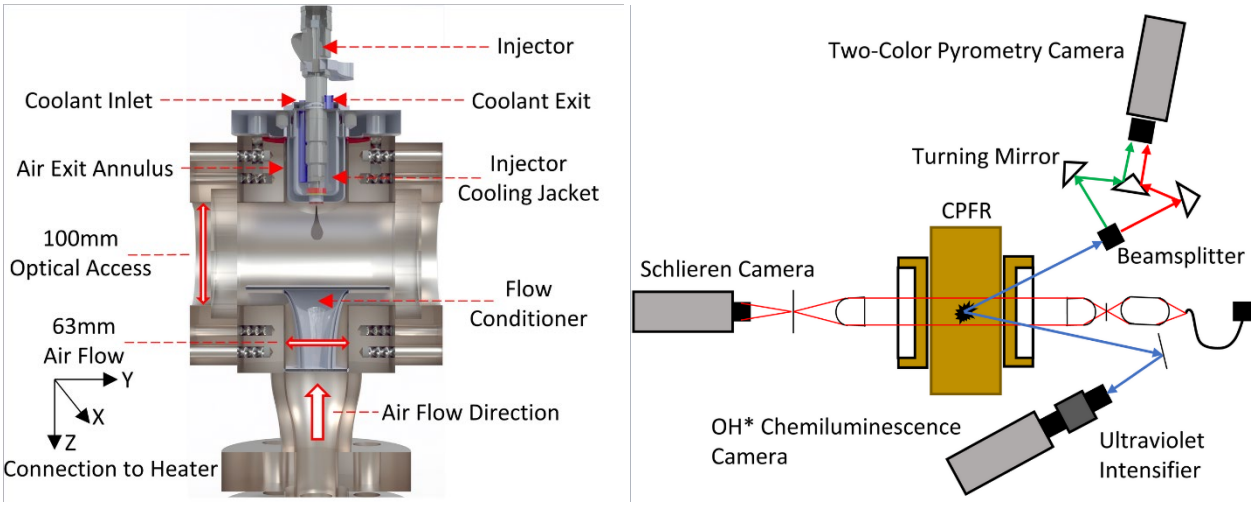

Figure 1. (left) Constant pressure flow rig used as test apparatus in this work, and (right) schematic of optical diagnostics. This is reproduced from Fig. 1 and 2 in Parker et al. publication.

Results

The major results are broken down into four sections. The first is the development of a methodology to identify representative injections from large data sets, the second is the development and application demonstration of a two-color pyrometry system including uncertainty analysis of quantitative soot measurements, and the third and fourth are the study of conventional reference fuels and Co-Optima identified candidate biofuels. The project goal of identifying relationships between typical fuel properties and the subsequent combustion behavior (i.e. sooting behavior, lift-off length, etc.) is discussed in detail.

Representative Injection Identification:

Given the large datasets capable of being generated by the test apparatus used in this project, it was critical to first develop a methodology to classify individual injections and identify a most representative single injection for comparison between operating conditions and fuel blends. This work is published as:

> Parker, A., Agrawal, A. & Bittle, J. Representative Phenomena of Cyclic Turbulent Combustion in High-Pressure Fuel Sprays. Flow Turbulence Combust 111, 675–696 (2023). https://doi.org/10.1007/s10494-023-00432-3

In this study, the constant pressure flow chamber was utilized to acquire data from 500 injections of transient, n-heptane spray reacting in high pressure, high temperature ambient air, while maintaining near-constant control of ambient and injection conditions. Analysis of high-speed images acquired by RSD, OH*CL and 2CP show remarkable injection-to-injection variations visually and in key global parameters. Analysis based on ensemble averaged images is called into question because of its inability to preserve the spatial and temporal gradients in measured and derived quantities. As a result, ensemble average analysis under-predicted global parameters compared to the results obtained from the analysis of individual injections and then averaged. A sample of this result is shown in the Fig. 2.

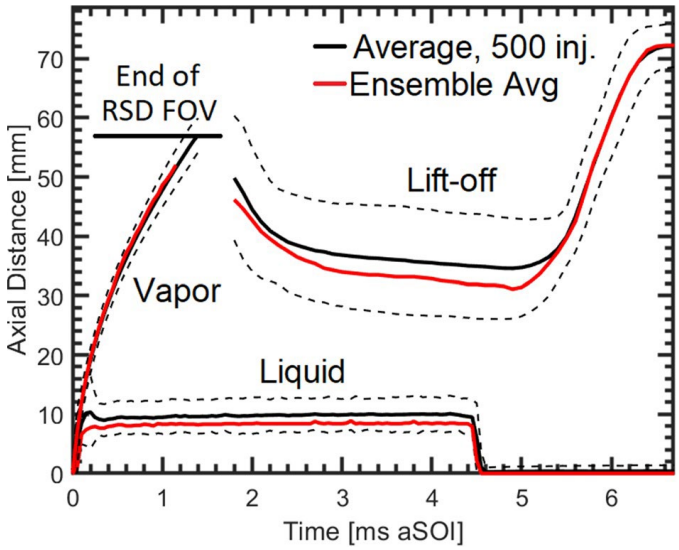

*Figure 2. Sample results showing liquid length, vapor length, and OH*CL based lift-off length as both an average (black lines) including repeatability intervals and ensemble average results (red lines). This is reproduced from Fig. 5 in Parker et al. publication.*

A rigorous examination of test conditions revealed no correlation with global parameters such as jet penetration length, ignition delay time, and lift-off length. This leads to the conclusion that the observed variations in injection-to-injection behavior are the result of a combination of spatial and temporal differences in the localized, small-scale turbulence throughout the jet and minor differences in rate of injection through the nozzle. The range of variation in ignition, flame and sooting behavior is evident in Fig. 3 which shows 6 sample injections as well as the representative injection. The range of behavior captures both the representative (Inj. F) and outlier injections. It is clear from these images that the method developed in this study to identify a representative injection would ensure that analysis of typical representative injection would be appropriate.

To this end, a statistical methodology to identify representative injection(s) from a relatively large data-set was presented and demonstrated to interpret injection-to-injection variation. The analysis is based upon z-score of user defined parameter(s), in this case, boundaries detected by each of the three diagnostics. The z-score measures the departure of a parameter from its average values and can be normalized and weighted to combine results from different diagnostics. Using this approach, the boundaries of the spray, reaction zone, or soot cloud of each injection are reduced to a single total z-score by averaging the local z-score at each axial position and time and assigning equal weights to each diagnostic.

This methodology requires a large dataset to obtain statistically converged results, which can be challenging or even prohibitive in some combustion applications. In view of the large injection-to-injection variation, the methodology proposed here allows one to screen an experimental data-set and determine a representative test case for further analysis. In contrast, current approaches rely on analyzing averaged behavior of localized values. The generalized approach to identify a representative injection presented here can easily be applied to any diagnostic that provides spatiotemporal data and for data sets that are sufficiently large to show convergence of the desired parameters.

Results of the developed approach are shown in Fig. 4 as a set of five injections that are all relatively close to the same overall scoring metric for representative. In contrast to the ensemble behavior, these cases clearly exhibit similar lift-off length and qualitative sooting quantity. Quantitative analysis of sooting behavior is presented in the following section of this report.

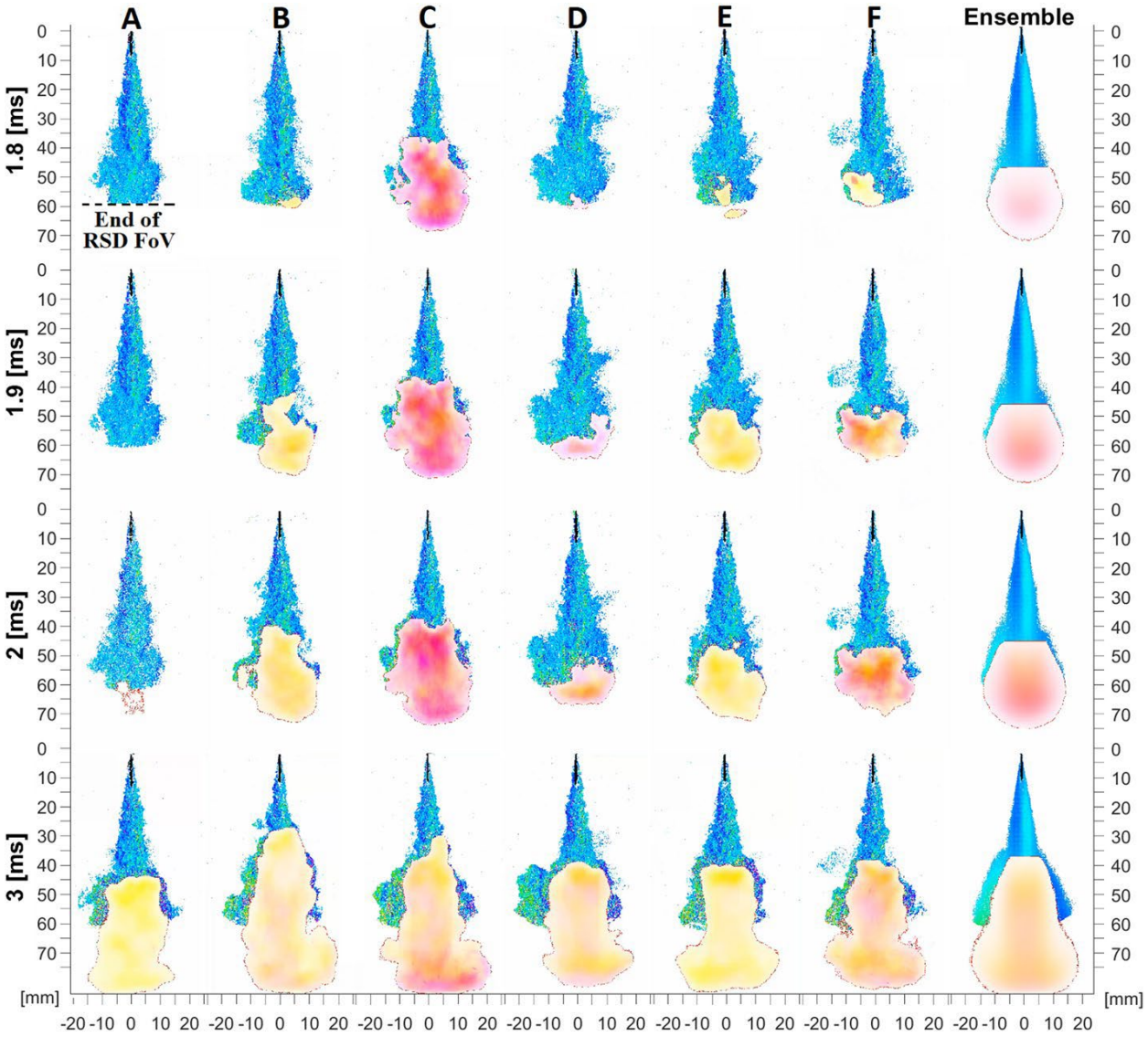

*Figure 3. Select times aSOI are shown for six single-shot injections, as well as ensemble-average images (right). Three frames show the times by which most injections achieve ignition (1.8, 1.9 and 2.0 ms aSOI), and an additional image at 3 ms is provided, after the beginning of the quasi-steady period. Each frame is a composite image of the videos recorded simultaneously by several diagnostics. As labelled in the top left; Rainbow Schlieren Deflectometry (RSD) is shown upstream (image backgrounds removed for clarity), OH*CL intensity is overlaid in yellow, and 2CP intensity in magenta. The OH*CL and 2CP intensities have been normalized across all frames shown. This is reproduced from Fig. 6 in Parker et al. publication.*

The benefits of applying the present analysis to computational fluid dynamics (CFD) development, validation, and analysis are also significant. Representative target values can be identified for models which aim to predict the fluctuating and inherently random turbulent combustion event. Additionally, experimental representative data can be compared directly with the results of a single large-eddy simulation (LES), instead of performing many LES realizations for the purpose of averaging and comparing to experimental ensemble-averages. The present approach quantifies and describes the range of variations in a phenomenon to a degree impossible with ensemble average analysis. A hitherto unavailable dimension of validation is therefore offered to the CFD community; as few as three LES

realizations may be sufficient to validate the models, if the representative individual injection behavior as well as the upper and low bounds of variation, quantified by an appropriate parameter, can be captured with acceptable accuracy. Further, while rate of injection cannot be measured in-situ, additional studies characterizing the range of variation for a specific injector would be helpful. As a result of these developments, the CFD parameters can also be refined to produce more physically meaningful phenomenological models.

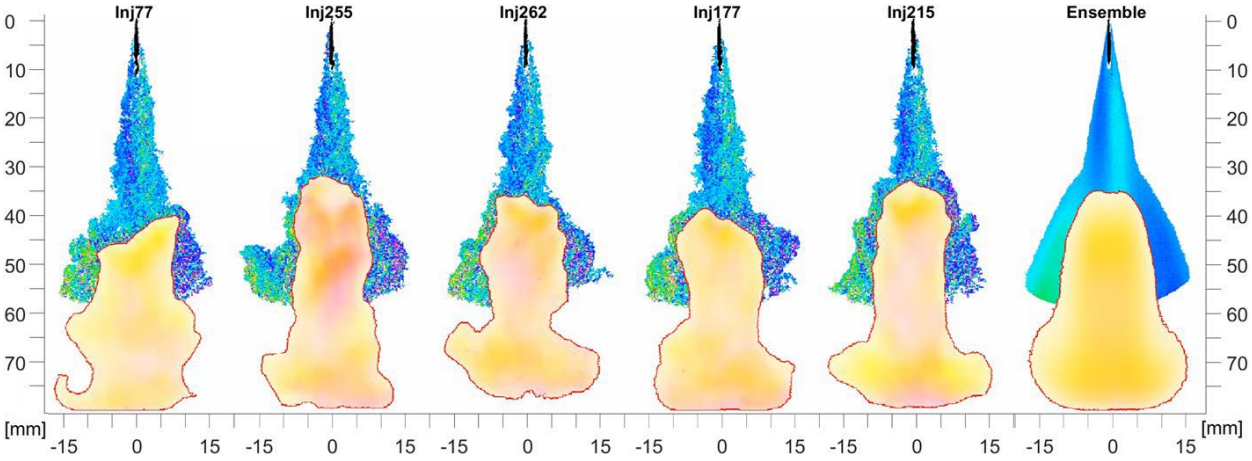

Figure 4. Composite images of the five lowest average z-score injections at 3 ms after start of injection. Contrasted to large range of variation in Figure 3, this subset exhibits clear consistency in behavior with Inj. F (262) being selected as most representative. This is reproduced from Fig. 14 in Parker et al. publication.

Two-color pyrometry system development:

With the basis for establishing a representative injection, the quantitative sooting behavior can be evaluated using the novel two-color pyrometry system developed during this project. Several publications ([4] and [10]) lead to the work summarized in this section. This full work is published as:

> Reggeti, S.A., Parker, A., Stevenson, A., Agrawal, A.K., Bittle, J.A. "Spatially-resolved soot evolution and statistics in high-pressure diesel spray flames using two-color pyrometry" Combustion and Flame, 261, 2023. https://doi.org/10.1016/j.combustflame.2024.113297

The same 500 injection data set from previous publication was used in this work but with a focus on the study of transient soot formation, oxidation, and transport processes. A novel optical configuration of 2CP was utilized together with pixel-by-pixel calibration to acquire spatially- and temporally-resolved line of sight soot measurements with high accuracy at all points on the sensor. Measurements were analyzed on a statistical basis to obtain converged ensemble average values at each time step and to quantify injection-to-injection variations in the sooting behavior in terms of root mean square variations and probability distributions, with the goal of providing experimental data in support of the soot modelling efforts.

While the representative injection study in Parker et al. [2] demonstrated the need to base evaluation on a single injection, there is still value in investigating ensemble average results at a high level as shown in Fig. 5. Results of planar OH*CL, soot mass, soot temperature, and soot transport are illustrated in time to show evaluation of soot formation dominated by premixed ignition to quasi-steady soot formation at lift-off length and jet core as well as the transport at the jet tip.

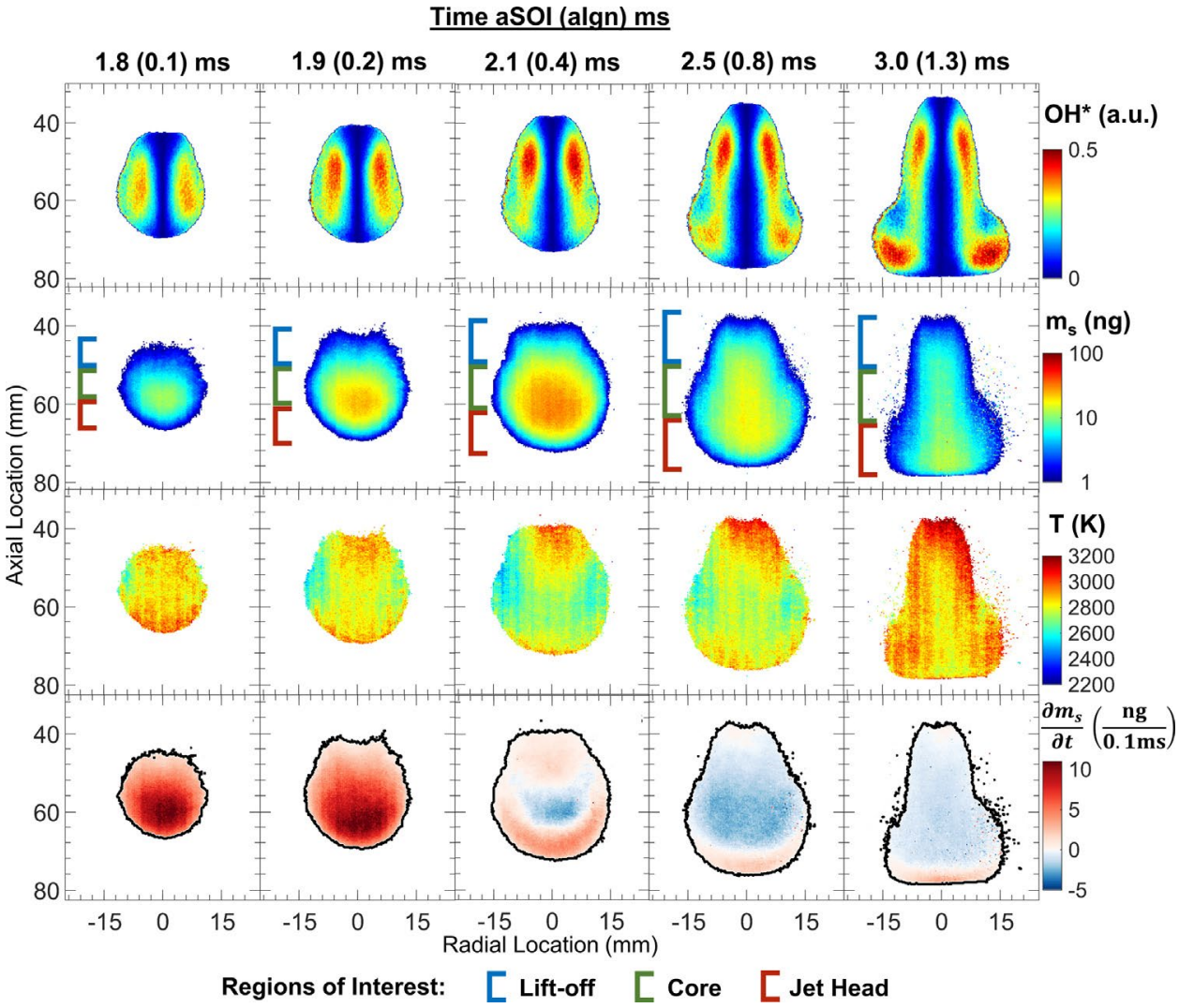

*Figure 5. Contours of average combustion behavior at select time steps with the inverted planar OH*CL signal in the top row, soot mass in the second row, soot temperature in the third row, and soot mass rate in the fourth row.*

By evaluating each injection and averaging soot formation in each region of the jet and by mass density, the results in Fig. 6 can be generated showing total soot in the field of view over time. For this operating condition, the soot peaks as result of the initial premixed ignition event around 2.2 ms after injection and decays as the overall long lift-off length and quasi-steady mixing behavior ultimately promotes a low total soot accumulation. This behavior will be contrasted to other fuels in the following sections of the report.

Large injection-to-injection variability in sooting behavior was detected and quantified in agreement with previous studies. The RMS soot mass (not shown here, but in the paper) indicates that majority of injections were low soot, but few injections had significantly high soot at these conditions. Further, these measurements of spatially-resolved soot mass quantities agree with literature suggesting that large soot masses take longer to be seen because of the time required to form primary particles in high concentrations and for them to agglomerate. Conditions for soot formation are most favorable in the jet core which was shown to have the highest probability of large soot masses. Although the 2CP technique cannot detect individual particle sizes, soot mass probability distributions follow a similar trend as particle size distribution studies by in-cylinder fast gas sampling of a diesel engine.

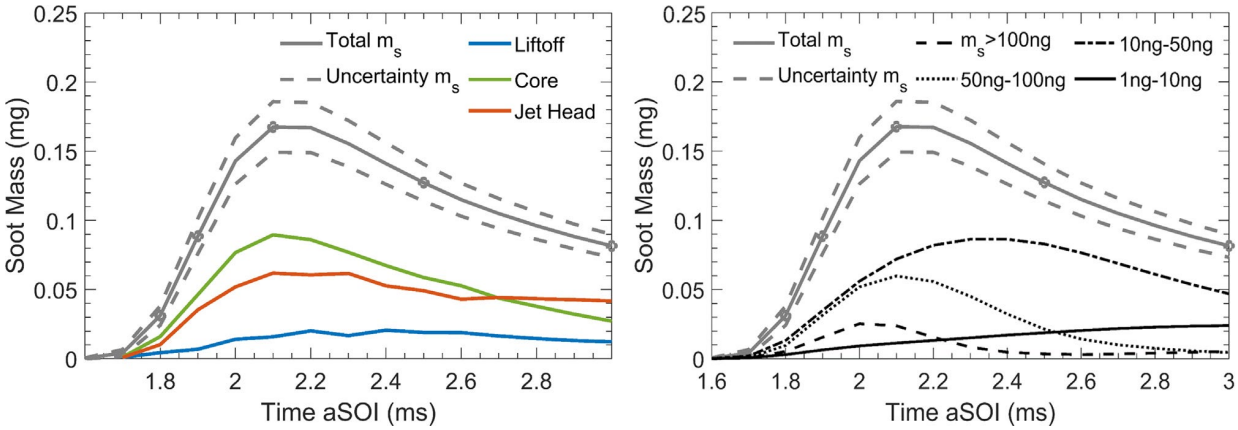

Figure 6. (left) Total soot mass accumulated in different axial sections of the flame, and (right) total soot mass binned by magnitude of soot mass in individual pixels. This is reproduced from Fig. 6 and 7 in Reggeti et al. publication.

The specific results provided here can be used to support model development and validation. More advanced soot modelling approaches could validate the soot number density function against the probability distributions. Further, the uncertainty results presented in the appendix of the paper, typically not available for 2CP, provide confidence bounds for the reported measurements. Future works on the effects of alternative fuels and blends at varying ambient and injection conditions and different combustion chamber designs can leverage the methods presented to obtain previously unavailable data on soot formation, oxidation, and transport processes using modest optical access.

Combustion of Primary Reference Fuels:

The quantitative soot measurements demonstrated in the prior work were used to evaluate behavior of fuels with similar and different thermophysical and chemical properties. This work will serve as the foundation for evaluating the Co-Optima candidate fuels in the final section of the report. This full work was published as:

> Parker, A., Reggeti, S.A., Bittle, J.A., Agrawal, A.K. "Limitations of cetane number to predict transient combustion phenomena in high-pressure fuel sprays" Combustion and Flame, 251, 2023. https://doi.org/10.1016/j.combustflame.2023.112723

In this study, the effect of a fuel's chemical and thermophysical properties were isolated by investigating three fuels under reacting conditions using a slightly modified diesel injector. The three fuels include n-heptane and two primary reference fuel blend of n-hexadecane and heptamethylnonane resulting in cetane numbers of 54 and 40 (called CN54 and CN40, respectively), chosen to create a set with similar thermophysical properties and/or similar cetane number rating; tests comparing trends with similar thermophysical properties but different cetane number (CN54 vs CN40) and visa-versa (n-heptane vs CN54) were considered. The test apparatus provided stable ambient conditions to perform 150 to 500 injections in quick succession for each fuel. Three high-speed optical diagnostics were used to simultaneously image the transient evolution of the jet including liquid fuel vaporization, vapor penetration, first stage ignition and LTHR, main ignition and HTHR, and soot formation. Analyses include Abel inverted schlieren and OH*CL data, obtained with the use of large number of injections, to monitor spray development, reaction zone movement, and related phenomena.

Figure 7 shows results of liquid length, vapor penetration and OH*CL lift-off length for the three fuels studied in same format as the first section of results evaluating the representative injection. Additionally, the bottom panel indicates the quantitative soot results for the two cases (the third is too low to measure). Thermophysical properties of the fuel determine the liquid length. N-Heptane has lower boiling point and

lower density which resulted in smaller liquid length of 10 mm at the test conditions. The higher boiling point and density of CN54 and CN40 increased the liquid length to about 18 mm. Fuel evaporation added negligible physical delay of only 0.1 ms to produce fully vaporized fuel for mixing within 0.15 to 0.25 ms after injection. The vapor penetration length was independent of the fuel indicating that fuel properties do not affect the overall entrainment of ambient fluid and mixing, a result in agreement with the findings in the literature.

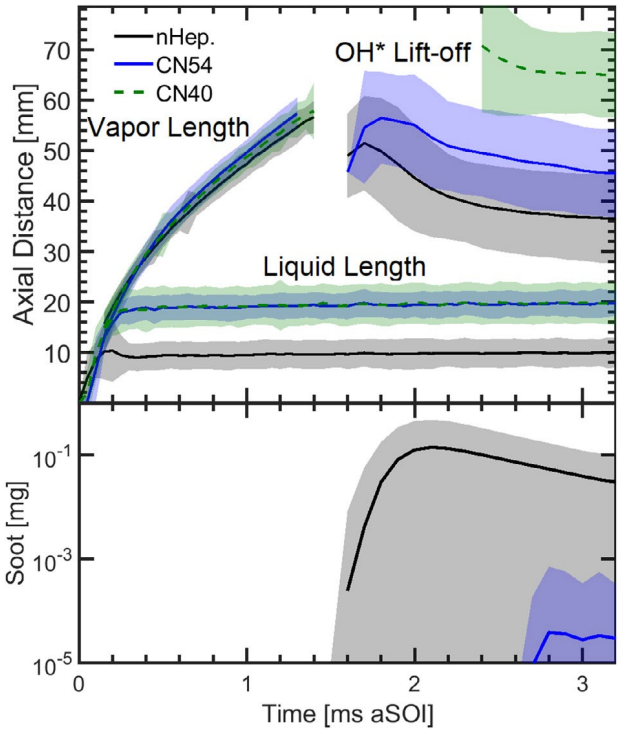

Figure 7. Average global parameters including (top) liquid- and vapor-penetration lengths, lift-off length, and (bottom) total soot mass. Shaded regions show the 95% CI of data. This is reproduced from Fig. 4 in Parker et al. publication.

The average ignition behavior is apparent in Fig. 7 at the start of OH/soot signal, while the distribution of ignition delay time across the full dataset is shown in Fig. 8. The ignition delay times are indistinguishable between n-heptane and CN54 indicating that the present experiment accurately replicated the CN behavior of these two fuels.

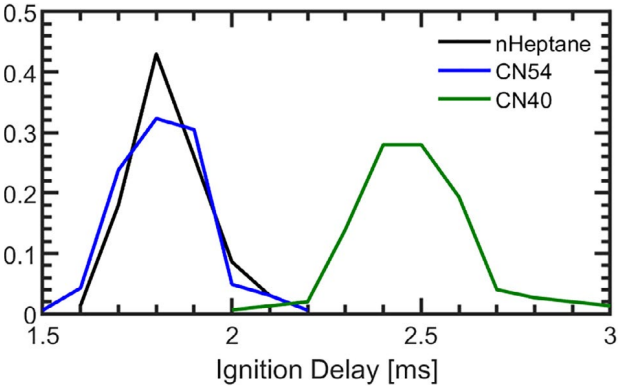

Figure 8. Normalized histograms of ignition delay time for each fuel (bin width = 0.1 ms). This is reproduced from Fig. 5 in Parker et al. publication

As shown in Fig. 9, and in spite of the same CN and ignition timing, the ignition and quasi-steady flame location occurred at different axial locations for n-heptane and CN54, indicating that these differences are caused by thermophysical effects as opposed to chemical effects of the fuel. Ignition location exhibited effectively no correlation with IDTs indicating that ignition occurs in localized kernels that can take different trajectories depending upon the turbulent mixing processes.

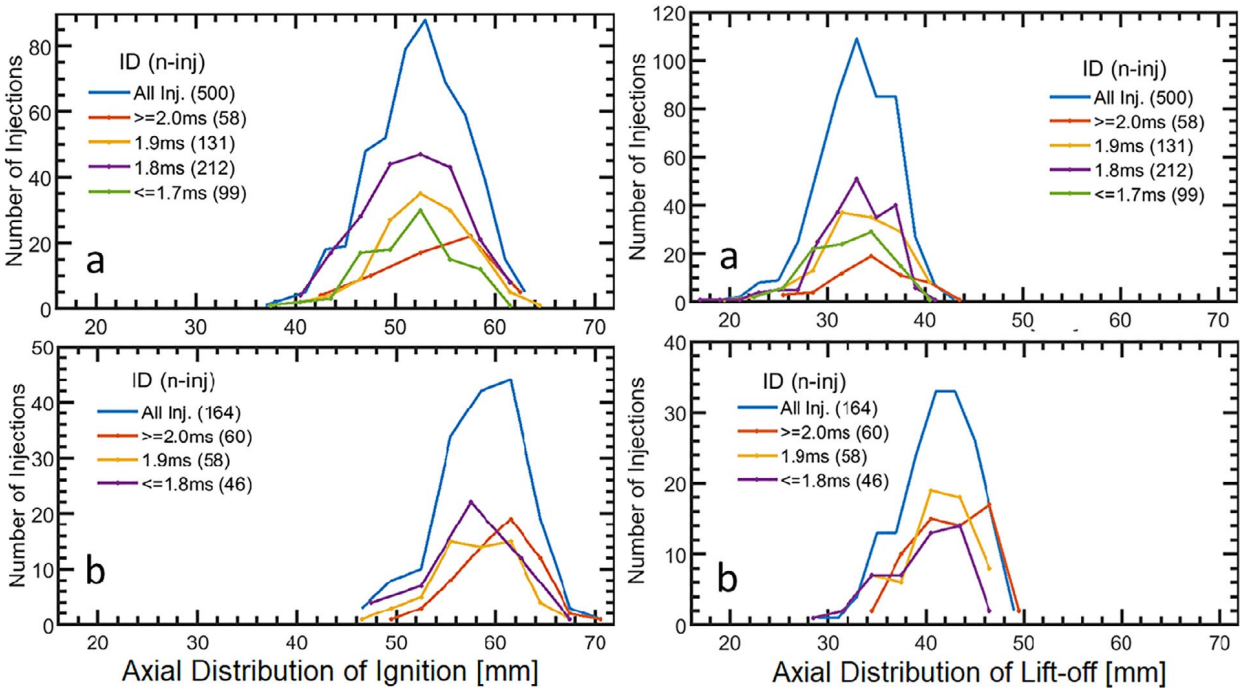

Figure 9. Histograms of the axial location of main ignition (left) and quasi-steady lift-off length (right) for (a) n-heptane and (b) CN54 (bin width = 1.5 mm). Different curves represent data segmented into bins of ignition delay times. The number of injections contributing to each curve is shown in the legend. This is reproduced from Fig. 6 and 6 in Parker et al. publication.

A unique portion of this work was the separate evaluation of the first-stage ignition/ low-temperature heat release (LTHR) behavior enabled with the RSD diagnostic. The results in Fig. 10 show that the LTHR timing was consistent between CN54 and heptane (supporting idea of ignition being a chemical dominated effect) however the location is closer to the injector for n-heptane followed by CN54 and then CN40. The quasi-steady lift-off length was also positioned in the same sequence, i.e., n-heptane, CN54, and CN40. This is linked to the thermophysical properties that cause increased liquid length and thus a likely richer mixture forcing LTHR and lift-off to occur further downstream.

The robust LTHR likely increased PAH formation before lift-off as precursors to soot. In agreement with existing correlations between soot mass and lift-off length, soot mass was highest for n-heptane, followed by CN54 and then CN40. This trend does not agree with measurements of a fuel's soot propensity based on simple flame configurations. All these factors lead to a measured peak soot mass of 100x less for the CN54 blend despite matching ignition timing as can be seen in Figure 7 above.

Even though the physical delay times for fuel vaporization are similar for different fuels, the axial location where vaporized fuel becomes available depended upon the liquid length, which was found to be the primary factor affecting LTHR, ignition locations, and lift-off length. All these parameters shifted downstream by about 8 mm (same as the difference in the liquid lengths) for CN54 compared to n-heptane leading to the observation that sooting behavior of a fuel in high-pressure diesel-like reacting sprays can be contrary to the expectations based on fundamental studies of fuel's molecular structure.

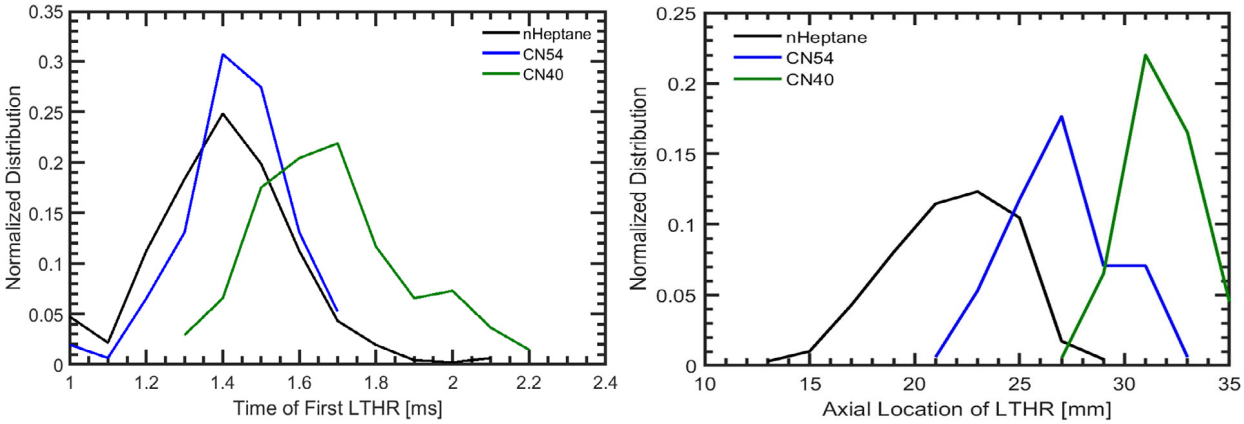

Figure 10. (left) Histogram plot of Low-Temperature Heat-Release (LTHR) timings for each fuel (bin width = 0.1 ms), and (right) Histogram plot of Low-Temperature Heat-Release (LTHR) location for each fuel (bin width = 2 mm). This is reproduced from Fig. 11 and 12 in Parker et al. publication.

Co-Optima Candidate Fuels Results:

In this study, two oxygenated biofuels, diesel-surrogate n-heptane blended with methyl decanoate (MDN) and dimethoxymethane (DMM) are investigated experimentally in the same apparatus and with same optical diagnostics set as discussed above. Results show that both biofuels have longer IDTs than n-heptane and this, together with increased LoL, contribute to a reduced soot formation in these fuel jets. Differences in soot-production in premixed vs diffusion flame zones emerge fuel-to-fuel but decrease with increasing ambient temperature and/or pressure. Additionally, a range of test conditions are explored in this work leading to observations of different regimes of soot formation between the different fuel blends.

Figure 11 shows similar results as in previous sections. As demonstrated in the work evaluating the CN54 compared to n-heptane, the fuel properties (boiling point and heat of vaporization) led to preferential evaporation of blended fuels. DMM is expected to evaporate faster than n-heptane, and so n-heptane controls the liquid length of the DMM20 blend; MDN is slower to evaporate, and so MDN20 has a longer liquid length. This longer liquid length for MDN20 is postulated to increase the lift-off length, and thus, reduce the soot production. OH*CL lift-off length varies fuel-to-fuel, although flame recession/stabilization behavior is remarkably consistent fuel-to-fuel. Introduction of more dense, oxygenated fuels to n-heptane postponed ignition delay and differences in ignition delay, lift-off, etc., were diminished as expected with increasingly high ambient pressures/temperatures. The conditions utilized in this study allowed improved differentiation of fuel effects while still being diesel-relevant.

Figure 12 shows the total average soot mass in red for each fuel blend and each test condition during the entire injection event. The contour shows the distribution of data overall injections. It is apparent that there are some significant sooting injections that draw the average up despite many injections showing very low soot in some cases.

In general, the blended candidate fuels significantly decreased produced soot-mass with sharp distinctions emerged between soot produced during the pre-mixed and diffusion-controlled combustion modes. Soot production from the pre-mixed mode is dominant at lower ambient pressure/temperature conditions, with diffusion behavior growing to dominate soot-production at the more intense conditions; this behavior is significantly impacted by blending of candidate fuels, with MDN slightly reducing the soot-production profile of n-heptane and DMM vastly reducing the diffusion-mode sooting.

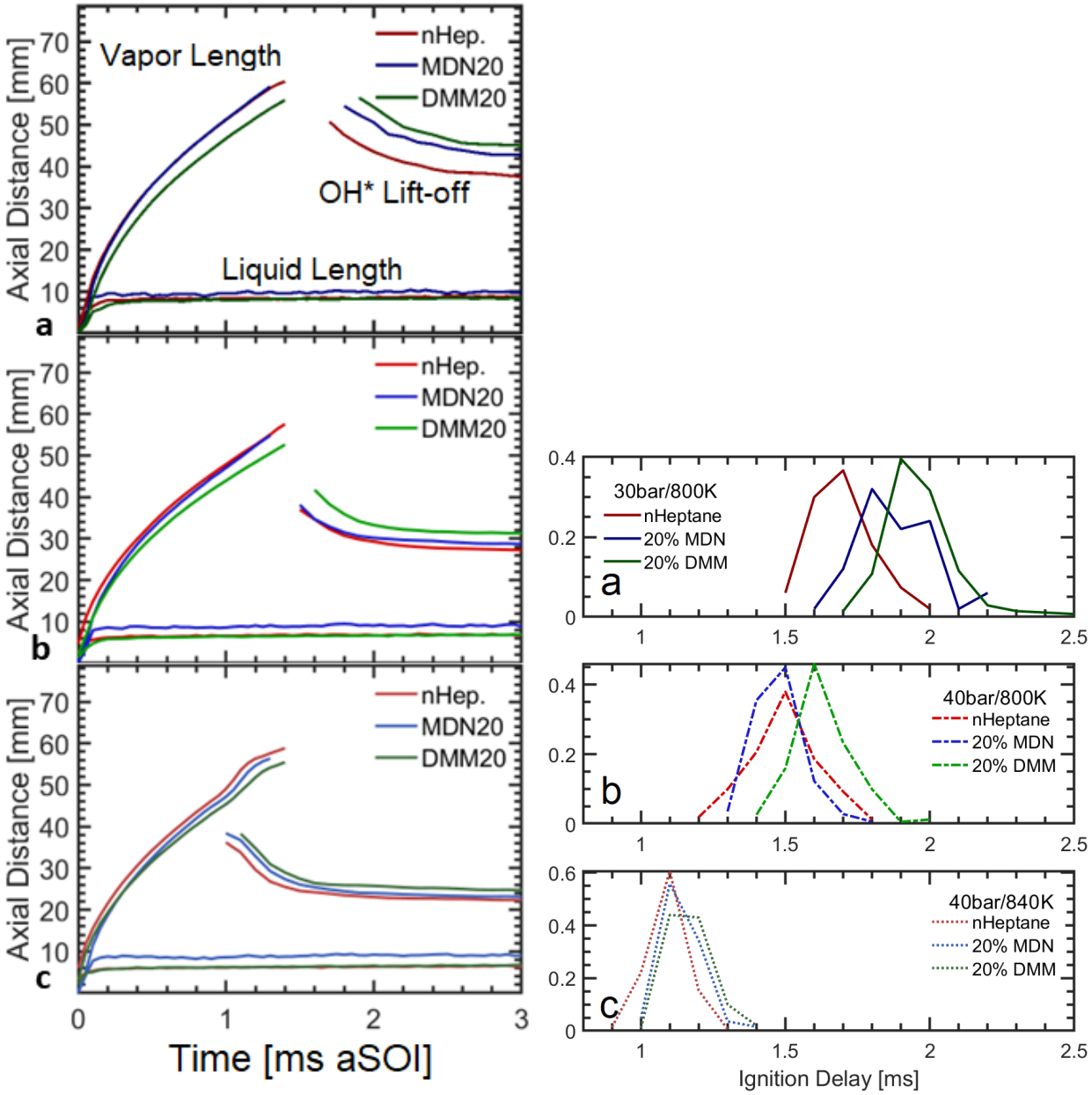

Figure 11. (right) Average liquid length, vapor length and OH lift-off length, and (left) Normalized distributions of ignition delay for each fuel blend over at least 150 injections and at three operating conditions.*

The candidate fuels MDN and DMM were observed to significantly lower sooting behavior in diesel-like settings when blended with n-heptane. Some undesirable combustion behavior resulted - elongated lift-off and greater ignition delay - however these differences diminished as ambient conditions approached true diesel-engine values. These sooting and combustion trends agree with results in the literature. Future work can extend this study to increasingly high-pressure/temperature conditions, and by vary blend ratios to determine the potential of candidate fuels to realize lower soot-production in-cylinder without significantly and adversely effecting critical combustion parameters at relevant conditions.

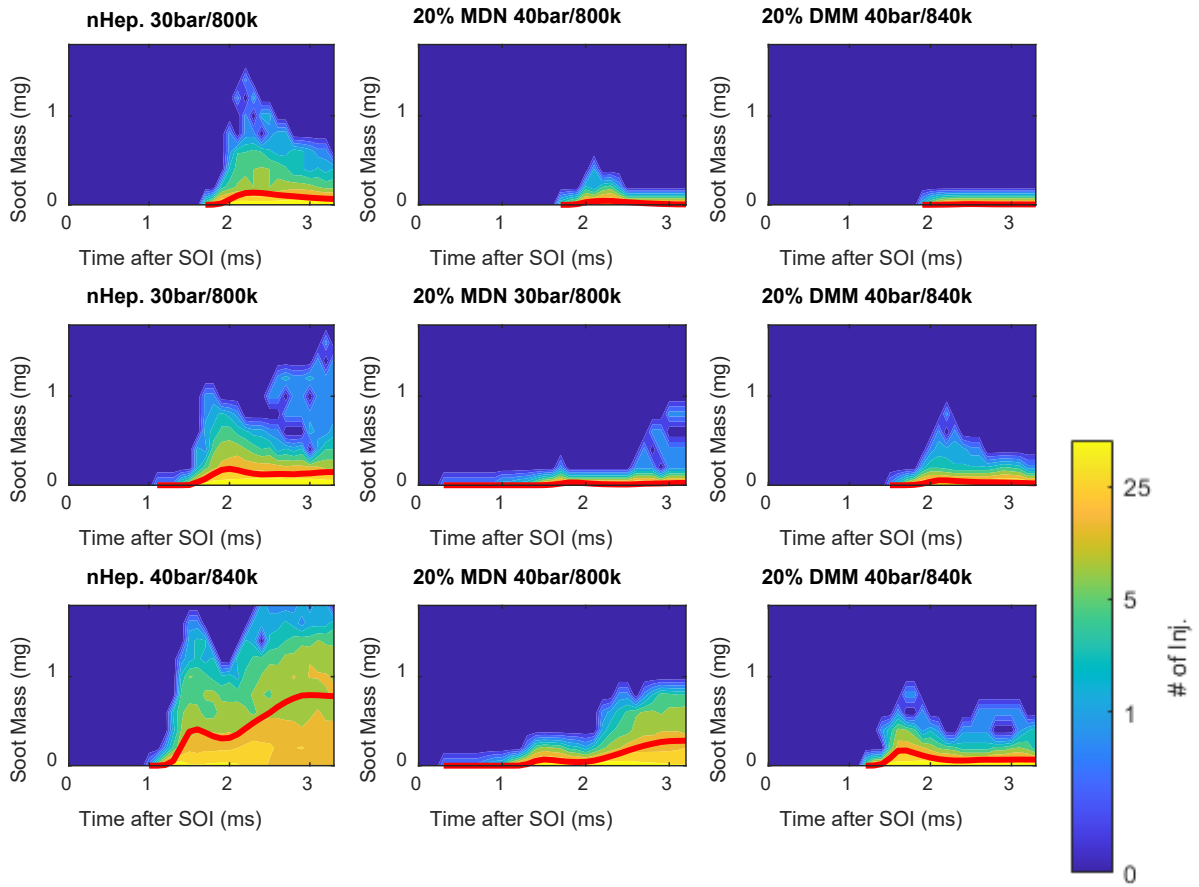

Figure 12. Total soot mass for all fuels and all test conditions. Redline indicates the average soot mass profile while the contour shows 2-D histogram of injection count at each time and bin level.

Conclusions

Consistent with literature and supported by present observations for both conventional primary reference fuels [3] and the co-optima fuel candidates, the spray development and mixing, low temperature heat release (if distinguishable), flame stabilization processes, and injection-to-injection variations can have greater impact on the sooting behavior than the chemical make-up of the fuel alone. Thus, this project suggests that fuel screening efforts should consider transient spray development and combustion at relevant ambient conditions, and how these phenomena are affected by fuel's chemical and thermophysical properties while utilizing large number of injection experiments.

Two Co-Optima identified fuel blend candidates, methyl decanoate (MDN) and dimethoxymethane (DMM) were tested at a range of diesel like conditions. Results show both the effect of thermophysical properties on the behavior as well as the chemical structure and subsequent reaction path ways effect on combustion and soot formation. Specifically, the MDN blend nearly completely suppresses any soot formation during premixed period near ignition while the DMM blend more effectively suppresses soot formation in the quasi-steady period.

This study shows that fuel screening process must consider thermophysical and chemical properties of the fuel and how it affects fuel-air mixing and spray development, which determines the equivalence ratio at the lift-off length and thus, soot formation in the downstream diffusion flame. Present test apparatus is ideal to conduct these evaluations using small quantities of fuel, on the order of 100 mL per test.

Acknowledgements

We would like to thank Chuck Mueller of Combustion Research Lab at Sandia National Laboratory for technical guidance and input on various aspects of this project.

Publications

The following papers were supported in full or in part by this award. Drafts or full papers of each are provided at the end of this report as attachments.

In preparation:

1. Parker, A., Reggeti, S.A., Agrawal, A.K., Bittle, J.A. "Effects of Selected Biofuel Blends on Transient Spray and Combustion at Diesel-Like Ambient Conditions" In preparation for submission to *Fuel*

Published:

1. Reggeti, S.A., Parker, A., Stevenson, A., Agrawal, A.K., Bittle, J.A. 2023, "Spatially-resolved soot evolution and statistics in high-pressure diesel spray flames using two-color pyrometry" *Combustion and Flame*, 261. https://doi.org/10.1016/j.combustflame.2024.113297
2. Parker, A., Agrawal, A., and Bittle, J.A., 2023, "Representative Phenomena of Cyclic Turbulent Combustion in High-Pressure Fuel Sprays," *Flow Turbulence Combust* 111, 675–696 (2023). https://doi.org/10.1007/s10494-023-00432-3
3. Parker, A., Reggeti, S.A., Bittle, J.A., Agrawal, A.K. "Limitations of cetane number to predict transient combustion phenomena in high-pressure fuel sprays" *Combustion and Flame*, 251, 2023. https://doi.org/10.1016/j.combustflame.2023.112723
4. Reggeti, S.A, Agrawal, A.K., Bittle, J.A., (2022) "Robust two-colour pyrometry uncertainty analysis to acquire spatially-resolved measurements", *Measurement Science and Technology*, 33 125201 https://doi.org/10.1088/1361-6501/ac88e9
5. Reggeti, S. A., Parker, A., Wanstall, C. T., Agrawal, A. K., and Bittle, J. A. (2021). "Comparing Global Spray Combustion Characteristics and Local Shot-to-Shot Variations in a Reacting *n*-Heptane Spray." ASME. *J. Eng. Gas Turbines Power*. September 2021; 143(9): 091018. https://doi.org/10.1115/1.4050868
6. Wanstall, C. Taber, Joshua A. Bittle, and Ajay K. Agrawal. "Quantitative concentration measurements in a turbulent helium jet using rainbow schlieren deflectometry." *Experiments in Fluids* 62 (2021): 1-13. https://doi.org/10.1007/s00348-021-03154-2
7. Allen Parker, C. Taber Wanstall, Shawn A. Reggeti, Joshua A. Bittle, Ajay K. Agrawal, (2020) "Simultaneous rainbow schlieren deflectometry and OH* chemiluminescence imaging of a diesel spray flame in constant pressure flow rig" *Proceedings of the Combustion Institute* 2020, https://doi.org/10.1016/j.proci.2020.05.045.
8. Wanstall, C. Taber, et al. "A Robust Statistical Algorithm for Boundary Detection in Liquid Sprays." *Atomization and Sprays* 29.12 (2019). https://doi.org/10.1615/AtomizSpr.2020032584
9. Wanstall, T., Agrawal, A., Bittle, J. (2019) "Implications of Real-Fluid Mixture Thermodynamics on Optical Properties under Compression Ignition Engine Conditions" *Combustion and Flame* 214 (47-56) https://doi.org/10.1016/j.combustflame.2019.12.023
10. Reggeti, S., Agrawal, A., Bittle, J. (2019) "Two-color pyrometry system to eliminate optical errors for spatially resolved measurements in flames" *Applied Optics* 58 (No. 32) (8905-8913) https://doi.org/10.1364/AO.58.008905

Effects of Selected Biofuel Blends on Transient Spray and Combustion at Diesel-Like Ambient Conditions

Allen Parker[c], Shawn A. Reggeti[c], Ajay K. Agrawal[c,d], Joshua A. Bittle[c]

[a] *University of Alabama, Alabama, United States*
[b] *corresponding author,aagrawal@eng.ua.edu*

Preprint submitted to Fuel *April 22, 2024*

Effects of Selected Biofuel Blends on Transient Spray and Combustion at Diesel-Like Ambient Conditions

Allen Parker[c], Shawn A. Reggeti[c], Ajay K. Agrawal[c,d], Joshua A. Bittle[c]

[c] *University of Alabama, Alabama, United States*
[d] *corresponding author,aagrawal@eng.ua.edu*

Abstract

Improved understanding of combustion processes is important to screen emerging biofuel candidates and advanced combustion modes with the potential to reduce soot and other airborne pollutants in diesel engines. In this study, two oxygenated biofuels, methyl decanoate and dimethoxymethane blended with diesel-surrogate n-heptane are investigated experimentally at high-pressure, high-temperature reacting conditions in an optically accessible test chamber. This chamber utilizes heated airflow to provide stable operating conditions at a constant pressure to perform a large number of injections in quick succession. Rainbow schlieren deflectometry, OH* chemiluminescence, and two-color pyrometry, all at high acquisition rates, are utilized to image different regions of the transient, reacting jet. Image analysis is performed to determine combustion parameters including ignition delay time (IDT), lift-off length (LoL), and soot zones. Results show that both biofuels have longer IDTs than n-heptane and this, together with increased LoL, contribute to the reduced soot formation. Differences in soot-production in premixed autoignition zone and quasi-steady diffusion flame zone emerge fuel-to-fuel, but decrease with increasing ambient temperature and/or pressure.

Keywords: Diesel Fuels, Co-Optima Project, Fuel Selection, Sooting Tendency, Optical Diagnostics

1. Introduction

Owning to their high energy density, liquid fuels are indispensable for applications requiring long range or duration of use, light weight, and intense heat release rates. Facilitating these uses of liquid fuels while also addressing increasingly stringent emissions regulations, particularly in the transportation sector, recent research has aimed to simultaneously co-optimize biomass derived fuels and advanced combustion modes to reduce emissions of nitric oxides (NOx), carbon monoxide (CO), particulate matter (PM)/soot, and greenhouse gases. Promising renewable biofuels from a wide range of available options have been identified for diesel engines [1, 2, 3]. Evaluating candidate biofuels to determine which merit further research and investment requires a fundamental understanding of the combustion processes and sooting behavior.

Conventional diesel combustion can be divided into two regimes: (1) rich premixed combustion at the lift-off length (LoL), and (2) mixing controlled, diffusion-combustion along the jet periphery [4]. Recent work has focused on altering the relative proportions of these two combustion modes using advanced fuel injection and mixing strategies [5]. The high jet momentum near the injector exit entrains the oxidizer where the fuel-air mixture preparation and premixed combustion processes are critically affected by the stoichiometric air-to-fuel mass ratio (AFR). Particularly, the equivalence ratio at the lift-off length (LoL) - the axial location for quasi-steady flame stabilization - has been correlated with soot formation in diesel combustion [6, 7, 8]. Oxygenated fuels, i.e., fuels containing oxygen molecules, require less oxygen for complete combustion, and thus, they could produce cleaner flames with lower soot formation [9, 10, 11].

Oxygenated fuels can also be less volatile, and less reactive, i.e., lower cetane number (CN) or longer ignition delay time (IDT), than conventional diesel fuels. Longer IDT increase time for fuel-air mixing to reduce soot formation [6, 7], but delayed ignition could adversely affect the thermodynamic cycle efficiency. Many researchers have noted these difficulties as barriers for widespread adoption of biofuels [12, 9, 13, 14]. Current research has focused on utilizing biofuels and other fuel additives without compromising the ignition behavior [15, 16, 17, 18]. However, the wide range of candidate fuels with different chemical and thermophysical properties makes the screening process of alternative fuels very difficult; this is increasingly true across different applications and operating conditions.

Several methods have been used to test and predict combustion behavior of candidate fuels, which can be currently very expensive to manufacture [14], besides the costly engine testing process. Droplet combustion, shock tubes, and micro flow reactors [19, 20] are each methods to experimentally simulate combustion while using small quantities of fuel. Computational metrics have been created to predict sooting and other combustion behavior based on experimental data from various fuels. For example, the Yield Sooting Index (YSI) has been used to characterize diesel fuels and their surrogates [21, 22, 23, 24]. However, these fundamental studies at simplified test conditions raise the concerns of applicability at in-cylinder, diesel-combustion environment.

Metal engines [10] and optical engines [9, 25, 11, 26, 12] have been used successfully to investigate combustion of biofuels and their blends, although these tests require larger fuel volumes. Optically accessible constant-volume [27] and constant-pressure [28, 29, 30] flow chambers offer a reasonable compromise between testing methods, because they can replicate in-cylinder processes while requiring only modest quantities of fuel. These optical chambers also provide convenient means to assess, via high speed diagnostics, the critical parameters governing spray development and combustion.

In this study, a constant pressure flow chamber (CPFC) is used to achieve high-pressure and high-temperature conditions to study transient, reacting sprays of n-heptane and blends of n-heptane with methyl decanoate (MDN) and dimethoxymethane (DMM) [14]. Experiments are conducted at diesel engine relevant conditions, though at slightly lower pressures and temperatures, to discern combustion differences, fuel-to-fuel and condition-to-condition. For each test campaign, at least 150 injections are recorded in quick succession at stable ambient con-

ditions to obtain reliable and statistically stationary values of global parameters including liquid length, vapor penetration length, LoL, IDT, soot mass, etc. Three optical diagnostics at high acquisition rates are applied simultaneously: (1) Rainbow schlieren deflectometry (RSD) to determine liquid and vapor penetration lengths [31, 29], (2) Hydroxyl (OH*) chemiluminescence (OH*CL) to determine IDT, flame recession, and LoL, and (3) Two-color pyrometry (2CP) to quantify the line of sight (LOS) soot mass at each pixel location [32, 33].

Biofuels in this study consist of MDN, a short-chain ester and DMM, a polymethylene ether, both identified as potential biofuels for further study [14]. The MDN, derived from oilseed crops, has been successfully blended with diesel fuels to achieve desired results including lower emissions and minimal impact on CN [25, 11, 12, 26]. The DMM is less widely studied, because of its lower CN, flash point, and boiling point [13], although it has been found to reduce soot and other emissions [9, 10]. In the present study, these fuels will be blended with n-heptane and tested for a range of ambient conditions to gain insight into combustion and sooting behavior. Experiments utilize only about 300 mL of fuel to record in excess of 450 injections at the three test conditions for each fuel.

2. Experimental Setup and Test Conditions

Figure 1 shows the CPFC that has been documented previously to provide stable operating conditions for a large number of consecutive fuel injections [29, 28]. In brief, air preconditioned to the desired temperature and pressure is flowed continuously through the chamber at near quiescent flow velocities compared to the fuel injection velocity (0.5m m/s vs 250 m/s, respectively), but sufficient to thoroughly flush combustion products from the chamber between injections at 8 s intervals. About 150 injections per hour can be recorded, limited by the video download speed of the cameras. The fuel is injected along the axis of the chamber by a Bosch CRIN3-18 injector modified to have a single 104 μm hole at the tip. Ambient and fuel test conditions are summarized in

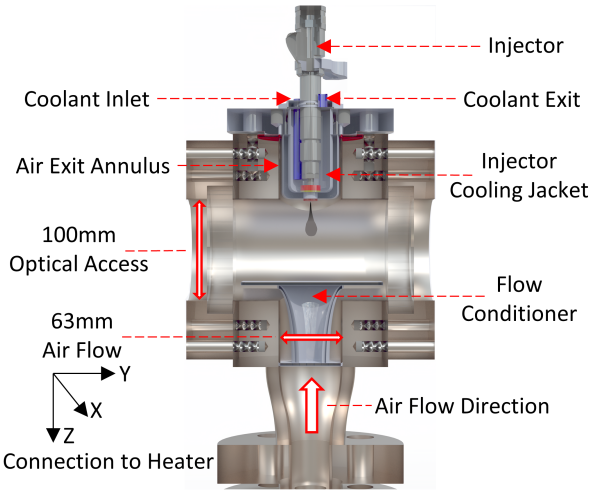

Figure 1: Schematic of the optically accessible constant-pressure flow rig (CPFR).

Table 1. Table 2 lists the properties of the component fuels used in this study. Fuel blends will be referred to as MDN20 (20% MDN/80% n-heptane) and DMM20 (20% DMM/80% n-heptane) throughout the remainder of this paper.

Figure 2 displays the layout of the three optical diagnostics employed simultaneously as discussed previously in detail [28, 30]. The RSD operated at ?? kHz enables detection of liquid and vapor penetration lengths [34], and quantification of local properties such as the average planar refractive index difference (related to density and equivalence ratio) [29, 31]. Another high speed camera at ?? kHz, combined with an intensifier (Invisible Vision Model 1850-10-S20) and band-passed (310 nm) ultraviolet (UV) filter, records OH*CL to determine IDT, LoL, and diffusion flame zones. Lastly, a third high-speed camera at ?? kHz records soot incandescence simultaneously at two wavelengths (550 and 650 nm) to enable spatially resolved LOS measurements of soot-density (KL) and temperature [32, 33].

2.1. Images and Data Analysis

In this section, images obtained by the three optical diagnostics will be displayed and the image analysis procedures used to extract important parameters

Table 1: Test conditions for CPFR experiments with ±95% sample confidence intervals. All experiments were conducted with air (21% oxygen) and 4.5 ms injection duration. Blended fuels contain 20% of the named fuel, by volume, with the remainder being n-heptane. Injected fuel was in all cases at 363±0.2 K, 99.3±0.1 MPa.

		heptane	
	3 MPa, 800 K	4 MPa, 800 K	4 MPa, 840 K
Ambient			
Temp. $[K]$	808±5.6	807±9.4	835±5.9
Pres. $[MPa]$	3.0±0.03	4.0±0.04	4.0±0.03
Den. $[\frac{kg}{m^3}]$	13.0±0.2	17.2±0.2	16.6±0.2
Fuel			
Temp. $[K]$	363.4±.23	363.4±.25	363.4±.22
Pres. $[MPa]$	99.1±0.81	99.1±0.74	99.0±0.69
		20% MDN	
	3 MPa, 800 K	4 MPa, 800 K	4 MPa, 840 K
Ambient			
Temp. $[K]$	805±6.5	809±4.1	839±6.0
Pres. $[MPa]$	3.0±0.03	4.0±0.05	4.0±0.03
Den. $[\frac{kg}{m^3}]$	12.9±0.2	17.2±0.3	16.5±0.2
Fuel			
Temp. $[K]$	363.4±.21	363.4±.20	363.4±.21
Pres. $[MPa]$	99.1±0.83	99.1±0.77	99.3±0.80
		20% DMM	
	3 MPa, 800 K	4 MPa, 800 K	4 MPa, 840 K
Ambient			
Temp. $[K]$	807±4.6	804±4.6	833±5.4
Pres. $[MPa]$	3.0±0.03	4.0±0.06	4.0±0.04
Den. $[\frac{kg}{m^3}]$	12.9±0.2	17.4±0.3	16.8±0.2
Fuel			
Temp. $[K]$	363.4±.18	363.4±.19	363.4±.21
Pres. $[MPa]$	99.0±0.76	99.0±0.80	99.1±0.67

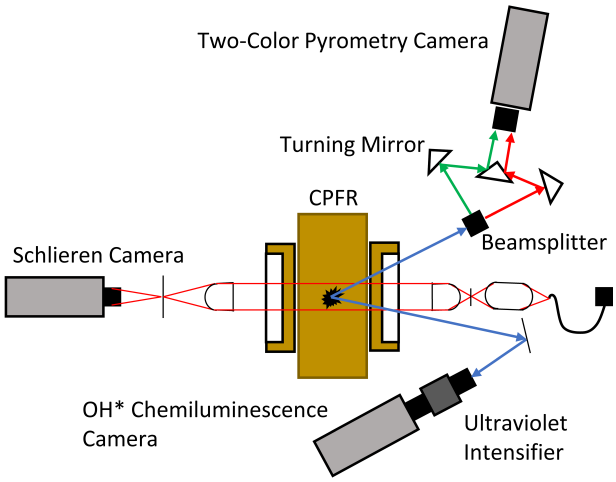

Figure 2: Simultaneous high-speed diagnostic setup including Rainbow Schlieren Deflectometry (RSD), OH* Chemiluminescence (OH*CL), and Two-Color Pyrometry (2CP). View angle of OH*CL and 2CP systems are exaggerated for illustration.

Table 2: Pure component fuel properties for n-heptane, methyl decanoate (MDN, and dimethoxymethane (DMM). Fuel properties as listed in DOE's Fuel Property Database [1].

	heptane	MDN	DMM
Mol. Weight $[\frac{g}{mol}]$	100.2	186.3	76.1
Mol. Formula	C_7H_{16}	$C_{11}H_{22}O_2$	$C_3H_8O_2$
Density $[\frac{kg}{m^3}]$	683.8^a	873.0^a	860^b
Boiling Point $[^\circ C]$	98.0	224.0	42.0
Heat of Vap. $[\frac{kJ}{mol}]$	36.57^b	46.0^a	27.9^f
Heat of Vap. $[\frac{kJ}{kg}]$	365^b	247^a	367^f
Heat Cap. $[\frac{kJ}{kg*K}]$	224.64	382.8	163.6
AFR $[\frac{mol}{mol}]$	11	15.5	4
AFR $[\frac{kg}{kg}]$	13.02	10.23	6.54
Cetane Number	$53.8^{c,d}$	52^c	29^c

$^a 20^\circ C$, $^b 25^\circ C$, ^{c}measured, ^{d}56 in [7] ^{e}definition ^{f}predicted

will be discussed. Figure 3 provides simultaneously acquired images from each diagnostic, with minimal post-processing for clarity. The RSD image is presented by preserving hue (the primary signal) within the jet, but with intensity and saturation set to 1.0, and background removed. The OH*CL and soot incandescence (at 650 nm), recorded in black-and-white, have been false-colored to yellow/magenta, respectively. The red outline shows where these signals fade to background levels. Yellow/magenta colors were chosen to represent OH*CL/2CP signals to maximize the contrast with RSD hues centered at around cyan ($180°C$). These false-colored images were combined to create the composite image at the right of Fig. 3. Images of this format will be used later to compare combustion processes among fuels/ambient conditions under this study.

The images of Fig. 3 contain extensive quantitative information. The RSD images have previously been used to determine liquid- and vapor-penetration lengths [29, 34]. The hues in the RSD image provide information about local density gradient [31] which is related to fuel-air mixing, cool-flames, and low-/high-temperature heat release [29**?**]. The OH*CL images are used to identify IDT and LoL using the methodology of Engine Combustion Network (ECN), which defines a threshold of 50% of the maximum observed intensity to distinguish reactions from the noise-floor. The high accuracy measurement of soot-mass along the LOS at each pixel location are integrated spatially to determine the total soot mass in the flame or soot mass at a specific axial location [32, 33].

3. Results

In this section, global parameters including liquid length, vapor penetration length, IDT, LoL, and soot mass at different ambient conditions will be compared for the aforementioned fuels. Results will include presentations of average behavior (over 150 injections per case), as well as selected images and data from instantaneous injections best representing their respective cases. Finally, the effect of liquid length on LoL and soot formation will be discussed. Ambient temperature/pressure have strong effects on soot oxidation and engine-out particulate levels, but this study focuses exclusively on soot formation during in-cylinder combustion only.

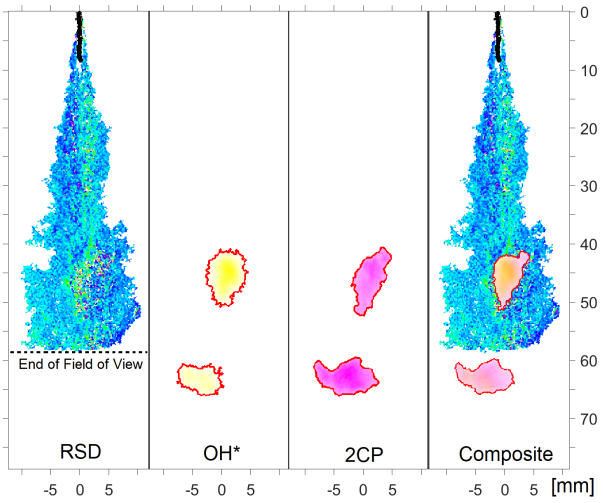

Figure 3: Combustion was simultaneously recorded by Rainbow Schlieren, OH* chemiluminescence (shown in yellow), and two-color pyrometry (in magenta) as shown in Fig. 2. Simultaneous images from each diagnostic are shown here, along with a 'composite' image to the right, in which the OH*CL and 2CP intensities are overlaid on top of the RSD hues. Red outlines were added to these intensities for heightened contrast.

3.1. Global Parameter Analysis

Figure 4 shows temporal profiles of average liquid length, vapor-penetration length, and LoL for the three fuels considered at each test condition (a/b/c, as labeled in each subplot). Prior work [35, 29, 30] and separate analyses (not shown) demonstrate that the average values in Fig. 4 achieve statistical stationarity after about 50 injections, which is far less than the 150 injections performed in this study to compute the averages. In the present study, standard deviations for liquid length, vapor penetration length, and LoL are, respectively, less than 1.5 mm, 1.0 mm, and 3.0 mm. Because of the high statistical accuracy of average values, and to improve the readability, confidence intervals (CIs) describing injection-to-injection variations are not included in Fig. 4.

Liquid Length. Figure 4 shows that the liq-

uid length in all cases increases linearly for about <0.2 ms, and then reaches a quasi-steady value which remains constant for the remaining test duration. Clearly, liquid length depends upon the fuel, but these results show that the vaporized fuel is available within 0.2 ms after start of injection (aSOI), and that the fuel vaporization time for different fuels is within 0.1 ms of each other. The liquid length measurements are highly repeatable, with standard deviation of about 1.5 mm. The liquid length is affected by ambient and fuel injection conditions [36, 37], and boiling point and heat of vaporization of the fuel. Considering the operating conditions are the same for all fuels within each case, the observed differences in the liquid length can be attributed to the differences in the thermophysical properties of the fuels.

The liquid length for MDN20 is slightly longer compared to that for other fuels. The difference increases slightly with increase in ambient pressure and/or temperature. Using data in Table 2, fuel jet evaporation would require 399 $\frac{kJ}{kg}$, 410 $\frac{kJ}{kg}$, and 358 $\frac{kJ}{kg}$, respectively, for n-heptane, MDN20, and DMM20. These differences do not solely explain trends in Fig. 4, which presents near-identical liquid lengths for n-heptane and DMM20. Considering the boiling point data in Table 2, preferential evaporation is the likely cause for the observed liquid length trends of Fig. 4. The DMM has much lower boiling point, and would evaporate first, followed by n-heptane in the DMM20 blend. This would result in nearly the same evaporation profile as n-heptane, with the only differences being the slightly lower amount of heat required to evaporate the DMM. Conversely, MDN20 blend has a longer liquid length because its n-heptane evaporates first, followed by MDN with a much higher boiling temperature. Preferential evaporation of component fuels in the MDN20 and DMM20 blends therefore offers the explanation for the observed differences in liquid lengths in Fig. 4.

Vapor Penetration Length. Figure 4 presents temporal evolution of average vapor penetration length until the jet passes beyond the RSD field of view. The vapor-penetration profiles diverge from the liquid length profiles once the latter reaches quasi-steady state. Interestingly, DMM20 has a slightly but consistently slower vapor penetration rate than the other fuels, even though the fuel injection parameters (densities, pressures, geometries, etc.) affecting jet penetration are nominally the same per Table 1) [38].

Except for the slight deviation for DMM20, the vapor penetration length is essentially the same for all fuels, and is highly repeatable with standard deviation of 1.0 mm. Note that the present approach to use lower ambient temperatures and pressures than found in diesel engines (ECN Spray-A, for instance [39]) helps to resolve case-to-case and injection-to-injection differences by the available diagnostics; standard deviations for case (c) at high pressure/temperature were much lower than those for case (a) at low pressure/temperature. The case-to-case differences are expected to reduce further at even higher temperatures and pressures. At the highest temperature case (c), the slight 'bump' in the vapor penetration length at about 1.0 ms aSOI coincides with the onset of main ignition detected by OH*CL, causing volumetric thermal expansion by high temperature heat release (HTHR).

Flame Location. Figure 4 also depicts the average axial distance of flame location from the injector exit determined from OH*CL images for all injections. The flame location was identified with respect to time between the main ignition event and quasi-steady LoL. Unlike small fluctuations in liquid length and vapor penetration length, the flame location data exhibited about 3 times larger injection-to-injection variations. In general, the flame location and LoL are shorter for n-heptane followed by MDN20 and then DMM20. Based on the comprehensive analysis of liquid length effects [29], the longer LoL for MDN20 compared to n-heptane is likely caused by differences in their liquid lengths since these two fuels have essentially the same CN. In contrast, the longer LoL for DMM20 compared to n-heptane is attributed to the low chemical reactivity (or low CN) of the former since both fuels have nearly the same liquid length. The differences among fuels decrease with increasing ambient temperature/pressure as expected, but the overall trends including upstream flame recession after ignition to reach quasi-steady LoL remain the same.

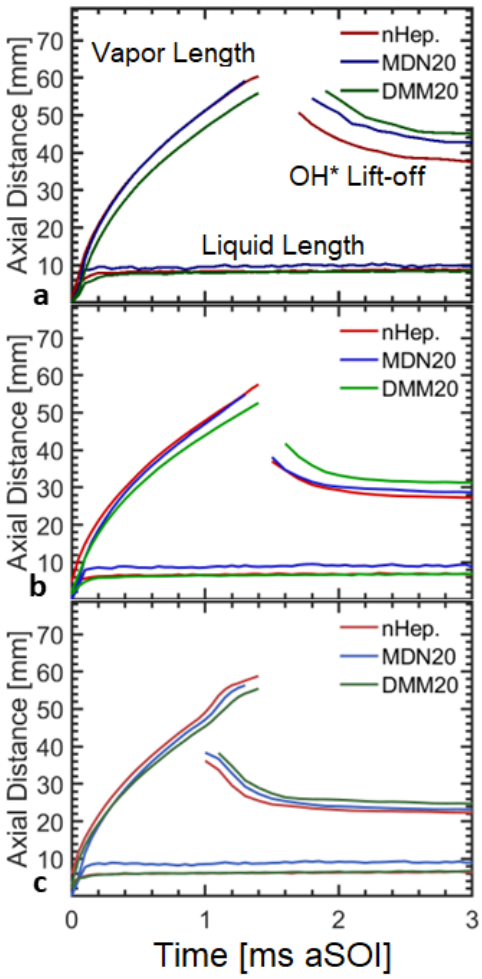

Figure 4: Liquid length, vapor penetration, and OH*CL lift-off are presented for each fuel, and each condition (a/b/c), tested.Which case is which

3.2. Ignition Delay Time

Figure 5 provides histograms of IDT for the three fuels studied; IDT is defined as the time aSOI when OH*CL is distinguishable from the noise-floor, consistent with the definition used by the ECN [39]. All fuels/conditions show a range of IDTs resulting from injection to injection variation with nearly Gaussian distributions. A rigorous analysis, not presented here, showed no correlation between slight test condition variation in Table 1 and IDTs [30]. From Fig. 5, it is clear that MDN20 has slightly higher IDT than n-heptane, and the difference diminishes completely at higher pressures/temperatures. This result is consistent with the mildly lower CN of MDN (CN = 52) compared to that of n-heptane (CN - 53.8). In contrast, DMM has much lower CN of 29 compared to n-heptane, and thus, DMM20 blend displays relatively longer IDTs, even at higher pressures/temperatures. As stated previously, these differences can be expected to reduce as ambient conditions approach true diesel-engine values, which would make it difficult to identify case-to-case differences owning to limited spatial and temporal resolutions of the available diagnostics.

3.3. Visualization of Combustion

The large number of injections required to achieve statistically stationary values in Fig. 4 suggests that injection-to-injection variation is caused by the stochastic nature of turbulent mixing. This hypothesis is independently explored in a separate work [30] to identify a representative single-injection that is closest to the ensemble average image which inherently smooths-out features of turbulence. For this reason, composite images of a representative single injection were created for each case in the style of Fig.3 using the methodology in [30]. Figure 6 presents composite images of a representative injection for each fuel for case (a) at 800 K, 3 MPa. Similarly, Figs. 7 and 8 show composite images, respectively, for case (b) at 800 K, 4 MPa and case (c) at 840 K, 4 MPa. Each injection is presented at two times aSOI, depending upon the case. The first row of Fig. 6 refers to the time of peak soot-production

after auto-ignition, and the second row pertains to the time of peak soot-production during quasi-steady injection times. The color-scales used to false-color OH*CL (yellow) and 2CP (magenta) signals in composite images are different for each fuel/case but they are the same for both rows.

Figure 6 illustrates differences in mixing, flame, and soot behavior depending upon the fuel. Composite images in the first row show a smaller mixing region for n-heptane compared to that for MDN20 and DMM20. Similarly, the initial flame region (yellow OH*CL signal) is closer to the injector tip for n-heptane compared to that for MDN20 and DMM20. The soot regimes are also different; a large intense soot cloud for n-heptane but small, low-intensity soot cloud for MDN20 and DMM20. These trends persist during the quasi-steady state as shown by the composite images in the second row. Here, the LoL is

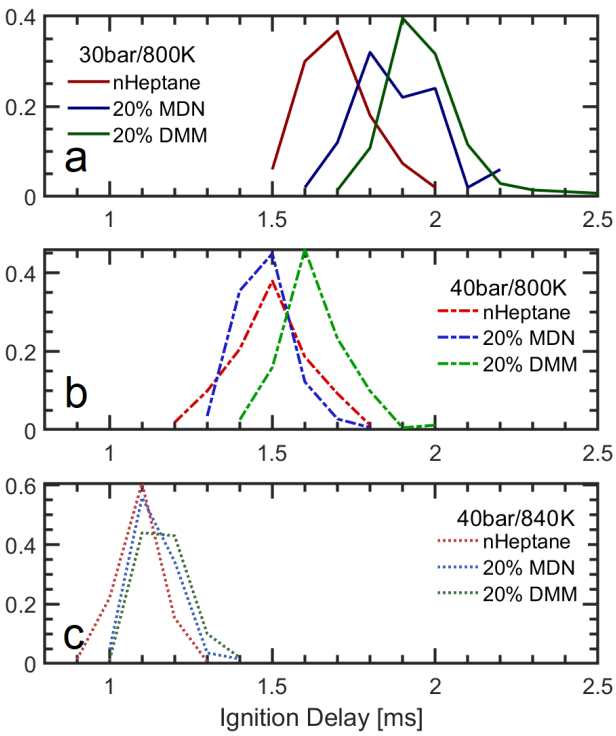

Figure 5: Normalized distributions of ignition delay for each fuel blend over at least 150 injections, determined via OH*CL signal.

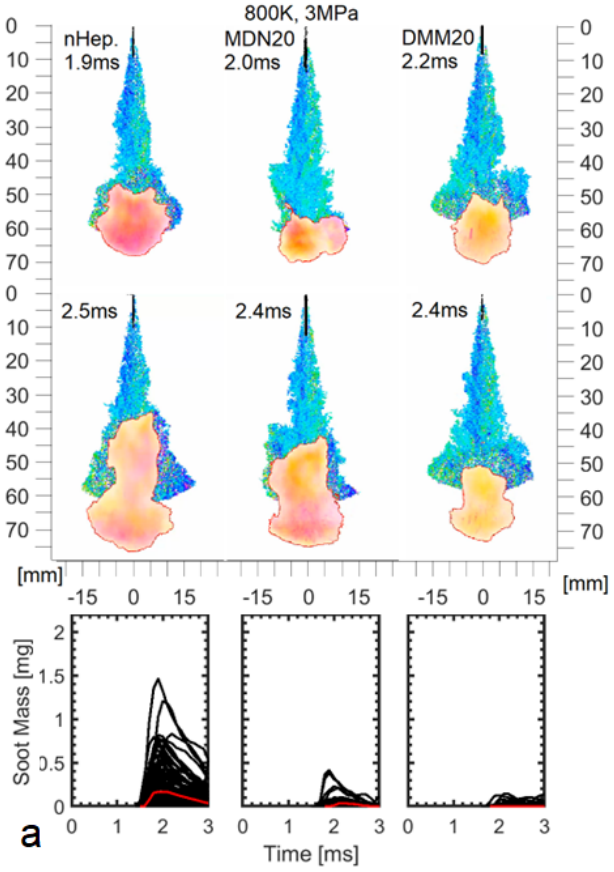

Figure 6: Composite images of representative injections from each fuel, at 800 K and 3 MPa, at select time steps. Top row corresponds to the time of peak premixed soot production, bottom row shows peak diffusion-flame produced soot. Beneath are soot-mass profiles for every injection of the respective cases, with the most representative profile - corresponding to the injections pictured above - shown in red.

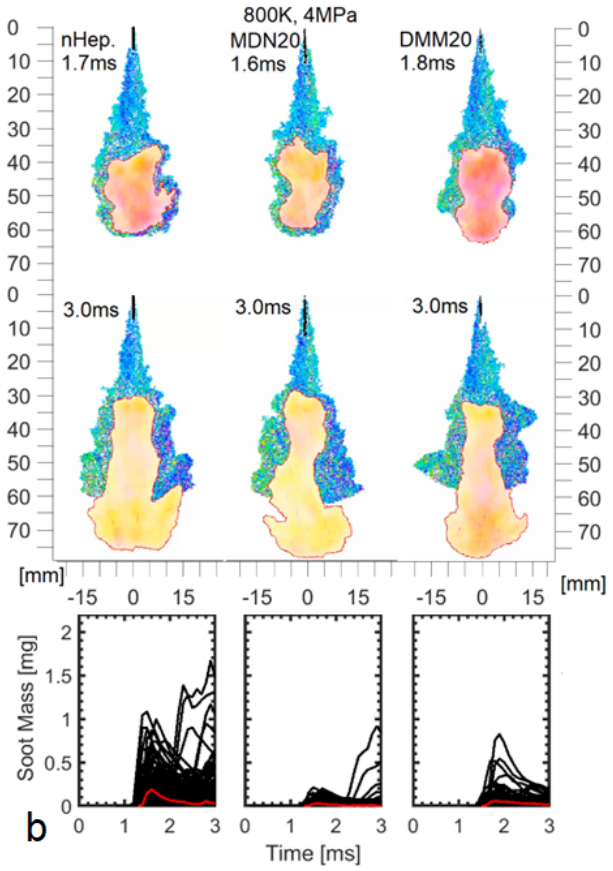

Figure 7: Composite images of representative injections from each fuel, at 800 K and 4 MPa, in the same format as Fig. 6

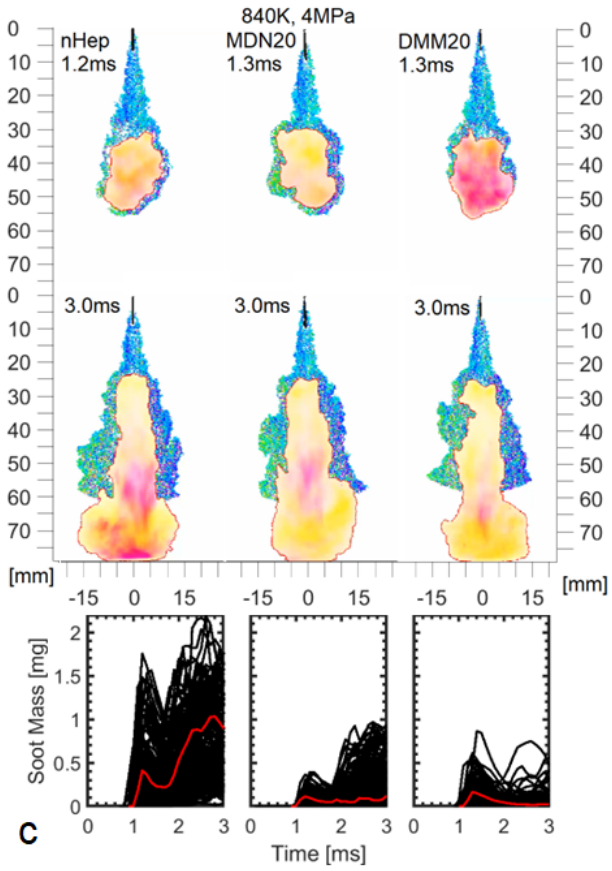

Figure 8: Composite images of representative injections from each fuel, at 840 K and 4 MPa, in the same format as Fig. 6

shortest for n-heptane and longest for DMM20, which is consistent with the results presented in Fig.4. Evidently, main ignition for n-heptane occurs earlier than the other fuel blends. However, MDN20 and DMM20 require additional time to build the radial pool required for combustion to take place.

The differences among fuels reduce at higher pressures and temperatures. For case (b) at 800 K, 4 MPa, Fig. 7 shows that the initial flame region and soot cloud are similar among fuels. Particularly, once the quasi-steady regime has been established, the LoL variation among fuels could not be distinguished from injection-to-injection variations; recall from Fig.4 that sample standard deviations for LoL were up to 3.0 mm. For this case, n-heptane and MDN20 have narrower sheaths of hot products/reactants surrounding and stabilizing the flame. For case (c) at 840 K, 4 MPa, the fuel-to-fuel differences in LoL reduce even further. Thus, the spatial/temporal resolutions of the present diagnostics are inadequate to resolve small differences at high pressures and temperatures.

Figures 6- 8 shows that MDN20 and DMM20 have remarkably different sooting behavior than n-heptane. Particularly, these fuel blends tend to reduce the soot-mass produced in the flame. However, two limitations of the present study must be stated; 1) experiments were conducted in a CPFC, not an engine, and so results pertain only to in-cylinder soot formation/oxidation, without after-treatment, and 2) soot behavior beyond 75 mm from the injector tip cannot be quantified in the present CPFC; the reacting jet impinges on the screens located at about 80 mm from the injector tip. The jet-tip reaches this distance at approximately 3.0 ms aSOI, and so discussion of soot formation will be limited to 0.0-3.0 ms aSOI, by which time the quasi-steady behavior has emerged; end-of-injection and subsequent blow-off are outside the scope of the present study.

3.4. Sooting Behavior

Figure 9 presents contour plots of average total soot-mass along the jet axis versus time until 3.0 ms aSOI for each fuel/condition. These plots were created by summing local soot-mass radially at each axial location to obtain 1-D representation of soot-mass at each time and then, averaging at that time for all injections. The results in Fig. 9 are presented as a spatiotemporal contour showing the axial (y-axis) development of soot-mass with time (x-axis). Because some conditions are over 10x sootier on average (and 100x sootier if single-injections are considered, rather than averages) than others, the contours in Fig. 9 are normalized by the number indicated in the lower left corner of each plot to show soot-mass on a visually discernible scale. For example, the 40 bar/840 K case (c) of n-heptane is on a scale 28 times greater than that of DMM20 for reference case (a) 30 bar/800 K.

For case(a), the first row in Fig. 9 shows a qualitatively similar soot zone for all there fuels. In each case, the soot mass increases after ignition, reaches a peak, and then decreases, all within a time span of about 1 ms. This soot formation/oxidation zone represents the transient stage after ignition and spans 5 mm to 10 mm axially depending upon the fuel; shortest for DMM20 and largest for n-heptane. Quantitatively, the peak soot mass is the least for DMM20, four times higher for MDN20, and 12 times higher for n-heptane. Note that the soot mass depends upon the distance between the injector tip and initial reaction zone; longer distance for DMM20 results in minimum soot mass. In each case, soot-mass produced in the early stage is mostly oxidized before quasi-steady LoL is reached. Only minor amounts of soot mass remains thereafter. More soot could be formed farther downstream, but these downstream locations are not accessible to the 2CP diagnostics.

Increasing the chamber pressure in case (b) shifts the soot zone towards the upper left corner, i.e., soot is formed earlier and closer to the injector tip as shown in the second row of Fig. 9. The soot mass increases for DMM20, decreases slightly for MDN20, and remains about the same for n-heptane. These differences highlight the role of pressure on soot kinetics depending upon the fuel. Figure 9 shows that at higher ambient pressure, a second soot zone can also be formed father downstream at times after quasi-steady LoL is reached, i.e., about 1 ms after main ignition. The demarcation point between these two soot mass zones can be denoted as the soot-lift-off length, akin to the LoL based on the OH*CL signal.

The second soot zone is barely visible for DMM20, is rather faint but distinct for MDN20, and and is quite noticeable for n-heptane. This second soot zone resides downstream of the LoL, i.e., in the diffusion flame region.

The most significant difference in soot mass takes place at the elevated ambient temperature of case (c) as shown in the third row of Fig. 9. Increase in ambient temperature shifts soot mass contours further upstream and earlier in time, which is consistent with shorter IDT and LoL. Noting the change in scale, the soot mass in the transient regime increases for all three fuels. In addition, an intense soot mass zone is evident in the diffusion flame region, especially for n-heptane and MDN20. These results show greater sensitivity of soot formation to increase in ambient temperature, compared to that for an increase in pressure. Figure 9 illustrates that soot mass in the diffusion flame region is highest for n-heptane, lowest for DMM20, and in-between these two limits for MDN20. These results depict that fuels with a shorter LoL tend to produce more soot mass. However, the faint soot mass zone in the diffusion flame region for DMM20 suggests a favorable soot kinetics with additional of DMM20 to n-heptane.

Need to rewrite from here onward after new Figure 10 is generated.

The sooting behaviors in premixed and diffusion modes are compared quantitatively in Fig. 10 showing profiles of the soot-mass produced by each mode, on average, through time. These profiles were generated by demarcating the axial location at which the premixed soot cloud declines sharply; soot-mass before this location was designated 'premixed', and after this location as 'diffusion'. The profiles for each case were normalized by the maximum soot-mass observed for either premixed or diffusion mode. Those values are shown in the parentheses of legends in Fig. 10. For example, the premixed n-heptane sooting of condition (a) peaked at 6.1 mg of soot-mass, and both the premixed and diffusion mode profiles were normalized accordingly.

Figure 10 shows that the diffusion-mode sooting in cases (b) and (c) increases sharply after the premixed sooting has peaked. Soot oxidation takes place after the premixed spike, and then the primary mode of soot production switches to diffusion mode for the remainder of the quasi-steady injection. This behavior is not evident at the lower pressure/temperature case (a), and is likely more pronounced in the more intense conditions of a diesel engine.

Fuel-to-fuel differences are likewise pronounced in Fig. 10. Case (a) shows differences in sooting onset and intensity, which correspond with AFR and fuel-oxidation. Case (b) demonstrates different behavior for DMM20, which does not mature to higher diffusion-mode sooting after the premixed spike. The increase in diffusion sooting for n-heptane is also very slight for case (b) as seen in Fig. 9, where n-heptane has a consistent soot-plume and DMM20 even has a soot lift-off which is recessed from the initial premixed spike. MDN20 at case (b) demonstrates the expected behavior, which is seen for both MDN20 and n-heptane at case (c). At the elevated conditions of case (c), the diffusion-mode sooting becomes vastly dominant for these fuels, and so in that plot the soot-profiles are normalized with regard to the diffusion-peak, not the premixed peak. It should be noted that the premixed soot peak has increased for these fuels (MDN20 and n-heptane) from case (b) to (c), just not nearly so much as the diffusion-mode sooting has. Interestingly, DMM20 at case (c) is still dominated by premixed behavior, with only slowly increasing diffusion soot-mass in Fig. 10 and a very faint soot-plume in Fig. 9.

These differences are caused by a combination of fuel-oxygenation, ignition timing (cetane number and reactivity differences), and boiling point differences. Preferential evaporation due to boiling point differences in fuel blends clearly effects liquid length, as discussed, and would therefore be expected to impact LoL and downstream mixing/soot production significantly; this cannot be definitively stated because of convolution with the aforementioned variables, merely postulated. The implication of these significant differences is that candidate biofuel and other blends, given additional and directed investigation, have strong potential to reduce soot formation at diesel conditions compared to traditional, predominately straight-chain hydrocarbon fuels.

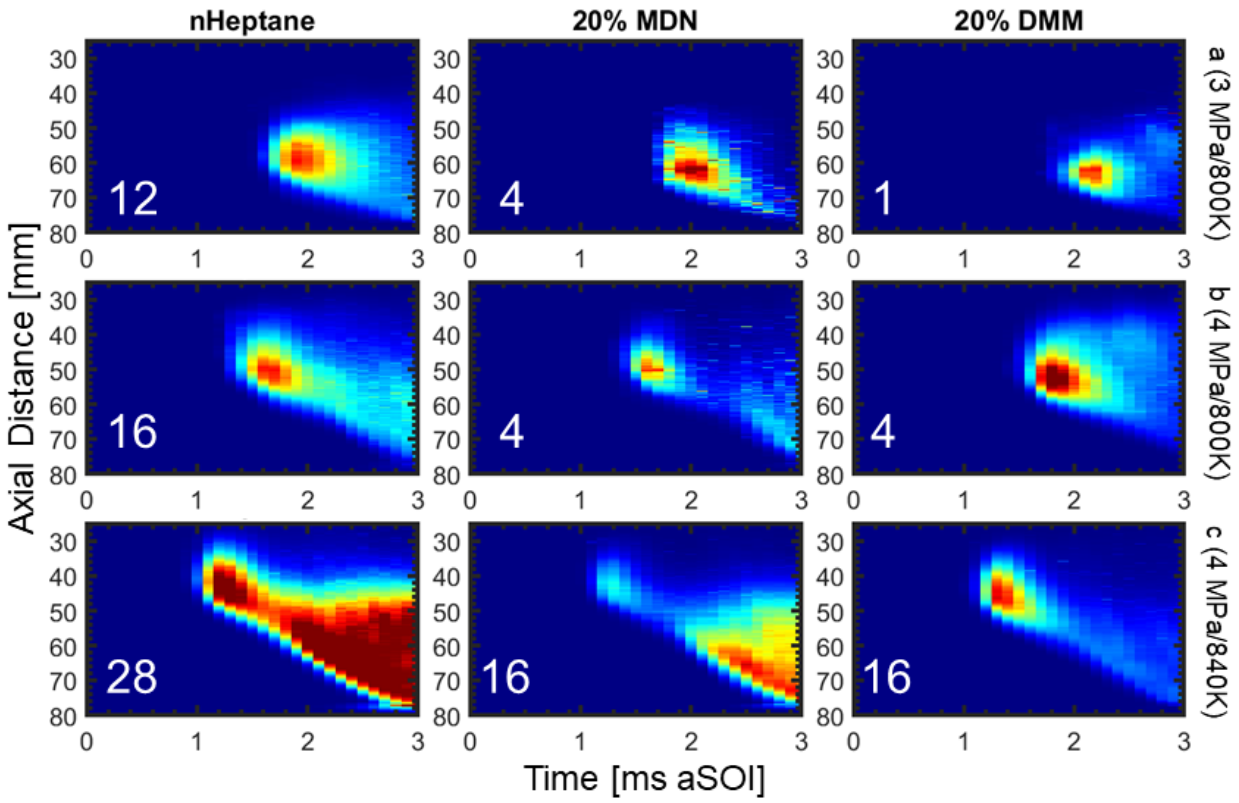

Figure 9: Spatiotemporal contours of axially resolved, average soot-mass produced by each fuel and condition

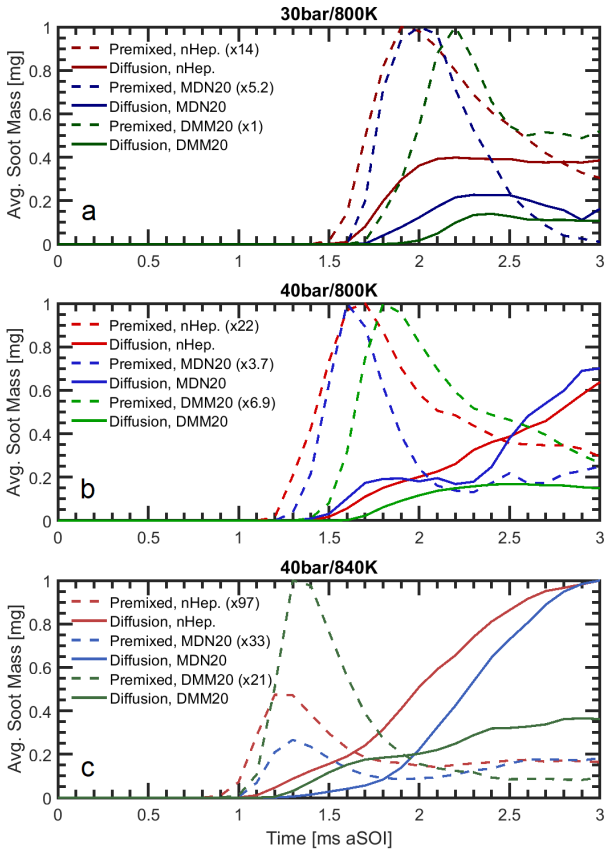

Figure 10: Soot mass produced in the pre-mixed and diffusion modes (normalized) for each fuel and condition (a/b/c). Profiles are normalized by the maximum value for each fuel/condition, and numbers in parentheses provide the peak soot-mass [mg] used to normalize each case.

4. Summary and Conclusions

In this study, two candidate biofuel fuels were blended with n-heptane to investigate the potential to reduce soot production at diesel-like conditions. Three high-speed optical diagnostics were employed simultaneously to image transient jet evolution and stabilization, and support analysis of jet penetration, fuel vaporization, ignition, flame lift-off location, and in-cylinder soot production by premixed and diffusion flame modes. Key conclusions of this study are as follows:

- Fuel properties (boiling point and heat of vaporization) led to preferential evaporation of blended fuels. DMM evaporates faster than n-heptane, and so n-heptane controls the liquid length of the DMM20 blend; MDN is slower to evaporate, and so MDN20 has a longer liquid length.
- Longer liquid length for MDN20 is postulated to increase the lift-off length, and thus, reduce the soot production.
- OH*CL lift-off length varies fuel-to-fuel, although flame recession/stabilization behavior is remarkably consistent fuel-to-fuel
- Introduction of more dense, oxygenated fuels to n-heptane postponed ignition delay.
- Differences in ignition delay, lift-off, etc., were diminished as expected with increasingly high ambient pressures/temperatures. The conditions utilized in this study allowed improved differentiation of fuel effects while still being diesel-relevant.
- Blended candidate fuels significantly decreased produced soot-mass.
- Sharp distinctions emerged between soot produced during the pre-mixed and diffusion-controlled combustion modes.
- Soot production from the pre-mixed mode is dominant at lower ambient pressure/temperature conditions, with diffusion behavior growing to dominate soot-production at the more intense conditions; this behavior is significantly impacted by blending of candidate fuels, with MDN slightly reducing the soot-production profile of n-heptane and DMM vastly reducing the diffusion-mode sooting.

In conclusion, the candidate fuels MDN and DMM

were observed to significantly lower sooting behavior in diesel-like settings when blended with n-heptane. Some undesireable combustion behavior resulted - elongated lift-off and greater ignition delay - however these differences diminished as ambient conditions approached true diesel-engine values. These sooting and combustion trends are in agreement with results in literature. Future work will extend this work to increasingly high pressure/temperature conditions, and vary blend ratios to determine the potential of candidate fuels to realize lower soot-production in-cylinder without significantly and adversely effecting critical combustion parameters at relevant conditions.

5. Acknowledgments

Funding provided by award from US Department of Energy, Office of Energy Efficiency and Renewable Energy (EERE) DE-EE0007980.

References

[1] U.S. Dept. of Energy, Fuel properties database, Available at `https://www.nrel.gov/transportation/fuels-properties-database/` (Accessed 2021/12/19).

[2] E. Polikarpov, G. Kukkadapu, R. Whitesides, M. Kass, G. Fioroni, L. Fouts, J. Luecke, D. Vardon, N. Huq, E. Christensen, X. Huo, T. Alleman, R. McCormick, Screening of potential biomass-derived streams as fuel blendstocks for mixing controlled compression ignition combustion, SAE International Journal of Advances and Current Practices in Mobility 1 (3) (2019) 1117–1138.

[3] T. Powell, J. Szybist, Fuel effects on advanced compression ignition load limits, in: SAE Powertrains, Fuels & Lubricants Digital Summit, SAE International, 2021.

[4] J. E. Dec, A conceptual model of dl diesel combustion based on laser-sheet imaging, SAE transactions (1997) 1319–1348.

[5] M. P. Musculus, P. C. Miles, L. M. Pickett, Conceptual models for partially premixed low-temperature diesel combustion, Progress in energy and combustion science 39 (2-3) (2013) 246–283.

[6] L. Pickett, D. Siebers, An investigation of diesel soot formation processes using micro-orifices, Proceedings of the Combustion Institute 29 (1) (2002) 655–662, proceedings of the Combustion Institute.

[7] L. Pickett, D. Siebers, C. Idicheria, Relationship between ignition processes and the lift-off length of diesel fuel jets, SAE Transactions 114 (2005) 1714–1731.

[8] L. Pickett, D. Siebers, Soot in diesel fuel jets: effects of ambient temperature, ambient density, and injection pressure, Combustion and Flame 138 (1) (2004) 114–135.

[9] D. Kocis, K. Song, H. Lee, T. Litzinger, Effects of dimethoxymethane and dimethylcarbonate on soot production in an optically-accessible di diesel engine, SAE Transactions 109 (2000) 2299–2308.

[10] M. Pan, W. Qian, Y. Wang, C. Wu, H. Huang, Effect of dimethoxymethane (dmm) additive on combustion and emission characteristics under different working conditions in ci engines, Fuel 284 (2021) 119304.

[11] H. C. Su, S. Kook, Q. N. Chan, E. R. Hawkes, M. K. Le, Y. Ikeda, A comparison of high-temperature reaction and soot processes of conventional diesel and methyl decanoate, Fuel 226 (2018) 635–643.

[12] J. Manin, S. Skeen, L. Pickett, E. Kurtz, J. E. Anderson, Effects of oxygenated fuels on combustion and soot formation/oxidation processes, SAE International Journal of Fuels and Lubricants 7 (3) (2014) 704–717.

[13] R. Zhu, X. Wang, H. Miao, Z. Huang, J. Gao, D. Jiang, Performance and emission characteristics of diesel engines fueled with diesel- dimethoxymethane (dmm) blends, Energy & Fuels 23 (1) (2009) 286–293.

[14] D. J. Gaspar, C. J. Mueller, R. L. McCormick, J. Martin, S. Som, G. M. Magnotti, J. Burton, D. Vardon, V. Dagle, T. L. Alleman, N. Huq, D. A. Ruddy, M. Arellano-Trevino, A. Landera, A. George, G. Fioroni, E. R. Sundstrom, E. Oksen, M. R. Thorson, R. T. Hallen, A. J. Schmidt, E. Polikarpov, E. Monroe, J. Carlson, R. W. Davis, A. Sutton, C. M. Moore, L. Cosimbescu, K. Kallupalayam Ramasamy, M. D. Kass, T. R. Hawkins, A. Singh, A. Bartling, P. T. Benavides, S. D. Phillips, H. Cai, Y. Jiang, L. Ou, M. Talmadge, N. Carlson, G. Zaimes, M. Wiatrowski, Y. Zhu, L. J. Snowden-Swan, Top 13 blendstocks derived from biomass for mixing-controlled compression-ignition (diesel) engines: Bioblendstocks with potential for decreased emissions and improved operability (7 2021).

[15] A. Al Zaabi, A. Raj, M. Elkadi, D. Anjum, A. Prabhu, G. D. Pena, L. Li, A. George, M. Nasser Al Shebli, Variation in sooting characteristics and cetane number of diesel with the addition of a monoterpene biofuel, alpha-pinene, Fuel 314 (2022) 123082.

[16] Y. Kidoguchi, C. Yang, R. Kato, K. Miwa, Effects of fuel cetane number and aromatics on combustion process and emissions of a direct-injection diesel engine, JSAE Review 21 (4) (2000) 469–475.

[17] A. F. Alhikami, C.-E. Yao, W.-C. Wang, A study of the spray ignition characteristics of hydro-processed renewable diesel, petroleum diesel, and biodiesel using a constant volume combustion chamber, Combustion and Flame 223 (2021) 55–64.

[18] B. Kerschgens, L. Cai, H. Pitsch, B. Heuser, S. Pischinger, Di-n-buthylether, n-octanol, and n-octane as fuel candidates for diesel engine combustion, Combustion and Flame 163 (2016) 66–78.

[19] S. Suzuki, M. Hori, H. Nakamura, T. Tezuka, S. Hasegawa, K. Maruta, Study on cetane number dependence of diesel surrogates/air weak flames in a micro flow reactor with a controlled temperature profile, Proceedings of the Combustion Institute 34 (2) (2013) 3411–3417.

[20] H. Nakamura, S. Suzuki, T. Tezuka, S. Hasegawa, K. Maruta, Sooting limits and pah formation of n-hexadecane and 2,2,4,4,6,8,8-heptamethylnonane in a micro flow reactor with a controlled temperature profile, Proceedings of the Combustion Institute 35 (3) (2015) 3397–3404.

[21] D. Das, C. McEnally, T. Kwan, J. Zimmerman, W. Cannella, C. Mueller, L. Pfefferle, Sooting tendencies of diesel fuels, jet fuels, and their surrogates in diffusion flames, Fuel 197 (2017) 445–458.

[22] D. Das, P. St. John, C. McEnally, S. Kim, L. D. Pfefferle, Measuring and predicting sooting tendencies of oxygenates, alkanes, alkenes, cycloalkanes, and aromatics on a unified scale, Combustion and Flame 190 (2018) 349–364.

[23] Y. Kim, B. Etz, G. Fioroni, C. Hays, P. St. John, R. Messerly, S. Vyas, B. Beekley, F. Guo, C. McEnally, L. Pfefferle, R. McCormick, S. Kim, Investigation of structural effects of aromatic compounds on sooting tendency with mechanistic insight into ethylphenol isomers, Proceedings of the Combustion Institute 38 (1) (2021) 1143–1151.

[24] M. Montgomery, D. Das, C. McEnally, L. Pfefferle, Analyzing the robustness of the yield sooting index as a measure of sooting tendency, Proceedings of the Combustion Institute 37 (1) (2019) 911–918.

[25] M. K. Le, R. Zhang, L. Rao, S. Kook, E. R. Hawkes, The development of hydroxyl and soot in a methyl decanoate-fuelled automotive-size optical diesel engine, Fuel 166 (2016) 320–332.

[26] A. Cheng, C. E. Dumitrescu, C. J. Mueller, Investigation of methyl decanoate combustion in an optical direct-injection diesel engine, Energy & fuels 28 (12) (2014) 7689–7700.

[27] L. Zheng, X. Ma, Z. Wang, J. Wang, An optical study on liquid-phase penetration, flame lift-off location and soot volume fraction distribution of gasoline–diesel blends in a constant volume vessel, Fuel 139 (2015) 365–373.

[28] S. Reggeti, A. Parker, C. Wanstall, A. Agrawal, J. Bittle, Comparing Global Spray Combustion Characteristics and Local Shot-to-Shot Variations in a Reacting n-Heptane Spray, Journal of Engineering for Gas Turbines and Power 143 (9) (2021).

[29] A. Parker, C. Wanstall, S. Reggeti, J. Bittle, A. Agrawal, Simultaneous rainbow schlieren deflectometry and oh* chemiluminescence imaging of a diesel spray flame in constant pressure flow rig, Proceedings of the Combustion Institute 38 (4) (2021) 5557–5565.

[30] A. Parker, J. Bittle, A. K. Agrawal, Representative phenomena of cyclic turbulent combustion in high-pressure fuel sprays, Flow, Turbulence and Combustion (Submitted 2022).

[31] C. Wanstall, A. Agrawal, J. Bittle, Implications of real-gas behavior on refractive index calculations for optical diagnostics of fuel–air mixing at high pressures, Combustion and Flame 214 (2020) 47–56.

[32] S. Reggeti, A. Agrawal, J. Bittle, Two-color pyrometry system to eliminate optical errors for spatially resolved measurements in flames, Applied Optics 58 (2019) 8905.

[33] S. Reggeti, A. K. Agrawal, J. Bittle, Robust two-colour pyrometry uncertainty analysis to acquire spatially-resolved measurements, Measurement Science and Technology (2022).

[34] C. T. Wanstall, A. Agrawal, J. Bittle, Phase boundary detection in transient, evaporating high-pressure fuel sprays by rainbow schlieren deflectometry, Applied optics 58 (25) (2019) 6791–6801.

[35] K. Bizon, G. Continillo, K. Leistner, E. Mancaruso, B. Vaglieco, Pod-based analysis of cycle-to-cycle variations in an optically accessible diesel engine, Proceedings of the Combustion Institute 32 (2) (2009) 2809–2816.

[36] K. Browne, I. Patridge, G. Greeves, Fuel property effects on fuel/air mixing in an experimental diesel engine, Tech. rep., Lucas CAV Ltd. (1986).

[37] B. T. Fisher, C. J. Mueller, Liquid penetration length of heptamethylnonane and trimethylpentane under unsteady in-cylinder conditions, Fuel 89 (10) (2010) 2673–2696.

[38] S. Kook, L. M. Pickett, Liquid length and vapor penetration of conventional, fischer–tropsch, coal-derived, and surrogate fuel sprays at high-temperature and high-pressure ambient conditions, Fuel 93 (2012) 539–548.

[39] Engine combustion network, `https://ecn.sandia.gov/diesel-spray-combustion/`, accessed: 2020-05-05.

Spatially-resolved soot evolution and statistics in high-pressure diesel spray flames using two-color pyrometry

Shawn A. Reggeti, Allen Parker, Anna Stevenson, Ajay K. Agrawal, Joshua Bittle*

Department of Mechanical Engineering, The University of Alabama, Tuscaloosa 35487, United States

Abstract

Previous studies of diesel spray flames have focused on details of the sooting behavior mainly during the quasi-steady period, but few have considered the spatially-resolved transient evolution in combination with injection-to-injection variations. In this study, a 500-injection data set is utilized to investigate the temporal evolution of a spray flame during auto-ignition, the premixed burn phase, and the quasi-steady period. Spatially-resolved OH* chemiluminescence data provide ignition delay times and reaction zone locations. Two-color pyrometry with a vastly improved optical system is used to quantify spatially-resolved soot evolution and its statistical variations. The ambient thermodynamic conditions are slightly below those in modern diesel engines, resulting in longer lift-off lengths and lower overall soot production. Spatially, soot formation in the lift-off region is small, but appreciable soot forms in the jet core and jet head regions, while it oxidizes gradually on the jet periphery. Total soot mass profiles indicate that regions with larger local soot mass take longer to form, but are the first to oxidize. Probability distributions of soot mass in localized regions indicate that a few injections with high soot mass bias the average soot mass data towards higher values. Overall, results show good agreement with previous studies employing different diagnostic techniques while providing sta-

*Corresponding author
Email address: jbittle@ua.edu (Joshua Bittle)

tistical details of transient and localized soot behavior in high pressure diesel spray flames in support of the related modeling efforts.

Novelty and Significance Statement

This work utilizes a newly developed two-colour pyrometry system to study spatially-resolved transient evolution of soot in high-pressure diesel-like fuel sprays. Soot size distributions and probability distributions are analyzed in localized regions of the reacting jet. Discussions of soot formation, transport, and oxidation align with others work in the literature while offering new quantitative insights. The large dataset of 500 repeated injections can be leveraged by the modelers to predict the range of behavior expected under otherwise stable conditions.

Author Contribution

SR developed two-colour pyrometry hardware, completed testing and analysis, and was primary author; AP lead testing and developed analysis tools; AS supported testing, calibration of pyrometer, data processing, AA guided conceptualization, methodology development, review and editing, and project administration, JB guided conceptualization, methodology development, review and editing, and project administration.

Keywords: transient sooting behavior; spatially-resolved soot measurements; two-color pyrometry; diesel spray combustion

---

1. Introduction

The compression ignition engine (i.e., the diesel engine) remains an attractive powertrain solution for medium- and heavy-duty transportation sectors because of its high efficiency, high power density, long range, proven durability and reliability, fuel flexibility, and affordability [1]. However, one of the primary drawbacks of diesel engines is the difficulty in managing soot and nitric oxides (NO_x) emissions. In-cylinder measurements (e.g. [2, 3, 4]) and computational fluid dynamics (CFD) modeling (e.g. [5, 6, 7]) have helped build fundamental understanding of combustion processes, but further studies are necessary

to evaluate the cyclic variation of combustion phenomena [8, 9], and refine related computational models. The complex physico-chemical processes of soot formation/oxidation in reacting fuel sprays are investigated in this experimental study of a n-heptane spray using two-color pyrometry (2CP) and OH* chemiluminescence (OH*CL) imaging. The large, 500-injection data set of this study provides spatially-resolved soot measurements with a vastly improved 2CP system to quantify the variation between injections and complement the current phenomenological understanding of diesel-like spray flames.

Past experimental studies have contributed to the conceptual understanding of soot formation/oxidation processes through physical measurements such as fast gas sampling probes [3] and optical diagnostics such as the laser extinction method (LEM) [10], laser-induced incandescence (LII) [2], diffused back-illumination (DBI) [11], and two-color pyrometry (2CP) [12]. The foundational understanding of soot formation in diesel engines was presented by Dec in 1997 based on results of laser sheet imaging by LII and planar laser-induced flouresscence (PLIF) [2]. Dec hypothesized that soot precursors form quickly during fuel-rich "premixed burn" phase followed by soot formation in the downstream jet core surrounded by a diffusion flame. Continued fuel injection leads to the "quasi-steady" period when soot and its precursors create a fuel-rich premixed flame stabilized at the lift-off length; soot formation rate is determined by the local equivalence ratio at flame lift-off length. The soot is formed in the low temperature, oxidizer-deficient jet core which is surrounded by a diffusion flame [2, 13].

Dec's model has been examined in greater detail through fundamental studies of soot formation in the quasi-steady period. Picket et al. performed studies using LEM and LII to evaluate sooting trends across different operating conditions and fuels. Results showed that peak soot increases with increasing ambient temperature and ambient density, and decreases with increasing fuel injection pressure [14]. Lift-off length was shown to relate inversely to sooting propensity because of its relationship to the local equivalence ratio [15]. A closer examination revealed that for short lift-off lengths, soot is formed mostly on the jet

periphery while for longer lift-off lengths, it is confined to the jet core [16].

In a later study, Manin et al. introduced DBI with tomographic reconstruction to enable quantitative planar soot volume fraction measurements in a diesel spray flame [11]. Du et al. simultaneously measured OH*CL and soot volume fraction (by DBI) and found that higher air entrainment (by increasing fuel injection pressure) resulted in reduced soot and thickened the planar OH*CL region near the lift-off length, which decreased the fuel-rich premixed core diameter and thus, the overall soot propensity [17]. Xuan et al. combined DBI with 2CP to obtain simultaneous soot volume fraction and planar temperature measurements, finding that the soot concentrations were highest in the jet core, away from the reaction zones surrounding it [18]. Numerous parametric studies have used 2CP to evaluate the effects of alternative fuels on overall sooting tendency (e.g. [19, 20, 21, 22]).

The above review focused on investigations of soot formation/oxidation in the quasi-steady period. However, only a few studies have analyzed the temporal evolution of soot in diesel engines. In-cylinder soot oxidation processes, particularly during late-cycle, are critical to engine out emissions [23]. Pungs et al. used in-cylinder fast gas sampling to determine the evolution of soot mass and particle size distribution in a 2.2 L four-cylinder direct-injected (DI) diesel engine (Mercedes-Benz). Findings indicated that soot forms quickly after ignition; small soot particles form initially and later grow and coagulate into larger particles. Then, these large soot particles (>70 nm) oxidize first, shifting the particle size distribution to smaller soot particles [3]. Kamimoto et al. used 2CP to quantify late cycle soot oxidation rate. They proposed a formula to convert spatially integrated soot optical density (KL) to total soot mass [23]. Results showed enhanced soot/oxidizer mixing in the optical engine tests compared to the rapid compression and expansion machine which resulted in faster soot oxidation rates, alluding to the importance of bulk fluid motion in the cylinder.

Recent work has begun to establish the importance of injection-to-injection variation of soot. Using DBI and 2CP, Xuan et al. observed large injection-

to-injection variation of soot concentration even though in-cylinder heat release rate was repeatable [8]. Reggeti et al. show significant injection-to-injection variation of spatially resolved soot mass, despite repeatable global parameters of ignition delay time and lift-off length [9]. Mueller et al. noted cyclic variation of soot through spatially integrated natural luminosity (SINL) measurements for both conventional diesel combustion and ducted fuel injection (DFI) in an optically accessible diesel engine [24]. In view of the large statistical variation, Parker et al. propose statistically-identified representative injection(s) from repeated experiments to gain additional insight into the ensemble average results [25]. However, injection-to-injection variation requires a large number of experiments to quantify the true range of sooting behavior across many injection cycles.

As a complement to experiments, CFD simulations can provide detailed flow physics and emissions predictions. The Reynolds-averaged Navier-Stokes (RANS) formulation has been used extensively for diesel engine simulations because of its computational efficiency, but the more computationally expensive Large Eddy Simulation (LES) is necessary to resolve the dominant turbulent length scales for realistic results [6]. Turbulent flow simulations coupled with detailed chemical kinetics, including soot kinetics, are prohibitively expensive [26]. Thus, soot is generally estimated by concentrations and distributions of soot precursors such as C_2H_2 and polycyclic aromatic hydrocarbons (PAH) [27]. This process, a necessary simplification for practical implementation of soot models, decouples the soot formation/oxidation from the gas phase chemistry and neglects mass exchange between gaseous species and solid soot particles. Semi-empirical soot models for RANS calculations typically provide limited information such as total soot mass and mean diameter [28, 29], while more advanced soot models based on sectional [30] or moment [31] methods are able to describe a soot number density function. However, statistically relevant experimental data are needed to validate these soot models - particularly soot emissions in RANS calculations which are employed most commonly by engine designers [6, 27].

In summary, the literature includes experimental studies on soot formation/oxidation in the quasi-steady period and at varying parametric conditions (e.g., injection pressure, ambient temperature, fuels). Few studies on temporal evolution of soot mass during an injection cycle are also available. However, spatially-resolved soot measurement in transient, high pressure diesel sprays are lacking in the literature. In addition, injection to injection variations that dictate the average and statistical distributions of soot mass are generally lacking in the literature.

This work represents a rigorous application of a vastly improved 2CP diagnostic to acquire spatially-resolved soot measurements in high-pressure diesel spray flames. Details of the optical setup and uncertainty analysis are provided in our prior publications [9, 32]. The 2CP methodology is applied in conjunction with OH*CL imaging to investigate a transient n-heptane spray at high-pressure and high-temperature (diesel-like) ambient conditions. Unlike prior studies that report only a few injections, a large dataset of 500 consecutive injections is acquired using a constant pressure flow rig (CPFR) test facility. Acquired data are processed to obtain ensemble average, root-mean-square (RMS), and probability distribution (PDs) of soot mass along the line of sight at each pixel location and at each time step to statistically describe the soot formation and oxidation processes. Concurrently, OH*CL data at each time step are ensemble averaged (across all injections), and the resulting axisymmetric distributions are Abel inverted into planar distributions of OH*CL intensity to help discern the temporal evolution of reaction zone(s) and their relationship to the sooting behavior of the flame. Results of this study provide insights into sooting propensity in different regions of the flame, and present soot mass data that can be used for CFD model validation [8, 24, 9, 6]. Moreover, the present methodology can be extended to different fuels and more aggressive diesel operating conditions.

The next section of this work presents a detailed description of the experimental apparatus followed by the data processing procedure in Sec. 3. Next, Sec. 4 shows ensemble average results for the temporal evolution of soot temperature and soot mass to identify primary soot formation and oxidation zones.

Soot evolution is explored further by assessing temporal trends of spatially integrated soot mass locally and in key regions. Finally, probability distributions of soot mass are presented to support the discussion of soot formation/oxidation phenomena.

2. Experimental Setup

The optically accessible CPFR operates at high ambient temperatures and pressures necessary for the auto-ignition of a high-pressure fuel spray as detailed in previous work [33, 9]. Air is preheated by an in-line electrical heater, and flows upward, passing through a diffuser and a flow conditioning mesh to enter the CPFR (Fig. 1). Then, the air enters into the optically accessible portion of the chamber and exhausts at the top through four 3 mm diameter holes which restrict the flow to control pressure within the chamber. Fuel is injected downwards from the top of the chamber into the relatively slow-moving air flow using a modified Bosch CRIN3-18 fuel injector modified to have a single, 104 µm orifice at the tip; fuel injection velocity is three orders of magnitude higher than the airflow velocity. The target ambient pressure and temperature are 30 bar and 800 K, respectively, and fuel injection pressure and temperature are 1000 bar, and 353 K, respectively. Steady thermodynamic conditions are maintained within the chamber throughout the repeated experiments; averages and 95% confidence interval of the mean temperatures, pressures, and other relevant experiment conditions are summarized in Table 1. Fuel-air mixing, auto-ignition, and combustion phenomena are viewed through two parallel 100 mm diameter quartz windows using high-speed optical diagnostics. Injections revealed typical features of a diesel spray flame, although ignition delay times and flame lift-off lengths are longer because the ambient pressure is lower than that in modern diesel engines.

Injection and subsequent auto-ignition and combustion processes are recorded by three time-synchronized high-speed optical diagnostics as shown in Fig. 2. Rainbow schlieren deflectometry (RSD) measurements were acquired during the

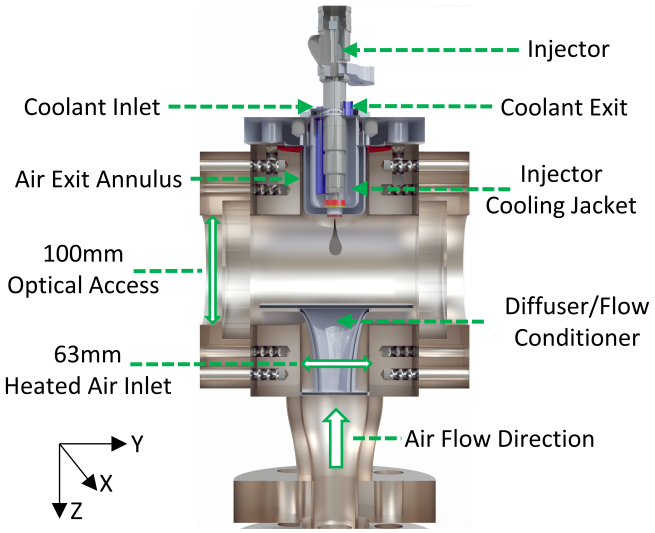

Figure 1: Schematic of the constant pressure flow rig (CPFR).

Table 1: Actual ambient air and fuel injection conditions for CPFR experiments. Variation indicates 95% confidence interval of the mean over 500 consecutive injections.

Property	Units	Value
Ambient Air		
Temperature	$[K]$	807 $\pm$4
Pressure	$[MPa]$	3.0 $\pm$0.02
Density	$[kg/m^3]$	13.0 $\pm$ 0.2
Fuel and Injector		
Type		n-heptane
Temperature	$[K]$	358 $\pm$0.2
Pressure	$[MPa]$	98.9 $\pm$0.8
Injector Orifice Size	$[\mu m)]$	104
Injection Duration	$[ms]$	4.5

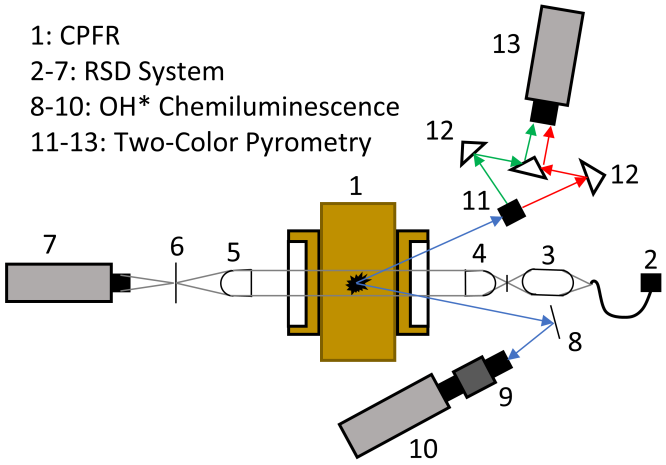

Figure 2: Above view of the experimental diagnostics layout. Numbered items refer to components of optical equipment which are detailed in the text.

experiment using components (2-7) to measure density gradients in the fuel spray/vapor zones [34, 33] but these results are not analyzed in the present work. The auto-ignition and reaction zones are detected by a high-speed OH*CL system, where light reflected by an ultraviolet (UV) turning mirror (8) is filtered by a 310 nm band pass filter and focused by a 105 mm UV lens onto an Invisible Vision UV intensifier (9) with a 70 μs gate time. The intensifier output focuses on a monochrome, 16-bit Photron SA5 camera with a 50 mm lens (10) operated at 10 kHz. The effective spatial resolution of the resulting image is 158.7 µm/pixel.

The 2CP system enables spatially-resolved measurements through an optical design that eliminates path length and parallax errors common in existing 2CP systems [35, 32]. Thermal emissions from the flame inside the chamber are bifurcated by the beamsplitter (11), filtered by bandpass filters centered at wavelengths of 550 nm and 650 nm, and then pass along a series of turning mirrors (12) to record spatially equivalent images on separate halves of a single camera sensor (13). The bandpass filters at wavelengths of 550 nm and 650 nm were selected carefully to filter out chemiluminescence from known combustion radicals including OH (306.4 nm), CH (431.4 nm), HCO (329.8 nm), C2 (516.5

nm), and NO (263.3 nm). The 2CP system camera is monochrome Phantom v7.3 with an image bit depth of 14 bits. The camera software maps the 14-bit images to 16-bit format when saving the files.

A 105 mm lens with f-stop of 2.0 provides a spatial resolution of 241.9 µm/pixel for images acquired at 10 kHz with an exposure time of 98 μs. The selections of lens and exposure time were optimized to image the range of soot incandescence from auto-ignition to the quasi-steady period and across repeated injections. Thus, the measurement range of the 2CP system was dictated by the sensitivity of the camera sensor as reported in our previous work [32]. Some instances of very faint soot incandescence could not be quantified accurately by the 2CP system because of the poor signal-to-noise ratio; these portions of the flame compose an insignificant fraction of the total soot mass, having minimal impact on the overall measurement [32].

The 2CP measures spontaneous thermal radiation from the flame at two wavelengths to determine line of sight (LOS) temperature and optical density (KL) of soot [36]. Although regarded as a qualitative diagnostic in the past, recent work has shown that spatially-resolved 2CP measurements agree with other optical diagnostics (DBI and LEM) at low-soot conditions (KL<1) [4, 37]. The test conditions of the present study resulted in soot measurements below this KL threshold. The measurement uncertainty of the present 2CP system, documented in [32], provides high confidence in results of this study.

The 2CP camera was calibrated to correlate the arbitrary units of camera intensity to physical units of radiance ($W/m^2\,nm\,sr$) using a 75 W StellarNet uniform illumination sphere (UIS) with NIST traceable radiance calibration. The calibration was completed with the UIS placed at the same distance from the 2CP system as the center plane of the fuel spray in the experiment (≈80 cm). All other optical components, such as mirrors, camera lens, etc., were arranged identically to the experiment and camera settings for calibration such as frame size, exposure time, and f-stop were the same as those for the experiment. A pixel-by-pixel calibration of the 2CP images was performed by applying a linear fit of camera intensity versus radiance at each pixel location to account for in-

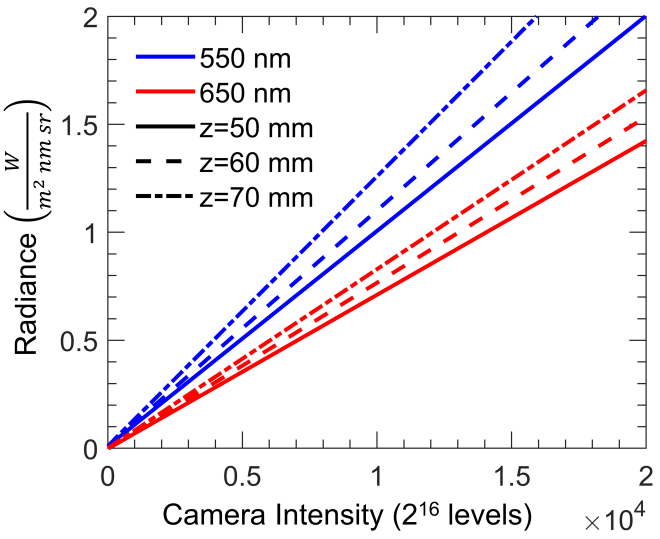

Figure 3: Sample single pixel calibrations at different axial locations along the centerline of the spray data. The significant variation in sensitivity to radiance at different locations on the sensor, likely caused by vignetting, shows the importance of pixel-by-pixel calibration.

tensity variation across the camera sensor, likely caused by vignetting. Further details of the calibration process are available in a recent work by the authors [32]. The calibration curves for each wavelength at several pixel locations along the centerline of the fuel spray in Fig. 3 show a linear relationship between camera intensity (horizontal axis) and radiance of the UIS calibration light source (vertical axis). For given camera intensity inputs, the variation in sensitivity for either wavelength across the sensor could lead to 20-60% variation in the KL factor once propagated through calculations. However, the pixel-by-pixel calibration employed in this study virtually eliminates such errors.

3. Data Processing

In this study, the RSD data are utilized for a qualitative representation of the injection liquid core and vapor region. The collimated light passes through the fuel injection region and undergoes extinction/scattering to quantify the liquid region and refraction to quantify density gradients along the line of sight

[9, 33, 34]. Quantitative analysis of the RSD data (e.g., vapor penetration, and fuel/air mixture fraction) is out of the scope of the present work, but contour plots of raw RSD data are shown in the results section to visualize the jet upstream of ignition/combustion.

In this work, OH*CL data are used to identify reaction zones where soot would likely be oxidized. OH*CL measurements from the 500-injection data set are ensemble averaged at each time step, and converted to planar measurements using an Abel transform as discussed in [33]. The contour plots of the planar OH*CL intensity are leveraged in the following section to depict the diffusion flame zone, its evolution through time, and its role on soot formation and oxidation processes.

The 2CP technique in this work is based on Planck's law of black body radiation and a correlation between emissivity and KL. Detailed derivations of 2CP equations are available in the literature [36, 12, 23, 38]. Equation 1 defines black body radiance ($I_{b,\lambda,\Omega}$) by Planck's law [39],

$$I_{b,\lambda,\Omega} = \frac{C_1}{\pi\,\lambda^5\left[e^{(C_2/\lambda T)}-1\right]} \tag{1}$$

where $C_1 = 3.742 \times 10^8\,\frac{W\cdot\mu m^4}{m^2}$ and $C_2 = 1.439 \times 10^4\,\mu m \cdot K$ are Planck's first and second constants, λ is wavelength, and T is temperature. Equation 2 shows that the actual radiance of an object can be represented by the black body radiance multiplied by the spectral emissivity (ϵ_λ) and equated to the black body radiance at an apparent temperature (T_a), which can be determined from the spectral radiance measured by the 2CP system.

$$I_{\lambda,\Omega}(T) = \epsilon_\lambda I_{b,\lambda,\Omega}(T) = I_{b,\lambda,\Omega}(T_a) \tag{2}$$

The emissivity of the soot cloud is determined by Eq. 3, which is a semi-empirical function of the soot optical density (KL) and experimentally determined tuning parameter, $\alpha = 1.39$ [40].

$$\epsilon_\lambda = 1 - e^{(-KL/\lambda^\alpha)} \tag{3}$$

Eqs. 1-3 are combined and solved for KL to obtain Eq. 4.

$$\begin{aligned} KL &= -\lambda_1^{\alpha} \ln\left[1 - \left(\frac{e^{(C_2/\lambda_1 T)} - 1}{e^{(C_2/\lambda_1 T_{a_{\lambda 1}})} - 1}\right)\right] \\ &= -\lambda_2^{\alpha} \ln\left[1 - \left(\frac{e^{(C_2/\lambda_2 T)} - 1}{e^{(C_2/\lambda_2 T_{a_{\lambda 2}})} - 1}\right)\right] \end{aligned} \tag{4}$$

The 2CP system measures the apparent temperatures at each wavelength (T_{a_1} and T_{a_2}) and then, Eq. 4 is solved iteratively to compute the actual soot temperature (T) and soot optical density (KL). The KL parameter is calculated at each pixel location and indicates the quantity of soot (along the line of sight) by combining the extinction coefficient, K, and the optical thickness of the flame, L. In utilizing Eq. 3, KL is assumed to be wavelength independent since α can be tuned for different wavelength ranges. The selected value for α has been determined experimentally for visible wavelengths [40], its perturbation has been shown to have negligible impact on measured values (within the visible wavelengths) [36], and has been used by several others for 2CP analysis [12, 41].

In this work, the KL measurements are converted to soot mass using the formula proposed by Kamimoto and Murayama [42]. This formulation assumes constant complex refractive index for soot defined by Williams et al. [43]. Manin et al. suggest that the complex refractive index of soot is likely wavelength dependent, however such experimental measurements are currently unavailable [11]. The soot temperature is approximated as equivalent to the surrounding gas temperature, since the time constant for thermal equilibrium between a particle and gas around it is on on the order of $1\,\mu$s in diesel flames [36]. The resulting soot mass formulation is defined by Eq. 5 [23]

$$m_s = \Delta a_{pix} \frac{\rho_p}{6\pi E(m)}\ KL \tag{5}$$

where Δa_{pix} is the area of a pixel, $\rho_p = 1.86\,g/cm^3$ is the particle density of soot, and $E(m) = 0.373$ is the complex refractive index of soot [43].The total soot mass is computed by the summation of soot mass at all pixel locations.

Temperature, KL, and soot mass are all highly non-linear with flame radiance (Eqs. 1-5). Thus, each parameter (i.e., temperature, KL, and soot mass) was calculated for each injection, timestep, and pixel to yield instantaneous, spatially-resolved measurements. Then, ensemble averages of each parameter at each timestep and each pixel were obtained by averaging across all 500 repeated injections. Furthermore, while these parameters are calculated from soot incandescence which dominates flame radiance [36], minor interference from chemiluminescence species is possible, especially for low sooting injections. Combustion radical CO is of particular concern since it emits broadly, with peak intensity around 410-420 nm [44]. In this study, the 2CP diagnostic setup (exposure time, f-stop, lens, etc.) was optimized for appreciable soot with a strong incandescence signal. Low soot regions with the most chemiluminescence interference do not affect the statistical analysis of this study because these regions converge to zero soot mass. However, low soot regions correspond to high 2CP temperatures, which must be interpreted with care with regards to radical species interference and LOS effects.

4. Results

In the CPFR, experiments can be performed in quick succession to acquire a large data set of injections unlike most studies with facilities, such as a constant volume chamber, report up to 10-50 repeated injections at a single test condition. In this study, 500 individual injections were performed to obtain ensemble averages, RMS deviations, and PDs of soot mass during the spray evolution process. The ensemble averages could be compared to RANS modelling results or to ensemble averages of repeated LES trials for validation(e.g. [7, 12, 5]).

Figure 4 shows typical time-synchronized raw instantaneous images acquired by RSD (left), OH*CL (middle), and 2CP 650 nm intensity (right). Fuel is injected downwards from the top of the image where the injector tip located at the origin. The RSD image is shown with saturation and intensity set to maximum for improved visualization see [9, 33, 34] for further details. The

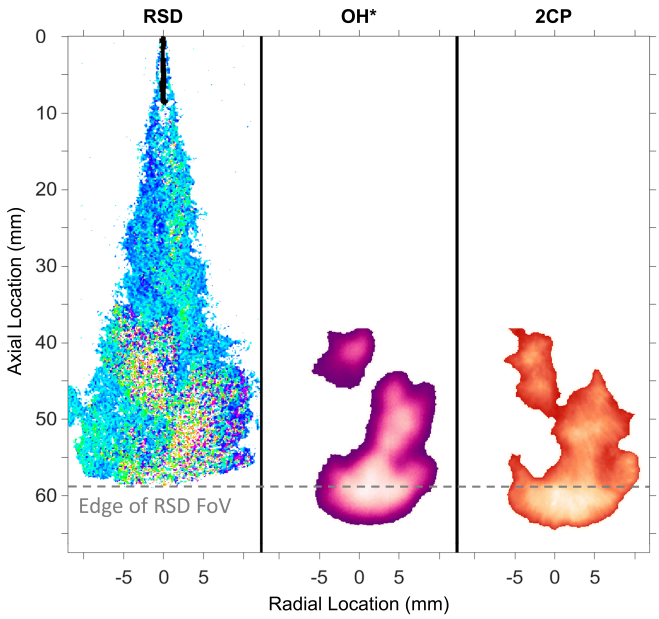

Figure 4: Time synchronized images from RSD (left), OH* Chemiluminescence (middle), and 2CP 650 nm intensity (right). A single injection at t=1.7 ms illustrates the fuel liquid and vapor penetration by RSD, and the corresponding raw OH*CL and soot incandescence intensities by qualitative false color scales.

raw OH*CL and 2CP intensity signals are false colored in shades of purple and orange, respectively. Figure 4 shows the liquid region as a small, dark jet that penetrates ≈9 mm from the injector tip (determined by methods in [45] near the top of the RSD image. Further downstream, the green/blue colors of the RSD image depict the vapor regions, as the jet spreads into the pressurized and heated ambient air [33]. Combustion is visualized at the downstream location z = 38 mm, by yellow/purple hues in RSD image and by OH*CL and 2CP imaging. Note, that the overlapping OH and 2CP structures in the image illustrate that the two diagnostics are precisely aligned, both spatially and temporally.

4.1. Ensemble Averaged Contour Plots

Figure 5 shows contour plots of results at different time steps arranged chronologically from left to right, as labelled at the top of each column of plots.

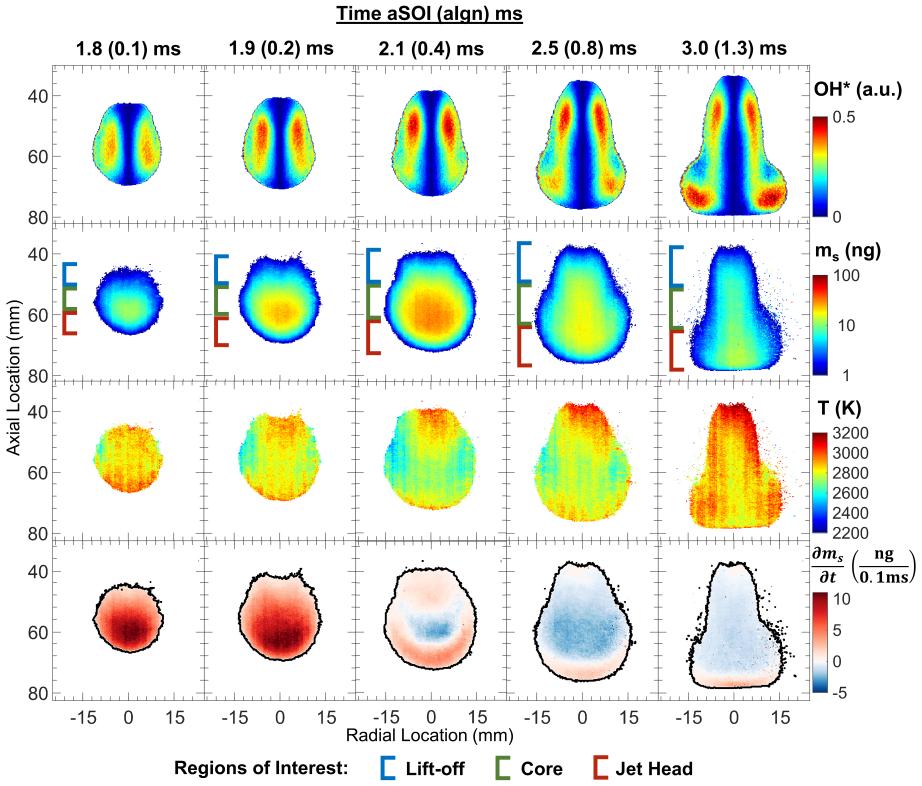

Figure 5: Contours of average combustion behavior at select time steps with the inverted planar OH*CL signal in the top row, soot mass in the second row, soot temperature in the third row, and soot mass rate in the fourth row.

These times were chosen to show the soot behavior at ignition, during transient jet development, and at quasi-steady lift-off. Each contour is an ensemble average of 500 injections at the given time step. Each row shows a different parameter labeled in the color scale on the right side. Ensemble averages converge to an axisymmetric behavior, even though instantaneous measurements are asymmetric because of the turbulence-induced variations in mixing and chemical reactions. From these result, one can infer that the off-axis view angle of the diagnostics (6.5 degrees from the center axis) does not affect the ensemble average results.

*4.1.1. Planar OH*CL Distributions*

The first row in Fig. 5 shows the planar distribution of OH*CL intensity obtained by Abel inversion of ensemble average images, converging to axisymemtric profiles because of the 500 injections, at each time step. The peak location of OH*CL intensity generally coincides with the diffusion flame front where soot oxidation takes place [13]. For all time steps, the high OH*CL intensity regions indicate the reaction zones. The flame recesses slightly upstream between times after start of injection, t = 1.8 ms and 1.9 ms, and then stabilizes between t = 2.1 and 2.5 ms. The OH*CL intensity shows reaction zone with an initially oval shape, which then elongates and grows radially at the downstream locations. At t = 2.5 ms, two intense OH*CL regions are observed, one near the lift-off length and another at the jet head. At t = 3.0 ms, the high OH*CL intensity regions pinch radially inward near the lift-off length while maintaining a larger width farther downstream, in agreement with [18] who noted a similar decrease in the radial extent of OH*CL intensity near lift-off and broadening downstream during the quasi-steady period.

The OH*CL intensity region is narrow at the upstream locations, z¡60 mm (about 18-24 mm in diameter) but it is much wider (about 35 mm in diameter) near the jet head at the downstream locations. Similar trends were identified by Du et al., where the OH*CL intensity was low near the long lift-off length [17], which allowed more time for fuel/air mixing to reduce the local equivalence ratio enabling the stoichiometric reaction zone (intense OH*) to move closer to the jet center. In the next section, the spatial correlation between intense OH*CL and soot mass regions will be examined to describe the soot oxidation processes.

4.1.2. Local Soot Mass

The second row of Fig. 5 shows contour plots of ensemble average soot mass along the LOS at each pixel location. Flame shape and soot mass measurements vary greatly from injection to injection [9, 8]. Thus, 2CP data might not exist at each pixel location and time step for every injection. The ensemble average soot mass tends to gradually approach zero near the edges where the soot mass

may not be present for all injections. The ensemble soot cloud was trimmed slightly by removing values below 1.0 ng to clean the edges of the contour and to focus on regions with appreciable soot. The bounds imposed by the 1.0 ng soot mass threshold were also applied to the remaining ensemble averaged contour plots. The measurement uncertainty at each pixel location was also calculated and those results are presented in Appendix A.

As expected, the highest average soot mass occurs in the core, in agreement with the existing literature [37, 4]. At t = 1.8 ms, the soot cloud volume is small as it forms from a locally fuel-rich auto-ignition zone in the premixed phase described by Dec's model [2]. At t = 1.9 ms, the soot cloud volume has increased as the flame recesses slightly upstream into the fuel-rich reactants, as well as by momentum transport towards the downstream. At t = 2.1 ms, the soot cloud has grown farther radially and axially and the soot mass reaches local peaks. At t = 2.5 ms, the soot cloud elongates and pinches radially inwards near the lift-off length, which can be attributed to soot oxidation in the reaction zone depicted by OH*CL intensity. The soot boundary retracts radially at t = 3.0 ms and shows a thin column of soot upstream but a broader region near the jet head. Furthermore, the maximum soot mass in the core decreases from about 50 ng at t = 2.1 ms to about 20 ng at t = 2.5 ms, and to about 8.0 ng at t = 3.0 ms. Note the "regions of interest" demarcated by colored brackets partition the flame into thirds, denoted as flame lift-off, jet core, and jet head.

4.1.3. Local Soot Temperature

The third row of Fig. 5 shows contour plots of ensemble average soot temperature. Some pixel locations did not have temperature data for all injections, and thus, these points were omitted from the ensemble averages. Similar to soot mass, temperature measured by 2CP is impacted by the LOS nature of the diagnostic. Effectively, the soot temperature is an average temperature weighted by radiant intensity, biased towards the higher temperatures along the LOS [12, 5]. High temperatures measured in the upstream fuel-rich region of the jet center are particularly uncertain because of the sparseness of data points and

low signal intensity. In these low-soot regions, corresponding to high OH*CL signal, 2CP temperature data could be affected by species chemiluminescence. The uncertainty in ensemble average temperature is discussed in Appendix A. Although the soot temperature measured by 2CP is not the actual temperature, the spatial trends of 2CP soot temperature can be informative. The temperature affects the molecular growth and fragmentation of soot precursors [46]. The uncertainty in ensemble average temperature is discussed in Appendix A. Lastly, the grid-like structures in the temperature contours are the result of low-level camera noise and pixel groupings on the sensor that are more apparent in the temperature contours than the soot mass contours.

Temperature contours at t = 1.8 ms show relatively high temperatures in the round soot cloud, which initiates the kinetics necessary to quickly form soot precursors and soot mass in the premixed burn phase [2]. At t = 1.9 ms, two distinct high temperatures regions, at lift-off and the jet head, are observed. At t = 2.1 ms, temperatures in the lift-off and jet head regions are high, but are relatively low in the jet core where the soot mass is observed to peak. Temperature distributions suggests fast kinetics at lift-off that both forms and fragments soot and its precursors; these pyrolized products transport into a cooler jet core where soot growth takes place. High temperatures near the lift-off are consistent with high OH*CL intensity between t = 2.1 ms and 3.0 ms, and indicate that soot formed near the lift-off oxidizes quickly along the jet periphery and/or transports downstream into the jet core. High temperatures at lift-off and jet head remain apparent at t = 2.5 ms, supporting a similar trend of soot formation/oxidation as the previous time step. At t = 2.5 ms, the low temperatures in the jet core are consistent with the low OH*CL intensity between z = 56 mm and 64 mm, substantiating poor oxidation in this region. At t = 3.0 ms, high temperatures effectively surround the soot cloud, indicating soot oxidation occurring in the diffusion flame along the jet periphery.

4.1.4. Local Rate of Change of Soot Mass

The fourth row of Fig. 5 shows the rate of change of soot mass at each pixel location in ng per 0.1 ms, which is the rate of change between consecutive frames at the 10 kHz framing rate. The rate of change of soot mass represents the combined effects of soot formation, oxidation, and transport at each pixel location. A positive rate (shade of red) signifies that the soot mass is increasing with time either by formation and/or by transport processes at that pixel location from the prior time step. At t = 1.8 ms and 1.9 ms, soot mass is increasing everywhere in the soot cloud, and the increase is most rapid near the jet head. At t = 2.1 ms, the flame recesses upstream towards the lift-off length where soot mass is formed newly. Similarly, the positive soot mass rate near the jet head is likely caused by soot transporting into this region from the upstream jet core. At t = 2.1 ms, negative soot mass rate in the jet core indicates a higher soot oxidation rate and/or downstream transport of soot mass. At t= 2.5 ms, the soot cloud has achieved nearly a quasi-steady behavior; the total soot mass is decreasing everywhere, except for small regions at the lift-off length and the jet head. At t = 3.0 ms, most of the jet is quasi-steady with slightly negative rate of soot mass change, except for an appreciable increase in soot mass at the jet head where downstream transport continues. Little to no soot is formed at the quasi-steady lift-off length which can be expected for the average equivalence ratio of less than two at the lift-off location [47]; a likely condition for this case with a relatively long lift-off length.

4.2. Integrated Soot Mass

Spatially-resolved data in the previous section provided insight into the average soot behavior during the transient evolution of the spray flame. In this section, soot mass data are leveraged to investigate further details of the sooting behavior. First, the total soot mass in different regions of the flame (i.e., lift-off, jet core, and jet head) was obtained by spatially integrating the soot mass in the corresponding pixel locations. Second, the soot mass at each pixel location was divided into four bins of varying quantities of soot mass (1-10 ng, 10-50 ng,

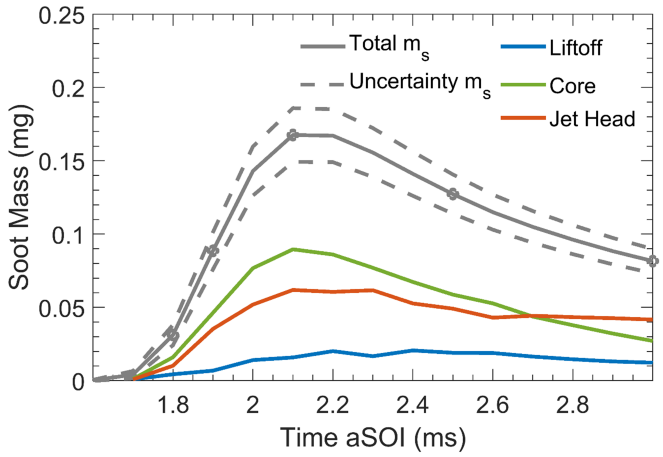

Figure 6: Total soot mass accumulated in different axial sections of the flame.

50-100 ng, and >100 ng) and each bin was integrated separately over the entire spray to determine the makeup of the total soot mass during the temporal evolution of the flame.

Figure 6 shows the temporal evolution of total soot mass, averaged over all injections, in the entire spray and in three localized regions of the flame: lift-off, jet core, and jet head. These regions were approximated by dividing the distance between soot lift-off length and jet head into thirds; the colored brackets in Fig. 5 demarcate each region. The extent of each of these axial regions changes with time as the total soot cloud volume increases. Figure 6 shows that throughout the injections, the jet core region is generally the most significant contributor to the total soot mass, followed by the jet head, and finally, the lift-off region.

Figure 6 shows a rapid increase in total soot mass soon after ignition (t = 1.7 ms) until it reaches a peak value of $m_s \approx 0.17$ mg at t = 2.1 ms. Thereafter, the total soot mass declines gradually until the jet head impinges on the flow conditioning mesh shortly after t = 3.0 ms. The soot mass profile is consistent with results in Fig. 5 which show the quick growth of the soot mass in the premixed burn phase, followed by gradual oxidation in the diffusion flame.

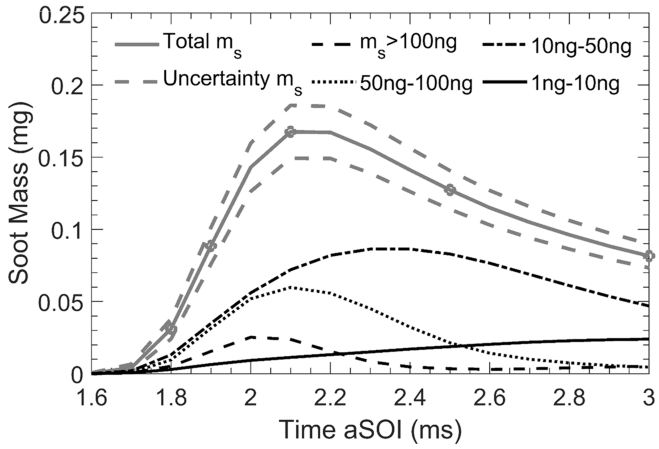

Figure 7: Total soot mass binned by magnitude of soot mass in individual pixels.

Figure 6 shows a gradual increase in the soot mass in the lift-off region reaching a relatively low steady value of $m_s \approx .015$ mg between t = 2.2 ms and 2.5 ms. The low soot mass in the lift-off region agrees with the corresponding region of contours in Fig. 5 which show small flame width and small-moderate amounts of soot mass. Conversely, the soot mass in the jet core increases quickly and then decreases gradually until t = 3.0 ms, which is similar to the trend for the total soot mass. Soot mass also rises quickly in the jet head region, presumably by soot formation in the premixed burn and by transport from the upstream jet core region. The soot mass in the jet head peaks slightly later than that in the jet core and then, it decreases slowly to reach a steady value at about t = 2.6 ms. As discussed previously, the jet head contains the most soot at the end of the data collection period (t = 3.0 ms). Overall, soot forms early during the premixed burn phase, and mainly in the jet core and jet head regions.

Figure 7 shows the makeup of the total soot mass to gain further insight into the soot formation and oxidation processes. Results show that the three largest bins of soot mass (>10 ng) are the main contributors of the total soot mass and each of these profiles peak and decay before the end of data collection. The smallest soot mass bin, 1-10 ng, contributes only a small fraction to the total soot mass and shows a slow, gradual rise throughout the injection. Figure 7 shows

that the soot formed in each bin reaches a peak, followed by decrease caused by soot oxidation. The peak is reached earliest for the >100 ng or largest soot mass bin followed by 50-100 ng and then 10-50 ng soot mass bins. Much of the soot mass is produced in the intermediate bins (50-100 ng and 10-50 ng) immediately after auto-ignition occurring at around t = 1.7 ms. The volumetric growth of the soot cloud between t = 1.7 ms and 1.9 ms increases the optical thickness of the flame, resulting in larger soot masses (in the >100 ng bin) along the LOS. The soot formed in the intermediate bins is also expected to contribute to the largest soot mass bin through mechanisms of particle growth and agglomeration.

Figure 7 shows that the largest soot mass bin is the first to reach its peak soot mass when oxidation begins at t = 2.0 ms. The 50-100 ng bin peaks next at t = 2.2 ms, and so on as the bin size decreases. As larger soot masses oxidize and reduce in size, they would cause the soot mass in the smaller bins to increase. Indeed, the soot mass in the smallest bin (1-10 ng) increases continuously as the larger soot masses oxidize and decompose into small segments. These trends are consistent with particle size distributions measured by fast gas sampling in a diesel engine [3]. In an engine, moderately sized particles form quickly after ignition, shortly thereafter soot concentration increases and larger sized particles appear, and then as soot is oxidized, the largest particles are the first to decrease [3]. Interestingly, the spatially-resolved soot mass measurements obtained by 2CP in this study are consistent with the findings based on particle size distributions.

4.3. Soot Behavior Across Injections

Figure 8 shows the spatio-temporal evolution of the RMS deviation of soot mass and soot temperature. The RMS deviation for each pixel was calculated as: $RMS = \sqrt{\frac{\Sigma(x-\bar{x})^2}{N}}$ where x would be substituted for soot mass or temperature, $\bar{x}$ is the ensemble average value, and N is the total number of elements in the ensemble average which may be less than the 500 total injections acquired as discussed in Sec 4.1.4.

The soot mass ranges over three orders of magnitude and thus, the RMS

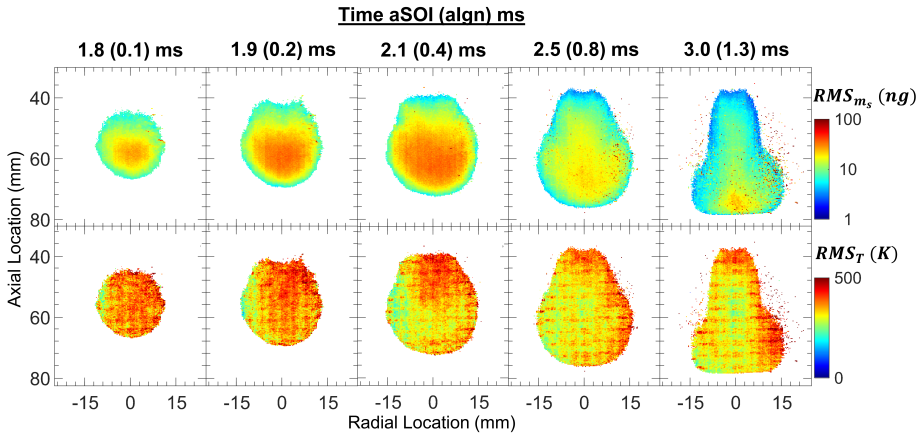

Figure 8: Contours of RMS deviation of soot mass (first row) and temperature (bottom row) at different selected time steps show the variability of soot distributions across injections.

deviation of soot mass is generally quite high, and in many parts of the spray, higher than the ensemble average soot mass value. Near ignition at t = 1.8 ms, the RMS deviations in the jet core are around 30 ng, whereby the ensemble average soot mass is about 10 ng. The larger-than-average RMS deviation indicates that some injections produce significantly greater than the average soot mass, but the majority of the data points have low or zero soot mass, which is common near ignition because of the slight differences in ignition delay time (some injections may not have ignited yet). Additionally, each injection ignites as one or more small ignition kernels at distinct locations. Thus, the ensemble average at auto-ignition results in a larger zone which encompasses the spatial variability of individual ignition locations.

At t = 1.9 ms and 2.1 ms, the RMS soot mass is highest in the jet core and deviations larger than the ensemble average soot mass are still typical. At t = 2.5 ms, the RMS soot mass has decreased since most injections have achieved quasi-steady lift-off length, when the peak variability is the lowest. Finally, at t = 3.0 ms, RMS_{m_s}) is at a minimum throughout the jet and especially in the upper half of the jet; increased variability at the jet head is likely caused by some injections impinging on the bottom plate.

RMS soot temperature contours in Fig. 8 show relatively low values compared to the ensemble average temperatures. Recall that the grid-like features in the RMS values are an artifact of the pixel groupings on the camera sensor which are characteristic of low-level noise inducing variability in the raw signal that are amplified when calculating RMS temperatures. At t = 1.8 ms and 1.9 ms, RMS temperatures in the ignition kernel vary between 400 and 500 K. At t = 2.1 ms, RMS temperatures increase slightly near the lift-off length and at the jet head while values in the jet core tend to decrease. These results can be attributed to injection to injection variations in lift-off length and jet head penetration length. RMS temperatures on the left side of the soot cloud are low, indicating slight asymmetry in the fuel spray. At t = 2.5 ms, RMS temperatures are highest along the outer edges of the averaged flame boundary. A similar trend is observed at t = 3.0 ms, whereby the RMS temperatures are highest at the likely location of the reaction zone on the edges of the flame. These results are in agreement with RMS temperature results from 16 repeated LES realizations by [6], which show the highest variations around the diffusion flame reaction front. Additionally, the high RMS temperature values are consistent with the location of the intense OH*CL intensity in the first row of Fig. 5.

4.4. Probability Distribution of Soot Mass

Figure 9 shows the PDs of soot mass at multiple time steps and for three axial sections of the flame, lift-off, jet core, and jet head, marked by the colored brackets in Fig. 5. Probability distributions are computed within each region at each time step for all injections. Note that the horizontal-axis of Fig. 9 is a log scale, and that the bin sizes are unequal, which allows for higher resolution for the small soot values that dominate the soot cloud in pixel count (but not mass). The probability of zero-soot mass, when no data exists within each region, is denoted in the plot legends. For example, at t = 1.8 ms, small ignition kernels initiate the combustion process, each with slightly different size and location. These different ignition kernels across injections average out to form a single round ignition region (left column of Fig. 5) where a significant portion of soot

mass data consists of zeros. Specifically, in the lift-off region at t = 1.8 ms, 22% of data points have zero soot mass as listed in the legend in Fig 9. In contrast, at t = 2.5 ms, the PDs have fewer pixel locations with zero soot mass; only 11% of data points in the lift-off region.

The top frame (t = 1.8 ms) of Fig. 9 shows that the PD of soot mass follows a somewhat normal distribution on a log scale with peaks at around 20-30 ng for all regions. The jet core shows the highest probability of appreciable soot mass, followed by the jet head, and lastly the lift-off region. This result is consistent with the integrated soot mass of each region in Fig. 6 at t = 1.8 ms. The second row of Fig. 9 for the next time step (t = 1.9 ms) shows an increase in probability for all regions but particularly of large soot masses both in the jet core and the jet head.

At t = 2.1 ms, the probability of all soot masses increases further in agreement with the increased integrated soot mass in all regions in Fig. 6. At t = 2.1 ms, Fig. 9 shows PDs with the greatest bias towards the large soot mass, in agreement with the total integrated soot mass results. At t = 2.5 ms, Fig. 9 shows peak probabilities similar to those at t = 2.1 ms, but the peaks have shifted toward smaller soot mass bins. The probabilities in the lift-off region have increased compared to those at the previous time steps, but most of the soot mass in this region is in bins with less than 30 ng. At t = 3.0 ms, Fig. 9 shows lower probabilities of soot mass in the jet core and higher probabilities in the jet head. The peak probabilities have all shifted toward lower soot mass bins compared to the previous time steps.

Consider the trends of Fig. 9 across all times steps. Initially, soot mass probabilities are low indicating that soot has not yet formed in the small auto-ignition zone. Up to t = 2.1 ms, the peak probability of each curve shifts towards the right with each time step, indicating a growing soot cloud with larger soot masses and potentially increasing particle size, as reported by [3]. The increased probability of large soot masses agrees with the trends shown in Fig. 7. At t = 2.5 ms, the peak probability of each curve shifts towards smaller soot mass indicating that soot oxidation dominates the flame and large soot masses are

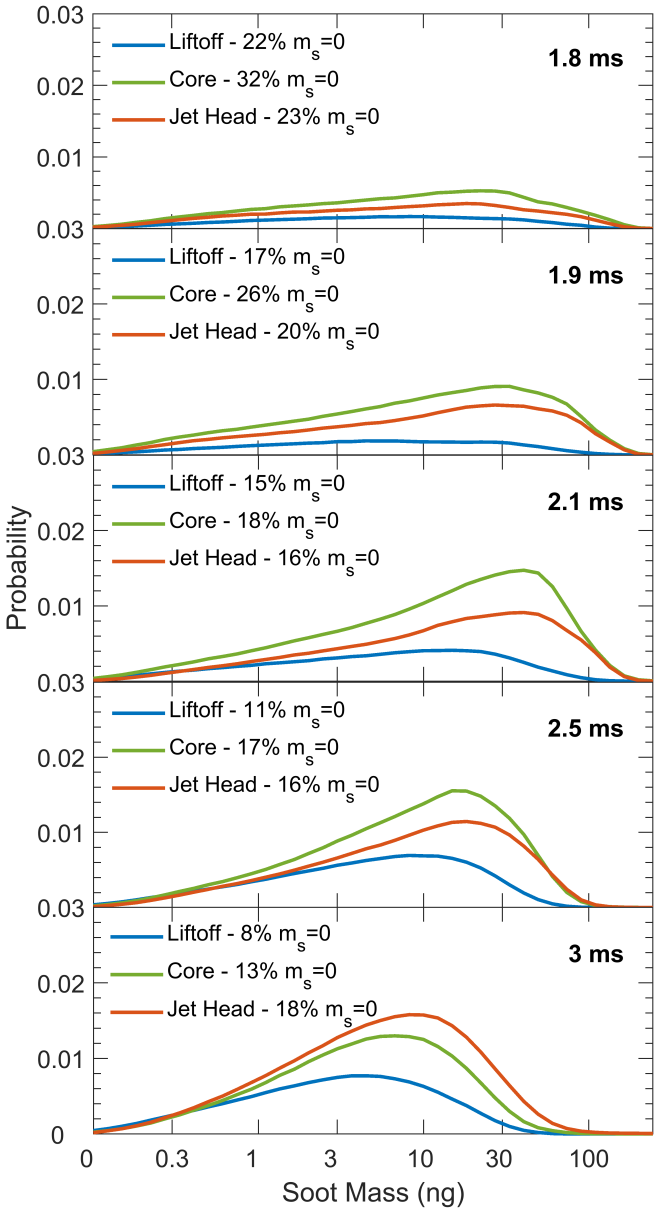

Figure 9: Probability distributions of soot mass in different axial regions: lift-off, core, and jet head which correspond to the ensemble average boundaries divided into axial thirds. The fraction of measurements with zero soot detected are noted in the legends. Each subplot corresponds to a different time step, marked in the upper right corner.

consumed. These trends are also replicated by the evolution plot of the integrated soot mass (Fig. 6) which show a decrease in soot mass after t = 2.1 ms. Between t = 2.1 ms and 2.5 ms, the soot mass probabilities are similar, but a shift towards smaller soot mass bins is evident. At the last time step (t = 3.0 ms), the peak probabilities have all shifted towards the left and most of the soot is located in the jet head, rather than in the jet core, unlike the previous time steps.

The PDs of soot mass could be particularly relevant to advanced soot modelling approaches such as the sectional models [30] or the method of moments [31] which compute a soot number density function. Typically, the soot distributions from these models indicate number of particles, particle diameter, and/or soot volume fraction, which cannot be compared directly to Fig. 9. However, some of these parameters could be combined and spatially integrated to match the line of sight (LOS) soot mass measurements of this work for comparison with the PDs obtained by 2CP.

5. Summary and Conclusions

A constant pressure flow rig was employed to acquire a large data set of n-heptane injections under reacting conditions to study the transient soot formation, oxidation, and transport processes. A novel optical configuration of 2CP was utilized together with pixel-by-pixel calibration to acquire spatially- and temporally-resolved line of sight soot measurements with high accuracy at all points on the sensor. Measurements were analyzed on a statistical basis to obtain converged ensemble average values at each time step and to quantify injection-to-injection variations in the sooting behavior in terms of root mean square variations and probability distributions, with the goal of providing experimental data in support of the soot modelling efforts.

The following summary and conclusions are drawn from this study:

- Most of the soot formed promptly after auto-ignition in the jet core indicating that for the present test conditions with long ignition delay and

lift-off length, the overall sooting propensity is pronounced in the premixed burn phase compared to that during the quasi-steady period.

- Following the premixed burn phase, the soot mass decreased by oxidation at the diffusion flame front determined by high OH*CL intensity. The soot cloud contracted radially, especially near the lift-off length to prevent appreciable soot formation during the quasi-steady period.

- Measurements suggest that relatively high temperatures near the lift-off length lead to fast chemical kinetics for production/destruction of soot precursors and/or soot depending on local mixture composition and turbulence. Moderate temperatures in the jet core favor the formation of soot particulates and larger agglomerates, in agreement with existing literature. High soot temperatures measured at the jet head indicate that the soot transported from the upstream is oxidized rapidly at the jet head.

- The soot mass in the jet core closely matches the trend of the total soot mass. The lift-off and jet head regions have greater access to oxygen, higher temperatures, and thus, higher OH*CL intensity, which tend to reduce the soot mass in these regions either through inhibited formation or promotion of oxidation.

- Large injection-to-injection variability in sooting behavior was detected and quantified in agreement with previous studies [9, 8]. The RMS soot mass indicates that the majority of injections were low-soot, but few injections had significantly high soot at these conditions.

- Measurements of spatially-resolved soot mass quantities agree with literature suggesting that large soot masses take longer to be seen because of the time required to form primary particles in high concentrations and for them to agglomerate. Conditions for soot formation are most favorable in the jet core which was shown to have the highest probability of large soot masses.

- Although the 2CP technique cannot detect individual particle sizes, soot mass probability distributions follow a similar trend as particle size distribution studies by in-cylinder fast gas sampling of a diesel engine [3].

The specific results provided here can be used to support model development and validation. More advanced soot modelling approaches could validate the soot number density function against the probability distributions. Further, the uncertainty results presented in Appendix A, typically not available for 2CP, provide confidence bounds for the reported measurements. Future works on the effects of alternative fuels and blends at varying ambient and injection conditions and different combustion chamber designs can leverage the methods presented to obtain previously unavailable data on soot formation, oxidation, and transport processes using modest optical access.

Acknowledgement

Funding for this work was provided by award from US Department of Energy, Office of Energy Efficiency and Renewable Energy (EERE) DE-EE0007980. The views expressed herein do not necessarily represent the views of the U.S. Department of Energy or the United States Government. This work was also supported by The University of Alabama's Center for Advanced Vehicle Technology (CAVT).

References

[1] J. B. Heywood, Internal combustion engine fundamentals, McGraw-Hill Education, 2018.

[2] J. E. Dec, A conceptual model of di diesel combustion based on laser-sheet imaging, SAE Transactions (1997) 1319–1348.

[3] A. Pungs, S. Pischinger, H. Bäcker, G. Lepperhoff, Analysis of the particle size distribution in the cylinder of a common rail di diesel engine during combustion and expansion, SAE Transactions (2000) 1926–1934.

[4] J. V. Pastor, J. M. Garcia-Oliver, R. Novella, T. Xuan, Soot quantification of single-hole diesel sprays by means of extinction imaging, SAE Int. J. Engines 8 (2015) 2068–2077.

[5] M. P. Musculus, S. Singh, R. D. Reitz, Gradient effects on two-color soot optical pyrometry in a heavy-duty di diesel engine, Combust. Flame 153 (2008) 216–227.

[6] Y. Pei, S. Som, E. Pomraning, P. K. Senecal, S. A. Skeen, J. Manin, L. M. Pickett, Large eddy simulation of a reacting spray flame with multiple realizations under compression ignition engine conditions, Combust. Flame 162 (2015) 4442–4455.

[7] R. Hessel, Z. Yue, R. Reitz, M. Musculus, J. O'Connor, Guidelines for interpreting soot luminosity imaging, SAE Int. J. Engines 10 (2017) 1174–1192.

[8] T. Xuan, J. V. Pastor, J. M. García-Oliver, A. García, Z. He, Q. Wang, M. Reyes, In-flame soot quantification of diesel sprays under sooting/non-sooting critical conditions in an optical engine, Appl. Therm. Eng. 149 (2019) 1–10.

[9] S. A. Reggeti, A. Parker, C. T. Wanstall, A. K. Agrawal, J. A. Bittle, Comparing global spray combustion characteristics and local shot-to-shot variations in a reacting n-heptane spray, J. Eng. Gas Turb. Power 143 (2021) 091018.

[10] L. de Francqueville, G. Bruneaux, B. Thirouard, Soot volume fraction measurements in a gasoline direct injection engine by combined laser induced incandescence and laser extinction method, SAE Int. J. Engines 3 (2010) 163–182.

[11] J. Manin, L. M. Pickett, S. A. Skeen, Two-color diffused back-illumination imaging as a diagnostic for time-resolved soot measurements in reacting sprays, SAE Int. J. Engines 6 (2013) 1908–1921.

[12] F. Payri, J. V. Pastor, J. García, J. M. Pastor, Contribution to the application of two-colour imaging to diesel combustion, Meas. Sci. Technol. 18 (2007) 2579.

[13] M. P. Musculus, P. C. Miles, L. M. Pickett, Conceptual models for partially premixed low-temperature diesel combustion, Prog. Energ. Combust. 39 (2013) 246–283.

[14] L. M. Pickett, D. L. Siebers, Soot in diesel fuel jets: effects of ambient temperature, ambient density, and injection pressure, Combust. Flame 138 (2004) 114–135.

[15] L. M. Pickett, D. L. Siebers, Fuel effects on soot processes of fuel jets at di diesel conditions, SAE Transactions (2003) 2044–2066.

[16] L. M. Pickett, D. L. Siebers, Soot formation in diesel fuel jets near the lift-off length, Int. J. Engine Res. 7 (2006) 103–130.

[17] C. Du, S. Andersson, M. Andersson, Two-dimensional measurements of soot in a turbulent diffusion diesel flame: the effects of injection pressure, nozzle orifice diameter, and gas density, Combust. Sci. Technol. 190 (2018) 1659–1688.

[18] T. Xuan, J. M. Desantes, J. V. Pastor, J. M. Garcia-Oliver, Soot temperature characterization of spray a flames by combined extinction and radiation methodology, Combust. Flame 204 (2019) 290–303.

[19] J. Zhang, W. Jing, W. L. Roberts, T. Fang, Soot temperature and kl factor for biodiesel and diesel spray combustion in a constant volume combustion chamber, Appl. Energ. 107 (2013) 52–65.

[20] W. Jing, Z. Wu, W. L. Roberts, T. Fang, Spray combustion of biomass-based renewable diesel fuel using multiple injection strategy in a constant volume combustion chamber, Fuel 181 (2016) 718–728.

[21] Q. Shi, T. Li, X. Zhang, B. Wang, M. Zheng, Measurement of temperature and soot (KL) distributions in spray flames of diesel-butanol blends by two-color method using high-speed RGB video camera, Vol. 2016-01-2190, SAE International Powertrains, Fuels & Lubricants Meeting, 2016.

[22] J. V. Pastor, A. García, C. Micó, F. Lewiski, An optical investigation of fischer-tropsch diesel and oxymethylene dimethyl ether impact on combustion process for ci engines, Appl. Energ. 260 (2020) 114238.

[23] T. Kamimoto, N. Uchida, T. Aizawa, K. Kondo, T. Kuboyama, Diesel flame imaging and quantitative analysis of in-cylinder soot oxidation, Int. J. Engine Res. 18 (2017) 422–435.

[24] C. J. Mueller, C. W. Nilsen, D. E. Biles, B. F. Yraguen, Effects of fuel oxygenation and ducted fuel injection on the performance of a mixing-controlled compression-ignition optical engine with a two-orifice fuel injector, Appl. Energy Combust. Sci. 6 (2021) 100024.

[25] A. Parker, A. Agrawal, J. Bittle, Representative phenomena of cyclic turbulent combustion in high-pressure fuel sprays, Flow Turbul. Combust. 111 (2023) 675—-696.

[26] V. Fraioli, C. Beatrice, M. Lazzaro, Soot particle size modelling in 3d simulations of diesel engine combustion, Combust. Theor. Model. 15 (2011) 863–892.

[27] D. Aubagnac-Karkar, J.-B. Michel, O. Colin, P. E. Vervisch-Kljakic, N. Darabiha, Sectional soot model coupled to tabulated chemistry for diesel rans simulations, Combust. Flame 162 (2015) 3081–3099.

[28] X.-S. Bai, M. Balthasar, F. Mauss, L. Fuchs, Detailed soot modeling in turbulent jet diffusion flames, in: Symposium (International) on Combustion, Vol. 27, Elsevier, 1998, pp. 1623–1630.

[29] M. Bolla, Y. M. Wright, K. Boulouchos, G. Borghesi, E. Mastorakos, Soot formation modeling of n-heptane sprays under diesel engine conditions us-

ing the conditional moment closure approach, Combust. Sci. Technol. 185 (2013) 766–793.

[30] K. Netzell, H. Lehtiniemi, F. Mauss, Calculating the soot particle size distribution function in turbulent diffusion flames using a sectional method, Proc. Combust. Inst. 31 (2007) 667–674.

[31] M. Mueller, G. Blanquart, H. Pitsch, Hybrid method of moments for modeling soot formation and growth, Combust. Flame 156 (2009) 1143–1155.

[32] S. A. Reggeti, A. K. Agrawal, J. A. Bittle, Robust two-colour pyrometry uncertainty analysis to acquire spatially-resolved measurements, Meas. Sci. Technol. 33 (2022) 125201.

[33] A. Parker, C. Wanstall, S. A. Reggeti, J. A. Bittle, A. K. Agrawal, Simultaneous rainbow schlieren deflectometry and oh* chemiluminescence imaging of a diesel spray flame in constant pressure flow rig, Proc. Combust. Inst. 38 (2021) 5557–5565.

[34] A. Agrawal, C. T. Wanstall, Rainbow schlieren deflectometry for scalar measurements in fluid flows, J. Flow Vis. Image Process. 25.

[35] S. A. Reggeti, A. K. Agrawal, J. A. Bittle, Two-color pyrometry system to eliminate optical errors for spatially resolved measurements in flames, Appl. Optics 58 (2019) 8905–8913.

[36] H. Zhao, N. Ladommatos, Optical diagnostics for soot and temperature measurement in diesel engines, Prog. Energ. Combust. 24 (1998) 221–255.

[37] J. V. Pastor, J. M. García-Oliver, A. Garcia, C. Mico, S. Möller, Application of optical diagnostics to the quantification of soot in n-alkane flames under diesel conditions, Combust. Flame 164 (2016) 212–223.

[38] M. P. Musculus, Measurements of the influence of soot radiation on in-cylinder temperatures and exhaust nox in a heavy-duty di diesel engine, SAE Transactions (2005) 845–866.

[39] T. L. Bergman, F. P. Incropera, D. P. DeWitt, A. S. Lavine, Fundamentals of heat and mass transfer, John Wiley & Sons, 2011.

[40] H. C. Hottel, F. Broughton, Determination of true temperature and total radiation from luminous gas flames, Ind. Eng. Chem., Anal. Ed. 4 (1932) 166–175.

[41] R. Yuan, J. Camm, T. Knight, M. Parker, S. Sogbesan, E. Long, V. Page, K. H. Graham, Evaluation of in-cylinder endoscopic two-colour soot pyrometry of diesel combustion, Combustion and Flame 242 (2022) 112207.

[42] T. Kamimoto, Y. Murayama, Re-examination of the emissivity of diesel flames, Int. J. Engine Res. 12 (2011) 580–600.

[43] T. C. Williams, C. R. Shaddix, K. A. Jensen, J. M. Suo-Anttila, Measurement of the dimensionless extinction coefficient of soot within laminar diffusion flames, Int. J. Heat Mass Tran. 50 (2007) 1616–1630.

[44] W. Hwang, J. Dec, M. Sjöberg, Spectroscopic and chemical-kinetic analysis of the phases of hcci autoignition and combustion for single-and two-stage ignition fuels, Combustion and Flame 154 (3) (2008) 387–409.

[45] C. T. Wanstall, A. K. Agrawal, J. A. Bittle, Quantifying liquid boundary and vapor distributions in a fuel spray by rainbow schlieren deflectometry, Appl. Optics 56 (2017) 8385–8393.

[46] H. Wang, Formation of nascent soot and other condensed-phase materials in flames, Proc. Combust. Inst. 33 (2011) 41–67.

[47] D. Siebers, B. Higgins, Flame lift-off on direct-injection diesel sprays under quiescent conditions, SAE Transactions (2001) 400–421.

Appendix A. Uncertainty of 2CP Measurements

Uncertainty of ensemble averaged 2CP results are a combination of the bias uncertainty of individual measurements and the precision uncertainty of the mean value. Measurement uncertainties originate in the calibration and image detection equipment. The full computational methodology of 2CP uncertainties are detailed in [32] and contours of uncertainty in ensemble soot mass and soot temperature are presented here for reference and context to the primary discussions Sec. 4.

The steps involved in the propagation of uncertainty are illustrated in Fig. A.1. As a summary of the methodology, the first step in the flow chart indicates that the optical hardware must measure the radiation from the same lines of sight (LsOS) through the flame for both wavelength images (made possible by the novel design used). Next, the 2CP system is calibrated as a unit to correlate the intensities registered by the camera ($I_{\lambda,px}$) to radiance values ($R_{\lambda,\Omega}$). The calibration process then accounts for the primary uncertainty terms: uncertainty of the radiance emitted by the calibration light source (δ_{UIS_λ}), uncertainty of the transmissivity of neutral density (ND) filters (δ_{τ_λ}), and uncertainty of due to camera intensity fluctuations or noise ($\delta_{I_{\lambda,px}}$). All the primary uncertainty terms combine to give the uncertainty in the measured radiance ($\delta_{R_{\lambda,\Omega}}$) through the calibration, which was evaluated by a Monte Carlo simulation. Uncertainty in radiance propagates through Eq. 1 to yield uncertainty in apparent temperature ($\delta_{T_{a_\lambda}}$). Finally, uncertainty in apparent temperature is propagated through Eqs. 4 and 5 to yield uncertainty in temperature (δ_T), uncertainty in KL (δ_{KL}), and uncertainty in soot mass (δ_{m_s}). Each step for combination of uncertainty employs the general formula in Eq. A.1 and propagation of uncertainty follows the general formula defined by Eq. A.2.

$$\delta a = \sqrt{\delta a_1^2 + \delta a_2^2 + \cdots} \tag{A.1}$$

$$\delta c = \sqrt{\left(\frac{\partial c}{\partial a}\delta a\right)^2 + \left(\frac{\partial c}{\partial b}\delta b\right)^2 + \cdots} \tag{A.2}$$

Precision uncertainty is defined by Eq. A.3 where z=1.96 is the z value for 95% confidence interval, σ is the standard deviation, and N is the number of samples included in the average. The uncertainty of the ensemble average was determined at each pixel by averaging the measurement uncertainty of each pixel value of temperature and soot mass and combining it with the precision uncertainty at that pixel using Eq. A.1.

$$\delta a_s = z\frac{\sigma}{\sqrt{N-1}} \tag{A.3}$$

Figure A.2 shows the resulting uncertainty of the ensemble average soot mass and temperature distributions. These spatially-resolved uncertainties correspond to the contours in Fig. 5. The top row of Fig. A.2 shows that the highest absolute uncertainties in soot mass occur in the core of the jet and follow similar trends as the soot mass distributions in Fig. 5. Indeed, the highest soot mass values are in the center, thickest part of the jet have the highest absolute uncertainty while the periphery has low absolute uncertainty but high relative uncertainty as the soot mass approaches zero on the jet periphery.

In contrast, the second row of Fig. A.2 shows that the highest absolute uncertainties in temperature occur on the jet periphery, which is the location of a high temperature diffusion flame, where soot is oxidized. Since there is little soot on the jet periphery it is difficult to measure and results in high bias uncertainty in temperature. Furthermore, the injection-to-injection variation of jet shape means that there are fewer number of elements (N) in the periphery of the jet ensemble, increasing the precision uncertainty.

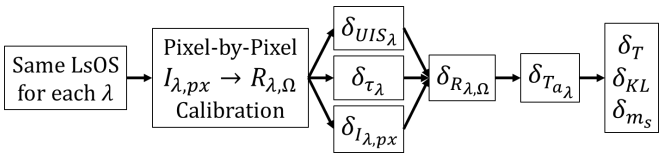

Figure A.1: Flow chart of uncertainty propagation process.

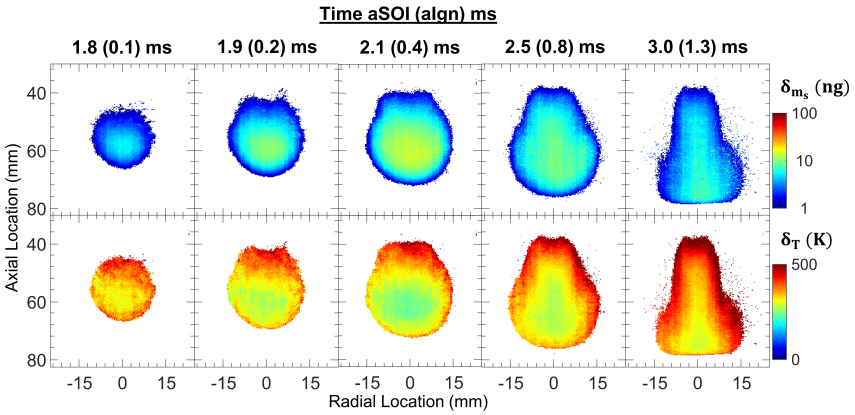

Figure A.2: Ensemble injection uncertainty.

Representative phenomena of cyclic turbulent combustion in high-pressure fuel sprays

Allen Parker[1], Ajay Agrawal[1] and Joshua Bittle[1*]

[1*]Department of Mechanical Engineering, The University of Alabama, Tuscaloosa, 35487, AL, USA.

*Corresponding author(s). E-mail(s): jbittle@eng.ua.edu;
Contributing authors: aparker14@crimson.ua.edu;
aagrawal@eng.ua.edu;

Abstract

Cyclic variations in conventional diesel combustion engines can lead to large differences in engine out emissions even at steady operation. This study uses an optically accessible constant-pressure flow chamber to acquire fuel injections in quick succession to analyze mixing, auto-ignition, and combustion of diesel-surrogate n-heptane using multiple high-speed optical diagnostics. Prior studies have utilized fewer injections and/or they rely on analysis of ensemble average behavior. These approaches do not yield information on injection-to-injection variation or provide confidence in utilizing individual injection measurements for high-fidelity computational fluid dynamics(CFD) model validation. In this study, a large set of 500 injections is used to obtain global parameters including liquid length, vapor penetration length, ignition delay time, and lift-off length. Results for multiple injections are presented to illustrate large injection to injection variations. Potential sources for these variations are analyzed to conclude localized, small scale turbulence and rate of injection variations as the likely sources. Then, a statistical method based on z-scores is proposed and implemented to identify instantaneous injections that best represent the bulk data-set of jet boundaries measured independently by three different diagnostics. This synthesis of statistics-guided screening of data set and ensemble-average analysis offers higher confidence for CFD model validation relying upon both a representative single and average injection results.

1 INTRODUCTION

The margins for gains in combustion efficiency for transient combustion events found in compression ignition 'diesel' engines have become smaller. Increased understanding of the fundamental physics that governs the spray breakup, vaporization, fuel-air mixing, ignition, and combustion processes, still offers the opportunity to mitigate in-cylinder criteria emissions (e.g. CO, NOx, THC) and total greenhouse gas (GHG) production through the use of drop-in biomass derived fuels. However, relating properties of these emerging fuel candidates to expected 'engine out' emissions remains a significant challenge in the screening effort. Part of this challenge can be attributed to the lack of clarity obtained from combustion experiments, even with exhaustive optical diagnostics. From droplet combustion to spray vessels, rapid compression machines, and optical engines, the ability to study various flow and combustion processes becomes increasingly challenging. Typically this results in a limited number of fuel injection events (in the case of spray chambers) acquired at steady operating conditions. The analysis then focuses on ensemble average behavior that may not represent an individual experiment/injection. As evident in the literature and investigated in this study, ensemble average analysis does have significant limitations since the injection-to-injection variation in the combustion process can be vast even under very steady operating conditions. Further, in both spark and compression ignition engines, the cycle-to-cycle variations represent a significant challenge to researchers and engine calibrators to push efficiency and reduce emissions. ~~Kircher et al.~~ Kircher et al (2022) demonstrated through simulation calibrated to experimental results that local variations in temperature coupled with effects of negative temperature coefficient (NTC) drive a wide range of main ignition delays. In that case, as ignition occurs from near

piston top center up to 10° later resulting in the maximum cylinder pressure for a cycle observed being 36% higher than lowest cycle. Experimentally, ~~Aleiferis et al.~~Aleiferis et al (2015) studied the impact of ambient flow field on the spray under non- and flash boiling sprays and noted large impact for flash boiling cases. To provide some measure of turbulence they report mean and RMS spray images results though focus on discussion of ensemble average behaviors.

The limitations of ensemble average results are not unique to combustion phenomena. For example, to simplify and streamline the costly manufacture of aircraft cockpits, the United States Army Air Force measured key dimensions of over 4,000 of its pilots in the 1950's. Ten of the most crucial design dimensions were chosen to confirm the one-size-fits-all design outlook, and the number of pilots that fell into the middle 30% of all parameters was determined to be zero. Not a single pilot was 'average' by the liberal definition of falling within the middle 30% of ten key parameters. Reducing this definition to include only three parameters excluded all but 3.5% of the pilots ~~Rose (2016)~~ (Rose (2016)). A popular 1945 contest centered around the 'Norma' statue ~~Creadick (2010)~~ (Creadick (2010)) arrived at the same conclusion; even in seemingly repeatable circumstances, nature exhibits remarkable diversity, and being normal never looks 'normal'.

Beyond extracting typical behavior from experimental results, the challenge also extends to the reliability of model based predictions as they are built and calibrated against measurements. While increasingly high-fidelity computational fluid dynamics (CFD) models of spray, combustion, and flame stabilization offer insights into the transient combustion process ~~Pei et al (2013)~~(Pei et al (2013)), these models

must be validated against experimental data. Large Eddy Simulations (LES) offer a significant advance in predicting localized turbulent combustion behaviors over Reynolds Average Navier Stokes (RANS) models ~~Liu and Haworth (2010); Li et al (2017); Schmitt et al (2015)~~ (Liu and Haworth (2010); Li et al (2017); Schmitt et al (2015)). However, it is not possible to meaningfully compare results from one experiment to a single LES realization ~~Sornette et al (2007)~~ (Sornette et al (2007)) because of the large injection to injection variations. Though both LES and RANS approaches can predict fluid flow and some global combustion parameters reasonably well ~~Som et al (2012)~~(Som et al (2012)), the fidelity and accuracy required to predict the bulk behavior (e.g. cylinder pressure) versus emissions is vastly different. This is true experimentally as well, for example, ~~Bizon et al.~~ Bizon et al (2009) utilized an optically accessible engine to report large injection to injection variations of in-cylinder luminosity at conventional diesel conditions, but less significant differences in pressure-traces~~Bizon et al (2009)~~ . Likewise, Wright observed repeatable ignition delay and pressure-traces but "substantial variations" in ignition location while testing n-heptane combustion at high pressures/temperatures in a constant volume chamber Wright et al (2010). ~~Donkerbroek et al.~~ Donkerbroek et al (2011) observed significant cycle-to-cycle variations in OH* chemiluminescence (OH*CL) signal in an optical engine~~Donkerbroek et al (2011). Sufficiently~~ .

Pal et al (2018) identified a single representative pressure trace out of a sample of cycles in spark-ignition engines. Maes et al (2020) reported results from 200 injection events quantifying variation in soot mass at a specific location in the spray. Payri et al (2015) and Wanstall et al (2019) both used probability maps to define spray boundaries under various conditions. It is clear that sufficiently large datasets are therefore necessary to extend the

understanding of injection to injection variations and to support CFD model validation. These datasets should provide spatiotemporally resolved measurements, typically from optical diagnostics. A rigorous statistical analysis could then identify/isolate a smaller set or a single case representing the entire datasets.

Large data-sets, while important for reliable statistical analysis, are prone to include a wide range of disparate outliers. Xuan et al. describe massive injection to injection variations in soot formation across 30-40 injections, recorded simultaneously with two color-pyrometry (2CP) and diffuse back-illumination (DBI); an otherwise nominal injection had a propensity for 'non-sooting' at particular thermodynamic conditions; this behavior was attributed to strong fluctuations of in-cylinder air flow caused by the piston movement Xuan et al (2019). Other work by Panagiotis has shown the strong impact of cyclic in-cylinder pressure oscillations on average values Kyrtatos et al (2014) in engine tests, and highlights the potential of LES in explaining these wide variations, as done by Li and others Li et al (2017); Schmitt et al (2015). Therefore, combustion models must be capable of predicting the range of variation, but model validation requires a reference 'nominal' behavior, which is difficult to isolate in a transient, turbulent combustion process Clark and Kook (2018). This work seeks to identify the 'nominal' behavior from a large dataset of repeated injection/combustion experiments in a constant pressure flow chamber (CPFC) to provide context to LES modeling efforts, as has been done in other fields where deviation from normalcy proves to be widespread.

The stochastic nature of turbulent flows has produced a long history of statistical tools in combustion research. Turbulent combustion models often involve assumptions such as assumed probability distributions to predict key

phenomena at limited spatial resolution Burluka et al (1997). Modern combustion systems take advantage of improved abilities to collect vast amounts of data - optical diagnostics are increasingly common, as are high sampling rates - to better utilize statistical tools. For example, modern aviation gas turbines collect over 2.5TB of data per day, and terms such as Combustion Machine Learning (CombML) have been coined Ihme et al (2022). Though this work does not leverage advanced statistical tools, the process of identifying 'nominal' or representative behavior from amongst a large data-set provides a targeted approach compared to data reduction through averaging, which can lead to misleading observations. The methodology of identifying a representative individual injection can be extended to various diagnostics or conditions to delineate most appropriate single-event results.

This work presents a methodology to describe the key features and deviations among transient, reacting turbulent jets to support improved modeling and model validation of the same. The methodology is built on multiple injections at fixed test conditions to illustrate the limitations of ensemble average analysis and to make the case for a representative injection. Hundreds of transient spray combustion experiments are performed in quick succession in a high-pressure, high-temperature environment, and fuel injection, mixing, and combustion processes are probed at high spatial and temporal resolutions simultaneously by three optical diagnostics, each focused on different aspects of the jet behavior. The diagnostics include Rainbow Schlieren Deflectometry (RSD) to visualize the early, non-combusting jet Reggeti et al (2021); Parker et al (2021), OH*CL to detect ignition and reaction zones Blocquet et al (2013), and 2CP to quantify produced soot mass Xuan et al (2019); Reggeti

et al (2021). The data-set is of sufficient size to accurately discern injection-to-injection variations Donkerbroek et al (2011); Xuan et al (2019); Reggeti et al (2021); Parker et al (2021); Li et al (2017).

The remainder of the paper presents the specifics of the experimental apparatus, test conditions, diagnostics and data processing in Sec. 2, followed by quantitative and visual analysis of the injection-to-injection variations in Sec. 3.1 - 3.2, and demonstrates stability of test conditions in Sec. 3.3.1. Finally, a methodology to identify a representative injection is presented in Sec. 3.4 together with a set of representative injections before summary and conclusions.

2 EXPERIMENTAL SETUP

The Constant Pressure Flow Chamber (CPFC) used in this study is illustrated in Fig. 1 is a continuous flow system, maintaining a nearly quiescent ambient environment in which to study fuel injection processes and enable the acquisition of about ∼500 injections in two hours Parker et al (2021); Wanstall et al (2019, 2020); Reggeti et al (2021). Pressurized, electrically preheated air is supplied to the chamber at an average speed of about 0.5 m/s (nearly three orders of magnitude less than the fuel injection velocity) in a counter flow arrangement, as shown in Fig. 1. The flow velocity is less than that in direct-injection studies Aleiferis et al (2015), and is much lower than the ambient velocity in diesel engines Xuan et al (2019). Air enters through a diffuser section followed by a flow conditioner consisting of six 0.5 mm thick, 100 micron mesh screens to break up eddies and uniformly distribute the flow across the CPFC. The air exits at the top of the rig through four 3 mm diameter holes, placed symmetrically around the injector tip. An upstream dome regulator controls air supply pressure, and the air flow rate is regulated by a downstream control

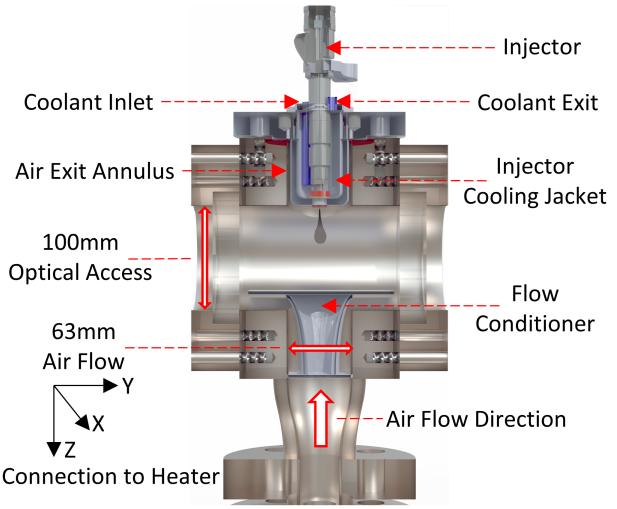

Fig. 1 Constant pressure flow rig (CPFR) schematic

valve. Fuel is injected by a Bosch CRIN3-18 injector modified to have a single 104 μm hole at the tip to create a spray along the axis of the rig.

A pneumatic pressure multiplying pump (300:1 ratio) provides fuel pressurization up to 2000 bar and is controlled remotely via an air pressure regulator feeding the pump. This type of pump results in low frequency (0.2-1 Hz) pressure fluctuations as the piston cycles. After reaching the desired ambient pressure and temperature conditions, the injector is triggered on the rising-edge of fuel pressure passing into the narrow tolerance window of 15 bar. An injection-to-injection dwell time of at least 8 seconds ensures that fresh air has completely displaced any residual combustion products (longer dwell times occur as the fuel pressure cycles before the next rising-edge trigger point). The fuel temperature is maintained at 355 K by circulating coolant in a jacket around the injector. The ambient air is maintained at nominal conditions of 800 K and 3 MPa (13 kg/m^3). Table 1 shows the test conditions and their variations during the experiment.

Table 1 Actual ambient air and fuel injection conditions for CPFR experiments. Variation indicates 95% confidence interval (CI) of individual injection events.

Property	Units	Value
Ambient Air Properties		
Ambient Temperature	$[K]$	807 $\pm$4.00
Ambient Pressure	$[MPa]$	3.00$\pm$0.0263
Ambient Density	$[kg/m^3]$	13.0 $\pm$0.1140
Fuel Properties		
Fuel Species		n-heptane
Fuel Temperature	$[K]$	355 $\pm$0.933
Fuel Pressure	$[MPa]$	98.9 $\pm$0.714
Injector Orifice Size	$[\mu m]$	104
Injection Duration	$[ms]$	4.5

Table 2 Simultaneous diagnostics specifications.

	RSD	OH*CL	2CP
Camera	Nova S9	SA5	v7.3
~~Spatial~~ Pixel Resolution	90 μm	160 μm	242 μm
Sampling Rate	20 kHz	10 kHz	10 kHz
Exposure Time	4 μs	100 μs	98 μs

2.1 Diagnostics

This experiment used three optical diagnostics to simultaneously acquire data for each injection consisting of liquid injection, vaporization, mixing, auto-ignition, flame stabilization, combustion, and soot formation, followed by venting of the combustion products. The diagnostics are RSD, OH* chemiluminescence (OH*CL), and 2CP. A schematic depiction of these diagnostics in Fig. 2 shows the arrangement of each high-speed camera. Table 2 provides additional details such as camera spatial (pixel) resolution, sampling rate, and exposure time for each diagnostic.

Rainbow Schlieren Deflectometry is used to quantify the deflection angle of light rays passing through a medium, in this case the vapor-jet region of the fuel spray. As shown schematically in Fig. 3 from left to right, broadband light (from an Energetiq EQ-99X fiber coupled broadband light source) is first refocused by two 75 mm focal length, 50 mm diameter lenses onto a 3 mm high

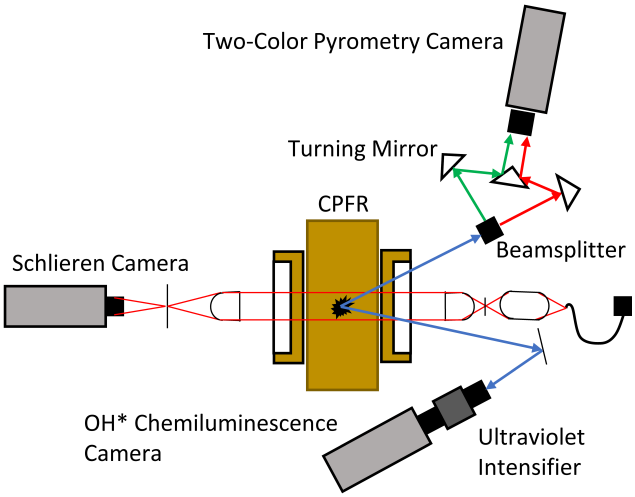

Fig. 2 Simultaneous high-speed diagnostic setup including Rainbow Schlieren Deflectometry, OH* Chemiluminescence, and Two-Color Pyrometry (2CP). View angle of OH* and 2CP systems are exaggerated for illustration purposes.

and 100 μm wide rectangular aperture located at the focal point of a 75 mm diameter, 250 mm focal length achromatic doublet lens Wanstall et al (2017); Agrawal and Wanstall (2018); Wanstall et al (2019). The collimated broadband light is directed through the test chamber. Density gradients deflect the light rays (some light will also be absorbed or scattered by liquid jet/spray) which exit through the parallel window on the chamber. Then, a matching achromatic doublet lens refocuses the light rays onto a rainbow-filter - a transparent rectangular strip with very fine, digitally printed color (hue) gradations - placed at the focal point as shown in Fig. 3. The undeflected light rays (dashed blue ray) pass through the cyan color at the center of the filter, which forms the background color in the schlieren image. A deflected light ray will focus at some (transverse) distance away from the center of the filter (solid blue ray). Thus, rays are color coded based on the transverse displacement on the rainbow filter. The filtered rays create the color (hue) schlieren image, while absorption and/or scattering by liquid region will reduce the ray intensity that

is recorded independently (red ray). A Photoron Nova S9 color camera, in conjunction with a 50 mm Nikon Nikkor lens, records the schlieren images as described in Table 2. The RSD has been used to quantify the density field in non-reacting jets Wanstall et al (2020, 2021), although in this work, intensity and hue signals are used to detect liquid and vapor boundaries, respectively. The specific methodology to identify liquid and vapor boundaries is presented in prior work Wanstall et al (2019, 2017).

The RSD diagnostic improves upon traditional shadowgraphy and other black-and-white imaging techniques Parker et al (2021); Agrawal and Wanstall (2018). Fo example, both the presence and degree of jet fluctuations can be quantified with the RSD hue signal. As in traditional schlieren and shadowgraphy, frame-to-frame deviations can be revealed by subtracting consecutive images. However, hue makes the resulting values more meaningful and, in this work, three distinct bands of frame-to-frame hue-variation are utilized. Lowest band pertains to the nearly imperceptible fluctuations at each pixel location in the image background, which are often very nearly zero in the quiescent flow in the CPFC. Highest band of variations refers to the pixels within the jet core, where the dense fuel jet (large hue displacements) moves quickly (large frame-to-frame shifts). Between these two hue bands is the shear layer of the jet periphery, where high intensity and background-like hues make it difficult to distinguish the jet from the background. By utilizing the hue signal of RSD and subtracting subsequent RSD image, this region becomes easily distinguishable as the true boundary of the vapor jet. This method of vapor detection is used in this study together with a typical threshold sensitivity analysis.

OH*CL at the 310 nm wavelength is an indicator of the reaction zone in the spray. As shown in Fig. 2, OH*CL signal is directed towards an Invisible Vision ultraviolet (UV) intensifier equipped with a 310 nm band pass filter

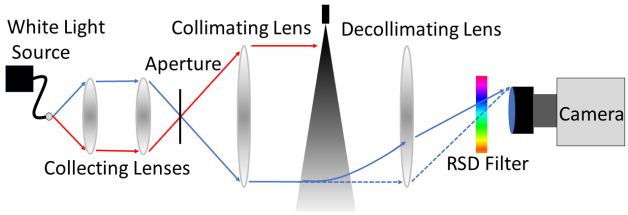

Fig. 3 Rainbow Schlieren Deflectometry (RSD) uses collimated, broadband light, which is then sent through a medium and focused onto a colored filter, encoding deflection angle as hue.

and UV focusing lens. The intensifier utilizes a phosphorous screen to produce visible light from UV (with a gate time of 70 μs in these experiments) which is acquired by a monochromatic Photron SA5 camera as described in Table 2. Per ECN definition ECN (2020), the farthest upstream location detected via chemiluminescence is the reported lift-off length. The algorithm recommended by the ECN was applied to OH*CL images to reliably differentiate OH*CL signal from the noise-floor; the first frame of detectable OH*CL signal was considered the ignition time.

The dataset includes full field 2CP measurements of the thermal radiation from soot, which dominates flame luminosity in the visible spectrum. The general layout of the 2CP optics and camera can be seen in Fig. 2. The flame luminosity passes through a 50/50 beamsplitter, which transmits half of the light and reflects the other half at 90° angle. Band-pass filters of central wavelengths (650 nm and 550 nm) each with 10 nm full width at half maximum bandwidths are attached to the beam splitter outlets. Each spectral signal is reflected by a turning mirror towards a knife-edge prism mirror, and then the two signals travel along parallel paths to the camera. This optical design ensures that both spectral signals have equal path lengths and are imaged on the same camera sensor without inducing parallax and path length errors common in existing 2CP designs. Further details of the optical setup and calibration procedures for this 2CP design can be found in Reggeti et al (2019,

2022). A Phantom v7.3, 14-bit, monochromatic camera with a Nikon Nikkor 105 mm lens is used as per Table 2. In this work, the relative difference in soot radiation intensity between injections is considered in relation to RSD and OH*CL signals.

2.2 Image Alignment and Analysis

The images of an injection using each of the three diagnostics will be presented to assess the fuel jet. Different wavelengths/optics used for each diagnostic require different arrangements and focus. Further, the regions of interest for the three optical methods are not identical, but they do have significant overlap to help with the alignment. Because images are recorded simultaneously by three high-speed cameras with different resolutions, it aids analysis to consolidate the information into a single, spatially aligned image. As shown in Fig. 2, all three cameras view the jet along the center-plane of the CPFC (OH*CL and 2CP view angles are exaggerated for illustration). The structure of the reaction front observed across the three diagnostics aligns very closely, the slight difference in view angles is insignificant.

Figure 4 presents the images recorded simultaneously by each optical diagnostic. The RSD (recorded in red-green and blue colors) is presented with hues as recorded; saturation and intensity have been increased for clarity. The OH*CL intensity (recorded in monochrome) is presented in yellow, and soot luminescence at 650 nm (also in monochrome, from 2CP) is shown in magenta with varying brightness according to the raw signal intensity; both OH*CL and 2CP images have been outlined in red where the signal fades to background noise. These colors were chosen to provide maximum visual contrast among the diagnostics.

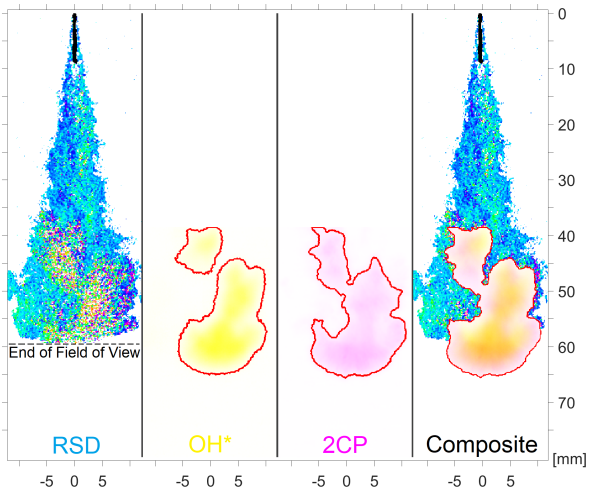

Fig. 4 Combustion was simultaneously recorded by Rainbow Schlieren (in color), OH*CL (BW camera, shown in yellow), and two-color pyrometry (BW, shown in magenta) as shown in Fig. 2. Images from each diagnostic, from the same time, are shown here, along with a 'composite' image to the right, in which the OH* and 2CP intensities are overlaid on top of the RSD hues (note the alignment with extreme hues in the left RSD frame). Red outlines were added to these intensities for heightened contrast.

In the rightmost panel of Fig. 4, the OH*CL and 2CP intensities are overlaid on the RSD image - wherever both OH*CL and 2CP are present, the intensities are added in their respective color-spaces. Thus, in the composite image, pure yellow corresponds to OH*CL without any concurrent 2CP intensity, and vice versa for pure magenta; orange results where both colors are present. In Fig. 4, the OH*CL/2CP signals cover entirely the bright regions of hue in the RSD image representing the ignition kernel, and confirm that the spatial alignment of the three diagnostics is precise. ~~Both OH*CL and 2CP~~ All three diagnostics are line-of-sight measurements, and thus, they do not provide local information about the flame structure in the jet core. However, the composite image illustrates the spatial non-uniformities and non-monotonic trends in mixing (hue signal) in radial and axial directions, auto-ignition, and soot behavior, and it is the basis for the analysis and methodology developed in this study.

3 RESULTS

This study makes the case that turbulent combustion phenomena should be depicted by representative instantaneous behavior rather than ensemble average behavior. Figure 5 shows profiles of liquid length, vapor penetration length, and lift-off length for the present data set. The results based on ensemble average images (average of 500 individual images) are shown in red, and the averages injections processed individually are shown in black. The 95% confidence interval of the sample (CI) bands are included for each parameter to quantify injection to injection variations ~~. In agrrement~~ of controlled test conditions. In agreement with the literature Wright et al (2010), the CI for lift-off length is much larger than that for liquid- and vapor-penetration lengths because dissimilarities magnify as combustion takes place. With the exception of vapor penetration length, the ensemble average lengths are shorter/closer to the injector tip than the average results.

These results show that the global parameters determined from ensemble average images are different from those obtained from individual images and then averaged. Further, the CI of each parameter cannot be determined from the ensemble average analysis. The difference between ensemble average and average results arises because the relationship between image signal and flow/combustion parameters derived from it are non-linear. Thus, ensemble averaging effectively functions as a low-pass filter. For example, with an ensemble average image, the changeover from the background to signal is smoother and less clearly defined, which makes boundary detection more arbitrary compared to individual images with steeper gradients at the boundary. By changing thresholds used for boundary detection between individual and ensemble results it could be possible to find a boundary that matches the

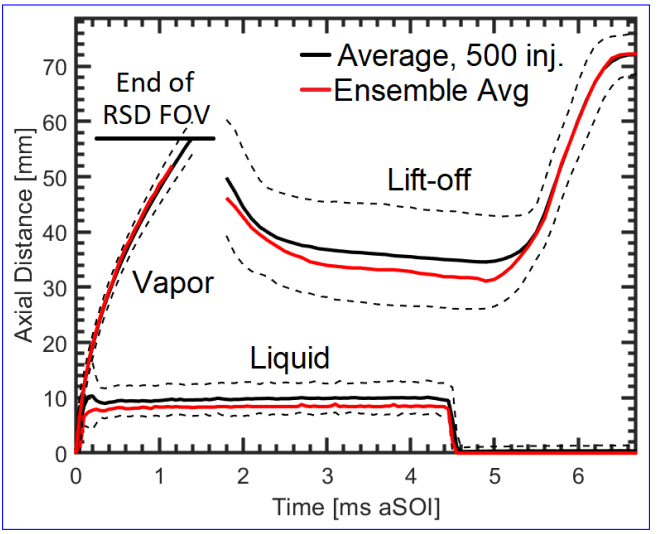

Fig. 5 Liquid and vapor penetration profiles are shown, along with the developing lift-off length. Black lines give the mean and 95% CI for the entire data-set, and the red lines display the same values as determined from the ensemble-average images.

average results. However, without knowing the average behavior this analysis could not be performed and thus, it would offer little additional insight.

In the following sections, the variation among selected injections will be explained and compared with ensemble average behavior. Next, stability and repeatability of the experimental test conditions will be evaluated to determine potential relationship with injection to injection variations. Then, correlations between test conditions and global parameters such as jet penetration, ignition delay, and lift-off length will be analyzed. Finally, the case for a representative injection will be made and a methodology for to identify it will be presented.

The composite images in Fig. 6 show time evolution for several injections near ignition to illustrate the variability in the test results. Each column refers to a single injection event, and is labelled for reference ~~as~~ from A to F. The rightmost column contains the ensemble-average images for the complete data-set and will be discussed in Section. 3.2. Rows of Fig. 6 correspond to different

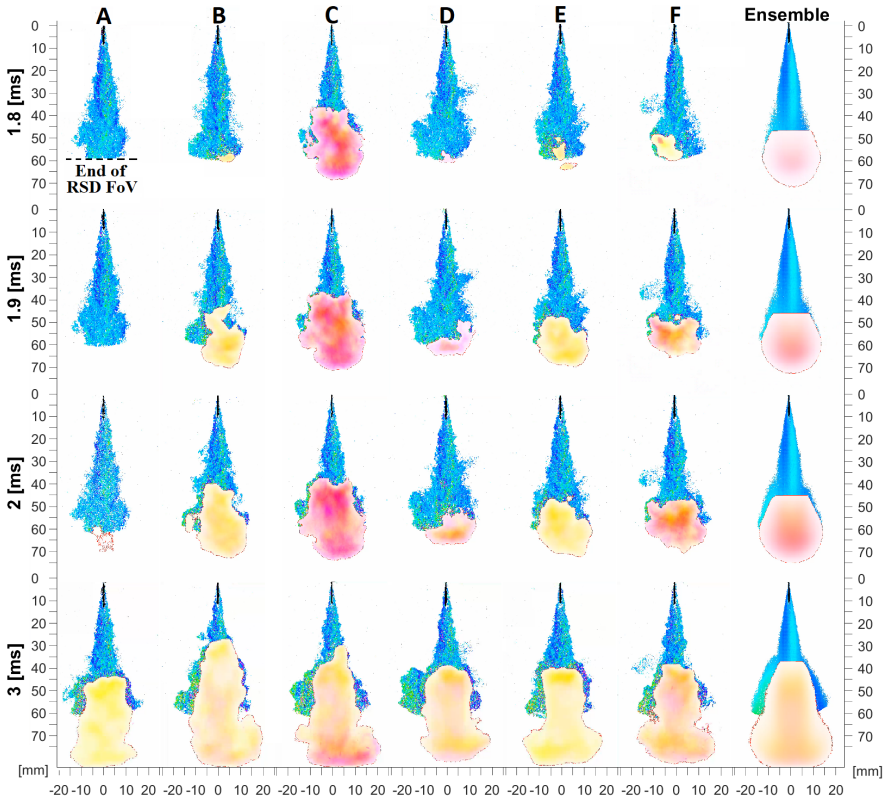

Fig. 6 Select times aSOI are shown for six single-shot injections, as well as ensemble-average images (right). Three frames show the times by which most injections achieve ignition (1.8, 1.9 and 2.0 ms aSOI), and an additional image at 3 ms is provided, after the beginning of the quasi-steady period. Each frame is a composite image of the videos recorded simultaneously by several diagnostics, in the same style as Fig. 4. As labelled in the top left; Rainbow Schlieren Deflectometry (RSD) is shown upstream (image backgrounds removed for clarity), OH*CL intensity is overlaid in yellow, and 2CP intensity in magenta. The OH*CL and 2CP intensities have been normalized across all frames shown.

time-steps after start of injection (aSOI), with the first three images depicting consecutive times typically after ignition, and the last row after 1 ms to represent the quasi-steady behavior before the flame impinges on the screens located downstream.

3.1 Description of Individual Injections

In Fig. 6, injections A-E are outliers in various ways, while Inj. F is the best representation of the overall data set, as will be shown in Sec. 3.4. Injection

A ignites very late at 2.0 ms aSOI and it's upstream vapor-jet maintains a constant cone-angle indicating consistent inert mixing. By 3.0 ms aSOI, the quasi-steady jet has produced OH*CL reaction zones with intensity and location similar to other injections, although the soot luminescence is negligible. Next, Inj.B shows a typical ignition delay time (IDT) of 1.8 ms aSOI; reactions start with a small ignition kernel that propagates upstream and spreads across the jet-width. Notice that this injection has very robust OH*CL signal, shown by bright yellow in Fig. 6, and the shortest steady lift-off length at 3.0 ms aSOI when modest soot luminescence (magenta) is also visible.

Injection C represents the sootiest of the injections observed. This injection ignited at 1.6 ms aSOI (not shown), and the ignition kernel spread quickly to produce strong OH*CL and soot luminescence signals in a large view area by 1.8 ms aSOI. The sub-areas of yellow/magenta at 1.8 ms aSOI show that the high-intensity OH*CL/2CP regions do not align, although they are increasingly homogeneous at later times. The jet achieves a stable lift-off between 2.0-3.0 ms aSOI, and the lift-off length is shorter and flame shape is different from most other injections. At 3.0 ms aSOI, soot can be detected upstream in the premixed lift-off region, as well as in the downstream region near the screens at impingement.

Injection D shows typical ignition behavior at 1.8 ms aSOI when a weak 2CP signal is present. The OH*CL is imperceptible at 1.8 ms aSOI, barely visible at 1.9 ms aSOI, and is stronger at 2.0 ms aSOI. The ignition kernel propagates upstream very slowly compared to other injections, and it does not spread quickly to cover the width of the jet. Quasi-steady behavior with a faint soot signal occurs at the typical lift-off length of 35-40 mm. Interestingly, this injection has strong vapor-jet protrusions on the left side of the reaction zone

at axial locations spanning from 40 mm to the end of the RSD field of view, and a smaller protrusion on the right upstream.

Injection E shows multiple OH*CL ignition kernels at 1.8 ms aSOI, which quickly widen to cover a larger and more homogenized region than those for Inj.B&D at 1.9 ms aSOI. In this case, the lift-off length is within the normal range, but soot signal is not visible either in the developing or quasi-steady jets. Injection F has a large ignition kernel (OH*CL signal) and small soot luminescence at 1.8 ms aSOI. Both OH*CL and 2CP signals quickly widen to spread across the jet width, grow axially, and intensify homogeneously. By 3.0 ms aSOI, the jet has a typical lift-off length and relatively small amounts of soot in the combusting region.

Lastly, the composite ensemble-average images in the right most column show symmetry about the centerline as random variations in instantaneous RSD, OH*CL and 2CP images are effectively filtered out. One additional feature that is most clearly visible in the RSD portion of the ensemble images is the reversal in hue about the centerline. Near the injector, the left size of the jet is darker blue and the right side is cyan. However, the colors reverse direction near the lift-off length as heat release by combustion switches direction of density gradients in the radial direction from relatively high density/low temperature reactants to low density/high temperature combustion products.

The ensemble average images show fairly uniform OH*CL and 2CP signals throughout the core at ignition; note that the red color is a blend of yellow and magenta. The reaction zone occupies nearly the entire jet head at ignition and during next few time steps (1.8 - 2.0 ms aSOI), similar to the individual injections. At quasi-steady period (3.0 ms aSOI), the spray transitions to stronger OH*CL signal (more yellow) but still with detectable soot luminescence in the core region.

3.2 Injection-to-Injection Variations

Figure 6 demonstrates drastic and significant differences in combustion behavior from injection to injection. Besides ignition timings, differences also occur in the axial location, signal intensity, and propagation of the initial ignition kernels. These disparities are outside the error bounds of the spatial and temporal resolutions of the diagnostics. In Fig. 6, ignition kernels are seen over an axial range of approximately 20 mm, and the axial length of those kernels ranges up to 15 mm. Most ignition kernels (yellow/orange) are approximately the same size (see Injs. B/D/E), although 5-10% of the injections had multiple, distinguishable kernels as seen in Inj. E. The 2CP signal or soot cloud (magenta/orange) at ignition is much more varied; Injs. C/D have strong signal, Inj. F has weak signal, and Injs. A/B/E have almost no signal. While no injection had an ignition kernel so large (or dim) as that shown by the ensemble average image, a few early, robustly reacting injections (e.g., Inj. C) are close to it at 1.8 ms aSOI.

Although large increases in the spatial extent and intensity of OH*CL and 2CP signals occur within a frame after ignition, neither of these trends persist thereafter. Instead, further time increments show homogenization of signal boundaries and intensities as seen in Fig. 6 for all injections at 2.0 ms aSOI (except Inj. A, which hasn't yet produced strong OH*CL and 2CP signals) . Injections with notable protrusions have filled in their gaps (Inj. B most obviously, and Injs. E/F are becoming more ovular). Injections B/E also have vastly reduced OH*CL and 2CP intensity gradients, and Injs. C/F maintain larger but uniform intensities at the core than those at the jet periphery. As temperatures and reaction rates increase within the jet, flame stabilization leads to more homogeneous signals at the lift-off length and downstream regions. In

contrast, ensemble average images in Fig. 6 portray homogeneous combustion at all times.

The quasi-steady state at around 3.0 ms aSOI in Fig. 6 demonstrates similarity, if not consistency, between injections. Lift-off lengths vary from 30 to 45 mm, and the OH*CL signal is strong in the 5-10 mm long premixed region near liftoff before reducing in intensity in the jet core and then rising again at the jet head. The volumetric expansion caused by premixed reactions is visible in the RSD images; the hot combustion products are likely present in the radial region between the OH*CL and RSD signal boundaries. The radial expansion of OH*CL (and often 2CP) signal at around 65-70 mm is a consequence of jet impingement on the screens located downstream. Taken together, Fig. 6 demonstrate that fuel injections undergoing autoignition at diesel-like conditions are not ~~reproducible~~repeatable. This observation highlights the challenge posed to combustion researchers and raises the question: what is the typical/average/nominal injection behavior?

3.3 Potential Sources of Variation

In this section, potential sources of variations in experimental results discussed above will be explored: (1) repeatability of experimental conditions to ensure accuracy and stability over the test duration to acquire large data-set, (2) assessment of global parameters (ignition, stabilization, and quasi-steady behavior) to determine if they are stochastic or predictive, and (3) stochastic differences caused by the localized, small-scale turbulent mixing process. Each of these potential sources of variation will be investigated next to ascertain the most significant cause(s) of injection to injection variations in transient spray combustion.

3.3.1 Repeatability of Experimental Conditions

The CFPC used in this study is intended to perform fuel injection experiments in quick succession at nearly identical test conditions. As shown in Table 1, chamber pressure is maintained within 0.02 MPa of target (3 MPa) for 95% of injections. The ambient air temperature has 95% CI of only ±4 °C. Finally, the fuel injection pressure is within 0.71 MPa of target (98.9 MPa) for 95% of injections. Thus, test conditions are steady and repeatable to less than one percent of the set values. Figure 7 plots the individual injection test conditions versus time to demonstrate the high degree of experimental consistency and lack of drift during the test. Next, Fig. 8 present the single injection and running average of IDT, at temporal resolution of 0.1 ms limited by the framing rate of OH*CL diagnostics. These results show that the IDT converges after about 200 injections, and that the present data set of 500 injections is more than adequate.

Next, the potential for injection-to-injection variation caused by residual product gases in the chamber is analyzed, in case the dwell time between injections was insufficient to flush out the products. Figure 9 shows three key parameters (vapor jet tip penetration at 1.0 ms aSOI, lift-off length, and IDT) for each injection plotted against the values from the previous injection. In these return plots (n vs n-1 values) of IDT (black symbols in Fig. 9), variable size symbols are used to convey the relative number of occurrences at each point. The lack of any trend, namely clusters removed from the x=y line, supports the conclusion that consecutive injections are independent, and thus, each injection is a distinct random sample.

Overall, the analysis shows that the test conditions are repeatable with no drift, and the sample size of the tests is more than adequate. Further, the inevitable, minor differences caused by the chamber air flow are much small

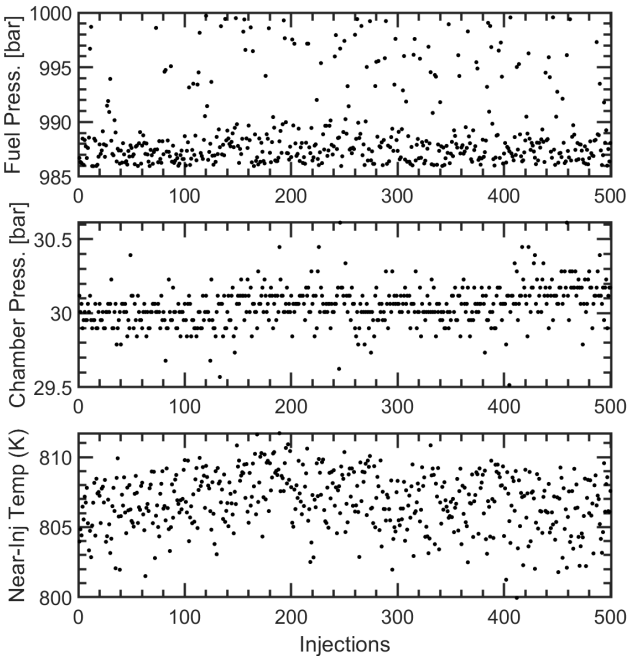

Fig. 7 Chamber thermodynamic conditions for each ignition are presented to demonstrate high degree of experimental repeatability.

compared to other test platforms, for example, optical engines Pastor et al (2017); Xuan et al (2019).

3.3.2 Global Parameter Correlations

In this section, the impact of ambient air temperature variation (as seen in Fig. 7) is investigated to determine systematic trends in IDTs. Thus, IDT was organized in bins of the corresponding air temperature to generate Fig. 10 showing mean IDT and 95% CI for that particular bin (black solid and dashed lines). The red solid curve represents the number of injections within each bin. Figure 10 displays a slight inverse relationship between IDT and air temperature as expected, however this trend should be considered within the context of IDT accuracy of ±0.1 ms. Figure 10 demonstrates that for the majority of the injections (within the temperature range of 804 K to 810 K), the mean

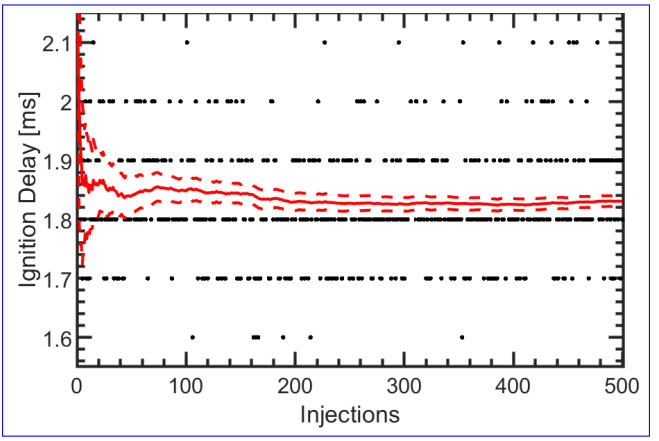

Fig. 8 Ignition delay results from OH* for 500 consecutive injections, and cumulative average (red line) demonstrating converged stationary average. The 95% CI of the mean is provided in dashed red lines.

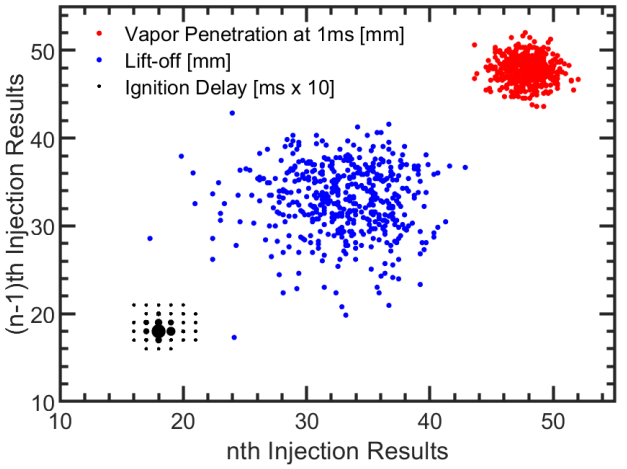

Fig. 9 A return-plot (nth vs $(n-1)$th injection results) is provided to demonstrate shot-to-shot independence based on three key global parameters: lift-off length, vapor penetration, and ignition delay.

IDT and CI are less than the 0.1 ms precision; less than 10 injections (out of a total of 500 injections) outside these temperature bounds have higher CI than measurement accuracy, and can be considered outliers.

Next, results are analyzed to determine any systematic correlation among parameters. For example, is the IDT inherently related to other global parameters ? The top left frame in Fig. 11 shows a histogram of IDTs for all injections,

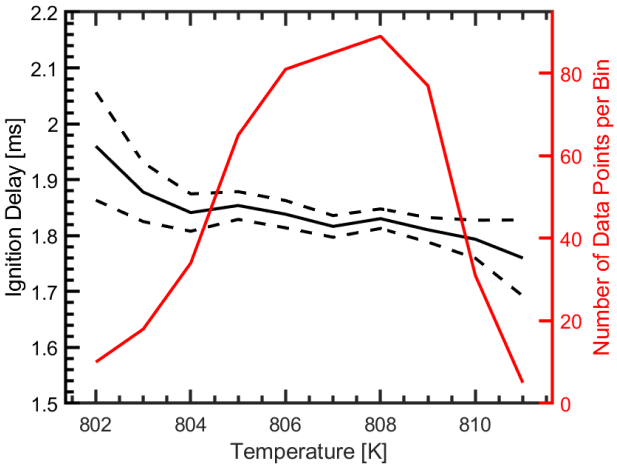

Fig. 10 Mean ignition delay (and 95% CI of the mean) is presented as a function of ambient temperature. The ambient temperatures recorded for each injection were binned to the nearest 1 K. Only five injections had temperatures outside this range, and were excluded.

the top right and bottom left plots show histograms of lift-off length and vapor penetration length, respectively, in bins of IDTs. A scatter plot of vapor penetration length versus lift-off length is shown on the bottom right. These three parameters were chosen for demonstration because they facilitate comparison with Fig. 9, and also because they inform other parameters discussed so far. In Fig. 11, the lift-off length has similar histogram distributions for different IDTs, indicating no direct correlation between the two parameters. Similarly, no correlation exists between vapor penetration length and IDT. No discernible trend between lift-off length and vapor penetration length can be identified from the scatter plot at 1.0 ms. Results in Figs. 8 to 11 show that injections are independent and can be treated as random samples in this cyclic turbulent combustion process. Multiple possibly-correlated parameters were analyzed in the same way as Figs. 9, 10, and 11, and all arrived at the same conclusion.

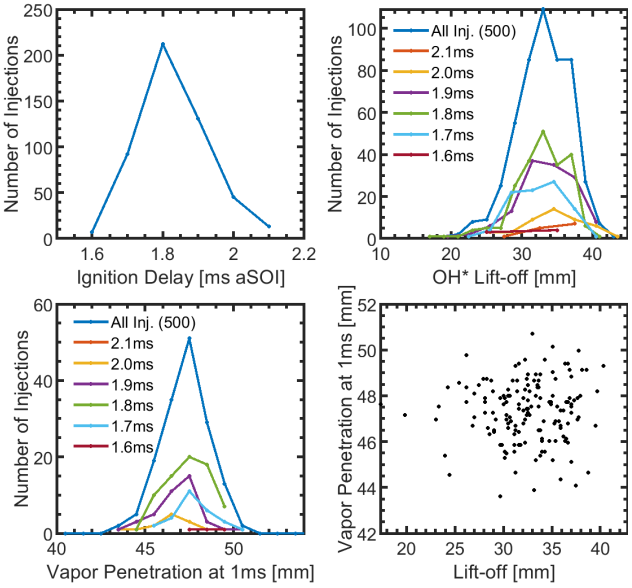

Fig. 11 The distribution of observed ignition delays among 500 injections (top left) is shown with the ~~Cumulative Distribution Functions~~ histograms of OH* Lift-off (top right) and vapor penetration (at 1 ms, bottom left). Both ~~CDFs~~ histograms are binned by ignition delay to demonstrate that these events have unrelated distributions. The relationship between lift-off and vapor-jet penetration is likewise shown (bottom right).

3.4 Representative Single Injections

Having evaluated and dismissed other causes of injection to injection variations, the localized, small scale turbulent mixing ~~remains~~ and rate-of-injection variations remain as the primary ~~source~~sources. The localized turbulence can be observed in single-injection images whereas important details are lost in the ensemble average images, as described in Sec. 3 and Sec. 3.1. As such, it is necessary to select a single (or a set of) injection that describes/represents the nominal/typical cyclic injection phenomena.

A large dataset is necessary to select a representative injection because turbulent combustion phenomena are remarkably adverse to repetition as shown and discussed in Sec. 3.1. Several previous studies have utilized limited datasets to characterize spray and combustion phenomena; $<$ 20 injections is widespread Wright et al (2010); Pickett et al (2011); Manin et al (2013, 2014);

Xuan et al (2019). However, injections that are nominal or outliers cannot be determined from the limited data-sets. Thus, our prior work has recommended a minimum of 100 injectionsParker et al (2021); Reggeti et al (2021) to identify a representative injection. Li has used LES to recommend at least 40 realizations to adequately ~~cdescribe~~ describe cycle-to-cycle variation in a gasoline direct-injection application Li et al (2017). In the present study, 500 injections, far exceeding those standards, are used to determine the representative injection(s) as discussed next.

The method to identify the most representative injection (Inj. F in Fig. 6) utilizes the concept of a z-score rating, which rates an event's deviation from the average (μ) in terms of standard deviations (σ). This follows the formula $z = \frac{x-\mu}{\sigma}$, where $z = 0$ indicates perfect adherence to the mean behavior, and $z = +1$ represents behavior consistent within one standard deviation from the mean. This method is demonstrated by applying it to determine an injection with representative image boundaries.

At each axial position and for each side of the RSD/OH*CL/2CP image boundaries, a z-score is calculated. The z-scores are calculated as radii at left (LB) and right (RB) boundaries at a given time, $r_{LB \text{ or } RB}(i, ax, t)$, relative to the average and standard deviations of all injections at that time/location, ~~$\overline{r}_{LB \text{ or } RB}(i, ax, t)$ and $\sigma_{r_{LB \text{ or } RB}}(i, ax, t)$~~ $\overline{r}_{LB \text{ or } RB}(ax, t)$ and $\sigma_{r_{LB \text{ or } RB}}(ax, t)$. The z-scores are averaged spatially and temporally for each injection and each diagnostic to identify superlative injections across several optical diagnostics Reggeti et al (2021). As shown in Eq.1, the total z-score for a specific diagnostic, $z_{tot,i}$ is the average over all time steps (from t_o to t_f) and spatial locations (from injector tip, $ax = 0$, to jet tip at that time, $ax = ax_{max,t,i}$) of the combined left and right boundaries' z-scores. Finally, an overall average is

obtained by dividing the total z-score by the number of axial steps and time steps, ax_{steps} and t_{steps}.

Because the RSD boundaries are relatively steady compared to OH*CL and especially 2CP boundaries, the $z_{tot,i}$ scores for each injection and diagnostic are normalized by the maximum $z_{tot,i}$ over all injections for that diagnostic. Thus, each diagnostic is equally weighted to calculate the average normalized total z-score across all three diagnostics. This ranking results in Inj. F in Fig. 6 to be the most representative injection. The other five injections presented in Fig. 6 are outliers in various ways having high z-scores in one or more diagnostics.

$$z_{tot,i} = \frac{\sum_{t_o}^{t_f} \sum_{ax=0}^{ax_{max,t,i}} \frac{r_{LB}(i,ax,t)-\bar{r}_{LB}(i,ax,t)}{\sigma_{r_{LB}(i,ax,t)}} + \frac{r_{RB}(i,ax,t)-\bar{r}_{RB}(i,ax,t)}{\sigma_{r_{RB}(i,ax,t)}} \sum_{t_o}^{t_f} \sum_{ax=0}^{ax_{max,t,i}} \frac{r_{LB}(i,ax,t)-\bar{r}_{LB}}{\sigma_{r_{LB}(ax,t)}}}{ax_{steps}\, t_{steps}} \qquad ax_{ste} \tag{1}$$

For visualization of the z-score metric, Fig. 12 presents RSD images for a single injection (a, left), and the ensemble average image at the same time-step (b, right). The red lines overlaid on both halves of Fig. 12a/b portray mean and 95% CI locations of the left and right jet-edges observed at each axial location at this time (2.5 ms aSOI) across all injections. The average boundary does not match with the boundary of the single injection (left image), neither does it align with the ensemble average boundary (right image). This unexpected result ~~stems~~ could stem from fuel vapor plumes randomly ejecting at all axial locations on both sides of the jet, for example, owing to cavitation within the injector although further investigation will clearly be necessary; Inj. F in Fig. 6 represents an example of this phenomena. The OH*CL and 2CP images resulted in similar differences (not shown) among individual injection, average, and ensemble average boundaries.

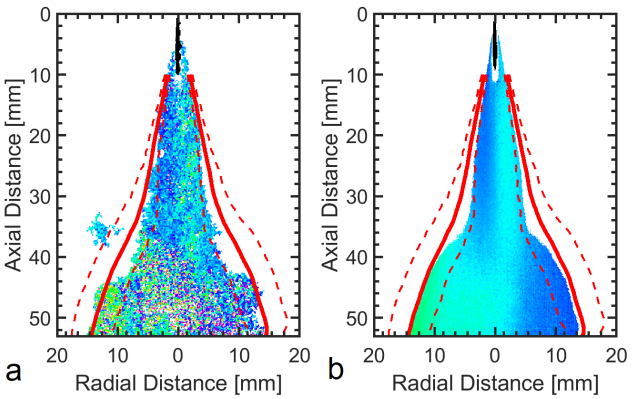

Fig. 12 RSD-images are shown in hue space for a) the Representative single injection (Inj. F in Fig. 6), and b) the ensemble image; both have had the background removed. Overlaid on both images, in red, is the mean and 95% CI determined from the full data-set of 500 injections.

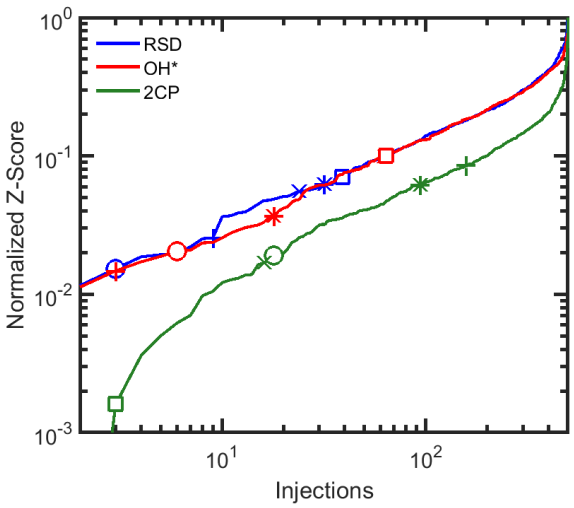

Fig. 13 Normalized total z-score distribution for each diagnostic with symbols marking the five injections with overall lowest average z-score across all diagnostics.

Table 3 Global parameter results for ~~four~~ five most representative injections based on average total z-score metric

Avg. Total Z-score (ranked order)	Injection Number	Ignition Delay [ms]	Vapor Length at 1 ms [mm]	OH* Lift-off Length [mm]
0.018	77	1.8	48.8	39.4
0.042	255	1.8	48.6	41.1
0.054 (Inj. F)	262	1.8	46.0	35.1
0.054	177	1.7	47.5	38.1
0.057	215	1.8	49.6	32.5
Overall Avg.		1.73	48.5	40.5

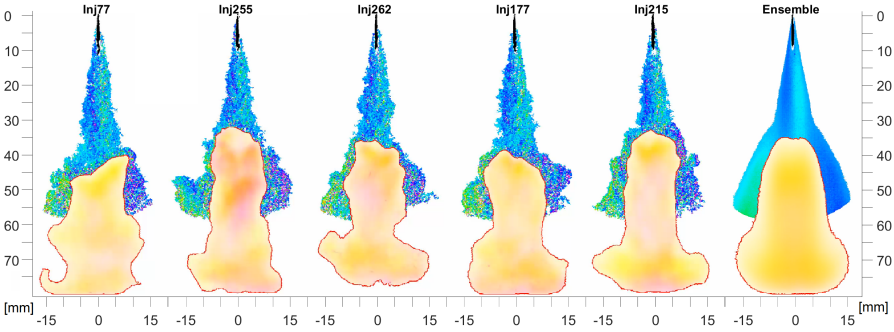

Fig. 14 Composite images of the five lowest average z-score injections at 3 ms after start of injection. Contrasted to large range of variation in Fig. 6, this subset exhibit clear consistency in behavior with Inj. F (262) being selected as most representative.

The z-score rankings of each diagnostic versus injections are shown in Fig. 13 plotted on a log scale. The normalized z-score values range from $< 10^{-3}$ for 2CP, and $< 10^{-2}$ for others, up to 1.0. The five injections with overall lowest average z-score across all diagnostics are identified by symbols in Fig. 13. The injection with the lowest z-score for 2CP, represented by the square symbol, has the highest z-score for RSD and OH*CL for the five injections shown. This example illustrates a single injection is unlikely to exhibit representative behavior in all regards. The effect of sample size on representative injection indicated that injections with the lowest z-score alternate within only a few candidate injections, and that a sample of 100+ injections will have a suitable and easily identifiable injection candidate based on our metric. Table 3 lists the z-scores and the key global parameters for the five injections with the lowest z-scores. Each of these injections shows IDT of either 1.7 or 1.8 ms (overall average is 1.73 ms), and vapor penetration length within 3.0 mm of the average. The main difference is observed in the lift-off length.

Figure 14 shows composite images at the quasi-steady for five injections with the lowest z-scores together with the ensemble average image in the last column. The consistency of injections in this small subset is clear, except for Inj. 255 showing higher soot than other injections; any of these injections could

represent the present data set. ~~Though~~ Although Inj. F (262) does not have the absolute lowest total z-score, it is ~~deemed~~ chosen as the most representative injection because of its overall symmetry and consistency in all three diagnostics.

While the z-score metric presented here focuses on the boundary characterization, it is reasonable to extend the analysis to include other parameters. For example global values such as ignition delay, lift-off length, etc. for each injection could be included. A number of alternative formulations of the overall ranking method were considered resulting in only minor differences in the final set of most representative injections identified.

4 SUMMARY and CONCLUSIONS

An optically accessible constant pressure flow chamber was utilized to acquire 500 injections of transient, n-heptane spray reacting in high pressure, high temperature ambient air, while maintaining near-constant control of ambient and injection conditions. Analysis of high-speed images acquired by rainbow schlieren deflectometery (RSD), OH* chemiluminescence (OH*CL), and two-color pyrometry (2CP) show remarkable injection-to-injection variations visually and in key global parameters. Analysis based on ensemble averaged images is called into question because of its inability to preserve the spatial and temporal gradients in measured and derived quantities. As a result, ensemble average analysis under-predicted global parameters compared to the results obtained from the analysis of individual injections and then averaged. A rigorous examination of test conditions revealed no correlation with global parameters such as jet penetration length, ignition delay time, and lift-off length. This leads to the conclusion that the observed variations in injection-to-injection behavior are the result of a combination spatial and temporal

differences in the localized, small-scale turbulence throughout the jet and differences in rate of injection through the nozzle.

Next, a statistical methodology to identify representative injection(s) from a relatively large data-set was presented and demonstrated to interpret injection-to-injection variation. The analysis is based upon a z-score of user defined parameter(s), in this case, boundaries detected by each of the three diagnostics. The z-score measures the departure of a parameter from its average values, and can be normalized and weighted to combine results from different diagnostics. Using this approach, the boundaries of the spray, reaction zone, or soot cloud of each injection are reduced to a single total z-score by averaging the local z-score at each axial position and time, and assigning equal weights to each diagnostics. This methodology requires a large data-set to obtain statistically converged results, which can be challenging or even prohibitive in some combustion applications. In view of the large injection-to-injection variation, the methodology proposed here allows one to to screen an experimental data-set and determine a representative test case for further analysis. In contrast, current approaches rely on analyzing averaged behavior of localized values. The generalized approach to identify a representative injection presented here can easily be applied to any diagnostic that provides spatiotemporal data and for data sets that are sufficiently large to show convergence of the desired parameters.

The benefits of applying the present analysis to CFD development, validation, and analysis are also significant. Representative target values can be identified for models which aim to predict the fluctuating and inherently random turbulent combustion event. Additionally, ~~single LES (or similar) realization~~ experimental representative data can be compared directly ~~against experimental representative data; this will greatly reduce the computational~~

~~cost of producing many~~ with the results of a single LES, instead of performing many LES realizations for the purpose of averaging and comparing to experimental ensemble-averages. The present approach quantifies and describes the range of variations in a phenomena to a degree impossible with ensemble average analysis. A hitherto unavailable dimension of validation is therefore offered to the CFD community; as few as three LES realizations may be sufficient to validate the models, if the representative individual injection behavior as well as the upper and low bounds of variation, quantified by an appropriate parameter, can be captured with acceptable accuracy. Further, while rate of injection cannot be measured in-situ, additional studies characterizing the range of variation for a specific injector would be helpful. As a result of these developments, the CFD parameters can also be refined to produce more physically meaningful phenomenological models.

Compliance with Ethical Standard

Funding. This work was supported in part by the U.S. Department of Energy's Office of Energy Efficiency and Renewable Energy (EERE) under the the Vehicle Technologies Office (VTO), award number DE-EE0007980 as part of the Co-Optimization of Fuels & Engines program. The views expressed herein do not necessarily represent the views of the U.S. Department of Energy or the United States Government.

Conflict of Interest. The authors have no competing interests to declare that are relevant to the content of this article.

Author Contribution. JB and AA lead development of test facility. JB, AA, and AP designed the study. AP conducted the experiments, analyzed data, prepared figures, and drafted manuscript. AA and JB drafted portions and revised the manuscript. All authors reviewed the manuscript.

References

(2020) Engine combustion network. https://ecn.sandia.gov/diesel-spray-combustion/, accessed: 2020-05-05

Agrawal A, Wanstall CT (2018) Rainbow schlieren deflectometry for scalar measurements in fluid flows. Journal of Flow Visualization and Image Processing 25(3-4):329–357

Aleiferis P, Van Romunde Z, Larson G, et al (2015) On the effect of ambient turbulence and thermodynamic conditions on fuel spray development for direct-injection spark-ignition engines. Flow, Turbulence and Combustion 95(1):29–60

Bizon K, Continillo G, Leistner K, et al (2009) Pod-based analysis of cycle-to-cycle variations in an optically accessible diesel engine. Proceedings of the Combustion Institute 32(2):2809–2816. https://doi.org/https://doi.org/10.1016/j.proci.2008.08.010, URL https://www.sciencedirect.com/science/article/pii/S1540748908003222

Blocquet M, Schoemaecker C, Amedro D, et al (2013) Quantification of oh and ho2 radicals during the low-temperature oxidation of hydrocarbons by fluorescence assay by gas expansion technique. Proceedings of the National Academy of Sciences 110(50):20,014–20,017. https://doi.org/10.1073/pnas.1314968110, URL https://www.pnas.org/content/110/50/20014, https://arxiv.org/abs/https://www.pnas.org/content/110/50/20014.full.pdf

Burluka A, Gorokhovski M, Borghi R (1997) Statistical model of turbulent premixed combustion with interacting flamelets. Combustion and flame 109(1-2):173–187

Clark LG, Kook S (2018) Correlation of spatial and temporal filtering methods for turbulence quantification in spark-ignition direct-injection (sidi) engine flows. Flow, Turbulence and Combustion 101(1):161–189

Creadick AG (2010) Perfectly Average: The Pursuit of Normality in Postwar America. University of Massachusetts Press

Donkerbroek A, van Vliet A, Somers L, et al (2011) Relation between hydroxyl and formaldehyde in a direct-injection heavy-duty diesel engine. Combustion and Flame 158(3):564–572. https://doi.org/https://doi.org/10.1016/j.combustflame.2010.09.024, URL https://www.sciencedirect.com/science/article/pii/S0010218010002750

Ihme M, Chung WT, Mishra AA (2022) Combustion machine learning: Principles, progress and prospects. Progress in Energy and Combustion Science 91:101,010

Kircher M, Popp S, Gierth S, et al (2022) Investigation of engine combustion and auto-ignition of a multicomponent surrogate fuel with ntc behavior under knocking conditions. Flow, Turbulence and Combustion pp 1–21

Kyrtatos P, Hoyer K, Obrecht P, et al (2014) Apparent effects of in-cylinder pressure oscillations and cycle-to-cycle variability on heat release rate and soot concentration under long ignition delay conditions in diesel engines. International Journal of Engine Research 15(3):325–337. https://doi.org/10.1177/1468087413483288, URL https://doi.org/10.1177/1468087413483288

Li W, Li Y, Wang T, et al (2017) Investigation of the effect of the in-cylinder tumble motion on cycle-to-cycle variations in a direct injection spark ignition (disi) engine using large eddy simulation (les). Flow, Turbulence and

Combustion 98(2):601–631

Liu K, Haworth D (2010) Large-eddy simulation for an axisymmetric piston-cylinder assembly with and without swirl. Flow, turbulence and combustion 85(3):279–307

Maes N, Skeen SA, Bardi M, et al (2020) Spray penetration, combustion, and soot formation characteristics of the ecn spray c and spray d injectors in multiple combustion facilities. Applied Thermal Engineering 172:115,136. https://doi.org/https://doi.org/10.1016/j.applthermaleng.2020.115136, URL https://www.sciencedirect.com/science/article/pii/S1359431119384170

Manin J, Pickett LM, Skeen SA (2013) Two-color diffused back-illumination imaging as a diagnostic for time-resolved soot measurements in reacting sprays. SAE International Journal of Engines 6(4):1908–1921

Manin J, Skeen S, Pickett L, et al (2014) Effects of oxygenated fuels on combustion and soot formation/oxidation processes. SAE International Journal of Fuels and Lubricants 7(3):704–717

Pal P, Kolodziej CP, Choi S, et al (2018) Development of a virtual cfr engine model for knocking combustion analysis. SAE International Journal of Engines 11(6):1069–1082. https://doi.org/https://doi.org/10.4271/2018-01-0187, URL https://doi.org/10.4271/2018-01-0187

Parker A, Wanstall C, Reggeti SA, et al (2021) Simultaneous rainbow schlieren deflectometry and oh* chemiluminescence imaging of a diesel spray flame in constant pressure flow rig. Proceedings of the Combustion Institute 38(4):5557–5565. https://doi.org/https://doi.org/10.1016/j.

proci.2020.05.045, URL https://www.sciencedirect.com/science/article/pii/S1540748920300936

Pastor J, Garcia A, Zhong W, et al (2017) An experimental study on diesel spray injection into a non-quiescent chamber. SAE Int J Fuels Lubr 10(2):394–406. URL https://doi.org/10.4271/2017-01-0850

Payri R, García-Oliver JM, Xuan T, et al (2015) A study on diesel spray tip penetration and radial expansion under reacting conditions. Applied Thermal Engineering 90:619–629. https://doi.org/https://doi.org/10.1016/j.applthermaleng.2015.07.042, URL https://www.sciencedirect.com/science/article/pii/S1359431115007267

Pei Y, Hawkes ER, Kook S (2013) A comprehensive study of effects of mixing and chemical kinetic models on predictions of n-heptane jet ignitions with the pdf method. Flow, turbulence and combustion 91(2):249–280

Pickett LM, Manin J, Genzale CL, et al (2011) Relationship between diesel fuel spray vapor penetration/dispersion and local fuel mixture fraction. SAE International Journal of Engines, 2011-01-0686 4(1):764–799

Reggeti S, Parker A, Wanstall C, et al (2021) Comparing Global Spray Combustion Characteristics and Local Shot-to-Shot Variations in a Reacting n-Heptane Spray. Journal of Engineering for Gas Turbines and Power 143(9)

Reggeti S, Agrawal AK, Bittle J (2022) Robust two-colour pyrometry uncertainty analysis to acquire spatially-resolved measurements. Measurement Science and Technology URL http://iopscience.iop.org/article/10.1088/1361-6501/ac88e9

Reggeti SA, Agrawal AK, Bittle JA (2019) Two-color pyrometry system to eliminate optical errors for spatially resolved measurements in flames. Appl Opt 58(32):8905–8913. https://doi.org/10.1364/AO.58.008905, URL http://ao.osa.org/abstract.cfm?URI=ao-58-32-8905

Rose LT (2016) The End of Average. HarperCollins Publishers Ltd.

Schmitt M, Hu R, Wright YM, et al (2015) Multiple cycle les simulations of a direct injection natural gas engine. Flow, Turbulence and Combustion 95(4):645–668

Som S, Senecal PK, Pomraning E (2012) Comparison of rans and les turbulence models against constant volume diesel experiments. In: 2012 Liquid Atomization and Spray Systems Meeting

Sornette D, Davis AB, Ide K, et al (2007) Algorithm for model validation: Theory and applications. Proceedings of the National Academy of Sciences 104(16):6562–6567. https://doi.org/10.1073/pnas.0611677104, URL https://www.pnas.org/content/104/16/6562, https://arxiv.org/abs/https://www.pnas.org/content/104/16/6562.full.pdf

Wanstall C, Agrawal A, Bittle J (2020) Implications of real-gas behavior on refractive index calculations for optical diagnostics of fuel–air mixing at high pressures. Combustion and Flame 214:47–56

Wanstall CT, Agrawal AK, Bittle JA (2017) Quantifying liquid boundary and vapor distributions in a fuel spray by rainbow schlieren deflectometry. Appl Opt 56(30):8385–8393. https://doi.org/10.1364/AO.56.008385, URL http://opg.optica.org/ao/abstract.cfm?URI=ao-56-30-8385

Wanstall CT, Agrawal AK, Bittle JA (2019) Phase boundary detection in transient, evaporating high-pressure fuel sprays by rainbow schlieren deflectometry. Appl Opt 58(25):6791–6801. https://doi.org/10.1364/AO.58.006791, URL http://ao.osa.org/abstract.cfm?URI=ao-58-25-6791

Wanstall CT, Bittle JA, Agrawal AK (2021) Quantitative concentration measurements in a turbulent helium jet using rainbow schlieren deflectometry. Experiments in Fluids 62(53). https://doi.org/10.1007/s00348-021-03154-2, URL https://doi.org/10.1007/s00348-021-03154-2

Wright YM, Margari ON, Boulouchos K, et al (2010) Experiments and simulations of n-heptane spray auto-ignition in a closed combustion chamber at diesel engine conditions. Flow, turbulence and combustion 84(1):49–78

Xuan T, Pastor JV, García-Oliver JM, et al (2019) In-flame soot quantification of diesel sprays under sooting/non-sooting critical conditions in an optical engine. Applied Thermal Engineering 149:1–10. https://doi.org/https://doi.org/10.1016/j.applthermaleng.2018.11.112, URL https://www.sciencedirect.com/science/article/pii/S1359431118355625

Limitations of cetane number to predict transient combustion phenomena in high-pressure fuel sprays

Allen Parker[a], Shawn A. Reggeti[a], Joshua A. Bittle[a], Ajay K. Agrawal[a,b]

[a] *University of Alabama, Alabama, United States*
[b] *corresponding author, aagrawal@eng.ua.edu*

Abstract

Fundamental understanding of in-cylinder processes in diesel engines is important to screen emerging biofuels and advanced combustion modes that can reduce greenhouse gas emissions and regulated pollutants including soot. In this study, the role of fuel properties on spray development and combustion is investigated by systematically isolating chemical and thermophysical effects. Three different fuels are considered, two with similar chemical properties and two with similar thermophysical properties with one fuel common to both groups. Experiments are performed in a constant-pressure flow chamber designed to provide stable test conditions and facilitate acquisition of at least 150 injections in quick succession for each fuel under reacting conditions at high-pressure, high-temperature ambient conditions using a modified conventional diesel engine injector. High speed optical diagnostics including rainbow schlieren deflectometry, OH* chemiluminescence, and a two-color pyrometry system are employed to simultaneously image the transient spray and reacting jets. Image analysis is performed to determine liquid length, vapor penetration length, timing and location of first stage and main ignition events, lift-off location, total soot mass, and more. Results show that fuels

with similar chemical properties or cetane number (CN) exhibit similar delay times for first stage and main ignition events as may be expected, but very different liquid length, first stage and main ignition locations, lift-off length, apparent turbulent flame speed, and soot formation. As such, the ability to characterize candidate biofuels with CN or other parameters derived from simple flame configurations is called into question. In this study, thermophysical properties controlling the liquid length are identified as the main contributing factor for the observed differences.
Keywords: Cetane Number, Biofuels, Transient Spray Combustion, Optical Diagnostics, Sooting behavior

---

1. Introduction

The high energy density of liquid fuels makes them the preferred source of energy for applications requiring extended mobility, light weight, and intense heat and/or power. The liquid fuel portfolio in the near to long term is expected to include an increasing proportion of biofuels produced from renewable biomass with net zero or negative carbon footprint. For example, the Co-Optima project aims to identify promising fuels for transportation from a wide range of candidates [1, 2, 3]. The project goals include co-optimization of fuels and combustion modes for diesel engines to reduce greenhouse gas (GHG) emissions as well as emissions of nitric oxides (NOx), carbon monoxides (CO), and particulate matter (PM) or soot. Achieving these goals, however, requires a fundamental understanding of the in-cylinder combustion processes and how fuel properties and/or advanced combustion modes affect them.

The combustion process in conventional diesel engines can be divided into two steps; rich, premixed combustion at the center of the jet followed by mixing controlled combustion at the periphery of the diffusion flame [4]. The relative split between premixed and diffusion combustion can be varied by advanced combustion modes introduced in recent years [5] to simultaneously reduce soot and NOx emissions. As the relatively cold fuel is injected directly into the hot environment of the cylinder, the high jet momentum entrains the oxidizer to facilitate vaporization and mixing, which produces a combustible mixture that begins reactions in the lifted flame region. The lift-off length - the distance between injector and the lifted flame location - and local equivalence ratio at the lift-off length have been shown to correlate

closely with soot formation in diesel sprays [6, 7, 8]. However, the role of fuel properties on spray dynamics and combustion behavior is not completely understood.

Fuel properties affecting in-cylinder processes can be divided into two groups, chemical and thermophysical. The chemical properties include the heating value, molecular structure, and chemical composition. These properties affect the heat release rate, ignition behavior, and chemical pathways for fuel fragmentation, oxidation, and soot formation; fuel's ignition behavior is characterized by the cetane number (CN). Fuels' thermophysical properties include density, viscosity, surface tension, boiling point/volatility characteristics, heat of vaporization, etc. These properties affect fuel storage and pumping as well as in-cylinder spray dynamics including fuel atomization and vaporization, entrainment and mixing, and related flow parameters affecting combustion and emissions. The large number of fuel properties makes it challenging to screen alternative fuels to predict combustion performance for specific applications and operating conditions.

The first requirement for compression ignition (CI) engines is to demonstrate correct ignition timing, characterized by fuels' CN. Traditional CN tests utilize a special single-cylinder engine, although the measured values are only reproducible within ±4.8 CN [9]. The derived CN of the fuel can also be measured in a constant-volume chamber using modern diesel injectors such as PAC CID 510 per ASTM 7668 [10] or in an an ignition quality test (IQT) system. Matching fuel's CN (or ignition timing) is important for performance optimization, but it does not correlate to combustion processes including soot formation. Much work has focused on mitigating soot emis-

sions via blending with biofuels and other additives while minimally changing CN [11, 12, 13, 14].

In recent years, Yield Sooting Index (YSI) [15, 16] has demonstrated success in relating a fuel's molecular structure to their sooting tendency in laminar premixed flames. The YSI has also been used by Das and others to study diesel fuels and their surrogates [17, 15, 18]. Measurements of YSI for surrogates used in the present work suggest inherent sooting tendency to be highest for iso-cetane, followed by n-cetane, and then n-heptane [15, 19]. Micro flow reactors have also been used to perform fundamental studies of combustion and soot formation using different fuels. For example, Ref. [20] found that the flame location was minimally affected by fuels including n-cetane, iso-cetane, n-heptane, and others considered in the study. For primary reference fuels (PRFs), Ref. [21] found that soot formation is correlated to the residence time in the reactor. However, it is not clear how these fundamental studies can be extended to predict sooting tendency in diesel-like environments with transient spray development, mixing, and flame stabilization, or how trends observed in simple configurations will hold up at more realistic test conditions.

Spray and combustion parameters in high-pressure, high-temperature diesel operation include liquid length, vapor penetration length, vapor cone angle, first stage ignition and low temperature heat release (LTHR), second stage ignition and high temperature heat release (HTHR), flame stabilization and lift-off length, soot precursor, soot formation and oxidation pathways, etc. In practice, these parameters are inter-linked and depend upon fuel properties and turbulence inherent in the system. One goal of the present study

is to analyze several of these parameters collectively under well-controlled reacting conditions by systematically varying fuels' chemical and thermophysical properties. A brief review of literature providing foundation for the present study is provided next.

In one example study, Kook and Pickett performed simultaneous imaging of liquid sprays and vapor fuel using Fischer-Tropsch, coal-derived, and surrogate fuels sprays in a non-reacting diesel environment to conclude that the vapor penetration is independent of the fuel properties while the liquid length depended upon the boiling point and the density of the fuel. They concluded that for fixed fuel injection and ambient conditions, the total ambient entrainment and mixing are not affected by fuel properties [22]. Study by Zheng et al. investigated gasoline-diesel blends in a constant volume chamber to measure liquid length, lift-off length, and soot concentrations. Results show that increasing gasoline in the fuel blend decreased liquid length, increased lift-off length, and significantly decreased soot concentration [23]. The observed correlation between lift-off length and soot formation is consistent with previous findings [6, 7]. However, varying gasoline in the fuel blend simultaneously changes fuels' thermophysical properties that reduce the liquid length as well as chemical properties that increase the ignition delay time (IDT). These two effects were coupled in the experiment, making it difficult to isolate individual effects. The study by Persson et al. found only a weak correlation between IDT and lift-off length [24]. McGann et al. provide comprehensive background on studies of CN effects in different test platforms, and highlight the role of low temperature fuel breakdown, ignition kernel growth, and heat release rates [25].

The flame stabilization mechanism at lift-off length is also not completely understood. In atmospheric-condition flames, the diffusion flame stabilizes by flame propagation to reach a balance between the jet flow speed and the flame speed. However, at high-pressure, high-temperature diesel conditions, flame stabilization at lift-off could occur via isolated ignition kernels formed upstream [26]. Another potential mechanism for flame stabilization is the turbulent mixing between incoming reactants and high-temperature combustion products found at jet edges [26]. The first stage ignition and LTHR could also play a role, which has prompted recent studies of fuel effects on first stage and overall ignition processes [27].

Regardless of the stabilization mechanisms, the correlation between lift-off length and soot formation is well established in multiple studies [6, 7]. Soot formation can also be affected by the structure of the fuel [2, 3]. For example, Ref.[23] shows that n-cetane (n-hexadecane) is the more soot prone fuel compared to heptamethylnonane (iso-cetane/HMN) based on higher concentrations of the measured polycyclic aromatic hydrocarbons (PAHs, with the exception of toluene).

In this study, the role of fuel properties on spray development and combustion is investigated by systematically isolating chemical and thermophysical effects. Two of the fuels have the same CN and ultimately IDT, but different thermophysical properties. Similarly, two of the fuels have similar thermophysical properties but different CN. One of the neat fuels is common to both groups, resulting in a total of three fuels investigated in this study. A constant pressure flow chamber (CPFC) is utilized to achieve stable high-pressure, high-temperature reacting conditions. Experiments are conducted

at slightly lower ambient pressure and temperature compared to those in operational diesel engines to increase the relevant length and time scales, and thus, differentiate fuel effects with sufficient spatial and temporal resolutions possible by the available optical diagnostics. At least 150 injections are performed in quick succession for each fuel at steady ambient conditions to obtain reliable statistics including mean, standard deviation, and histogram distributions during the complete temporal evolution of the jet, and not just during the quasi-steady period.

Three high-speed optical diagnostics techniques are utilized to simultaneously visualize and quantify various spray and combustion parameters. Rainbow schlieren deflectometry (RSD) is used to quantify liquid and vapor penetration lengths by a single diagnostics, and also to locate and quantify first stage ignition and associated LTHR. Benefits of RSD to provide quantitative data under reacting conditions have been demonstrated in recent studies [28, 29]. OH* chemiluminescence (OH*CL), a well established diagnostics for flame detection [30], is used to visualize the main ignition event and the flame stabilization at lift-off. A two color pyrometry (2CP) system is used to obtain soot mass measurements within the flame. The 2CP used in this work provides spatially resolved measurements of soot mass with high accuracy as described in previous works [31, 32].

2. Experimental Setup and Test Conditions

Figure 1 (previously reported in [29]) illustrates the CPFC used to collect data presented in this study. Fuel is injected into a continuous flow of high pressure, electrically preheated air flowing at nearly quiescent velocity

(0.5 m/s) through the CPFC. Compressed air enters through a flow conditioner that uses several 100-micron mesh elements to break up eddies and a diffuser section to uniformly distribute flow across the CPFC. A Bosch CRIN3-18 injector, modified to have a single 104 μm hole at the tip, injects fuel along the axis of the chamber. All tests are performed at the same nominal ambient air conditions of 800 K, 13 kg/m^3 and fuel injection temperature and pressure of 360 K and 100 MPa, respectively. The CPFC enables acquisition of 150 consecutive injections per hour to study transient combustion phenomena with adequate flush time between injections so as to avoid residual effects on injection-to-injection behavior. For each fuel, at least 150 injections were performed to compute various global and time resovled parameters. Specific test conditions are listed in Table 1 which includes 95% sample confidence interval (CI) ranges, demonstrating steady experimental conditions in the chamber.

Figure 2 portrays the layout of the three optical diagnostics, recorded simultaneously, as discussed in [33]. An Energetiq LDLS broadband light source and Photron Nova S9 are used along with standard optics hardware to capture the RSD images. The RSD system uses a continuously graded color filter (see Fig. 2), instead of a knife-edge, to convert light ray deflections by the test media into colors or hues in the schlieren image. Undeflected rays will pass through the center of the filter to produce a cyan ($180°C$) background of the schlieren image. Rays with positive deflection angles will take colors on the left side of the filter, and vice versa, to produce the color schlieren image amenable to quantification [34]. The RSD uses hue to provide quantitative information about the vapor-jet penetration similar to traditional schlieren,

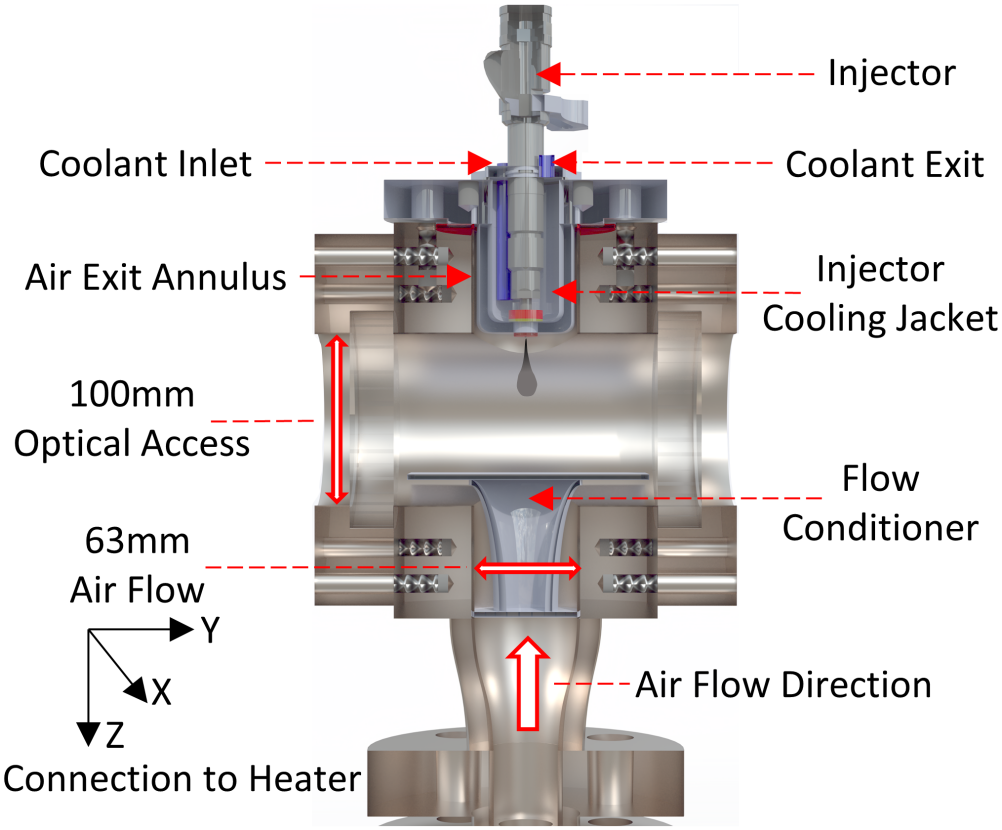

Figure 1: Schematic of the optically accessible constant-pressure flow chamber (CPFC).

but also enables simultaneous detection of liquid length by the independent intensity signal as discussed by Wanstall [35]. In this study, the RSD will also be used to detect first stage ignition and phenomena associated with it including quantification of LTHR using Abel inverted average planar refractive index fields (related to temperature or density fields) as demonstrated previously in reacting jets [29].

In addition, OH*CL in band-passed (310 nm) ultraviolet (UV) spectrum is recorded by an Invisible Vision UVi intensifer (Model 1850-10-S20) coupled to a Photron SA5 high-speed camera used to detect the main ignition event. Ignition delay time is defined by the first frame after start of injection (aSOI) which records OH*CL (with a precision of 0.1 ms dictated by 10 kHz framing rate). Abel inverted average planar OH*CL data will be used to determine the reaction zones and movement of the diffusion flame. Finally, soot incandescence at two wavelengths is recorded simultaneously by a single Phantom v7.3 high-speed camera in a 2CP system consisting of a beam-splitter, band-pass filters (650 and 550 nm, 10 nm FWHM), and turning mirrors to enable spatially resolved measurements of soot-temperature and soot density (KL) to calculate the total soot mass along the line of sight [32, 31]. This novel 2CP system eliminates many of the known optical uncertainties to provide high accuracy measurements of soot mass along at each pixel location in the image [31]. The image acquisition rate and spatial resolution for RSD, OH*CL, and 2CP are, respectively, 10 kHz and 90 μm, 20 kHz and 160 μm, and 10 kHz and 262 μm.

The fuels under study are pure n-heptane (CN = 53.8 per ASTM D6890 ignition quality test (IQT), CN = 56 per ASTM D613/engine test [36]) and

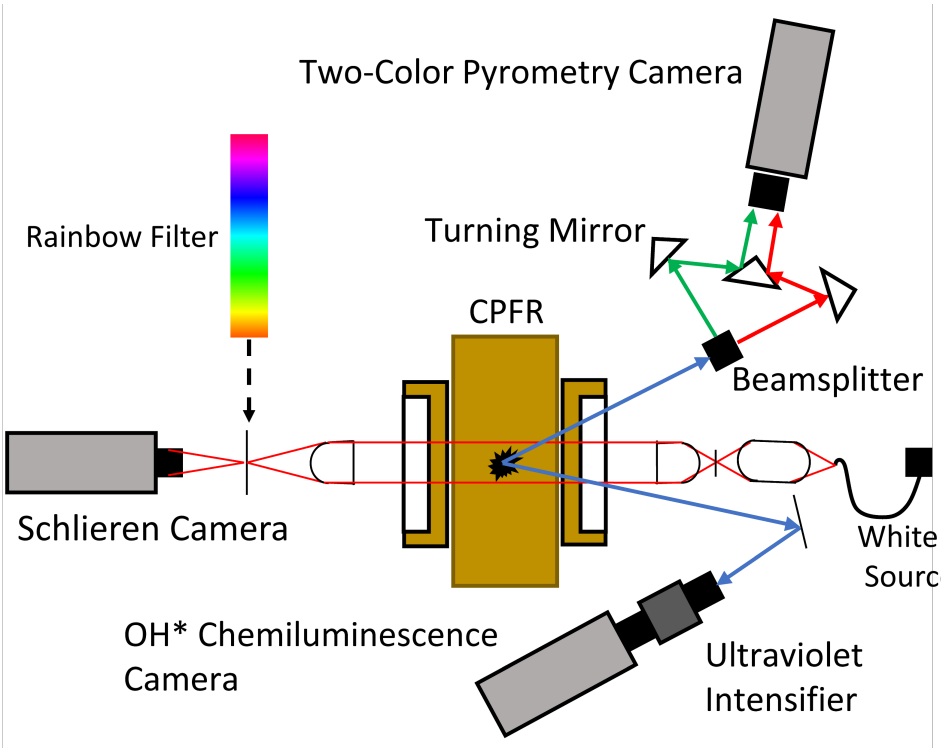

Figure 2: Simultaneous high-speed diagnostic setup including Rainbow Schlieren Deflectometry (RSD), OH* Chemiluminescence (OH*CL), and Two-Color Pyrometry (2CP). View angle of OH*CL and 2CP systems are exaggerated for illustration.

Table 1: Test conditions for CPFC experiments with ±95% sample confidence intervals. All experiments were conducted with air (21% oxygen) and 4.5 ms injection duration.

	heptane	CN=40	CN=53.8
Ambient			
Temperature [K]	807±4	810±4	809 ±7
Pressure [MPa]	3.0±0.03	3.0±0.05	2.9±0.03
Density $[\frac{kg}{m^3}]$	13.0±0.1	13.0±0.2	12.9±0.2
Injector			
Temperature [K]	356 ±1	364 ±1	366 ±1
Pressure [MPa]	98.9 ±0.7	98.9 ±0.7	100 ±0.9

two blends of n-hexadecane (n-cetane) and iso-cetane/HMN - the PRFs for CN determination - having CN = 53.8 and 40. For brevity, these blends will be referred to as CN54 (matching the CN of n-heptane) and CN40. Both blends are mixed to a precision of ±0.425 CN based on the graduated cylinders used to mix blends. Table 2 lists the key properties of n-heptane, n-cetane, HMN, CN54 and CN40. The two reference fuels have higher densities, and higher boiling point temperatures compared to n-heptane among other differences.

2.1. Image Processing and Data Analysis

This section will present the images obtained experimentally, demonstrate time synchronization among diagnostics, and describe the data analysis procedures to obtain important spray and combustion parameters. Figure 3 contains examples of the instantaneous images acquired simultaneously by

Table 2: Fuel properties for n-heptane, n-hexadecane (n-Cetane), heptamethylnonane (HMN), CN54, and CN40. Pure component fuel properties as listed in DOE's Fuel Property Database [1].

	heptane	n-Cctane	HMN	CN40	CN54
Mol. Weight $[\frac{g}{mol}]$	100.2	226.4	226.4	226.4	226.4
Mol. Formula	C_7H_{16}	$C_{16}H_{34}$	$C_{16}H_{34}$	45.6% n-cetane 54.4% HMN^f	29.4% n-cetane 70.6% HMN^f
Density $[\frac{kg}{m^3}]$	683.8^a	773.4^a	793.0^b	784.0	787.2
Boiling Point $[°C]$	98.0	287.0	240.0	-	-
Heat of Vap. $[\frac{kJ}{kg}]$	365.0^b	359.5^b	202.3^b	274.0	248.5
Heat Cap. $[\frac{kJ}{kg*K}]$	2.24	2.21	2.03	2.11	2.08
AFR $[\frac{kg}{kg}]$	13.02	12.94	12.94	12.94	12.94
Cetane Number	53.8^{c,d}	100^e	15^e	40^e	54^e

$^a20°C$, $^b25°C$, ^{c}measured, ^{d}56 in [7], ^{e}definition, ^{f}by volume

the three diagnostics, with minimal post-processing to improve clarity. The RSD image, recorded in color, is presented with intensity and saturation set to maximum values of 1.0 (except in liquid region where intensity is zero), while the primary signal, hue/color, representing light ray deflections is unchanged, and the background has been removed. Raw, unaltered RSD images used to depict the first stage ignition will be presented and discussed later in Fig. 10. The intensities of OH*CL and soot incandescence at wavelength of 650 nm (both recorded in black-and-white) have been false-colored, respectively, to yellow/magenta based on raw intensity, and red outlines were added to provide contrast at the signal boundaries. The OH*CL/2CP images are then overlaid on the RSD image to create the right, composite image of Fig. 3. The RSD hues are centered on cyan (hue = $180°C$), so contrast was maximized by utilizing the other subtractive colors, yellow and magenta, for false-coloring.

The three diagnostics employ separate hardware and imaging cameras to view various regions of the jet from different angles. Thus, it is important to ensure that diagnostics are truly synchronized, spatially and temporally as discussed next. Figure 3 corresponds to an instant soon after autoignition, and while more exhaustive analysis is not shown here, the instantaneous shape and location of the reaction zone identified by RSD, OH*CL, and 2CP are nearly identical. These results provide confidence in image synchronization, and demonstrate that findings from one diagnostics can be connected to those from other diagnostics. Images of the same format seen in Fig. 3 will later be used to compare spray development and combustion behavior of different fuels. Next, the quantitative nature of these images is explored.

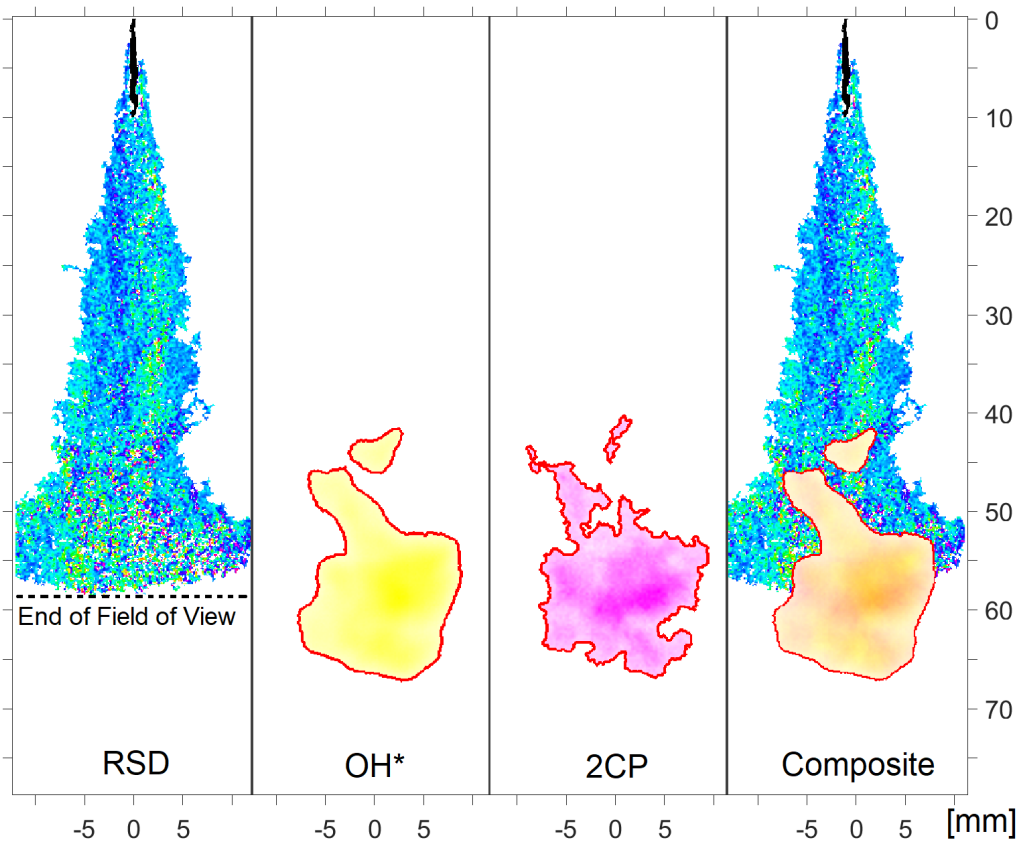

Figure 3: Combustion was simultaneously recorded by RSD, OH*CL (shown in yellow), and 2CP (in magenta) as shown in Fig. 2. Instantaneous images from each diagnostic acquired simultaneously are shown along with a 'composite' image to the right, in which OH*CL and 2CP intensities are overlaid on top of the RSD hues. Red outlines were added to increase contrast.

The RSD diagnostic has been shown to discriminate between liquid- and vapor-phase regions of the spray [29, 35], and to provide quantitative information simultaneously about liquid and vapor boundaries and penetration length (until the vapor jet exceeds the RSD field of view, FOV). The high sensitivity of RSD also provides important information on first stage ignition and LTHR, where the jet cone angle increases suddenly (here around 45 mm downstream), as will be discussed later. The OH*CL coincides with HTHR [30], and is the basis of ignition delay time and lift-off length measurements.

The ECN defines 50% of the maximum observed OH*CL intensity to be a reasonable threshold for distinguishing reaction signals from the noise-floor [37], and the same method is used here to define IDT (the first frame after injection with pixels surpassing that threshold) and lift-off length (the furthest upstream location above that value, corresponding to about 42 mm in Fig. 3. Lastly 2CP measurements of soot incandescence at multiple wavelengths (550 and 650 nm in this study) are used to determine the soot-mass along the line of sight at each pixel location of each frame [32, 31].

3. Results

In this section, first the global parameters such as liquid length, vapor penetration length, ignition location, lift-off length, and total soot mass will be compared for different fuels. These parameters will be obtained by averaging individual values over all injections performed for each fuel, and 95% CI of injection-to-injection variations will be noted. Next, histogram plots of ignition delay time, ignition location, and lift-off location will be presented to identify potential correlation with the CN. This will follow with over-

laid ensemble averaged images of RSD, soot mass, and OH*CL to visualize the spray dynamics including fuel-oxidizer mixing, LTHR, main ignition and flame recession to lift-off length, and sooting behavior. Then, the concept of the apparent turbulent flame speed (ATFS) will be introduced. Next, raw RSD images will be analyzed in detail to determine the time and location of first stage ignition. The analysis will show the important effects of liquid length on first and main ignition events, and the lift-off length. Finally, semi-quantitative analysis of RSD-based planar average refractive index distributions will be used to explain the role of first stage ignition and LTHR on flame stabilization and sooting behavior.

3.1. Global Parameters

The top of Fig. 4 shows average liquid length, vapor-penetration length, and lift-off location versus time aSOI for the three fuels considered with shaded regions indicating instantaneous 95% CI bands to quantify the range of injection-to-injection variation over all injections. The bottom of Fig. 4 provides the corresponding total soot mass data for n-heptane and CN54 only. For the present ambient conditions, CN40 ignited farther downstream and with very low soot signal prior to the flame impinging downstream on the metal screen of the flow diffuser located at a distance of ∼80 mm from the injector as shown in Fig. 1. Thus, only limited data will be provided for this fuel blend, but that will have negligible effects on the outcomes of this study. For each case, at least 150 injections (500 for n-heptane) were performed to compute the averages in Fig. 4. An independent study with a comprehensive analysis of injection to injection variations (not shown here) revealed that the

average values for these particular parameters were statistically stationary when about 50 injections were utilized [38].

Liquid Length. Figure 4 shows that the liquid length for n-heptane increases linearly for about 0.15 ms, and then reaches a quasi-steady value of about 10 mm and remains constant thereafter. In contrast, the liquid length for CN54 and CN40 blends increases linearly for about 0.25 ms aSOI to reach a steady value of 19 mm for both blends. These results show that fully vaporized fuel is available within 0.1-0.3 ms, and that the increased fuel vaporization time for CN40/CN54 blends has a negligible effect on the physical delay time, i.e., an increase by no more than 0.1 ms. Figure 4 shows that the liquid length measurements are repeatable, with 95% CI of about 1.5 mm. The liquid length is affected by ambient and fuel injection conditions [39, 40, 41], but these conditions are the same for all fuels in this study. Thus, the observed differences in the liquid length can be attributed to the differences in the thermophysical properties of the fuels.

Using boiling point and heat of vaporization data in Table 2, fuel jet evaporation in this study would require 399 $\frac{kJ}{kg}$, 634 $\frac{kJ}{kg}$, and 589 $\frac{kJ}{kg}$, respectively, for n-heptane, CN54 (45.65% cetane/54.35% HMN by volume), and CN40 (30% cetane/70% HMN). Thus, CN54 and CN40 produce longer liquid lengths compared to n-heptane because additional heat must be supplied by the entrained ambient fluid. These findings are consistent with previous studies in the literature showing a decrease in the liquid length for more volatile fuels [22, 23]. Kook and Pickett (2012) also show that fuels with higher densities have longer liquid lengths. Table 2 shows that CN54 and CN45 blends have higher densities compared to n-heptane. Thus, longer liq-

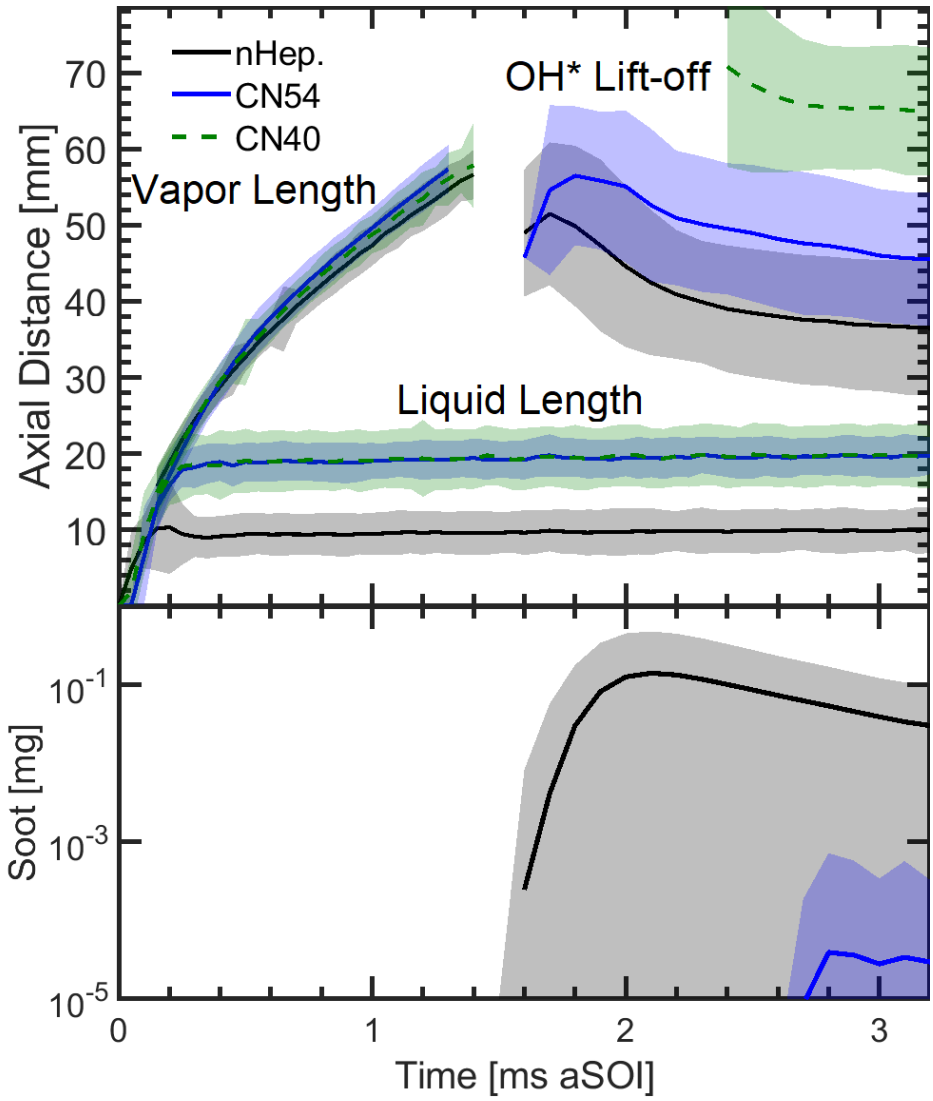

Figure 4: Average global parameters including (top) liquid- and vapor-penetration lengths, lift-off length, and (bottom) total soot mass. Shaded regions show the 95% CI of data.

uid length for CN54 and CN40 is a combined effect of their higher boiling point temperatures and higher densities compared to n-heptane. These thermophysical properties of CN54 and CN40 are sufficiently close to each other,

and thus, liquid length measurements of the two could not be distinguished.

Vapor Penetration Length. Figure 4 shows temporal evolution of average vapor penetration length until the jet is no longer visible in the RSD images at around 60 mm. Initially, the liquid- and vapor-penetration profiles follow each other, but they diverge once the liquid length reaches quasi-steady state. The vapor penetration length is essentially the same for all fuels, and no correlation with fuel properties is found. The narrow bands of standard deviation in Fig. 4 demonstrate that the vapor penetration length measurements are highly repeatable, with relatively small injection-to-injection variations. The cone angles for all fuels (not shown here) were similar, and only minor differences were caused mainly by the image processing algorithm. These results agree with data presented by Kook and Pickett [22], who show that the vapor penetration length and associated momentum flux are functions of injector pressure drop and hole diameter only, and are independent of the fuel density and other thermophysical properties affecting the liquid length.

Note that this study differs from Kook and Pickett [22] in two significant ways: (1) present experiments were performed in a reacting environment while [22] utilized non-reacting ambient conditions. Thus, the findings that fuel's thermophysical properties affect the liquid length, but not the vapor penetration length still apply to situations when LTHR could be present during the mixing process; (2) the ambient temperature (900 K) and pressure (60 MPa) for [22] are higher than those in the present study. Thus, the present approach to study mixing at lower temperatures and pressures would result in longer IDTs and lift-off lengths to enable resolution of the fuel effects

by the available diagnostics.

Flame Location. Figure 4 also depicts the average flame location determined from OH*CL images for all injections. The flame location was identified continuously from the main ignition event to quasi-steady lift-off since images were acquired at high-speed. Results show that even though n-heptane and CN54 have similar CN, the flame location for these two fuels is different at all times. Both flames show a gradual recession upstream between ignition location and quasi-steady lift-off. For n-heptane, ignition occurs at 50 mm from the injector exit and the flame stabilizes at about 36 mm. The corresponding values for CN54 are 60 mm and 45 mm, signifying a difference of about 10 mm from n-heptane.

Figure 4 shows that unlike minor fluctuations in liquid length and vapor penetration length, the flame location data exhibit relatively large injection-to-injection variations. However, the observed differences in flame location for n-heptane and CN54 persist throughout the injection. As expected, the CN40 ignites farther downstream because of its low CN and correspondingly long IDT. As discussed earlier, CN40 data are overwhelmingly impacted by impingement on the metal screen located downstream. However, these results clearly show that ignition location and lift-off length are affected by not only the chemical effects (as in case of CN54 and CN40) but also the thermophysical effects as discussed later in case of n-heptane and CN54.

Total Soot Mass. The bottom of Fig. 4 provides total soot mass obtained by summing local soot mass data across the soot cloud versus time. The data are shown for n-heptane and CN54 only, since CN40 soot mass measurements were too small and deemed unreliable as explained above. Figure 4

shows that the total soot mass measurements exhibit the largest injection-to-injection variations, indicating that even though the upstream fuel-oxidizer mixing is repeatable on a global scale, the soot chemistry is extremely sensitive to the local fuel/oxidizer mixture fluctuations inherently present in the flow. Figure 4 shows that in the case of n-heptane soot forms quickly, reaches a peak value, and then soot oxidization dominates and gradually reduced the soot mass before impingement on the screens. In contrast, soot formation is delayed for CN54 and apparently never reaches the peak or oxidation phase within the available field of view. Most importantly, the relative amounts of total soot mass are dramatically different for n-heptane and CN54 fuels; the measured peak soot mass is nearly 100 times more for n-heptane than that for CN54 (note the log scale for soot mass). The higher soot mass for n-heptane can likely be attributed, at least in part, to the shorter lift-off length for n-heptane compared to CN54, as accepted widely in the literature [6, 7]. Present trends however do not agree with YSI measurements of fuels' inherent sooting tendency in idealized flame configurations [15, 19].

Next, Table 2 shows that the stoichiometric air-fuel mass ratio for the two fuels is similar; 13.0 for n-heptane and 12.9 for CN54. Thus, flame stoichiometry for the two fuels is similar. Further, n-heptane is a lighter molecule with only 7 carbon atoms compared to 16 carbon atoms in the heavier CN54 molecule. Thus, CN54 is expected to produce higher soot concentrations based upon measurements in micro flow reactors and YSI measurements [15, 19]. Interestingly, experimental observations presented so far cannot be supported fully by the available explanations in the literature. The remainder of this work will provide context and show how liquid length

and first stage ignition lead to these unexpected differences in lift-off length and soot formation.

3.2. Ignition Delay Time

Instantaneous OH*CL images were used to determine the start of main ignition, and to create the histogram plots of IDT for the three fuels as shown in Fig. 5. In these and all subsequent histogram plots, data for each bin is shown at the mid-point and bin width is listed in the figure caption. Recall that n-heptane had 500 injections while CN54 and CN40 blends had 150 injections. Thus, plots in Fig. 5 are normalized by the number of total injections. Despite repeatable ambient and fuel injection conditions, the IDT varies in a turbulent environment [9], and so a distribution results. In

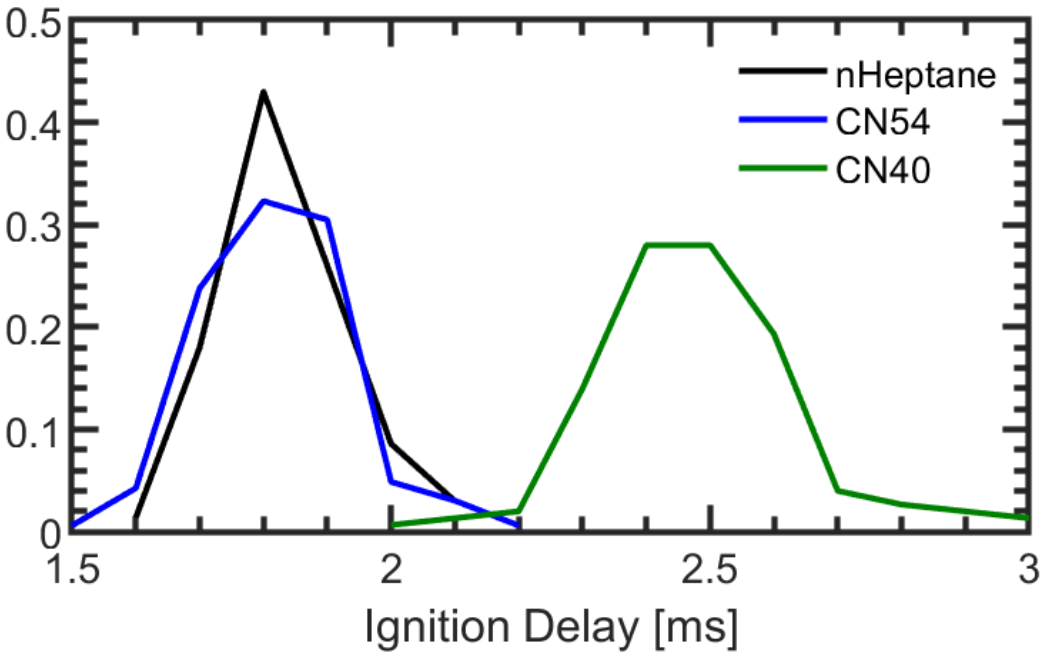

Figure 5: Normalized histograms of ignition delay time for each fuel (bin width = 0.1 ms).

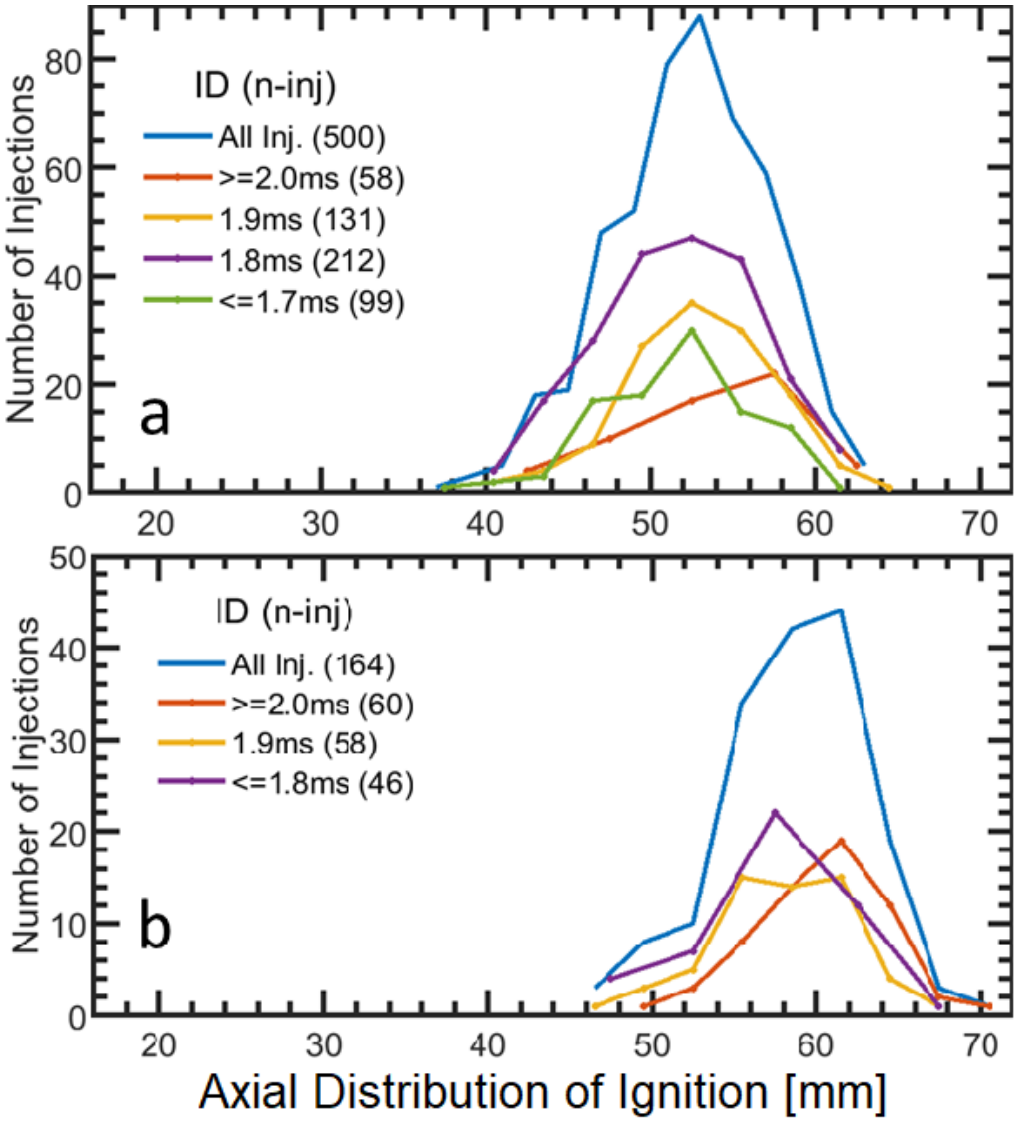

Figure 6: Histograms of the axial location of main ignition for (a) n-heptane and (b) CN54 (bin width = 1.5 mm). Different curves represent data segmented into bins of ignition delay times. The number of injections contributing to each curve is shown in the legend.

the present study, the ambient conditions are such that injection-to-injection variations in IDT are relatively high. This variation in IDT is present, though less, even at higher temperatures and pressures relevant to diesel engines.

Figure 5 shows that IDT histogram plots for n-heptane and CN54 align almost perfectly, and CN40 has the expected longer average IDT distribution. The differences in IDT between n-heptane and CN54 are too minute to be detected by the 10kHz framing rate used in this study. The excellent match in IDT for n-heptane and CN54 IDT demonstrates that the kinetic features affecting ignition process are very similar or perhaps the same, and that the present experimental facility indeed correlates with standardized tests used to determine fuel's CN. This outcome is fortuitous since the correlation between CN and IDT cannot be replicated in general, as reported in the experimental study of fuel effects by [24] utilizing an operational diesel engine.

All three fuels show nearly symmetric distributions of IDT indicating a stochastic phenomenon. Rigorous analysis of ambient conditions in the chamber (Table 1) revealed no systematic departures from the set pressures and temperatures. Thus, the IDT distributions can be attributed to the random variations in the local ignition kernels created by the turbulent mixing process. The presumed similarity in kinetic mechanisms during the ignition processes of n-heptane and CN54 fuels also suggests that the differences in ignition and lift-off locations in Fig. 4 must originate in fuel's thermophysical properties.

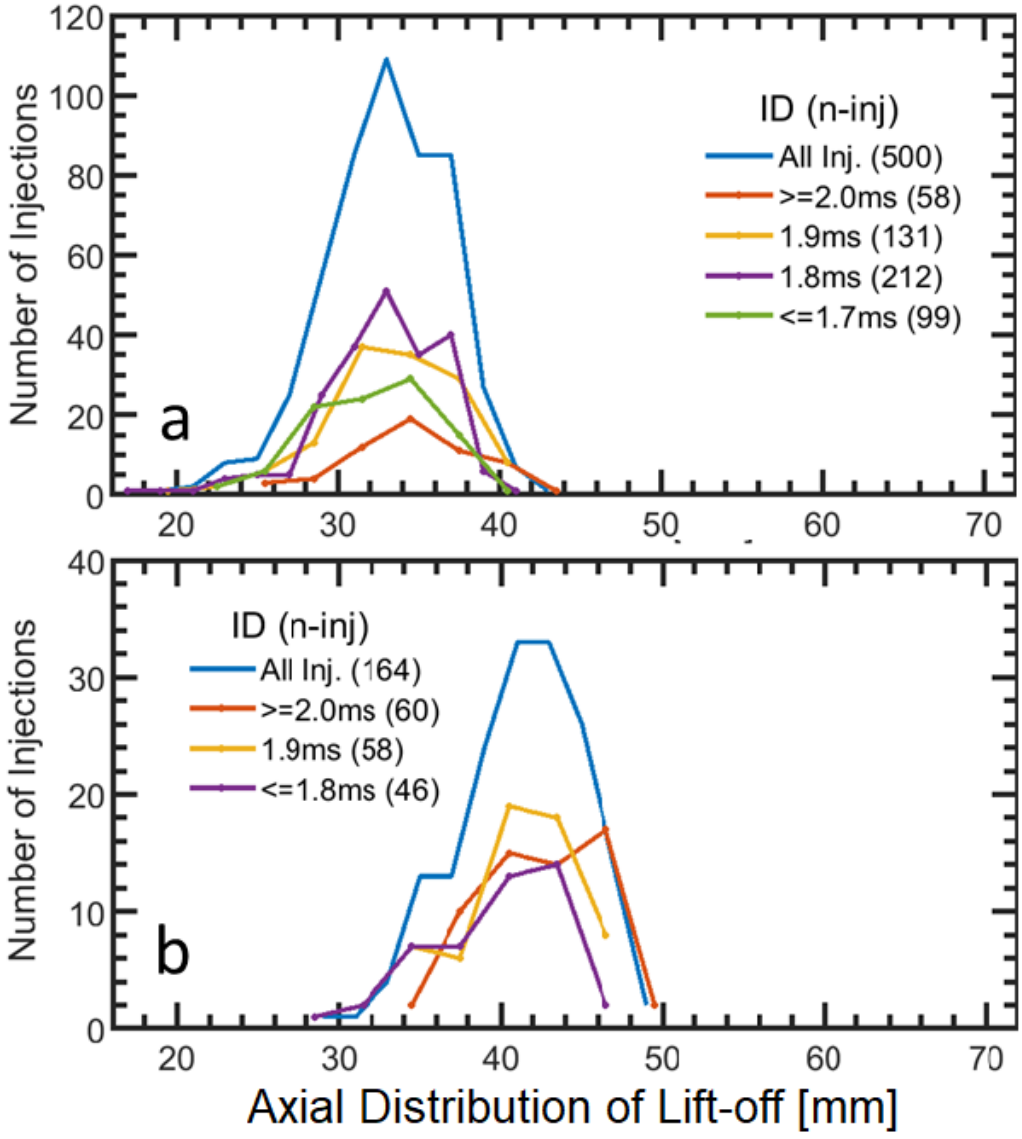

Figure 7: Histograms of the axial location of quasi-stready lift-off length for (a) n-heptane and (b) CN54 (bin width = 1.5 mm). Different curves represent data segmented into bins of ignition delay times. The number of injections contributing to each curve is shown in the legend.

3.3. Flame Location

Local variations in ignition kernels affect ignition location and lift-off length and are observed via OH*CL imaging. Figure 6 shows the histogram plots of ignition location for n-heptane and CN54 to quantify these fluctuations. The blue curve in Fig. 6 represents all injection events, and it shows a relatively symmetric distribution for ignition location of n-heptane over a range of axial distances from 40 mm to 65 mm. For CN54, the distribution is also symmetric, but the ignition occurs at a noticeably downstream axial location, and its variation between 48 mm and 68 mm is still quite wide.

Initially, it was hypothesized that the variations in ignition location would correlate with variations in IDT, i.e., a longer IDT would correspond to an ignition location farther downstream, the jet having penetrated farther. Thus, injection data were divided into bins of different IDTs to generate multiple histogram plots, represented by different colors in Fig. 6. Each IDT bin still has more than 50 injections to obtain sufficiently resolved distributions. Results show only a very weak correlation between IDT and ignition location, indicating that ignition does not occur at the farthest extent of the jet tip. Instead, ignition occurs in localized kernels that can take different trajectories depending upon the turbulent mixing processes.

Figure 4 showed that the reaction front recesses gradually upstream from ignition location to lift-off length. Figure 7 presents histogram plots of the quasi-steady lift-off length for n-heptane and CN54 for all injections as well as for injections divided into bins of IDTs. Results show that histograms are symmetric for all cases, and the lift-off length varies between 25 mm and 40 mm for n-heptane and between 33 mm and 50 mm for CN54, regardless

of the IDT bin used to generate the plot. Thus, this heavily mixing-driven process contains enough randomness to obscure any relationship between IDT and stable lift-off length, a result consistent with previous studies [42, 26, 43, 44]. Considering the lack of a matching trend between IDT and lift-off length within the data set, and the matching IDTs between n-heptane and CN54 in Fig. 5, the observed difference in the lift-off length between these two fuels must be attributed elsewhere. Note that the separation of 8 to 10 mm between the lift-off lengths of these fuels is close to the difference between their liquid lengths.

3.4. Temporal Evolution of Spray and Combustion

Large injection-to-injection variations in the combustion phenomena such as IDT, ignition location, lift-off length, and soot mass make it difficult to analyze the instantaneous images to describe the spray dynamics, ignition, flame stabilization, and soot formation. Thus, images acquired by RSD, OH*CL, and 2CP were ensemble averaged to depict the temporal evolution of spray and combustion processes. For each diagnostic, ensemble averages were obtained at each time step by averaging relevant data across all injections. For sufficiently large number of injection events (>50), this averaging process resulted in axisymmetric distributions for the quantities of interest.

In case of RSD, this approach provides axisymmetric distributions of light ray deflection angles (related to hues) resulting from density gradients in the test media. Then, an Abel transform is used to obtain the local distributions of average refractive index difference across the whole field, which can be related to local temperature, species concentrations, and pressure prior to the

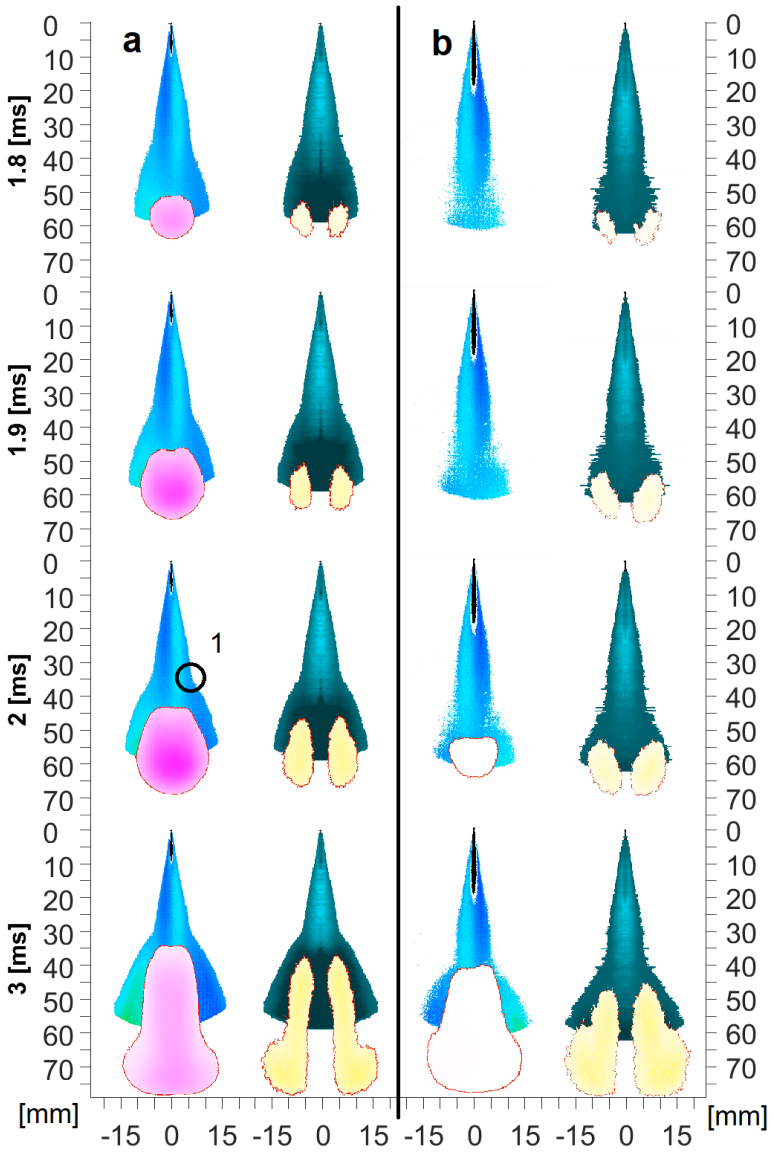

Figure 8: Composite images of developing a) n-heptane and b) CN54 combustion including (left column) ensemble average hues (RSD) and soot mass (2CP), and (right column) normalized planar average refractive index and planar average OH*CL. Deflection angle in hue, soot mass in magenta, and planar OH*CL in yellow, and planar refractive index in teal are all plotted on same arbitrary scale for both fuels.

onset of any chemical reactions. Similarly, for OH*CL, axisymmetric ensemble averaged data across the whole field will be inverted by Abel transform to obtain the local distributions of average OH*CL to identify the reaction zone of the diffusion flame. The soot mass measurements from 2CP are ensemble averaged across all injections to create the axisymmetric soot cloud at each time step. For ease of visualization, the soot cloud image will be superimposed upon the ensemble averaged RSD hue image at each time step. Separately, the average refractive index difference field obtained from RSD and the average reaction zone determined from OH*CL are superimposed to determine their relative behavior with time.

Figure 8 presents composite images at several time-steps between ignition and near quasi-steady periods of the reacting spray. The figure is divided into n-heptane images on the left half (a) and CN54 images on the right half (b). In each half, images on the first column combine RSD hue and soot mass data and those in the second column show RSD refractive index difference data superimposed with OH*CL reaction zone data. The time stamps, identified in Fig. 8, are 1.8, 1.9, and 2.0 ms aSOI to describe phenomena near ignition, and 3.0 ms aSOI to show the quasi-steady behavior before impingement on screens located downstream. First, the temporal evolution of n-heptane will be discussed followed by that for CN54.

In Fig. 8a (1st column) for n-heptane, the composite image displays a thin black strip near the injector tip representing the liquid phase (where light is attenuated as discussed by [35]) and vapor phase regions shown by hue variations (blue/green colors) consistent with the design of the RSD filter shown in Fig.2. The shades of blue and green appear, respectively, on the left

and right sides of the images. The jet width increases suddenly at point 1 in the figure. The images show that downstream of this jet expansion location, the color gradations switch direction from left to right and vice versa.

Note that the density gradients in the jet can occur by concentration gradients (heavier fuel near the center diffusing into lighter ambient on the outside), temperature gradients (hot ambient on the outside to cooler fuel near the center) or both. Light rays bend inward in fuel rich dense regions and outwards in hot low density regions, although the two effects cannot be discriminated. The sudden jet expansion at point 1, and switch in color gradations thereafter indicate significant LTHR has taken place at and prior to this location. Details of LTHR resulting from first stage ignition will be discussed in section Sec. 3.6.

The OH*CL intensity and raw 2CP intensity are shown, respectively, in shades of yellow and magenta. At the time of ignition at 1.8 ms aSOI, a soot cloud is formed typically at the jet head along with the reaction zone of the diffusion flame. At 1.9 ms aSOI, both soot cloud and reaction zone have grown axially. Subsequently, at 2.0 and 3.0 ms aSOI, the soot cloud and diffusion flame have grown downstream by convection and upstream by flame propagation. The images show excellent symmetry in all parameters owing to the large number of injection utilized to create these averaged plots. Moreover, the diffusion flame location is very well correlated with the location of the soot cloud; the soot cloud is positioned mainly within the jet core and jet head regions and it is surrounded by the reaction zone where soot oxidation takes place. Finally, quasi-steady conditions are achieved at 3.0 ms aSOI; the soot cloud is thinner near lift-off, longer and thicker at jet head,

and contains less soot mass indicating that soot oxidation has taken place at this time. The reaction zone is consistent with the soot cloud, diffusion flame has stabilized at the lift-off length located downstream of the jet expansion point 1, and the reaction zone extends all the way towards the downstream impingement screens.

Figure 8b has identical layout for CN54, and displays a longer liquid length for CN54. The jet expansion by LTHR develops less intensely for CN54, and stabilizes farther downstream than that of n-heptane. Less robust formation of hot-products is seen in decreased sheath-thickness and the more gradual left/right hue-reversal downstream of the jet expansion location. At the time of ignition at 1.8 ms aSOI, the soot cloud cannot be observed even though the reaction zone is visible at the end of the jet head. At 1.9, 2.0, and 2.1 ms aSOI, the soot cloud appears and grows gradually but it contains much less soot mass, indicated by the white color (color scale for heptane and CN54 is the same). At these times, the reaction zone has developed, although the diffusion flame is thicker and oriented differently from the n-heptane flame. Finally, by 3.0 ms aSOI, the diffusion flame recesses and stabilizes downstream of the jet expansion region, similar to n-heptane. However, in this case the jet expansion length and the lift-off length are both located 8-10 mm downstream of those for n-heptane.

Results in Fig. 8 show that the flame recesses and propagates upstream and stabilizes slightly downstream of the sudden expansion resulting from the LTHR. Although this description of flame stabilization shares ideas from previous studies (e.g., ignition kernels and/or mixing with hot products), it provides a new explanation based on strong experimental evidence. The

preheating and precursor accumulation by LTHR seems to be far greater for n-heptane compared to that for CN54. In case of CN54, the jet expansion occurs farther downstream, which allows more time and distance to increase air entrainment and lower the overall equivalence ratio, and ultimately, increase the lift-off length. A detailed analysis of first stage ignition and LTHR will be presented in section Sec. 3.6. Recall that the relative difference in soot for n-heptane and CN54 observed in this study is aligned with the results from others works [6, 7], which document the connection between lift-off length and soot formation.

3.5. Apparent Turbulent Flame Speed

Relatively repeatable ambient conditions listed in Table 1 and shown in Fig. 4 give the impression that local mixing and ignition dynamics are likewise repeatable. However, local fuel-air mixing differences manifest in similar global parameters (liquid length and vapor penetration length) and yet vastly different ignition, lift-off, and sooting behavior. The ignition, lift-off, and sooting behavior depend upon both fuels (even with matched CN) and injection-to-injection variations.

One attribute often viewed as a global parameter, but also intrinsically linked to local mixing behavior, is the concept of turbulent flame speed. Though the mechanism of upstream flame propagation is imprecise, it is still reasonable to characterize mixing in terms of an apparent turbulent flame speed at the lift-off location when quasi-steady conditions have been achieved.

Previous work has reported use of simultaneous schlieren and OH*CL images to determine an apparent turbulent flame speed (ATFS) of the reacting

jet [33]. Schlieren images capture the initial vapor penetration profile of the jet (as in Fig. 4), which establishes a relationship between jet-tip location and velocity. The red curve in Fig. 9 (top) shows the jet-tip velocity (and its variance) as function of jet-tip location for n-heptane. Note that the jet-tip velocity for injections is fairly constant. The black curve in Fig. 9 (top) shows the histogram of the lift-off length, as determined from the analysis of instantaneous OH*CL images. The combination of these two results allows a histogram of the ATFS to be generated. As an example, the arrow in Fig. 9 (top) shows how a lift-off length of 40 mm is converted to an ATFS of 30 m/s by intersecting with the profile of the jet-tip velocity. Repeating this process for each axial location on the top plot yields the histogram of ATFS shown in the bottom plot. This methodology discussed in Ref [33] has acknowledged shortcomings, namely that the velocity detected from RSD is the jet-head velocity rather than the velocity within the jet interior at steady conditions, but this difference is relatively minor and the reported trends are expected to be reliable.

The same procedure is followed for the CN54 blend to obtain histogram plot of ATFS shown in blue in Fig. 9 (bot.). For n-heptane, the ATFS varies from 20 to about 50 m/s, with an average value of 33 m/s across all times and injections. For CN54, the range is between 10 and 36 m/s, and the average ATFS is about 26 m/s. Thus, the CN54 blend has approximately 20% lower ATFS compared to that for n-heptane. The reduced ATFS for CN54 seems to results from a longer mixing time/distance prior to the onset of HTHR, which allows the flame to be essentially soot-free under these ambient and fuel injection conditions. The ATFS parameter (average values and distribution)

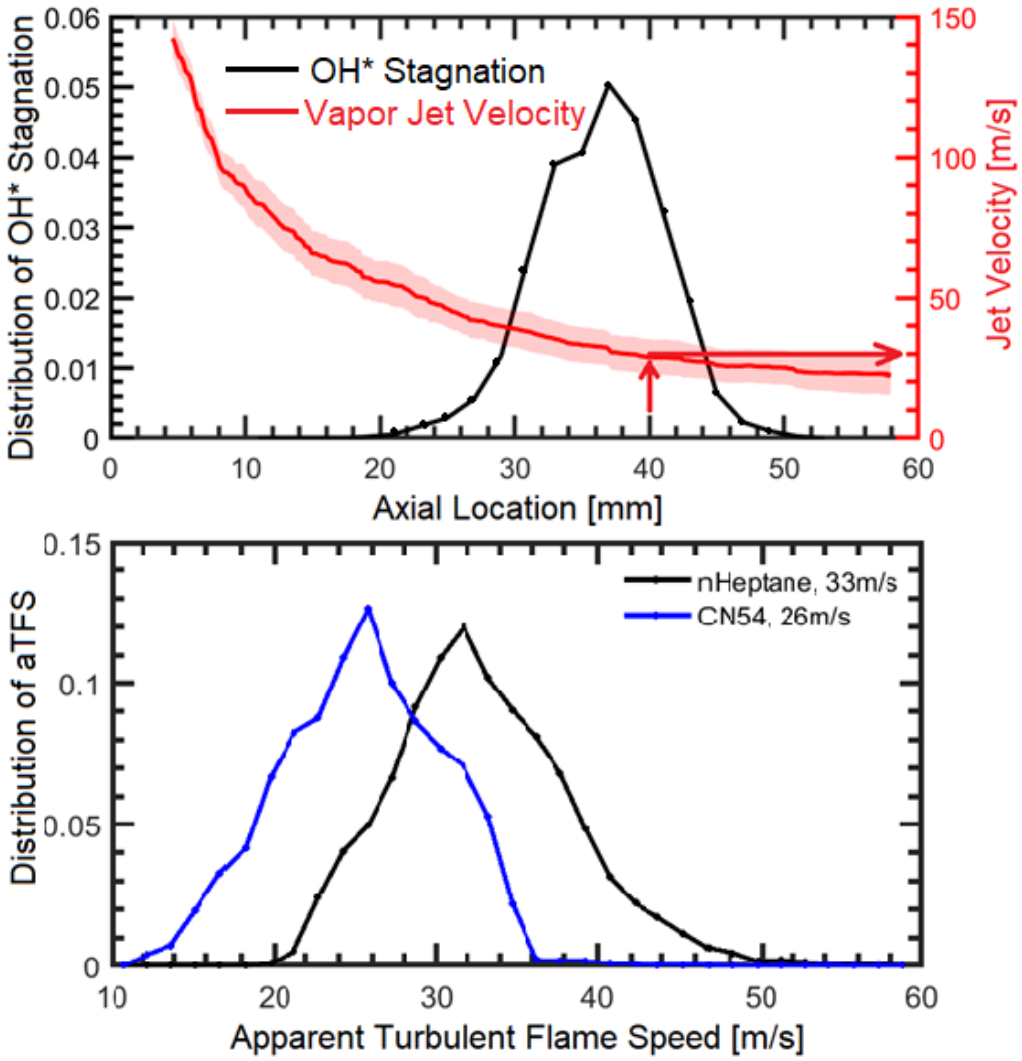

Figure 9: Normalized histogram of (top) OH*CL stagnation locations and average jet-tip velocity for n-heptane (with 95% CI, not shown for CN54) (bin width = 2 mm), and (bottom) apparent turbulent flame speed (ATFS) for both heptane and the CN54 blend (bin width = 2 m/s). Mean values in legend.

could be correlated with soot measurements to quantify the sooting behavior.

3.6. First Stage Ignition

Fuel-air mixtures at high-temperatures and high-pressure undergo early stage endothermic and exothermic reactions, generally manifested by LTHR and referred to as first stage ignition in the engine literature. First stage ignition at diesel conditions has been investigated previously [45, 29, 27] although it can be difficult to characterize quantitatively and requires special diagnostics such as formaldehyde imaging. The LTHR mildly heats the jet by these early reactions to introduce changes in density gradients, and thus RSD is well equipped to image not only the LTHR behavior [29] but also to quantitatively identify the first stage ignition location and timing. As LTHR reactions progress, the corresponding regions of the jet become invisible to the RSD.

The RSD is used first to identify the key features of the first stage ignition, and then to determine ignition timing and location algorithmically for each fuel. For this reason, raw RSD images for the three fuels are presented in Fig. 10 at 0.2 ms intervals during 1.0 to 2.0 ms aSOI, as well as at 3.0 ms aSOI. The first six image frames show first stage ignition and onset of LTHR in the fuel jet, and the final frame at 3.0 ms aSOI illustrates main ignition in the quasi-steady period for comparison. As an example, the RSD images for n-heptane will be used to describe the ignition and LTHR phenomena within the FOV of about 60 mm max.

At 1.0 ms aSOI, the n-heptane jet has fully vaporized downstream of the liquid length, and the vaporized fuel core is denser than the surrounding

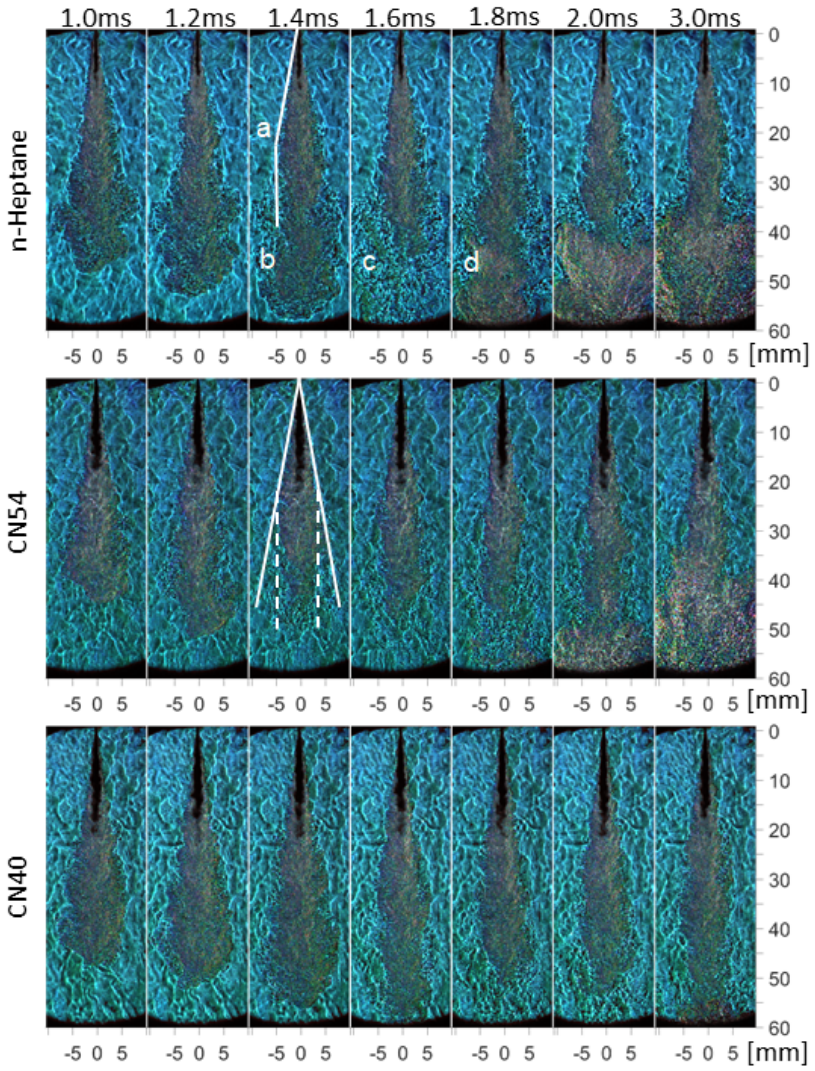

Figure 10: Raw RSD images at early time steps for (top) n-heptane, (middle) CN54, and (bottom) CN40 jets illustrating first-stage combustion development.

ambient air on account of fuel's high molecular weight and lower initial temperature. At this time, the cone-angle of the jet is nearly constant indicating entrainment and mixing with the ambient air. By 1.4 m aSOI, first stage ignition has taken place at the jet periphery, where the jet spreading apparently contracts suddenly at around 20 mm downstream marked by point (a). Farther downstream, point (b) displays an area previously occupied by the jet at 1.2 ms aSOI, that now matches the background color. The jet has neither contracted at point (a) nor is it absent in the region (b). Rather, the LTHR at 1.4 ms has raised the temperature locally such that the density gradients have diminished by the opposite effects of fuel fraction gradients and temperature gradients. Thus, the jet refractive index very nearly equals that of the ambient, which has the effect of making the jet disappear as its hue matches the background hue. Note, however, that the structures in these areas are much smaller than those in the background near the injector. This fine-scale turbulence makes the true width of the jet visible to the eye, and the fact that these structures (and hues associated with them) move between image frames (unlike the quiescent background) makes it possible to identify them algorithmically by frame-subtracting consecutive images.

By 1.6 ms aSOI, the LTHR has occurred throughout the jet beyond point (c) located at about 45 mm downstream of the injector. At first glance, the jet appears to have shortened axially. This LTHR behavior and retraction, radially at point (b) and axially at point (c), has been documented previously in the literature [45, 29]. The first stage ignition spot, for example, at point (a) can be difficult to recognize owning to the faint signal at this location. Beyond 1.6 ms aSOI, main ignition or HTHR takes place. The HTHR reac-

tions emit significant light, which obscures RSD images somewhat - this is seen after point (d) in Fig. 10, where the image is noticeably brighter than the upstream jet. The HTHR reactions raise the temperature significantly, and thus product gas is locally less dense than the surrounding air. The switch from more-dense to less-dense than ambient coincides with a reversal of hues in the ensemble-average images in Fig. 8.

Having stepped through the LTHR behavior of n-heptane in Fig. 10, the effect of different fuels can be compared. First, n-heptane has a significantly shorter liquid-length than CN54 and CN40, which have about the same liquid length. However, both n-heptane and CN54 have similar onset of LTHR, maturing to HTHR around 2.0 ms aSOI; injection-to-injection variations of IDT account for the small differences in ignition timing between the injections in Fig. 10. These results indicate that n-heptane and CN54 have similar chemistry-driven behaviors, because their ignition timings match very closely. However, the downstream phenomena such as flame recession, lift-off length, and sooting do not match between these fuels seemingly due to the effects of thermophysical properties and turbulent mixing. In contrast, the CN40 blend shows LTHR along the jet periphery at 1.6 ms aSOI, but it is much weaker than that observed for n-heptane and CN54. Main ignition has not occurred by 2.0 ms aSOI, and even at 3.0 ms aSOI, the HTHR is barely visible in the FOV of the RSD camera.

The RSD images were analyzed to determine the onset of first stage ignition in terms of its timing and location. The LTHR was algorithmically located using the traditional shadowgraphy method of subtracting consecutive image-frames [46, 47] between SOI and main ignition as presented in

Fig. 5. Very high frame-to-frame hue variations define the jet core, while the jet periphery - where fuel vapor exists at densities near ambient levels - has small hue variations. In these regions, hues in the RSD images vary because of the fast-moving jet, even though fluctuations are small and hues are close to the background hue. The background, meanwhile, is quiescent and does not exhibit frame-to-frame hue variations. In this way, the jet periphery is distinguished, and the axial location where it suddenly thins can be determined to locate the first stage ignition. Recall that the mixing and LTHR reactions slowly raise the temperature at the periphery to match the hue to that of the background, causing the aforementioned contraction near location (a) in Fig. 10.

Figure 11 shows histogram plots of first stage IDT for different fuels. Results show that n-heptane and CN54 both undergo first stage ignition at about the same time, i.e., 1.4-1.5 ms aSOI. This result indicates that CN of these two fuels is also a good indicator of the onset timing of cool flame chemistry. In spite of this match, Fig. 10 shows that the LTHR associated with first stage ignition is more robust for n-heptane than that for CN54 indicating that a physical process is affecting the results. For CN40, the first stage ignition takes place at about 1.7 ms aSOI, which is consistent with the lower CN of the fuel.

Next, Fig. 12 presents histogram plots of the axial location for each fuel where the first stage ignition begins, as at (a) in Fig. 10. Figure 12 demonstrates that on average, the axial location for first stage ignition depends upon the fuel. It is closest to the injector for n-heptane, and at least 5 mm downstream for CN54 on average, and another few millimeters downstream

for CN40. The separation between n-heptane and CN40 can be explained by the lower chemical reactivity of CN40. However, axial separation between n-heptane and CN54 ignition location seems unlikely to be a chemical effect because these two fuels have matching IDTs for first stage and main ignition events. Interestingly, Fig. 12 shows that first stage ignition occurs downstream of the liquid length even though large injection-to-injection variations are present. Histogram plots show that first stage ignition occurs at 13 mm or greater for n-heptane (liquid length is 10 mm) and at 21 mm or greater for CN54 whose liquid length is 18 mm.

These results demonstrate that even though n-heptane and CN54 exhibit similar first stage and main ignition behavior, and the physical delay times for fuel vaporization are similar (see Figure 4), the vaporized fuel for n-heptane is available closer to the injector (by about 8 mm) because of its smaller liquid length. Thus, all subsequent phenomena including first stage ignition, main ignition, and lift-off occur closer to the injector (by about the same 8 mm) for n-heptane compared to those for CN54. Overall fuel vapor availability at a farther downstream location for CN54 causes the mixing process to entrain more oxidizer into the fuel jet, which likely causes less robust LTHR and reduces the local equivalence ratios (and ATFS as shown in Fig. 9) at lift-off length to reduce soot formation in the flame. Recall that complete fuel vaporization takes 0.1 ms longer for CN54 compared to n-heptane, i.e., the physical delay time associated with complete fuel vaporization is insignificant compared to the first stage IDT of 1.4 ms and main IDT of about 1.8 ms.

As shown in Fig. 12, LTHR for CN54 occurs farther downstream, allowing for additional fuel-air mixing, and hence, less robust heat release rate.

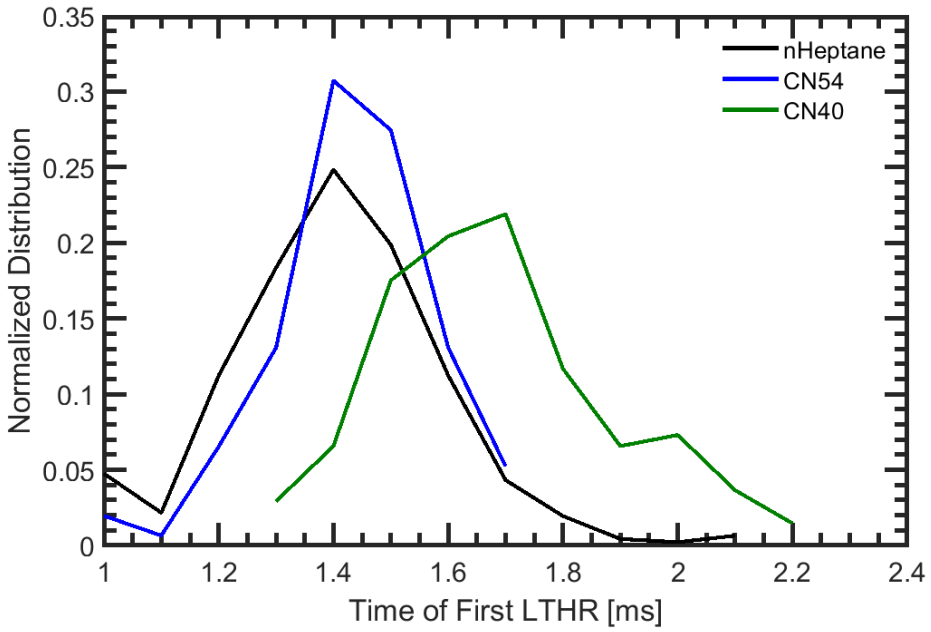

Figure 11: Histogram plot of Low-Temperature Heat-Release (LTHR) timings for each fuel (bin width = 0.1 ms).

In Fig. 12, the further displacement of first stage ignition for CN40 must be primarily chemically-driven, given its lower CN and thermophysical properties similar to CN54. It seems clear that the onset of first stage ignition and related phenomena such as LTHR, sudden jet expansion, main ignition location, and flame stabilization affecting lift-off length are all determined by the availability of the vaporized fuel at the end of the liquid length, established by the thermophysical properties of the fuel.

3.7. Refractive Index Difference Profiles

Figure 13 displays the LTHR behavior quantitatively using average normalized refractive index difference profiles at select axial locations obtained

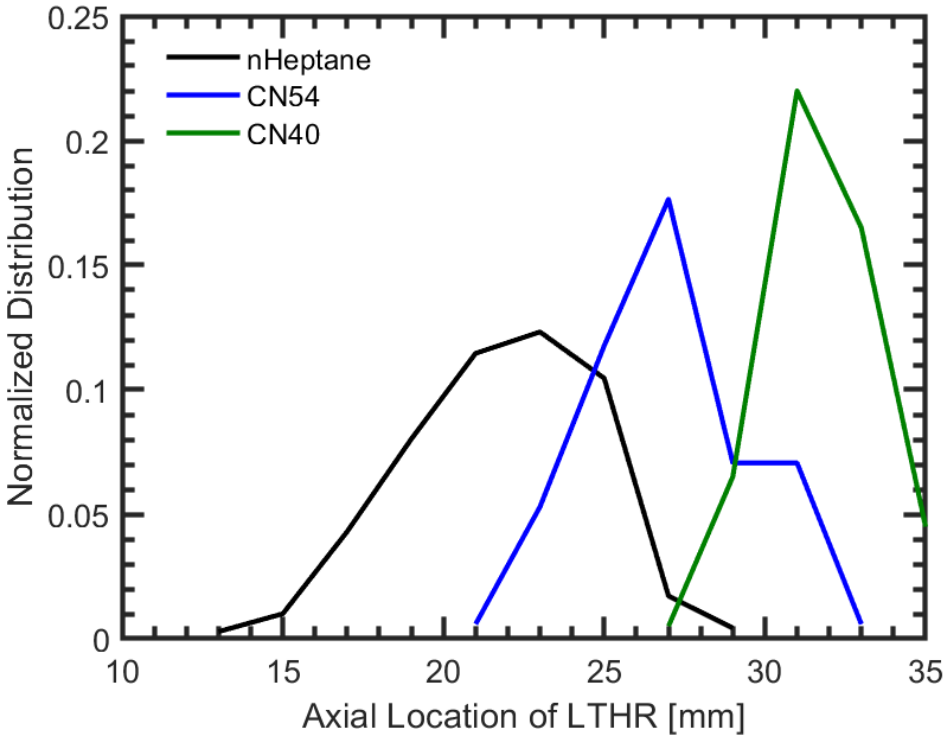

Figure 12: Histogram plot of Low-Temperature Heat-Release (LTHR) location for each fuel (bin width = 2 mm).

by RSD ($\eta = n/n_o - 1$, where n is local and n_o is background refractive indexes, respectively); conversion of recorded hues to n utilizes a rigorous calibration process discussed in prior works [29, 28]. η is calculated from Abel inversion of ensemble-averaged axisymmetric deflection angle data from RSD. Note that n depends upon density, which is a function of the pressure (constant in this study), gas constant, and temperature, the last two depending upon local fuel-air mixture. Assuming adiabatic mixing in non-reacting flows, a unique relationship can be developed to relate measured η to fuel mole fraction [28]. However, applying those methods to fuel sprays under reacting conditions is not been well documented in the literature, and thus results are presented as η. Since fuel vapor has a higher molecular weight or refractive index than air, a positive η corresponds to low-temperature fuel-rich regions, while negative η would occur where the mixture temperature rises, for example, by chemical reactions. The narrowing of the RSD-based vapor boundaries previously described is a result of the shift through $\eta = 0$ as LTHR increases local mixture temperature during the mixing process.

Figure 13 shows radial profiles of refractive index difference at selected axial locations at 1.8 ms aSOI when the main ignition has just occurred at a farther downstream location and the presented profiles are not affected by the HTHR. For each fuel, profiles are shown at three axial locations: the location where jet expands suddenly (point labelled 1 in Fig. 8), 4 mm upstream of it, and 4 mm downstream of it. The jet expansion locations are 33 mm and 44 mm, respectively, for n-heptane and CN54. The magnitudes of η cannot be compared directly between fuels, but rather the trends are important. In both cases, profiles show slight radial expansion and a decrease in η values

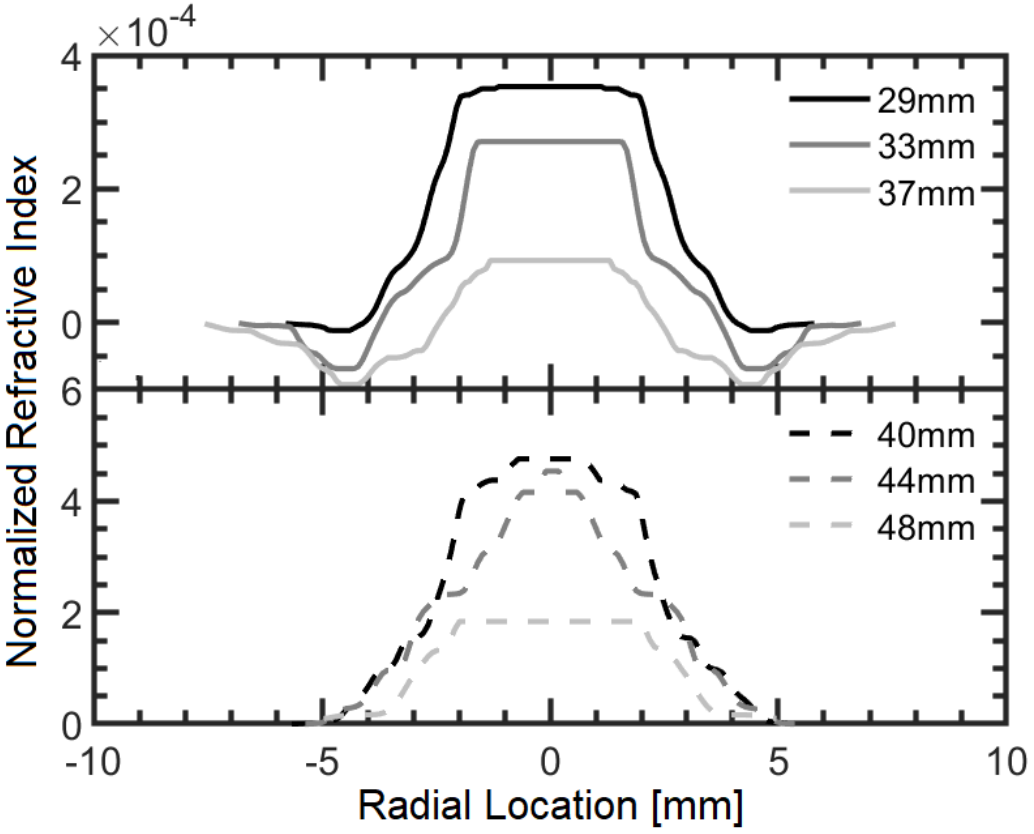

Figure 13: Normalized refractive index difference (η) profiles at 1.8 ms aSOI are shown for ensemble-averaged n-heptane (top) and CN54 (bottom) at fuel-specific locations at/near volumetric expansion before high-temperature heat release (HTHR).

across the radius as the axial distance increases. This trend can be attributed to the mixing process, whereby the jet width increases, and at the same time, entrained fluid mixes with the fuel to decrease the fuel fraction and increase the temperature of the local mixture; both of these effects decrease the local refractive index.

The profiles in Fig. 13 reveal significant differences between n-heptane and CN54 in the outer regions of the jet. In case of n-heptane, the η profile at 33 mm, where sudden expansion takes place, shows negative values that cannot be explained by the mixing alone. Instead, significant heating by LTHR has taken place in these regions to depress the refractive index difference into the negative range. This heating is also accompanied with radial expansion of the jet, and both trends continue at the downstream location of 37 mm. For CN54 the η profile edges are still positive, indicating minimal if any significant temperature rise by LTHR at these positions in the jet. In the jet core, refractive index difference changes mainly by the mixing process, and thus the two fuels exhibit similar trends. Overall, Fig. 13 provides quantitative evidence of significant heating by LTHR for n-heptane, which has access to vaporized fuel closer to the injector exit. Heating by LTHR has likely progressed sufficiently to accumulate PAH fragments (formation begins between 900 and 1000 K [21]) upstream of the lift-off length that subsequently leads to extensive soot formation in the core of the diffusion flame.

4. Summary and Conclusions

In this study, the effect of a fuel's chemical and thermophysical properties were isolated by investigating three fuels under reacting conditions using a

slightly modified diesel injector. The three fuels include n-heptane and two primary reference fuel blend of n-hexadecane and heptamethylnonane resulting in cetane numbers of 54 and 40 (called CN54 and CN40, respectively), chosen to create a set with similar thermophysical properties and/or similar cetane number rating; tests comparing trends with similar thermophysical properties but different cetane number (CN54 vs CN40) and visa versa (n-heptane vs CN54) were considered. The constant-pressure test facility used in this study provided stable ambient conditions to perform 150 to 500 injections in quick succession for each fuel. Three high-speed optical diagnostics were used to simultaneously image the transient evolution of the jet including liquid fuel vaporization, vapor penetration, first stage ignition and LTHR, main ignition and HTHR, and soot formation. Analyses include Abel inverted schlieren and OH*CL data, obtained with the use of a large number of injections, to monitor spray development, reaction zone movement, and related phenomena. The following are key summary and conclusions of this study:

- Thermophysical properties of the fuel determine the liquid length. n-Heptane has lower boiling point and lower density which resulted in smaller liquid length of 10 mm at the test conditions. The higher boiling point and density of CN54 and CN40 increased the liquid length to about 18 mm. Fuel evaporation added negligible physical delay of only 0.1 ms to produce fully vaporized fuel for mixing within 0.15 to 0.25 ms after injection.
- The vapor penetration length was independent of the fuel indicating that fuel properties do not affect the overall entrainment of ambient fluid and mixing, a result in agreement with the findings of Kook and Pickett [22].

- The ignition delay times for the first stage ignition and main ignition were indistinguishable between n-heptane and CN54 indicating that the present experiment accurately replicated the CN behavior of these fuels.
- In spite of the same cetane number and ignition timing, the first stage ignition and main ignition occurred at different axial locations for n-heptane and CN54, and the lift-off length for these two fuels was also different indicating that these differences are caused by thermophysical effects as opposed to chemical effects of the fuel.
- The delay times for first stage ignition and main ignition for n-heptane/CN54 and CN40 were easily separable as expected because of the different CNs of these fuels.
- Ignition location exhibited effectively no correlation with IDTs indicating that ignition occurs in localized kernels that can take different trajectories depending upon the turbulent mixing processes.
- Low-temperature heat release (LTHR) was robust and closer to the injector for n-heptane followed by CN54 and then CN40. The quasi-steady lift-off length was also positioned in the same sequence, i.e., n-heptane, CN54, and CN40. The robust LTHR likely increased PAH formation before lift-off as precursors to soot.
- In agreement with existing correlations between soot mass and lift-off length, soot mass was highest for n-heptane, followed by CN54 and then CN40. This trend does not agree with measurements of a fuel's soot propensity based on simple flame configurations.
- Composite schlieren, OH*CL, and 2CP images provided excellent visualization of the diffusion flame and its relationship to the soot cloud. The

reaction front recessed upstream to stabilize at the lift-off length, seemingly determined by the LTHR.

- The apparent turbulent flame speed at the lift-off length was higher for n-heptane compared to CN54, and it correlated with LTHR upstream of the lift-off length.
- Refractive Index Difference profiles confirmed that n-heptane received significantly more heating by LTHR, much closer to the injector, than CN54.
- All these factors lead to a measured peak soot mass of 100x less for the CN54 blend despite matching ignition timing.
- Even though the physical delay times for fuel vaporization are similar for different fuels, the axial location where vaporized fuel becomes available depended upon the liquid length, which was found to be the primary factor affecting LTHR, ignition locations, and lift-off length. All these parameters shifted downstream by about 8 mm (same as the difference in the liquid lengths) for CN54 compared to n-heptane.

The present study utilized fuels with single or two species with similar boiling points. However, real fuels contain a large number of chemical species with varying boiling points, as defined by fuels' volatility curve. Further, end of injection behavior can contribute significantly to eventual engine out emissions, however exploring those effects was out of the scope of this work. Thus, further work will be needed to study the impact of more complex fuel blends and end of injection effects.

In conclusion, these measurements and observations highlight the critical connection between fuel properties and flame stabilization mechanism (and thus, soot formation) in transient reacting sprays at high-pressure, high-

temperature ambient conditions. Particularly, the liquid length, determined by fuels' boiling point temperature and density, can greatly affect the first availability of the vaporized fuel, and thus, first and main ignition locations, LTHR, lift-off length, and soot mass. Results show that the sooting behavior of a fuel in high-pressure diesel-like reacting sprays can be contrary to the expectations based on fundamental studies of fuel's molecular structure. Consistent with literature and supported by present observations, spray development and mixing, LTHR (if distinguishable), flame stabilization processes, and injection to injection variations can have greater impact on the sooting behavior than the chemical make-up of the fuel alone. Thus, fuel screening efforts should consider transient spray development and combustion at relevant ambient conditions, and how these phenomena are affected by fuel's chemical and thermophysical properties while utilizing a large number of injection experiments.

5. Acknowledgments

This work was supported by funding from US Department of Energy, Office of Energy Efficiency and Renewable Energy (EERE) award DE-EE0007980.

References

[1] U.S. Dept. of Energy, Fuel properties database, Available at `https://www.nrel.gov/transportation/ fuels-properties-database/` (Accessed 2021/12/19).

[2] E. Polikarpov, G. Kukkadapu, R. Whitesides, M. Kass, G. Fioroni, L. Fouts, J. Luecke, D. Vardon, N. Huq, E. Christensen, X. Huo, T. Alleman, R. McCormick, Screening of potential biomass-derived streams as fuel blendstocks for mixing controlled compression ignition combustion, SAE Int. Journal of Advances and Current Practices in Mobility 1 (2019) 1117–1138.

[3] T. Powell, J. Szybist, Fuel effects on advanced compression ignition load limits, SAE Technical Paper Series 2021 (2021).

[4] J. E. Dec, A conceptual model of dl diesel combustion based on laser-sheet imaging, SAE transactions (1997) 1319–1348.

[5] M. P. Musculus, P. C. Miles, L. M. Pickett, Conceptual models for partially premixed low-temperature diesel combustion, Prog. Energy Combust. Sci. 39 (2013) 246–283.

[6] L. Pickett, D. Siebers, An investigation of diesel soot formation processes using micro-orifices, Proc. Combust. Inst. 29 (2002) 655–662.

[7] L. Pickett, D. Siebers, C. Idicheria, Relationship between ignition processes and the lift-off length of diesel fuel jets, SAE Transactions 114 (2005) 1714–1731.

[8] L. Pickett, D. Siebers, Soot in diesel fuel jets: effects of ambient temperature, ambient density, and injection pressure, Combust. Flame 138 (2004) 114–135.

[9] M. J. Murphy, J. D. Taylor, R. L. McCormick, Compendium of experimental cetane number data, Tech. Rep. NREL/SR-540-36805, National Renewable Energy Laboratory (2004).

[10] D. ASTM, 7668-17, standard test method for determination of derived cetane number (dcn) of diesel fuel oils - ignition delay and combustion delay using a constant volume combustion chamber method (2017).

[11] A. Al Zaabi, A. Raj, M. Elkadi, D. Anjum, A. Prabhu, G. D. Pena, L. Li, A. George, M. Nasser Al Shebli, Variation in sooting characteristics and cetane number of diesel with the addition of a monoterpene biofuel, alpha-pinene, Fuel 314 (2022) 123082.

[12] Y. Kidoguchi, C. Yang, R. Kato, K. Miwa, Effects of fuel cetane number and aromatics on combustion process and emissions of a direct-injection diesel engine, JSAE Review 21 (2000) 469–475.

[13] A. F. Alhikami, C.-E. Yao, W.-C. Wang, A study of the spray ignition characteristics of hydro-processed renewable diesel, petroleum diesel, and biodiesel using a constant volume combustion chamber, Combust. Flame 223 (2021) 55–64.

[14] B. Kerschgens, L. Cai, H. Pitsch, B. Heuser, S. Pischinger, Di-n-buthylether, n-octanol, and n-octane as fuel candidates for diesel engine combustion, Combust. Flame 163 (2016) 66–78.

[15] D. Das, P. St. John, C. McEnally, S. Kim, L. D. Pfefferle, Measuring and predicting sooting tendencies of oxygenates, alkanes, alkenes, cycloalkanes, and aromatics on a unified scale, Combust. Flame 190 (2018) 349–364.

[16] M. Montgomery, D. Das, C. McEnally, L. Pfefferle, Analyzing the robustness of the yield sooting index as a measure of sooting tendency, Proc. Combust. Inst. 37 (2019) 911–918.

[17] D. Das, C. McEnally, T. Kwan, J. Zimmerman, W. Cannella, C. Mueller, L. Pfefferle, Sooting tendencies of diesel fuels, jet fuels, and their surrogates in diffusion flames, Fuel 197 (2017) 445–458.

[18] Y. Kim, B. Etz, G. Fioroni, C. Hays, P. St. John, R. Messerly, S. Vyas, B. Beekley, F. Guo, C. McEnally, L. Pfefferle, R. McCormick, S. Kim, Investigation of structural effects of aromatic compounds on sooting tendency with mechanistic insight into ethylphenol isomers, Proc. Combust. Inst. 38 (2021) 1143–1151.

[19] P. C. St. John, M. Bartlett, S. Kim, Ysi esimtator, Available at `https://ysi.ml.nrel.gov/` (Accessed 2021/12/19).

[20] S. Suzuki, M. Hori, H. Nakamura, T. Tezuka, S. Hasegawa, K. Maruta, Study on cetane number dependence of diesel surrogates/air weak flames in a micro flow reactor with a controlled temperature profile, Proc. Combust. Inst. 34 (2013) 3411–3417.

[21] H. Nakamura, S. Suzuki, T. Tezuka, S. Hasegawa, K. Maruta, Sooting limits and pah formation of n-hexadecane and 2,2,4,4,6,8,8-heptamethylnonane in a micro flow reactor with a controlled temperature profile, Proc. Combust. Inst. 35 (2015) 3397–3404.

[22] S. Kook, L. M. Pickett, Liquid length and vapor penetration of conventional, fischer–tropsch, coal-derived, and surrogate fuel sprays at high-temperature and high-pressure ambient conditions, Fuel 93 (2012) 539–548.

[23] L. Zheng, X. Ma, Z. Wang, J. Wang, An optical study on liquid-phase penetration, flame lift-off location and soot volume fraction distribution of gasoline–diesel blends in a constant volume vessel, Fuel 139 (2015) 365–373.

[24] H. Persson, Ö. Andersson, R. Egnell, Fuel effects on flame lift-off under diesel conditions, Combust. Flame 158 (2011) 91–97.

[25] B. McGann, K. Kim, T. Lee, J. Temme, C.-B. Kweon, Effect of the cetane number on jet fuel spray ignition at high-temperature and -pressure conditions, Energy Fuels 34 (2020) 1337–1346.

[26] L. Pickett, S. Kook, H. Persson, Öivind Andersson, Diesel fuel jet lift-off stabilization in the presence of laser-induced plasma ignition, Proc. Combust. Inst. 32 (2009) 2793–2800.

[27] E. Mayhew, C. Mitsingas, V. Coburn, J. Temme, C.-B. Kweon, Effects of fuel blending on first stage and overall ignition processes, Proc. Combust. Inst. 38 (2021) 5733–5740.

[28] C. Wanstall, A. Agrawal, J. Bittle, Implications of real-gas behavior on refractive index calculations for optical diagnostics of fuel–air mixing at high pressures, Combust. Flame 214 (2020) 47–56.

[29] A. Parker, C. Wanstall, S. Reggeti, J. Bittle, A. Agrawal, Simultaneous rainbow schlieren deflectometry and oh* chemiluminescence imaging of a diesel spray flame in constant pressure flow rig, Proc. Combust. Inst. 38 (2021) 5557–5565.

[30] A. Donkerbroek, A. van Vliet, L. Somers, N. Dam, J. ter Meulen, Relation between hydroxyl and formaldehyde in a direct-injection heavy-duty diesel engine, Combust. Flame 158 (2011) 564–572.

[31] S. A. Reggeti, A. K. Agrawal, J. A. Bittle, Robust two-colour pyrometry uncertainty analysis to acquire spatially-resolved measurements, Measurement Science and Technology 33 (2022) 125201.

[32] S. Reggeti, A. Agrawal, J. Bittle, Two-color pyrometry system to eliminate optical errors for spatially resolved measurements in flames, Appl. Opt. 58 (2019) 8905.

[33] S. Reggeti, A. Parker, C. Wanstall, A. Agrawal, J. Bittle, Comparing Global Spray Combustion Characteristics and Local Shot-to-Shot Variations in a Reacting n-Heptane Spray, Journal of Engineering for Gas Turbines and Power 143 (2021).

[34] A. Agrawal, C. T. Wanstall, Rainbow schlieren deflectometry for scalar measurements in fluid flows, Journal of Flow Visualization and Image Processing 25 (2018).

[35] C. T. Wanstall, A. Agrawal, J. Bittle, Phase boundary detection in transient, evaporating high-pressure fuel sprays by rainbow schlieren deflectometry, Appl. Opt. 58 (2019) 6791–6801.

[36] G. E. Bogin, A. DeFilippo, J. Y. Chen, G. Chin, J. Luecke, M. A. Ratcliff, B. T. Zigler, A. M. Dean, Numerical and experimental investigation of n-heptane autoignition in the ignition quality tester (iqt), Energy Fuels 25 (2011) 5562–5572.

[37] Engine combustion network, `https://ecn.sandia.gov/diesel-spray-combustion/`, accessed: 2020-05-05.

[38] A. Parker, A. Agrawal, J. Bittle, Representative phenomena of cyclic turbulent combustion in high-pressure fuel sprays, Under review at Flow Turbul. Combust. (2023).

[39] K. Browne, I. Patridge, G. Greeves, Fuel property effects on fuel/air mixing in an experimental diesel engine, Tech. rep., Lucas CAV Ltd. (1986).

[40] D. Siebers, Liquid-phase fuel penetration in diesel sprays, SAE Transactions 107 (1998) 1205–1227.

[41] B. T. Fisher, C. J. Mueller, Liquid penetration length of heptamethylnonane and trimethylpentane under unsteady in-cylinder conditions, Fuel 89 (2010) 2673–2696.

[42] Y. Pei, S. Som, E. Pomraning, P. K. Senecal, S. A. Skeen, J. Manin, L. M. Pickett, Large eddy simulation of a reacting spray flame with multiple realizations under compression ignition engine conditions, Combust. Flame 162 (2015) 4442–4455.

[43] F. Tagliante, L.-M. Malbec, G. Bruneaux, L. Pickett, C. Angelberger, Experimental study of the stabilization mechanism of a lifted diesel-type flame using combined optical diagnostics and laser-induced plasma ignition, Combust. Flame 197 (2018) 215–226.

[44] F. Tagliante, T. Poinsot, L. Pickett, P. Pepiot, L.-M. Malbec, G. Bruneaux, C. Angelberger, A conceptual model of the flame stabilization mechanisms for a lifted diesel-type flame based on direct numerical simulation and experiments, Combust. Flame 201 (2019) 65–77.

[45] S. A. Skeen, J. Manin, L. M. Pickett, Simultaneous formaldehyde plif and high-speed schlieren imaging for ignition visualization in high-pressure spray flames, Proc. Combust. Inst. 35 (2015) 3167–3174.

[46] J. D. Naber, D. L. Siebers, Effects of gas density and vaporization on penetration and dispersion of diesel sprays, SAE transactions (1996) 82–111.

[47] J. V. Pastor, J. M. García, J. M. Pastor, L. D. Zapata, Evaporating diesel spray visualization using a double-pass shadowgraphy/schlieren imaging, Tech. rep., SAE Technical Paper (2007).

A Novel Two-Color Pyrometry System for Improved Spatially Resolved Measurements in Flames

Shawn A. Reggeti, Ajay K. Agrawal and Joshua A. Bittle*

Department of Mechanical Engineering, University of Alabama, Tuscaloosa, AL, USA

*E-mail: jbittle@eng.ua.edu

Received xxxxxx
Accepted for publication xxxxxx
Published xxxxxx

Abstract

Two-Color (2C) pyrometry technique has been used extensively to quantify temperature and/or soot concentration in flames. Originally developed for point measurements, 2C pyrometry has increasingly been used with high-speed camera systems to acquire temporally and spatially resolved measurements. Several optical designs of 2C pyrometry are available in the literature, but most tend to introduce undesirable errors such as parallax and unequal optical path lengths. In this study, a novel 2C pyrometry setup using off-the-shelf optics is presented to minimize these optical aberrations by design rather than post-processing compenstation. The setup is integrated with a high-speed camera to obtain measurements in flames. Experiments were conducted to demonstrate the errors introduced by existing designs, and then the capabilities of the system are demonstrated by acquiring temperature and soot concentration measurements in a flickering diesel wick flame.

Keywords: two-color pyrometry, soot measurements, temperature measurements

1. Introduction

Particulate Matter (PM) or soot emissions from combustion have long been recognized for their harmful effects on human health and environment. Exposure to PM can cause respiratory irritation, asthma-like symptoms, and increased risk of cancer [1]. PM emission is second only to carbon dioxide in its impact on climate forcing [2]. Combustion strategies that improve fuel efficiency such as gasoline direct injection (GDI), compression ignition (CI) or diesel engines tend to increase PM emissions [3]. In recent years, advanced engine strategies as well as new fuel blendstocks have been and continue to be explored to enable cleaner combustion [4]. Two-Color (2C) pyrometry (also called the 2-Color method or 2-Color thermometry) has been used since the 1930s to characterize the sooting tendency of flames to account for fuel chemistries and combustion conditions in a variety of studies for diesel engines [5,6].

The principle of 2C pyrometry is based on the detection of radiative emissions from soot along the line-of-sight in the flame at two distinct wavelengths in the visible light spectra. Then, the signal is mathematically manipulated to quantify the soot concentration and temperature representing the line-of-sight. Numerous optical system designs to facilitate the application of 2C pyrometry to suit different test scenarios have been developed. Based on a review of the literature, and specifically the prevalent optical designs, key weaknesses have been identified and addressed by a novel optical design presented in this work. The present design aims (1) to reduce uncertainties associated with the optical hardware affecting the two spectral signals, and (2) to construct a simple system using off-the-shelf optical components. The following sections provide a brief theoretical background and calibration process, an assessment of the errors associated with existing designs, an optical design and how it overcomes existing drawbacks, and an application example in a simple flickering flame to illustrate the methodology.

2. Background

2C pyrometry is an established diagnostic with extensive publications over the last century for combustion and other applications such as thermal plasma [7] and metallurgical processes [8, 9]. The underlying principles of 2C pyrometry are presented in this paper, and for details, the reader is referred to the existing literature [10, 11, 12]. Originally used for spatially averaged measurements employing a photodetector, new methodologies for 2C pyrometry have been developed to acquire spatially resolved data by camera systems employing a 2D imaging sensor [13, 14, 15].

2.1 2C Pyrometry Principles

Thermal radiation from soot particles dominates the flame luminosity – this is the basis of 2C pyrometry. The detection of thermal radiation at two distinct wavelengths allows for the calculation of soot concentration and temperate in the flame [16]. The starting point for this analysis is the Planck's equation of spectral blackbody radiation:

$$E_{b,\lambda} = \frac{C_1}{\lambda^5 \left[e^{\left(C_2/\lambda T \right)} - 1 \right]} \tag{1}$$

$E_{b,\lambda}$ – spectral emissive power of a blackbody at temperature T (W/m^2·μm)
λ – wavelength (μm)
T – temperature (K)
C_1 – Planck's first constant =3.742×10^8 (W·μm^4/m^2)
C_2 – Planck's second constant =1.4388×10^6 (μm·K)

Multiplying Eq. 1 by the monochromatic emissivity, ϵ_λ, yields the spectral emissive power of a non-blackbody at the same temperature.

$$E_\lambda(T) = \epsilon_\lambda E_{b,\lambda}(T) \tag{2}$$

Spectral emissive power of a non-blackbody at temperature, T, can be equated to the spectral emissive power of a blackbody at a reduced or apparent temperature, T_a.

$$E_\lambda(T) = E_{b,\lambda}(T_a) \tag{3}$$

Substituting Eq. 3 into Eq. 2 yields:

$$\epsilon_\lambda = \frac{E_{b,\lambda}(T_a)}{E_{b,\lambda}(T)} \tag{4}$$

Next, a widely used relationship from one of the original works on 2C pyrometry by Hottel and Broughton is often used [6]. The basis of this relationship is Kirchoff's law of thermal radiation which states that for a surface in thermal equilibrium with its surroundings, spectral emissivity is equal to spectral absorptivity ($\epsilon_\lambda = \alpha_\lambda$). Thermal equilibrium of the soot with the surrounding gases (< 1 K difference) occurs very quickly for in-cylinder diesel combustion, within 10^{-50} and 10^{-6} second [7], which lends credibility to this assumption. The Hottel-Broughton relationship in Eq. 5 establishes the linkage among momochromatic emissivity, soot concentration and wavelength.

$$\epsilon_\lambda = 1 - e^{-KL/\lambda^\alpha} \tag{5}$$

α – constant (~1.39 for visible) based on the wavelength range of the measurement
K – absorption coefficient (proportional to number density of soot particles)
L – depth of the flame (characteristic length)

The product KL indicates soot concentration in the flame, and it is a physical quantity independent of the wavelength. With some algebraic manipulation, Eqs. 1, 4, and 5 can be combined to solve for the product KL in terms of wavelength, λ, apparent temperature, T_a, and actual temperature, T. In 2C pyrometry, the product KL is obtained for two different wavelengths and equated to one another. Thus,

$$(KL)_{\lambda_1} = (KL)_{\lambda_2} = \left[1 - \left(\frac{e^{(C_2/\lambda_1 T)} - 1}{e^{(C_2/\lambda_1 T_{a_1})} - 1} \right) \right]^{{\lambda_1}^\alpha} = \left[1 - \left(\frac{e^{(C_2/\lambda_2 T)} - 1}{e^{(C_2/\lambda_2 T_{a_2})} - 1} \right) \right]^{{\lambda_2}^\alpha} \tag{6a,b}$$

The apparent temperatures (T_{a_1}, T_{a_2}) are measured by 2C pyrometry. Then, the soot temperature, T, and product KL can be calculated from Eqs. 6a, and 6b. Note that 2C pyrometry is a line of sight technique, and hence, T and KL represent respectively temperature and soot concentration along the line of sight. Particularly in turbulent flames of diesel engines, variations and gradients along the optical axis of the flame cannot be distinguished by the 2C pyrometry measurement [17]. Other diagnostics techniques can be used for more accurate measurement of soot concentration such as laser-induced incandescence (LII) [18] or 2C diffused back-illumination [19], but these require greater optical access, which is not always possible. Even though 2C pyrometry does not yield an absolute measurement, it does provide a strong indication of trends in soot concentration and temperature in flames and is often used for quantitative comparison of results at different test conditions. Error propagation in 2C pyrometry caused by uncertainty in properties such as soot emissivity and particle morphology are analysed in [20, 21].

2.2 2C Pyrometer Calibration

Each 2C pyrometer is unique in design and application and thus, it requires calibration to relate the measured spectral signals to the property of interest. The goal of the calibration is to correlate the spectral intensity measured by the camera to the spectral emissive power of a blackbody ($E_{b,\lambda}$) at a given temperature. Ideally, a blackbody at a known temperature would be used as the source to deliver known emissions to the

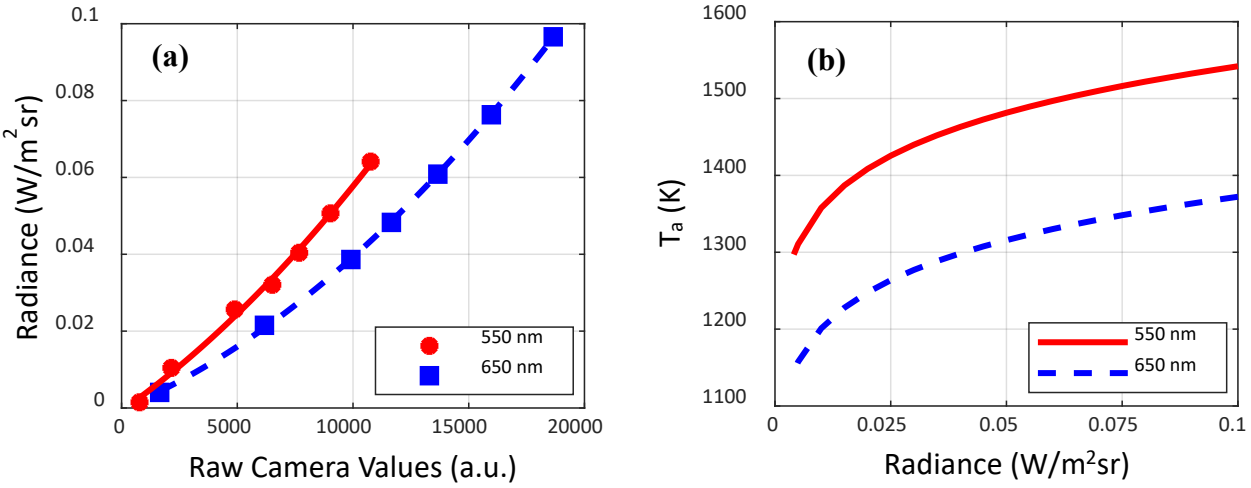

Figure 1: a) Calibration curves for the two wavelengths (exposure time: 98 µs, f-strop: 1.4, distance from source: 0.61 m, b) Apparent temperature versus radiance for each wavelength.

2C pyrometer, which can then be correlated to the intensity measured by the camera with specific settings (f-stop, exposure time, and camera distance from the emitter). This process must be repeated at different blackbody temperatures to develop the calibration curve between camera intensity and blackbody emission at various temperatures. Thereafter, when collecting data from a flame, the measured camera intensity can be correlated to the apparent blackbody temperature based on the calibration curve for each wavelength.

However, the use of a blackbody calibration source is often impractical because of the high cost. As a result, many studies report calibrations carried out with a tungsten filament lamp. The lamp emulates blackbody behavior by passing an electrical current to heat the filament invoking thermal radiation. Although such lamps do not exactly follow a blackbody emission spectrum, their radiance across the visible spectrum is known from manufacturers' calibration; radiance is spectral emissive power divided by π. Certainly, as has been pointed out in the literature [22], the calibrated tungsten lamp method is less accurate than a true blackbody. However, this calibration approach is often sufficient since a properly calibrated lamp has NIST traceable calibration. In any case, the most rigorous calibration method is not crucial since 2C pyrometry is not an absolute measurement.

The 2C pyrometer in this study was calibrated with a tungsten uniform illumination sphere (UIS) from StellarNet. The UIS had three calibration points based on a variable power setting to yield three corresponding radiance spectra. To create a more continuous calibration curve, neutral density (ND) filters were used to decrease the radiance at a known power setting by a fraction (given by the optical density of the ND filter) which yields additional data points to relate camera intensity to radiance values. With this method, a series of images were recorded by the camera using the various power settings and ND filters; intensity values measured across the UIS emission port were averaged to build the calibration curve in Figure 1a. Radiance values are then converted to apparent temperatures as discussed previously. When processing flame data, the intensity measured at a given pixel location is related to the radiance value using the calibration curve for the particular wavelength in Fig. 1a and then the apparent temperature is obtained from Figure 1b. The camera signal will of course vary based on the exposure time, f-stop, and distance from the source; therefore, calibration is performed for the settings used for data acquisition.

2.3 Previous 2C Pyrometer Optical Configurations

The literature is full of various optical configurations of 2C pyrometers that have been constructed and used for data collection over a variety of flame types and devices. Each of these designs have their respective pros and cons but all employ the same basic approach, i.e., record and analyze an object's radiative emissions at two distinct wavelengths. The early versions of 2C pyrometers utilized a bifurcation module to split the emissions (light) from the object into two paths, then two distinct bandpass filters would be placed in each light path and subsequently, spectral light in each path would be measured by photodiodes, as described by Zhao et al [10]. The photodiodes in effect "average" the light intensity over the field of view of the optics and therefore did not resolve spatial variations. With the introduction of the high-speed digital cameras (whose sensors can be thought of as an array of photodiodes), the emissions from the flame could be spatially and/or temporally resolved across the field of view.

Singh et al. devised a hybrid system with a photodiode and a high-speed camera [14]. This unique design was equipped with three photodiodes to provide an additional wavelength detection in the near-infrared region. The camera detected the natural luminosity of the flame to yield qualitative information about regions with high soot concetrations and temperatures. However, the intensity was averaged across the field of view

to calculate the product KL and temperature. Thus, this setup could not be used to spatially resolve soot concentration and temperature across the field of view.

In more recent works, the 2C pyrometer designs take full advantage of the spatial data processing capabilities of digital cameras. For example, Densmore et al. applied a beam-splitter and bandpass filters to direct the spectral images to two individual monochromatic cameras [13]. Some works have circumvented the need for splitting the image by using a color camera and demosaicing the image from the built-in color filter of the camera [5, 22, 23]. A color camera eliminates the need for additional optical components since the signal is channeled directly to the camera and is separated into distinct wavelengths in post processing. This approach limits data collection to built-in color filters of the camera, and spectral responses of the camera must be well known. Additionally, some resolution of the flame is lost during the demosiacing process since pixels are divided among the mosaic filter.

Other unique experiments in 2C pyrometry have extended traditional methodologies to produce more accurate results. The development and evaluation of multi-spectral pyrometry (collecting measurements with more than two wavelengths) can reduce uncertainties by providing multiple measurements to validate the results [25]. With a multi-camera setup to image the flame at different angular orientations, Moinul et al produced 3D reconstructions of flame temperature and emissivity using the 2C pyrometry technique [26].

Two prevalent 2C pyrometer optical designs shown schematically in Fig. 2 are discussed next. The first, Fig. 2a, utilizes a commercially available image doubler (stereoscope), a bandpass filter pair, and a monochromatic camera [12, 24]. Such a design offers simplicity since the image doubler is mounted on the camera like a lens and the system is ready for calibration and data collection. There would be no need to select, configure and align optical components – as was necessary for the work presented in this paper. However, the cost of a commercially available image doubler is much greater than the off-the-shelf optical components used in this study. Perhaps the most significant error to consider with this system is the parallax or the discrepancy produced by viewing the same object from two different points of view. Ideally, the test media (or flame) must be imaged from the same point for both wavelengths to ensure precise pixel-to-pixel mapping, which is crucial to pair the apparent temperatures at each pixel location in the two images and thus, to spatially resolve the measurements. The parallax depends on the spacing between light entrance paths on the image doubler and the distance between object and image doubler. As can be inferred from Fig. 2, placing the 2C pyrometer too close to the test media will increase the parallex angle (θ) and thus, each spectral image would be acquired from a substantially different point of view. Placing the 2C pyrometer far away from the test media will reduce the parallex angle (θ) but at the expense of the spatial resolution and/or overall signal intensity. Errors associated with parrallax are discussed in detail in the results section of this work.

Payri [11] utilized a similar scheme as in [12, 24] but with the addition of a beamsplitter to eliminate the parallax as shown in Fig. 2b. However, the optical path length upstream of the camera sensor is different for each wavelength. Thus, the images recorded by the camera will be of different sizes and one or both will be slightly out of focus. The typical approach is to resize one of the images in post-processing to match the pixel locations in the two images, which can be a

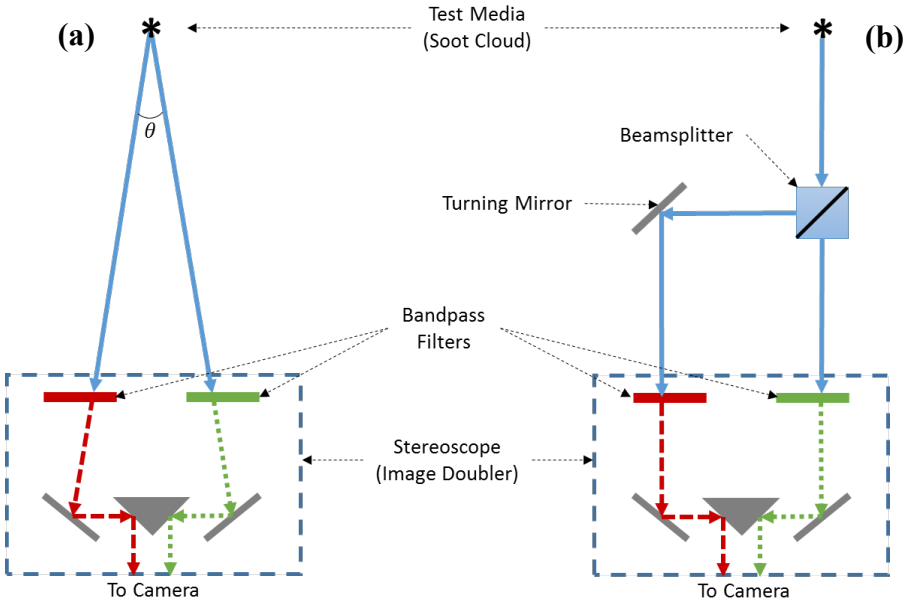

Figure 2: Schematic showing image doubler with a) separate viewpoints causing parallax, and b) single viewpoint and a beamsplitter causing difference in the optical path length.

source of significant error. Furthermore, the pixel resolution of the image is limited by the smaller of the two images. In the results section, the effect of path length differences is analyzed in greater detail.

2.4 New Optical Configuration

The 2C pyrometer presented in Fig. 3 provides a practical, cost-effective solution using off-the-shelf optics to resolve issues associated with previous designs. Additionally, it will be shown that parallax and path length differences can aversely affect the results, making them physcially meaningless in some cases. In particular, this will be the case when a camera sensor is used to acquire spatially resolved measurements, for example, in turbulent flames with embedded structures of different length and time scales.

The present setup uses a beamsplitter as the primary optics for light collection and it is oriented at 45° angle with respect to the camera sensor, thereby dividing the image symmetrically about the axis of the camera lens. Bandpass filters are attached to the beamsplitter to pass the light through the system at the desired wavelengths. Filters with 550 nm and 650 nm central wavelengths respectively and bandwidth of 10 nm FWHM are used [12]. A pair of turning mirrors reflect the two signals towards a right-angle prism mirror which directs the signals toward the high speed camera (Phantom v7.3) for imaging on the same but separate portions of the sensor.

The present design provides several additional benefits. Use of a monochromatic camera offers flexibility in choosing the bandpass filters and bandwidths. A design with off-the-shelf optics offers flexibility to use any combination of bandpass filters for different ranges of sensitivity, and to easily change the field of view by changing the camera lens. However, most importantly, this setup has equal path lengths for each signal which eliminates the need to resize the image in post-processing and the beamsplitter eliminates the parallax present in other designs.

3. Experimental Setup

The experiments presented in this work were designed first to analyze the errors introduced by parallax and differing path lengths, and then to apply the new 2C pyrometer to demonstrate its benefits and measurement capabilities. The effect of image parallax is assessed by simulating a stereoscope with receiving optics spaced 12.5 cm apart to introduce the parallax angle (θ) (see Fig. 2a) for varying distances from the test media. The effect of signal path length is evaluated by displacing the right-angle prism mirror by 1.25 cm, thereby simulating a 2C pyrometer with path length difference of 2.5 cm between the two wavelengths. Lastly, the 2C pyrometer with the new optical design was constructed and images of a flickering flame were acquired and analyzed.

All experiments were conducted with a simple diesel-fueled wick flame as the test media. The flame was created by pouring a small amount of diesel fuel into a beaker and using a cotton wick to draw up the fuel for burning. The result was similar to a candle flame but one end of the wick was immersed in diesel and on the other end, the flame steadily burned while producing considerable amounts of soot. The same flame was used in experiments with each of the three pyrometer constructions.

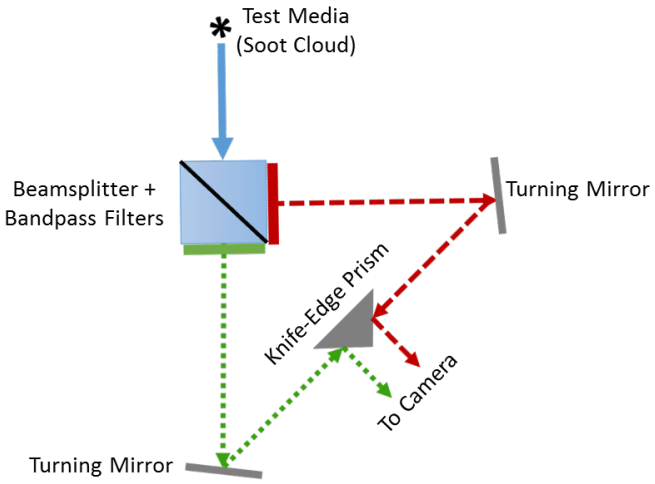

Figure 3: Schematic of Optical Configuration for the new 2C pyrometer

4. Results

4.1 Flame Similarity and Alignment

The beamsplitter in the 2C pyrometer design presented here permits recording of the flame emissions from the same point of view for both wavelengths with equal path lengths, and therefore the intensity characteristics of the two images can be precisely correlated at each pixel location, which is crucial to obtain reliable pixel-to-pixel mapping with high spatial resolution. Indeed, flame images acquired without the bandpass filters (i.e. natural luminosity) showed that the intensity distributions in the two images matched each other. Ideally, intensity distributions in the two images without bandpass filters would be identical; slight differences can be attributed to an imperfect 50-50 split by the beamsplitter which is accounted for by the calibration process.

4.2 Parallax Error Analysis

Ideally, in 2C pyrometry, the two images must be identical except for the wavelength dependent intensity variations. This is feasible with the use of a beamsplitter allowing imaging of the object (or flame) at the two different wavelengths from the same point of view. However, as discussed earlier, some systems in the literature have used commercially available stereoscopes that view the object at different locations to create a stereoscopic image using a set of mirrors. Even a

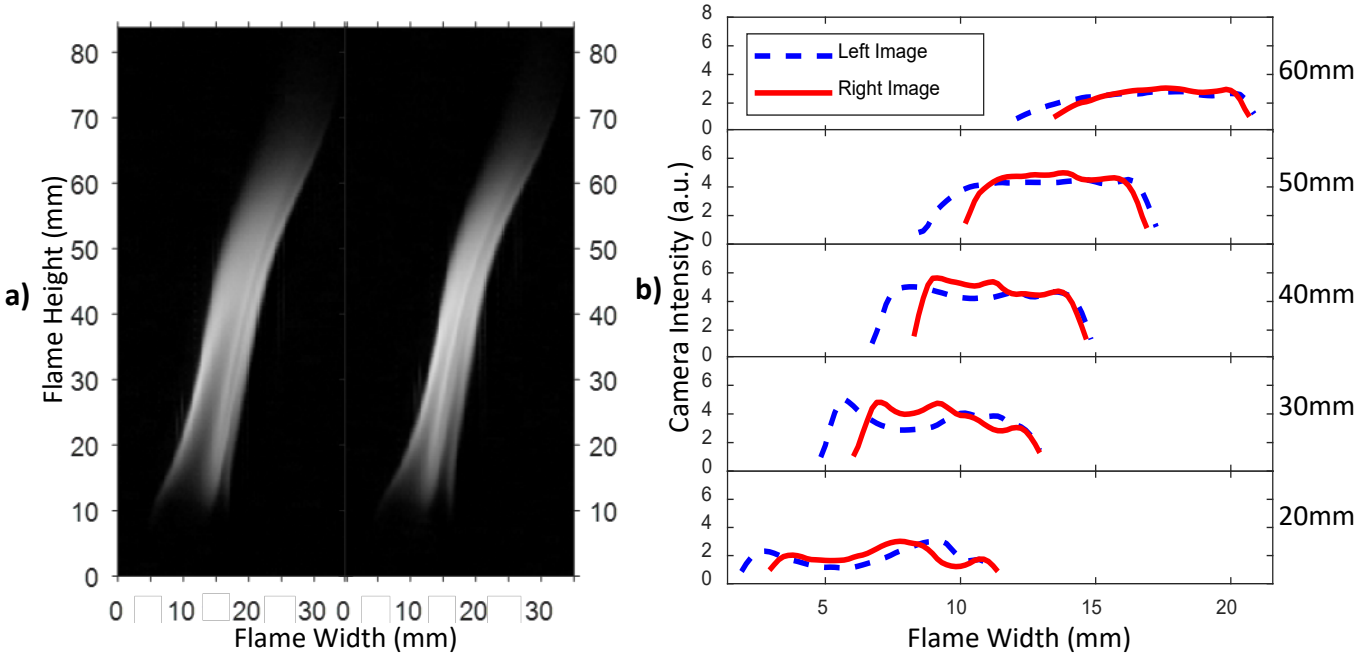

Figure 4: a) Flame images for parallax angle of 9.9°, and b) Transverse profiles of intensity at varying axial locations

small difference in the viewpoint introduces parallax that can be significant depending upon the parallax angle (θ).

Thus, a stereoscope setup was emulated with a pair of turning mirrors and a right-angle prism mirror to measure the natural luminosity of the flame. The diesel burning wick flame was placed at distances of 0.61 m and 1.22 m away from the pyrometer setup, yielding parallex angle, θ (Fig. 2) of 9.9° and 5.6°, respectively. Two natural luminosity images (without bandpass filters) were recorded simultaneously with a high speed camera and are shown in Fig. 4a. This setup demonstrates noticeable differences in the images acquired from different viewpoints, because the flame is asymmetric. Upon close observation of Fig. 4a, it is apparent that the image on the left is wider than the one on the right and the features in the right image are more pronounced and grouped within a smaller radial extent. These differences are evident in Fig. 4b, which shows the transverse profiles of intensity at different axial locations. For example, the crests and troughs of intensity profiles for the two images appear out of phase in Fig. 4b. This misalignment of flame images is a result of the 9.9° parallax angle and indicates that the individual pixels in the two images cannot be mapped precisely with each other which would result in non-physical solutions for the actual temperature and KL values.

Figure 5 shows images of a flame placed at a greater distance away from the 2C pyrometer to decrease the parallax angle. As a result, the separation between the two viewpoints is not as great as in Fig. 4 and thus, the images in Fig. 5a appear similar to one another. However, the intensity profiles at various axial locations in Fig. 5b show that the intensity profiles for the two views do not match and appear out of phase, similar to Fig. 4b. Furthermore, greater more pixilation can be observed in Fig. 5a compared to that in Fig. 4a due to the reduction in parallax angle being accompanied by a loss in the spatial resolution. This effect may be addressed partially by using a higher focal length camera lens but at a trade-off of light throughput because of a potentially lower lens f-stop and more diffuse soot radiance at a longer distance from the flame. While a minimum parallax angle can be prescribed to reduce this type of error, the addition of a beamsplitter completely eliminates the parallax.

The line-of-sight nature of 2C pyrometry introduces additional complexities with parallax. Each pixel of the camera images the thermal emission integrated along a particular line-of-sight. However, with parallax, the line-of-sight will be different for the two wavelengths, making the use of Eqs. 6a, b physically inconsistent. For example, consider a hypothetical case in which the red light (650 nm) of one soot particle and the green light (550 nm) of another soot particle are measured and used to solve for the temperature. If a numerical solution is even possible, it will not represent the temperature of either of the two soot particle, i.e., the result is effectively meaningless. Again, the problem is completely avoided by incorporating a beamsplitter in the optical design of the 2D pyrometer.

4.3 Effect of Path Length

To simulate the effect of different path lengths, the right-angle prism mirror in Fig. 3 was moved towards one of the

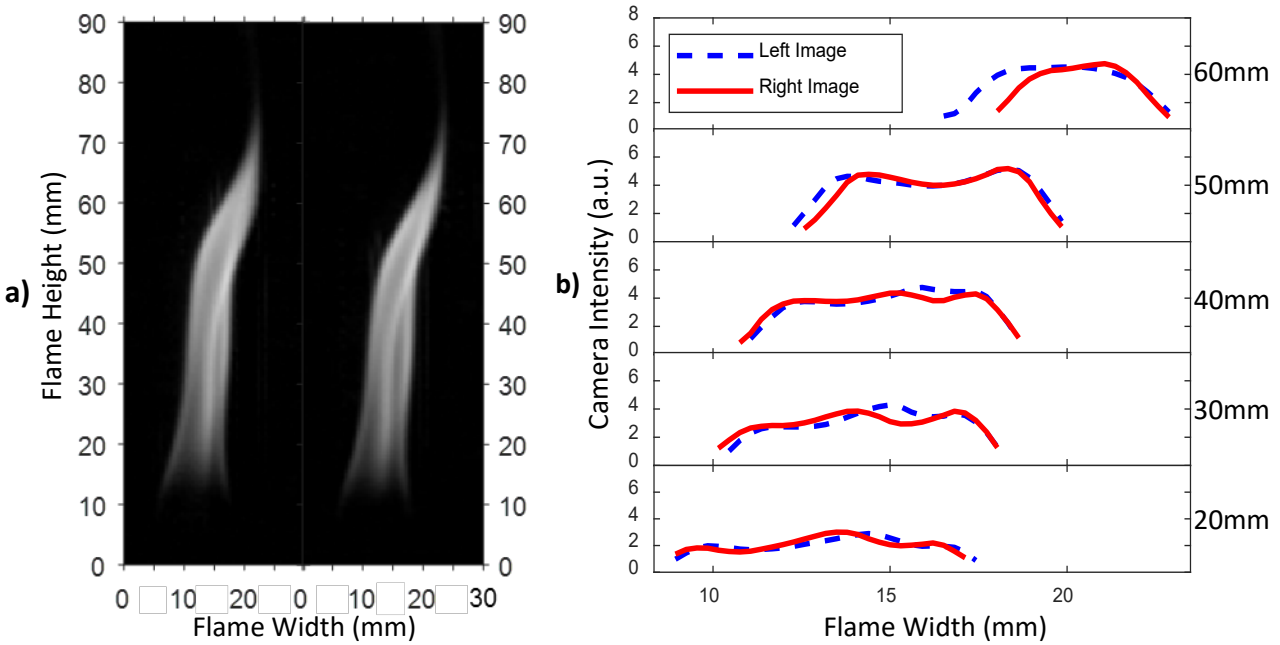

Figure 5: a) Flame images for parallax angle of 5.5°, and b) Transverse profiles of intensity at varying axial locations

turning mirrors to increase the length of one path by 1.25 cm and decrease the length of the other path by 1.25 cm causing a path length difference of 2.5 cm. In this case, Fig. 6a shows that one of the recorded flame images is smaller than the other. In Fig. 6a, the smaller image is on the left was resized to match the larger image and then the intensity profiles for both flames were plotted in Fig. 6b. Contrary to Figs. 4 and 5, Fig. 6b shows matching intensity profiles for the two images albeit after resizing in post-processing. The scaled intensity profiles are similar since the beamsplitter ensures a single viewpoint for both wavelengths. While this setup is a viable option, the image resizing represents a potential source of error. Resizing can be difficult or impractical in turbulent flames containing structures with multiple length and time scales. Additionally,

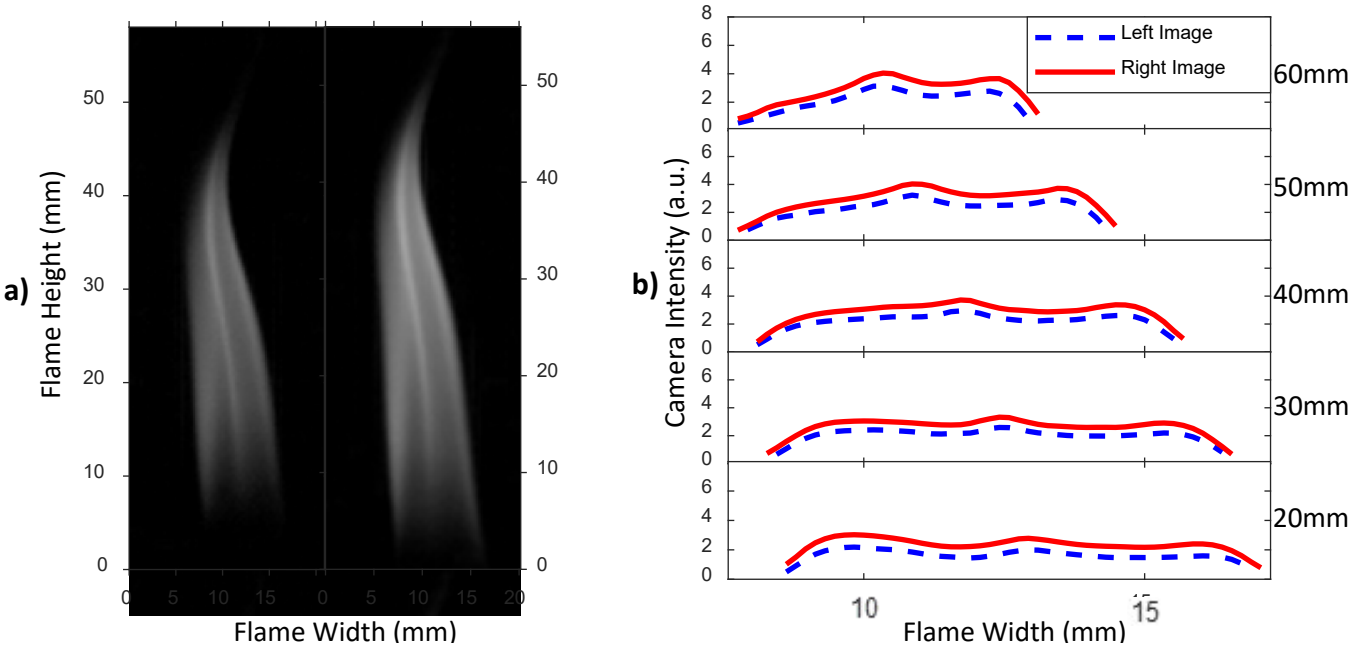

Figure 6: a) Flame images for path length difference of 2.5 cm, b) Transverse profiles of intensity at varying axial locations; the small image was scaled up to the size of the larger image at each axial location.

it is impossible to focus both images due to their differences in focal length. This lack of focus is manifested as bluring of the image(s). In effect, the blurring would prevent proper resolution of turbulent structures in the soot cloud causing a more spatially averaged measurement, rather than pixel mapping corresponding to precise physical locations in the flame. Again, the present system eliminates these problems by design to maintain equal path lengths for the two signals.

4.5 Sample Results from New Design

The capability of the new 2C pyrometer design is demonstrated by again collecting data on the aforementioned diesel wick flame. The 2C pyrometer in Fig. 3 was constructed and then calibrated using the UIS system to obtain calibration curves shown in Fig. 1. Flame images were recorded at 10,000 frames per second with an exposure time of 98 μs and pixel resolution of 5.8 pixels/mm.

Figure 7 demonstrates the ability of the 2C pyrometer design to map the features of the flame in the two images recorded by the camera. The images in Fig. 7a were taken with bandpass filters to enable 2C pyrometry processing, rather than the broadband natural luminosity images shown in Figs. 4-6. In effect, the intensity distribution in the two images is different because of the spectral emissions from the flame are different at the two wavelenghts. Figure 7b shows transverse intensity profiles at various axial locations demonstrating excellent match in profiles shapes for the two images at all axial locations. Specifically the difference in intensities of the two images is much smaller at the bottom of the flame compared to that at the top of the flame. The signficance of this effect is discussed in the following section.

To demonstrate the 2C pyrometry image processing procedure, Fig. 8 shows results for three timesteps at 10 ms intervals to depict the flickering of the flame. For each instant and pixel location, the intensity measured by the camera is converted to radiance value using the calibration curve for the corresponding wavelength (Fig. 1a). The radiance values for the two wavelengths are converted to a pair of apparent temperatures (Fig. 1b), and then Eq. 6 is used to solve for the actual temperature (T) and the product KL. Detailed analysis of the specific features of the flame is beyond the scope of this work, but as expected, the soot concentration is highest at the flame tip where the temperature is the lowest due to lack of air resulting in rich combustion.

4.5 Extent of Measurement Capabilities

An important strength of 2C pyrometry is its ability to output two useful variables, temperature and soot concentration, from apparent temperatures measurements for two wavelengths. Figure 9 exhibits the viable solutions to Eqn. 6 in a graphical form. This style of plot was inspired by Hottel and Broughtons' work on 2C pyrometry in 1932 [6] although similar computations and predicitons of measurement ranges have been performed in recent studies [27, 28]. In Fig. 9, experimental data from the diesel wick flame are superimposed to show the range of values actually observed in the measurements. The flame temperature varied from around 1450 K to 2400 K, yet the apparent temperature for the 650 nm wavelength ranged between 1300 K and 1500 K.

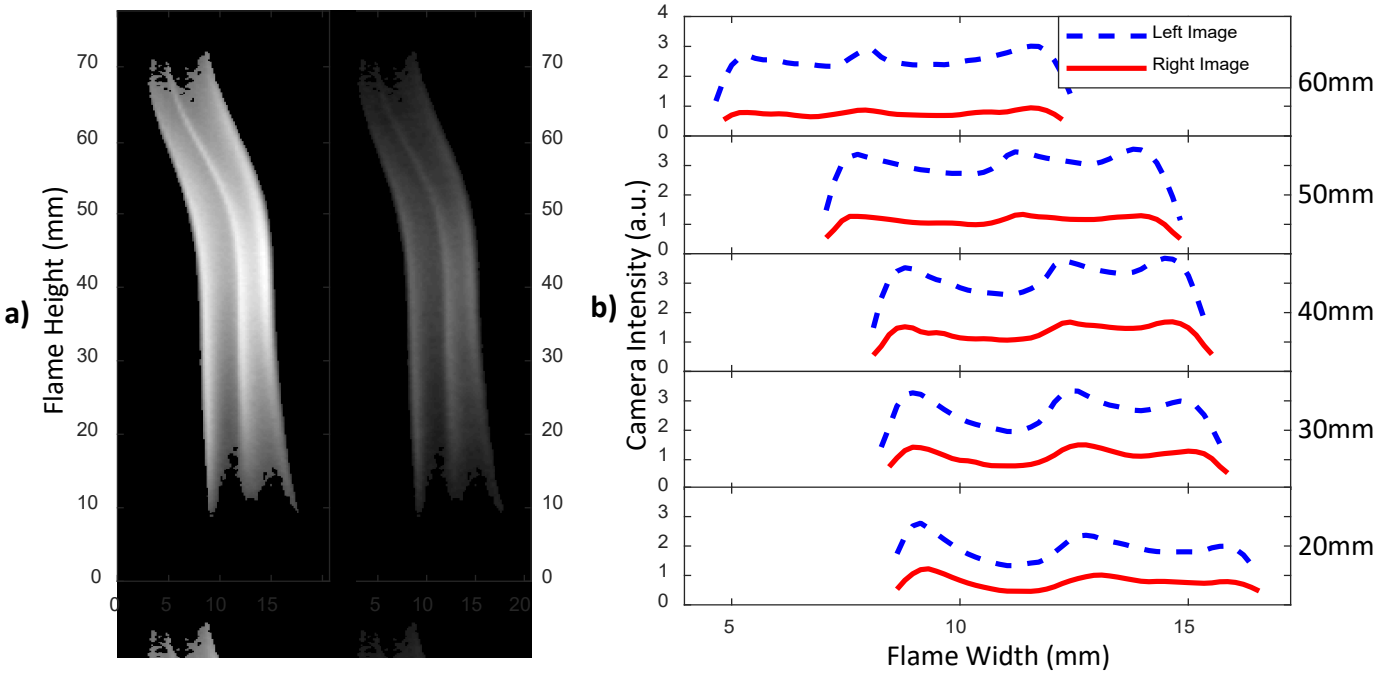

Figure 7: a) Flame images obtained by the present 2C pyrometer design, left and right images were obtained with 650 nm and 550 nm band-pass filters respectively, b) Transverse profiles of intensity profiles at varying axial locations.

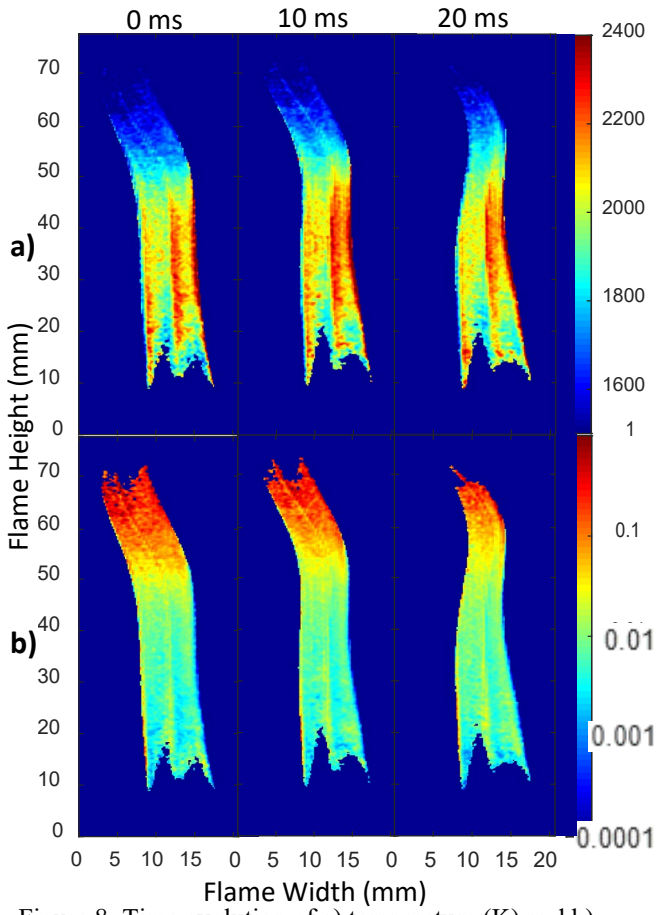

Figure 8: Time evolution of a) temperature (K) and b) product KL in a diesel wick flame

According to Eq. 5, an increase in KL will also increase ϵ_λ. Thus, increasing soot concentration causes soot emission to behave more like a blackbody. Indeed, for very high soot concentration or KL, the two apparent temperatures would be the same and equal to the blackbody temperature. The top portion of Fig. 9 depicts these conditions when the measured apparent temperatures are close to each other ($\Delta T_a \approx 10$ K); the soot concentration or KL is large and the temperature, T_a is only slightly greater than the apparent temperatures. For the diesel wick flame in this study, the smallest difference in apparent temperatures was 9.2 K, resulting in KL of approximately 1.0 and monochromatic emissivity of 0.84 and 0.90 respectively for wavelengths of 650 nm and 550 nm. Only a few experimental data points resided in this region. Conversely, low soot concentration implies low emissivity or a significant departure from the blackbody behavior. Experimental results is Fig. 9 show that the flame temperature is lower in regions of high soot concetration. This result can be explained by recognizing that the soot tends to form at fuel-rich conditions where temperatures are far below the stoichiometric flame temperature. The bottom of Fig. 9 pertains to near stoichiometric conditions where soot is burned off at high flame temperatures.

The left bound of the experimental data in Fig. 9 results from the camera noise threshold utilized to process the images, i.e., data to the left of the experimental points in the plot were filtered out. Conversely, if the flame brightness were to saturate the camera sensor, a similar cut-off would need to be implemented on the right side of the experimental data. Therefore, while the isolines in Fig. 9 represents all possible measurement conditions, the actual range can be constrained by the dynamic range of the camera.

5. Conclusions

In this study, a new optical design for 2C pyrometry is presented to eliminate errors associated with parallax and optical path length difference for the two wavelengths; parallax occurs when an object is imaged from separate viewpoints and optical hardware placement in 2C pyrometry setup can introduce path length differences. Although these errors have been acknowledged in past studies, they have not been fully addressed. The present system overcomes these problems by optical design, built from off-the-shelf hardware components, to develop a highly flexible and cost effective device utilizing a single imaging camera.

First, the device was configured to simulate parallax and show that it displaces (spatially) features within the flame in images acquired at the two wavelengths. Thus, the basic principle of 2C pyrometry requiring intensity, radiance or apparent temperature measurements at the same physical location for both wavelengths is violated. Consequently, the derived quanitities of temperture and soot concentration could be numerically intractable, physically irrelevant, or spatially unresolved, depending upon the parallax angle.

The configuration simulating different optical paths for the two wavelengths confirms that intensity measurements must be scaled in post-processing to account for the differences in image sizes to yield intensity data at the same physical location in both images. Image scaling can be challenging, especially in practical turbulent flames containing embedded vortical structures of multiple length scales.

Next, the improved measurement capability of the new 2C pyrometer compared to the existing designs was demonstrated, and then the system was used to obtain contours of temperature and soot concentration in a flickering diesel wick flame. Results are considered spatially resolved since matching pixels in both images represent the same physical location in the flame. However, 2C pyrometry is a line-of-sight technique, and thus, multiple views and tomography techniques will be required to obtain the local measurements in asymmetric turbulent flames. Still, the present spatially resolved single view measurements can be effective to compare different portions of the flame and/or flames at different operating conditions such as varying fuel type, ambient temperature, fuel injection strategies, etc.

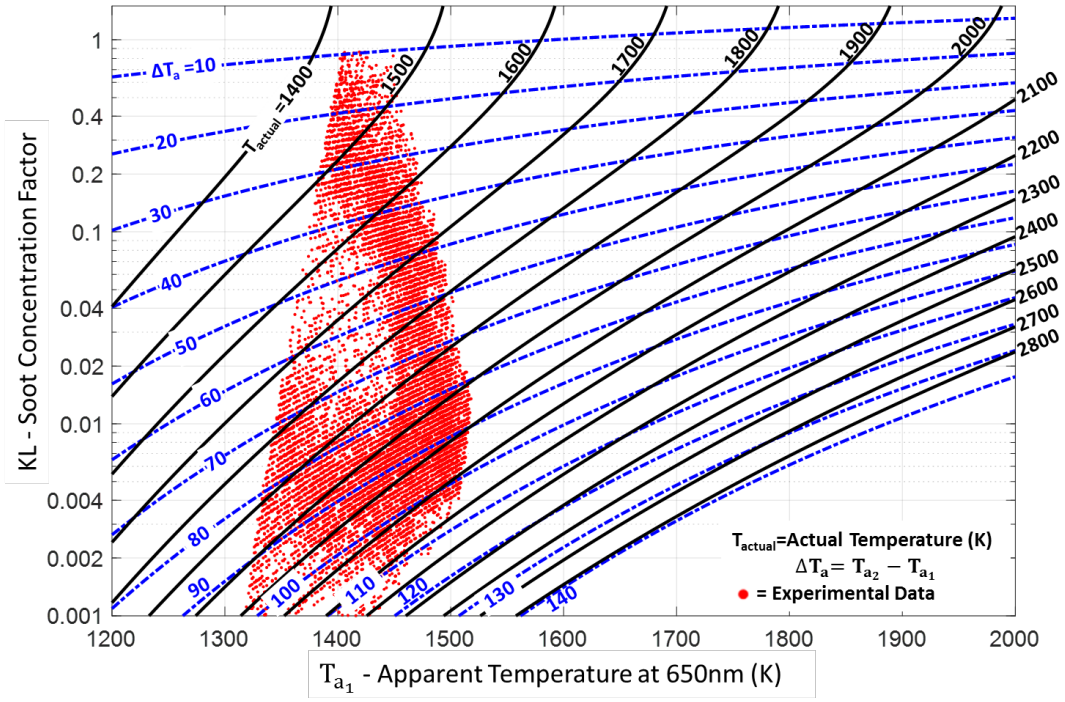

Figure 9: Relationship between apparent temperatures measured at 650nm and 550nm and temperature and product KL or soot concentration. Experimental data for the diesel wick flame are overlaid on the plot.

Acknowledgements

This research was supported in part by US Department of Energy award DE-EE0007980.

References

[1] Wichmann, H-E. "Diesel exhaust particles." *Inhalation toxicology* 19.sup1 (2007): 241-244.

[2] Bond, Tami C., et al. "Bounding the role of black carbon in the climate system: A scientific assessment." *Journal of Geophysical Research: Atmospheres* 118.11 (2013): 5380-5552.

[3] Chan, Tak W., et al. "Black carbon emissions in gasoline exhaust and a reduction alternative with a gasoline particulate filter." *Environmental science & technology* 48.10 (2014): 6027-6034.

[4] *Co-Optimizations of Fuels and Engines: FY17 Year in Review*. 2017, US Department of Energy, www.energy.gov/sites/prod/files/2018/04/f50/Co-Optima_YIR2017_FINAL_Web_180417_0.pdf.

[5] Das, Dhrubajyoti D., et al. "Sooting tendencies of diesel fuels, jet fuels, and their surrogates in diffusion flames." *Fuel* 197 (2017): 445-458.

[6] Hottel, Hoyt C., and F. P. Broughton. "Determination of true temperature and total radiation from luminous gas flames." *Industrial & Engineering Chemistry Analytical Edition* 4.2 (1932): 166-175.

[7] Mishin, J., et al. "Two-colour pyrometer for the statistical measurement of the surface temperature of particles under thermal plasma conditions." *Journal of Physics E: Scientific Instruments* 20.6 (1987): 620.

[8] Müller, Bernhard, and Ulrich Renz. "Development of a fast fiber-optic two-color pyrometer for the temperature measurement of surfaces with varying emissivities." *Review of scientific instruments* 72.8 (2001): 3366-3374.

[9] Jorgensen, F. R. A., and M. Zuiderwyk. "Two-colour pyrometer measurement of the temperature of individual combusting particles." *Journal of Physics E: Scientific Instruments* 18.6 (1985): 486.

[10] Zhao, Hua, and Nicos Ladommatos. "Optical diagnostics for soot and temperature measurement in diesel engines." *Progress in energy and combustion science* 24.3 (1998): 221-255.

[11] Payri, Francisco, et al. "Contribution to the application of two-colour imaging to diesel combustion." *Measurement science and technology* 18.8 (2007): 2579.

[12] Zhang, Ji, et al. "Soot temperature and KL factor for biodiesel and diesel spray combustion in a constant volume combustion chamber." *Applied energy* 107 (2013): 52-65.

[13] Densmore, John M., et al. "High-speed two-camera imaging pyrometer for mapping fireball temperatures." *Applied optics* 50.33 (2011): 6267-6271.

[14] Singh, Satbir, Rolf D. Reitz, and Mark PB Musculus. "2-color thermometry experiments and high-speed imaging of multi-mode diesel engine combustion." *SAE transactions* (2005): 1605-1621.

[15] Musculus, Mark PB. "Measurements of the influence of soot radiation on in-cylinder temperatures and exhaust NOx in a heavy-duty DI diesel engine." *SAE transactions* (2005): 845-866.

[16] Bergman, Theodore L., et al. *Fundamentals of heat and mass transfer*. John Wiley & Sons, 2011.

[17] Musculus, Mark PB, Satbir Singh, and Rolf D. Reitz. "Gradient effects on two-color soot optical pyrometry in a heavy-duty DI diesel engine." *Combustion and flame* 153.1-2 (2008): 216-227.

[18] Quay, B., et al. "Spatially resolved measurements of soot volume fraction using laser-induced incandescence." *Combustion and Flame* 97.3-4 (1994): 384-392.

[19] Manin, Julien, Lyle M. Pickett, and Scott A. Skeen. "Two-color diffused back-illumination imaging as a diagnostic for time-resolved soot measurements in reacting sprays." *SAE International Journal of Engines* 6.4 (2013): 1908-1921.

[20] di Stasio, Stefano, and Patrizio Massoli. "Influence of the soot property uncertainties in temperature and volume-fraction measurements by two-colour pyrometry." *Measurement Science and Technology* 5.12 (1994): 1453.

[21] Beatrice, C., et al. "Two-colour pyrometry measurements of soot loading in a diesel engine burning model fuels of varying quality." *Combustion science and technology* 110.1 (1995): 321-339.

[22] Shi, Qi, et al. "Measurement of Temperature and Soot (KL) Distributions in Spray Flames of Diesel-Butanol Blends by Two-Color Method Using High-Speed RGB Video Camera." *SAE International* 2016-01-2190 (2016).

[23] Densmore, John M., et al. "High-speed digital color imaging pyrometry." *Applied Optics* 50.17 (2011): 2659-2665.

[24] Jing, Wei, et al. "Measurements of soot temperature and KL factor for spray combustion of biomass derived renewable fuels." *Energy* 91 (2015): 758-771.

[25] Araújo, António. "Multi-spectral pyrometry—a review." *Measurement Science and Technology* 28.8 (2017): 082002.

[26] Hossain, Md Moinul, et al. "Three-dimensional reconstruction of flame temperature and emissivity distribution using optical tomographic and two-colour pyrometric techniques." *Measurement Science and Technology* 24.7 (2013): 074010.

[27] Fu, Tairan, et al. "The theoretical prediction analyses of the measurement range for multi-band pyrometry." *Measurement Science and Technology* 17.10 (2006): 2751.

[28] Fu, Tairan, et al. "The measurement coordinates for multi-band pyrometry." *Measurement Science and Technology* 17.2 (2006): 379.

Proceedings of the ASME 2020 Internal Combustion Engine Fall Technical Conference
ICEF 2020
November 1 - 4, 2020, Denver, CO, USA

DRAFT-ICEF2020-3007

COMPARING GLOBAL SPRAY COMBUSTION CHARACTERISTICS AND LOCAL SHOT-TO-SHOT VARIATIONS IN A REACTING N-HEPTANE SPRAY

Shawn Reggeti, Allen Parker, Ajay Agrawal, Joshua Bittle*
Department of Mechanical Engineering
University of Alabama
Tuscaloosa, AL, 35487

ABSTRACT

In support of efforts to develop improved models of turbulent spray behavior and combustion in diesel engines, experimental data and analysis must be obtained to guide and validate them. For RANS-based CFD modeling approaches it is important to have representative ensemble average experimental results. For models that provide high fidelity local details such as LES-based CFD simulations, it is desirable to have precise individual experiment results. Making comparisons however is a challenge as it is impossible to directly compare local parameters between a given experiment and LES simulation.

An optically accessible constant pressure flow rig (CPFR) is utilized to capture injection and reaction behavior with three optical diagnostic techniques: rainbow schlieren deflectometry (RSD), OH* chemiluminescence (OH*), and two-color pyrometry (2CP). The benefit of these high-speed, simultaneous diagnostics is that local measurements can be made for every stage of a single injection event, observing both how much injections differ one from another, and also how such differences evolve temporally. The CPFR allows a sufficiently large number of repeated injection experiments to be performed for proper statistical analysis and ensemble convergence, while maintaining highly repeatable, nominally constant test conditions. Even given such stable conditions however, variations in local turbulent fuel-air mixing introduce a degree of variability which may manifest as significant differences in OH* and 2CP results. A statistical method is utilized to analyze the extent of this variability, and to identify superlative injections within the data set for discussion and analysis of shot-to-shot variation.

Experimental measurements of characteristic parameters including liquid and vapor jet penetration, lift-off length, soot temperature and concentration, and turbulent flame speed, along with the shot-to-shot variability of each, are presented and discussed. While the results shown here can only postulate about the causation, the framework to characterize shot-to-shot variations could be leveraged to enable direct comparison with high-fidelity simulations without the need for averaging multiple realizations.

INTRODUCTION

It is common to consider and describe reacting fuel sprays, like those found in diesel engines, in terms of average behavior. Parameters such as liquid length, lift-off length, and ignition delay time describe the result of an experiment for a given fuel, injected into some controlled ambient. Significant work has been done to develop methodologies and to compare between ensemble average spray behavior and various modeling approaches (e.g. [1, 2]). Computational fluid dynamics (CFD) spray modeling using Reynolds Averaged Navier Stokes (RANS) approaches were developed to simulate average/ensemble behavior of spray experiments. As computational power has increased, it has become possible to apply large eddy simulations (LES) with smaller grid scales, which are able to resolve the turbulent flow behavior in sprays [3, 4] and relevant emission formation processes. Comparisons between LES simulations and experiments are still largely based on global parameters and qualitatively on local structures or properties as a comprehensive direct replication of an experimental conditions is not possible in simulation. In addition to exploring the physics of spray mixing and combustion processes, both RANS and LES based approaches are leveraged to enable reliable development of engine combustion control strategies.

To support development of these modeling approaches, researchers have created a variety of spray vessels with different features such as constant-volume or -pressure, and precombustion or electric heating (see [5] for description of some such systems). Regardless of the approach, the primary goal of these chambers is to enable controlled experimentation on fuel sprays at engine-relevant thermodynamic conditions. As the primary means by which features of the spray evolution can be quantified, these vessels are typically equipped with

*Corresponding Author: jbittle@eng.ua.edu

some combination of optical diagnostic techniques. In this work, an electrically heated constant-pressure flow rig (CPFR) is used in combination with Rainbow Schlieren Deflectometry (RSD), OH* Chemiluminescence (OH*), and two-color pyrometry (2CP) imaging to acquire measurements from 100 repeated injection experiments at nominally the same ambient conditions. While many studies report ensemble results or highly detailed investigations into measurements from a single injection, very few studies have explored shot-to-shot variations. In one example, Swantek et al. used x-ray imaging to generate statistical data on mass distributions from a single hole injector over 32 injections [6].

While RANS modeling is generally able to capture average behavior, and LES is able to capture single injection behavior, there remains the challenge in identifying which single injection to use to guide the design. It is critical to understand the bounds of shot-to-shot injection behavior that can be expected as combustion design efforts push the limits of combustion stability through hardware and control methods. It is often not economical to run large parametric sweeps (many realizations) of LES simulation to capture range of behavior, and thus this work aims to provide a new methodology and motivation for quantifying shot-to-shot variations.

Here we will demonstrate how ensemble-averaged axisymmetric results can be obtained (and consider how many injections are required to achieve convergence) as well as present an analysis of different classifications of individual injection behavior. Single injection events that can be considered the most average or most unique (or other classifications in between) – identified using a statistical approach – will be considered alongside the ensemble results. Through this approach, this work will demonstrate how much variation can be observed in both global and local behavior even at nominally the same experimental conditions.

As an additional focus of this work, apparent turbulent flame speeds and their variations are extracted and discussed. Turbulent flame speed is a critical parameter for characterizing any turbulent combustion system, and one that is a challenge to measure and model. Many canonical experiments have been conducted to study the impact of geometry and conditions on turbulent flame speed and also provide data for model development. A recent work by Kolla et al. [7] presented validation of a turbulent flame speed model against experimental work from studies published between 1966-2006. They sampled this work in order to include results from a number of canonical flames such as V-shape, planar, and conical. The need to sample such a wide time span for validation data indicates that a relatively limited set of canonical results are available, let alone application specific results such as for diesel fuel sprays. Despite the availability of turbulent flame speed models such as [7, 8], it is typical to estimate the turbulent flame speed in spray modeling by extrapolating it from the laminar flame speed and the associated turbulent wrinkling of flame front [9]. While the complexity of the experiment is only compounded by the challenge of modeling, we present a method to measure the apparent turbulent flame speed OH* chemiluminescence and RSD imaging; by spatially and temporally processing the vapor jet tip and the OH* based lift-off length, and combining the associated velocities, the reaction front velocity can be determined.

The remaining sections describe the experimental setup, including test apparatus, diagnostics, and data processing, followed by results and conclusions. The results will first focus on demonstrating experimental repeatability in typical global parameters such as liquid length, vapor penetration, and lift-off length. Then, considering global repeatably, the local differences in shot-to-shot behavior will be considered for the RSD liquid and vapor penetration lengths, OH* reaction zones and intensity, and finally 2CP temperatures and soot concentrations. The major implication of the work is that despite repeatable global parameters, there are clear local differences in fuel-air mixing and subsequent ignition that would result in wide variations in emissions and overall combustion efficiency, especially important in cases when combustion stability is a concern.

EXPERIMENTAL SETUP

System operation and capabilities

The constant pressure flow rig (CPFR) utilized in this study is shown in Fig. 1. This rig provides line-of-sight optical access to the nearly quiescent environment into which fuel is injected. Injections enter downward, in a counter-flow arrangement as shown. Air velocity is approximately three orders of magnitude less than the fuel injection velocity, and thus, air can be considered as quiescent (this is also confirmed by RSD high-speed images). Electrically preheated, pressurized air enters the chamber at approximately $0.5\frac{m}{s}$ through a flow conditioner to produce near-uniform inlet velocity distribution. The flow conditioner consists of six, 0.5 mm thick, 100 micron mesh elements, as well as a diffuser. The continuous upward air flow efficiently flushes repeated injections from the chamber, and thus, large datasets can be quickly generated ($\sim$360 injections/hour). Air exits the chamber through four, symmetrically placed, 3 mm diameter holes. The pressure of supplied air is regulated by a dome regulator (upstream), and the flow rate is controlled by a control valve (downstream).

Fuel is supplied by a pneumatic pressure multiplying pump. The injector return flow, which increases with pressure (even when not injecting), results in pulsation as the pump repressurizes. In order to ensure repeatable injection pressures, the data acquisition and injection triggering systems are configured to automatically trigger on a rising edge of the pressure signal occurring within range of the desired injection pressure. Fuel is injected along the axis of the rig through a Bosch CRIN3-18 injector with a single 100 μm hole at the tip. The injector body and fuel temperatures are maintained by circulating coolant; specific test conditions are described below with details summarized in Table 2.

Diagnostics

The layout of the three simultaneous optical diagnostics utilized in this study is shown in Fig. 2: Rainbow Schlieren Deflectometry (RSD), chemiluminescence (or OH*), and two-color pyrometry (or 2CP). A summary of sampling rate and spatial resolution is provided in Table 1.

RSD is arranged perpendicular to the chamber windows in

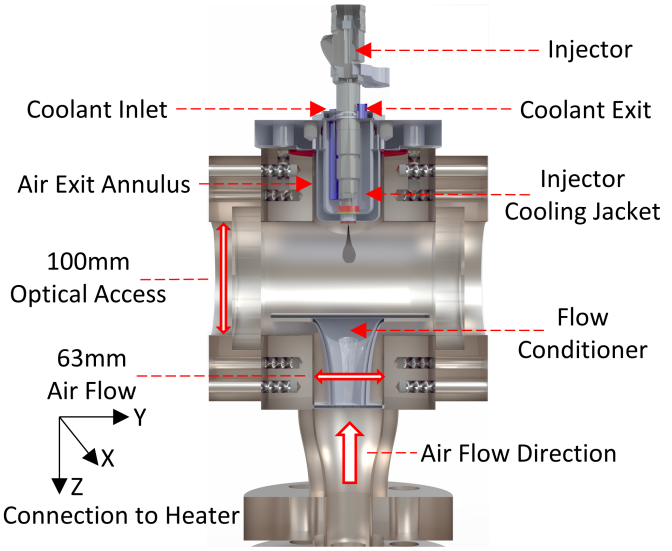

FIGURE 1. Constant pressure flow rig schematic.

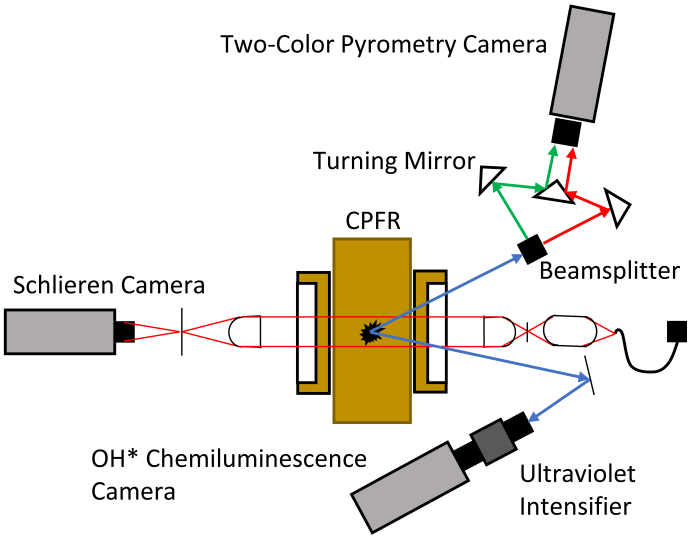

FIGURE 2. Simultaneous high-speed diagnostic setup including Rainbow Schlieren Deflectometry, OH* Chemiluminescence, and Two-Color Pyrometry (2CP). View angle of OH* and 2CP systems are exaggerated for illustration purposes.

alignment with its light source; OH* chemiluminescence and 2CP signals are viewed at a slight, off-set angle. An Energetiq EQ-99X fiber coupled broadband light source is used for the RSD system. This light is refocused by two 75 mm focal length, 50 mm diameter lenses onto a 3 mm x 100 μm rectangular aperture, located at the focal point of a 75 mm diameter, 250 mm focal length achromatic doublet lens. As shown in Fig. 2, the collimated light passes through the CPFR and then, it is decollimated (focused) by a matching achromatic doublet lens and focused onto a rainbow filter. The digitally designed and printed rainbow filter is a transparent strip with very fine (4 μm) hue (color) linearly distributed gradations, and it is placed at the lens imaging plane. Directly behind the filter plane is a Photron Nova S9 color camera, acquiring RSD images at 20 kHz with 4 μs exposure time and 512 x 784 pixel resolution. A Nikon Nikkor 50 mm lens provides 90 $\mu m/px$ spatial resolution. This camera was used to synchronise the two other cameras by generating an trigger pulse every other frame resulting in acquisition rates of 10 kHz for OH* and 2CP high-speed cameras.

OH* chemiluminescence from the reacting spray is reflected by a UV mirror through a 310 nm band pass filter, a Nikon UV lens, an Invisible Vision UV intensifier (gate time 70 μs, and into a monochromatic Photron SA5 camera. The images are acquired over 896 x 848 pixels, with spatial resolution of 160$\mu m/px$ and framing rate of 10 kHz.

The thermal radiation from soot, which dominates flame luminosity in the visible spectrum, is detected by the 2CP camera at two distinct wavelengths. Based on the calibrated apparent temperatures at the two wavelengths the actual soot temperature and concentration can be calculated [10, 11]. The general layout of the pyrometer collecting optics can be seen in Fig. 2. The flame luminosity passes through a 50/50 beamsplitter, which allows half of the light to be transmitted through and reflects the other half at a 90° angle. Band-pass filters of central wavelengths, 650 nm and 550 nm, each with 10 nm FWHM bandwidths, are attached to the outlets of the beamsplitter. Each spectral signal is reflected off of a turning mirror, towards a knife-edge prism mirror, and then along parallel paths to the camera. Both spectral signals follow paths of equal lengths and are imaged on the same camera sensor thereby avoiding the need for spatial resolution scaling or parallax errors induced by other designs. More details of this novel pyrometer design can be found in [12]. A Nikon Nikkor 105 mm lens is used with a Phantom v7.3, 14-bit, monochromatic camera, giving spatial resolution of 242$\mu m/px$. The 2CP system is triggered at 10 kHz framing rate.

TABLE 1. Simultaneous diagnostics specifications.

	RSD	OH*	2CP
Spatial Resolution	90 μm	160 μm	242 μm
Sampling Rate	20 kHz	10 kHz	10 kHz

Data Processing

Where possible, identical or similar programs analyzed images from each diagnostic for consistency of results; given the spatial differences, and the key fact the RSD images are derived from hue (color) while chemiluminescence and 2CP are intensity-based, this is not always feasible.

Determination of ignition delay is common to both OH* (chemiluminescence) and soot (2CP) signals. To calculate ignition delay, an intensity-signal background-threshold was first established from mean and standard deviation of images before start of injection (bSOI), for each injection. The intensity signals recorded for the presence of OH*/soot vastly differentiate themselves from this threshold, so the program flagged the first frame to contain signals in statistical excess of this threshold as the ignition delay. Start of injection (SOI) was ascertained visually via captured RSD images, with frame-rates then applied to convert frame number into ignition delay in milliseconds.

The method to determine the vapor and liquid penetration lengths is similar to that for lift-off length. Liquid phase boundary detection is described in detail by Wanstall et al. [13]. Briefly, liquid phase is distinguished by extremely low intensity, or lack of signal, in RSD images due to light attenuation through scattering or absorption during interaction with the dense liquid. The vapor jet is easily distinguishable from the background by the conventional method of subtracting from each frame the value of the previous, thus removing any quiescent background structures and leaving only the spray region containing any significant signal. This differential signal can easily be processed to find the spray boundary using statistical threshold analysis. For identifying and tracking reaction zones in OH* and 2CP images, the methodology is very similar. For each injection, a radial mean of OH* chemiluminescence and raw 2CP signals (at 650nm) is referenced for each frame. Upstream (non-reacting) locations provide a threshold to determine the first downstream instance of statistically apparent signal, which is recorded as the lift-off length.

Having determined the vapor jet penetration and the lift-off length for OH* signal, local velocities are calculated from derivatives of the aforementioned lengths as a function of time. Note that the vapor/jet speed is absolute, with respect to the stationary frame of reference; the OH* signal speed is likewise, and thus the local turbulent flame speed (relative to the jet) is identified when the flame is stationary, indicating its equivalence with the jet velocity. The significance of this parameter is discussed further in the Results section.

A key focus of this study is to highlight the significant shot-to-shot variability observed in repeated experiments even when common global spay characteristics are nominally the same. To this end, and as the culmination of several processing techniques, a methodology was developed to identify for comparison the instantaneous data from the most superlative single injections from each diagnostic. The technique previously discussed to identify vapor phase penetration was used to demarcate two-dimensional boundary lines, and was utilized across all diagnostic techniques to identify spray, OH*, or soot boundaries. Maintaining shot-to-shot history of the boundary lines for the right and left sides of each injection, such lines were compared across all injections (of the same diagnostic) to establish a mean(μ) and standard deviation(σ) of injection boundaries. Consider that the boundaries and mean/standard deviation lines have radial [mm] values stored at each axial location; radial boundary values are then converted to a non-dimensional standard score (also called z-score, $z = \frac{x-\mu}{\sigma}$). Thus the z-score is the number of standard deviations away from average that a boundary is, for a single injection at a particular time and axial location.

Boundaries are defined fractionally relative to the mean. Rejecting statistical outliers, such z-scores are averaged axially, and then averaged again in the time dimension. Only frames between the start of injection and the end of reliable signal are considered in the temporal average. For RSD, this means prior to ignition, when the collimated light is the only source of light. However, OH* and 2CP intensities are reliably recorded at all times. Each injection is thereby described by a singular number (on both the right and left side) representing how far away that injection's edges are, on average, from a typical injection as it develops through time. Ascribing a physical meaning to this statistical parameter, it could be said that an injection of z-score = 1.5 is best represented by the iso-line of μ+1.5σ as it develops. The right and left sides of the spray are maintained separately to support a wide range of superlative discovery. Consider that Z¿0 indicates that the spray favors the positive radial direction; separate left/right values allow the determination of more than 'rightmost' or 'leftmost' injection because one side can be negated, in which case the greatest total z-score would represent the 'widest', and the least the 'thinnest'. The absolute value of both sides could be averaged to locate the 'most representative' or deviant injections, regardless of directionality. Thus the 'widest', 'thinnest', etc., injections are ascertained from each diagnostic and presented for comparison and discussion. Of course, any desired superlative or metric for identifying such can be used and this study only serves to highlight the large difference amongst nominally the same injection events.

Specific Test Case and Repeatably Demonstration

The global thermodynamic state of the CPFR was held constant for each injection experiment with values and ranges provided in Table 2. Ambient pressure and temperature were nominally 3 MPa and 800 K with a corresponding density of 13 kg/m^3. *n*-heptane was injected for 2 ms with the fuel and injector body maintained at 90 $^\circ C$. Finally, the injection pressure was set to 100 MPa. All actual measured values are shown in Table 2 with uncertainty indicating 95% confidence interval based on repeatability for any single injection over the 100 injection experiments included in the data set for this study.

Given a very stable ambient and injection condition, it is expected that the subsequent spray mixing and ignition would be repeatable. The ignition delay results as determined from both OH* and 2CP imaging techniques are shown in Fig. 3. While the imaging rate (10 kHz) limits the ability to precisely identify the onset of ignition, it is clear from these results that the OH* signal precedes the first observations of soot signal by less than 0.1 ms on average. This corresponds to slightly less than 1 frame with an average ignition delay of $1.71 \pm 0.16 ms$ from OH* and $1.79 \pm 0.2 ms$ from 2CP – again with a 95% confidence interval for any individual injection. This additional delay between OH* and 2CP signals is expected based on the extremely complex process by which soot particles are formed from conglomeration of carbon atoms. Many detailed soot formation and oxidation models of various complexity can be found in literature, such as [14–16].

RESULTS

Global Parameters

The global thermodynamic condition, injection settings, and ignition delay are examples of properties generally considered as global parameters. It is expected then that for a given fuel, injected into a given ambient, the ignition delay will be a repeatable number. Global parameters such as this are often used to describe a spray or experiment and subsequently used to guide or generalize discussion. Of course this type of spray combustion experiment is more complex than a premixed combustion

TABLE 2. Actual ambient air and fuel injection conditions for CPFR experiments. Variation indicates 95% confidence interval over consecutive 100 injections.

Property	Units	Value
Ambient Air Properties		
Ambient Temperature	$[K]$	806 $\pm$3
Ambient Pressure	$[MPa]$	3.01 $\pm$0.03
Ambient Density	$[kg/m^3]$	13.0 $\pm$0.13
Fuel Properties		
Fuel Species		n-heptane
Fuel Temperature	$[K]$	364 $\pm$3
Fuel Pressure	$[MPa]$	99.1 $\pm$0.9
Injector Orifice Size	$[\mu m]$	100
Injection Duration	$[ms]$	2

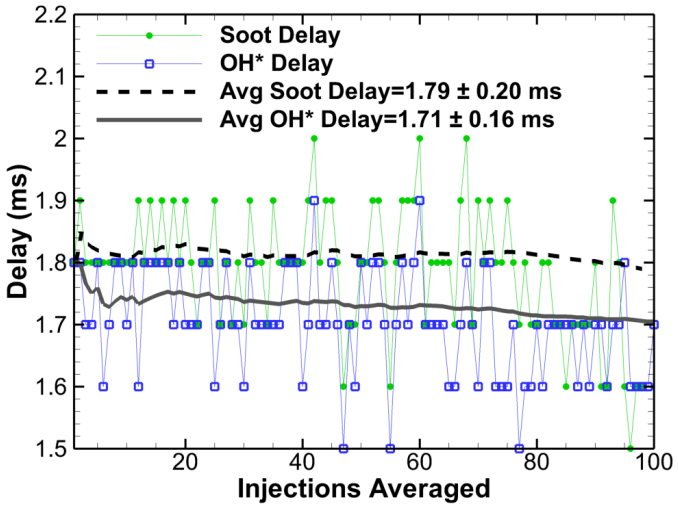

FIGURE 3. Ignition delay results from both OH* and 2CP diagnostics for 100 consecutive injections demonstrating converging average and final average results with 95% CI.

system that might be modeled using detailed kinetics as a zero-dimensional homogeneous reactor, but the principle is similar. In this section global parameters such as those already shown are considered for their repeatability across the 100 injection data set. Figure 4 shows the average vapor and liquid penetration profiles as well as lift-off lengths as determined from both OH* and 2CP imaging techniques; all averages are bounded by single shot 95% confidence intervals.

Often liquid length and lift-off length are considered global parameters as well. Typically they are quantified based on quasi-steady spray combustion results and thus allow a single scalar value to be used to characterize an experiment. In this study, the transient behavior of vapor, liquid, and lift-off length from the two diagnostics are considered based on Fig. 4. Note that the vapor penetration profile ends abruptly at 1.25 ms aSOI as

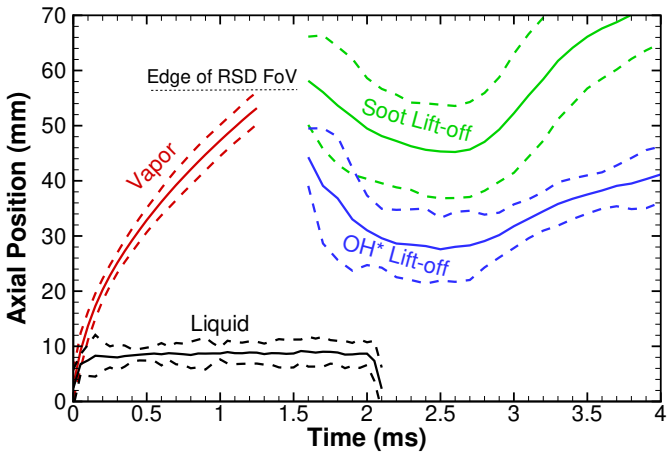

FIGURE 4. Ensemble average vapor and liquid penetration (determined by RSD) and time-resolved lift-off length from both OH* and 2CP diagnostics. All ensemble results include 95% confidence intervals capturing individual injection variation.

it leaves the schlieren system field-of-view . The consistency of the vapor penetrations over repeated experiments is clear based on the approximately $\pm$ 2 mm range observed even at 50 mm downstream of the injector tip. Further, the stability of liquid length in both time and across injections suggests the fuel and injector temperature control was effective.

The 2 ms injection duration can be visualized by the drop in liquid length right at that time. Relative to the OH* and 2CP based lift-off lengths, this end-of-injection timing clearly shows that a quasi-steady lift-off length was perhaps only just achieved at around 2.5 ms, before reaction zones are transported downstream by jet momentum after end-of-injection. After initial reaction at 1.6 ms takes place downstream, the relatively high turbulent flame speed causes the lift-off lengths of both OH* and 2CP to recess back towards the injector. The lift-off length eventually stabilizes only to begin increasing immediately at a location where the jet velocity and flame speed are momentarily equal. The lift-off lengths begin to increase again after 2.5 ms as they are swept downstream with the last of the fuel and the mixture becomes very lean as the entrainment wave passes [17].

The distinct phases of initial penetration, ignition, stabilization, and end-of-injection are clearly evident in this experiment. Note that it is possible that, given a longer injection duration, the quasi-steady lift-off lengths would be slightly shorter than those minimum values observed in this study. As may be expected based on the slightly longer delay before 2CP signal is detected compared to OH* (from Fig. 3), the lift-off length based on 2CP is longer than that from OH*. In the spatial frame of reference, later in time corresponds to further downstream from the injector. In this particular case, the relatively low ambient pressure, compared to those found in actual engines, results in a relatively long ignition delay. This propagates and results in longer lift-off lengths as well; however, the trends and relative locations of both vapor, liquid and lift-off lengths progress as expected. As a result of the relatively long ignition delay (again compared to engine conditions) the differences in local fuel-air mixing from shot-to-shot seem to be causing a relatively high variation in the lift-off

length measured by both OH* and 2CP techniques. This leads to the consideration that the relatively repeatable ignition delay results in Fig. 3 may actually represent substantial variations. The remaining results sections will explore this observation further.

While the field-of-view of the schlieren system is limited, the vapor penetration can reasonably be expected to continue roughly proportional to the square-root of time. If one considers extrapolating the vapor penetration profile, it is clear that the OH* presence is first detected slightly behind the jet-head plume in time and space. The 2CP signal is first detected slightly closer to the leading edge of the jet likely emanating from the rich core slightly after reactions begin as indicated by OH* signal. This discussion will be supplemented in the following sections which includes images of the sprays for each diagnostic and discussion of apparent turbulent flame speeds based on these results in Fig. 4.

Range of Shot-to-shot Variation for each Diagnostic

As described in the Data Processing section, a statistical approach for analyzing the boundaries of RSD, OH* and 2CP results at each time step was developed to identify superlative injections such as the 'widest', 'thinnest', and 'most representative'. This analysis is cumulative over the entire injection event, however the superlative description is suitable even at an instant in time. Figure 5 shows these superlative injections alongside the ensemble average results for RSD, OH*, and soot temperature and concentration from processed 2CP data. As the spray has moved beyond the RSD field of view before ignition, results for it are shown at 1 ms after start of injection (aSOI) while for the other diagnostics results are shown at 2.5 ms aSOI when when the average lift-off lengths are at a minimum as seen in Fig. 4. On each frame of Fig. 5 the specific injection number, time stamp, and boundary from the ensemble result is overlaid. The ensemble boundary gives context to the classification indicated at the top of the columns. The spatial scaling is uniform throughout all images while color bars are constant for each injection within a diagnostic parameter. Each diagnostic was considered separately when identifying superlative injections and thus the 'widest' injection for RSD is not necessarily, and in fact is not, the same injection for OH* or 2CP*. The injection number stamp in each frame illustrates this identification. Of course, the choice could have been made to identify superlatives with one diagnostic and then compare the same injections for the other diagnostics.

First considering the RSD superlatives, the 'widest' injection clearly stands out as being wider than the others while the 'thinnest' is only marginally so compared to the 'most representative' injection and the differences are mostly obscured behind the overlaid average boundary. While the instantaneous RSD images do not appear to have much structure to their hue distributions, the ensemble averaged image clearly shows the distinct hue distributions that enables RSD to be quantitative.

The OH* images show much more significant differences between the various superlative classifications. The ensemble result clearly shows a repeatable split reaction zone behavior with one peak at 50 mm and the other between 65 mm and 70 mm. Only the 'widest' superlative injection shows this behavior, however, this structure must be common to all injections to be visible in the ensemble. The relative size of the 'thinnest' injection is clearly the smallest overall reaction zone of the three while the shape of the 'most representative' is slightly off from the ensemble. As with the RSD results, the behavior of an individual injection is only loosely connected with the ensemble result. In this case the 'most representative' injection does not have a split reaction zone, though it does have a slightly wider reaction zone further downstream from the injector. However the magnitude is clearly reduced due to averaging (effectively filtering), though OH* magnitude is normalized and only used qualitatively in this case.

OH* location and magnitude primarily serves to mark regions where certain reactions in the overall-reaction kinetic-pathways are taking place, rather than any specific details. So while OH* intensity is only loosely related to subsequent combustion and emissions formation, measurements of soot temperature and concentration from the 2CP system provide a direct measurement of soot formation processes and can be correlated with expected exhaust soot levels. It is important to note that while soot is clearly forming under the test conditions in this study, for this well-mixed spray condition, it is likely that very little net soot would be left in exhaust stream. After soot forms in the rich core of the spray it can be expected that most of the soot is consumed through oxidation as it is transported through the primary stoichiometric reaction region at the jet head and edges. However, it is also possible that the high sooting regions in the edges of the jet may experience reduced heat release and thereby transport soot out of the reaction zone [18]. Based on the complexity of soot formation, oxidation, and transport processes, it is perhaps not surprising that 2CP results show the most dramatic shot-to-shot variations observed.

Considering either the soot temperature (T) or concentration (KL), it is apparent that between the 'widest', 'thinnest', and 'most representative' injections, a wide range of local behavior is observed. As compared to the RSD and OH* results, the spatial size and temperature of the 'most representative' injection actually closely resembles the average values, and yet due to the high sensitivity to temperature at low KL values [12] the instantaneous KL values are significantly different than the average values. The higher sensitivity of soot formation to local fuel-air mixing is expected based on complexity of soot formation processes [15]. As with the OH* results, this averaging has a significant impact as it smooths the local peaks observed in single injection results. Despite only having a few millimeters different lift-off length, the total apparent soot concentration for the 'thinnest' injection is significantly less than any of the other injections or ensemble results. It also has some of the highest peak temperatures suggesting better fuel-air mixing and perhaps near to stoichiometric reactions occurring and thereby avoiding soot formation altogether. On the other hand the 'widest' injection has the most cool soot regions which results in higher concentrations. Note that a pyrometer optimized for a lower temperature range may in fact capture soot temperatures over a larger volume for the 'thinnest' injection. Regardless, the trends and takeaways from the analysis in this work will be unchanged.

The larger reaction regions in both OH* and 2CP data can be correlated to the slightly wider initial RSD images but the actual mechanism is not so apparent. Typically a wider jet would sug-

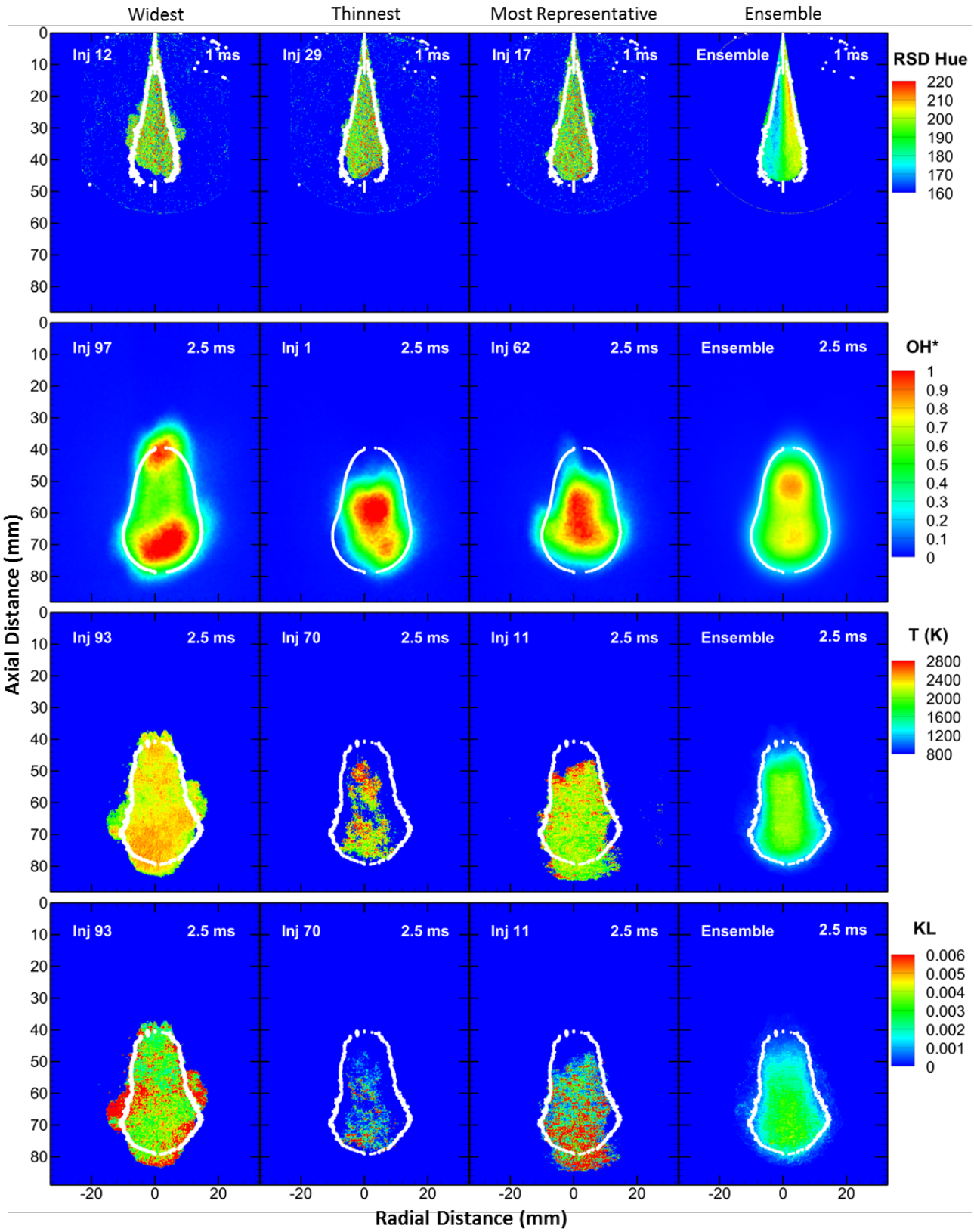

FIGURE 5. Instantaneous results for characteristic injections alongside ensemble results for RSD, OH*, and soot temperature (T) and concentration (KL) based on 2CP measurements. Specific injection numbers and time stamps label each sub-frame, with ensemble based boundaries overlaid on instantaneous results for relative comparison to classification labels at top of columns.

gest more entrainment and better mixing. This is supported by the larger OH* reaction region indicating higher overall reactivity, but is perhaps contradicted by the soot concentrations. Again, it is likely that all soot formed will be oxidized prior to end of combustion. Finally, while time histories of the results in Fig. 5 are not provided, time steps before and after those shown were investigated to determine if one or more of the instantaneous results were just a frame or so behind the others and would show similar structures a few tenths of a millisecond later. The relative differences remain clear for OH* and especially 2CP results even 0.5 ms earlier or later.

Apparent Turbulent Flame Speed

As demonstrated, the relatively repeatable global spray characteristics, such as those shown in Figs. 3 and 4, can give the impression that the local fuela-ir mixing and ignition dynamics are repeatable as well. Even amongst the RSD results in Fig. 5 there are no dramatic difference between repeated injections. However, for OH* and 2CP results in Fig. 5 it is clear local deviations from average mixing behavior exist that result in significant differences in OH* and particularly 2CP results. While the shot-to-shot variation in the lift-off length for both OH* and 2CP is significantly higher than the variation in vapor penetration, this observation does not provide insight into why these difference are occurring. The question to ask is, how do local mixing differences between different injections manifest with nominally similar global characteristics and yet have substantially different local ignition and sooting behavior?

One such parameter that can be observed at a more global scale, but that is more closely linked with local fuel-air mixing, is the turbulent flame speed. As mentioned in the introduction, incorporating this parameter into models is a challenge still being addressed in both fundamental and applied research today. By comparing relative velocities of the OH* based lift-off length at a given time step and spatial location with corresponding values from the vapor penetration profile, some interesting and meaningful results can be obtained. Figure 6 shows the vapor penetration and OH* lift-off location velocities, both calculated as the derivative of position with time, plotted versus position (top) and time (bottom).

Though it obscures the changes with time, first consider the spatial results in the top frame of Fig. 6. It is clear that the reaction front initially recesses upstream (negative velocity) towards the injector. Then the reaction front is transported downstream slightly slower than the initial vapor jet due to the reduced momentum flux after end-of-injection. Note that there is no direct measurement of local velocities and they are only derived values based on vapor penetration and lift-off results in Fig. 4. At the point where the OH* lift-off location reaches zero velocity it can be interpreted that the average turbulent flame speed along the reaction front is equal to the spray velocity at that point in time – in this case approximately 42.5 m/s as illustrated.

This analysis is most appropriate under true quasi-steady conditions; however, the bottom frame of Fig. 6 actually illustrates that this case does not in fact have a quasi-steady period. While results are not available to confirm at this time, it can be expected that a truly quasi-steady condition would result in a sustained period of zero velocity OH* (and 2CP) lift-off lengths. This can be achieved by simply having a longer injection period or shorter ignition delay in future experiments. For the results shown here, while the lift-off length certainly seems to stabilize based on Fig. 4, the calculated lift-off location velocity only momentarily crosses zero from negative to positive as the front begins to be carried downstream after end-of-injection.

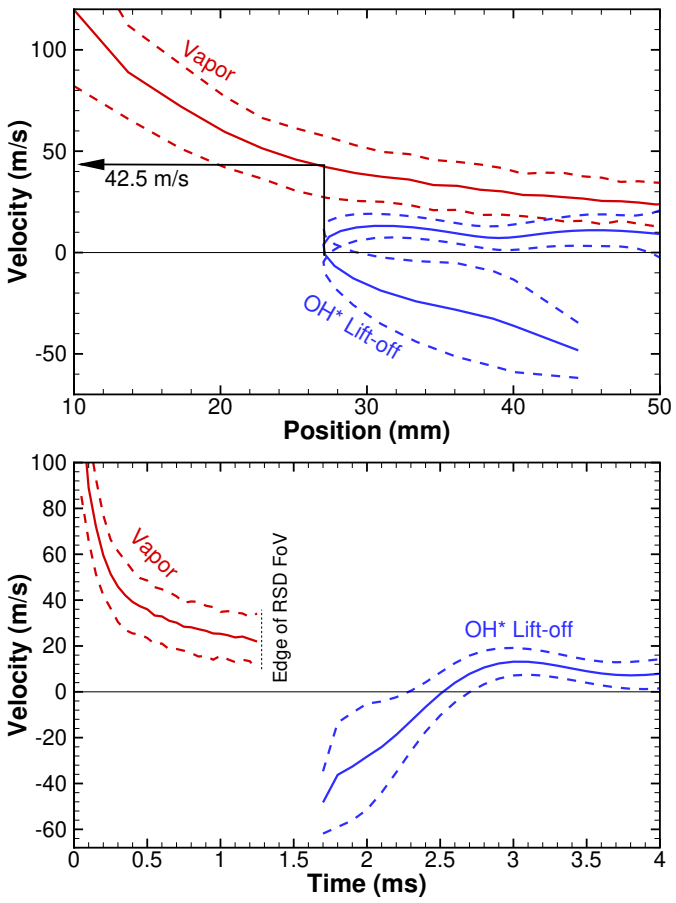

FIGURE 6. Vapor tip penetration velocity and OH* lift-off location velocity results as a function of axial distance (top) and time (bottom) indicating apparent turbulent flame speed. Minor zero-phase IIR filtering is applied to the individual injection OH* based velocities prior to averaging. All ensemble results include 95% confidence intervals, capturing individual injection variation.

Consider the variation in the OH* lift-off location velocity illustrated as confidence interval bounds in the bottom frame of Fig. 6). This large variation offers insight into how the variability in local fuel-air mixing ultimately leads to the difference in the sooting behavior. During the reaction front recession (where velocity is negative) the variability is large compared to after it begins to be transported downstream after end-of-injection. While all injections ignite within ± 0.2 ms of each other, the initial recession velocity varies from nearly 60 m/s (fast) to 10 m/s (slow). While individual lift-off location velocities are not shown, analysis shows that the 'widest' injection from Fig. 5 has a correspondingly higher apparent flame-speed and the 'most representative' and 'thinnest' have decreasing initial flame speeds. The initial flame speed correlates strongly with the subsequent size of the

reaction zone as well as with the time it takes to reach zero velocity at the minimum lift-off length. Without further study, it can only be postulated that the faster initial reactions lead to a slightly shorter lift-off length which can then lead to an overall richer reaction front. Though based on simple jet modeling, it is clear that radial averaged equivalence ratio can be expected to increases rapidly closer to the injector [17]. This gives some support to the significant differences observed.

While this discussion does not directly explain how or why the local fuel-air mixing may be different from shot-to-shot, it does indicate that the average apparent turbulent flame speed as determined in this work correlates well with local reaction and sooting behavior. Future work will explore this approach further with comparisons to local fuel-air mixing and variance results from quantified rainbow schlieren deflectometery.

SUMMARY AND CONCLUSIONS

The connection between experiments and modeling efforts in any field is a critical feedback loop, and one that evolves with advances in both areas. For models only able to capture average behaviors, it is often a challenge to perform enough experiments to ensure fully converged ensemble-averaged results. In contrast, capturing local details in a individual experiment is often possible and complex models capable of simulating these features are more and more prevalent. This introduces the new challenge for direct comparison, since subtle shot-t–shot differences are not sufficiently resolved in model configuration or experiment to precisely define initial conditions. As a result, multiple simulations or realizations based on uncertainty in initial conditions might be necessary to generate an average model prediction.

Expanding the understanding of shot-to-shot variations in high pressure diesel-like fuel sprays is a critical topic that needs exploration. This work provides a preliminary demonstration of a potential methodology for quantifying the variability between multiple injection experiments that exhibit nominally repeatable global characteristics. Bounding the shot-to-shot variation for these experiments may provide greater confidence to modeling efforts that will not require extensive parametric, multi-realization campaigns to enable a direct comparison with experimental results. Results shown in this study demonstrate that under stable ambient and fuel injection test conditions, many of the global spray characterization parameters are repeatable and values converge neatly to an ensemble behavior. In particular, ignition delay, vapor and liquid penetrations and lift-off lengths based on OH* and two-color pyrometry (2CP) all show relatively repeatable behavior when averaging individual injection results or processing the ensemble average signal. Further, the distribution is well characterized by normal distribution standard deviation statistical approaches. However, when considering individual characteristic injections, there is clear deviation from average behavior for both OH* and especially 2CP soot concentration and temperature results.

By analyzing spatial and temporal vapor jet penetration velocity and lift-off length position, it is possible to assess the apparent average turbulent flame speed for a given injection experiment. Comparison of experiments with fast or slow initial reaction front velocities to a corresponding spray contour for both OH* and 2CP results shows a distinct connection. Fast initial reaction front velocity drives a larger reaction volume and slightly shorter lift-off length. This manifests as higher apparent soot concentrations, though total emission is not clear as total soot mass quantification is not part of this work. Despite this connection it is still not clear what local fuel-air mixing differences are leading to high or low initial reaction speeds.

The methodology and observations made here may be further developed to enable more direct comparison with highly resolved spray simulations. Future work will expand the methodology to more thermodynamic conditions, fuels, and injection strategies to provide insight into the impact each may have on shot-to-shot variations. Additionally, with analysis of local fuel-air mixing and variance using RSD imaging, a more complete understanding of the spray combustion process can be observed. Complementing this work with other more detailed local measurement techniques is also desirable.

ACKNOWLEDGMENT

Funding for this work was provided by award from US Department of Energy, Office of Energy Efficiency and Renewable Energy (EERE) DE-EE0007980.

REFERENCES

[1] Bruneaux, G., 2005. "Mixing process in high pressure diesel jets by normalized laser induced exciplex fluorescence part i: Free jet". In 2005 SAE Brasil Fuels and Lubricants Meeting, SAE International, 2005-01-2100.

[2] Pickett, L. M., Manin, J., Genzale, C. L., Siebers, D. L., Musculus, M. P., and Idicheria, C. A., 2011. "Relationship between diesel fuel spray vapor penetration/dispersion and local fuel mixture fraction". *SAE International Journal of Engines, 2011-01-0686,* ***4***(1), pp. 764–799.

[3] Xue, Q., Som, S., Senecal, P. K., and Pomraning, E., 2013. "Large eddy simulation of fuel-spray under non-reacting ic engine conditions". *Atomization and Sprays,* ***23***(10), pp. 925–955.

[4] Huo, H., and Yang, V., 2017. "Large-eddy simulation of supercritical combustion: Model validation against gaseous h2–o2 injector". *Journal of Propulsion and Power,* ***33***(5), pp. 1272–1284.

[5] Engine combustion network. https://ecn.sandia.gov/diesel-spray-combustion/. Accessed: 2020-05-05.

[6] Swantek, A., Kastengren, A., Duke, D., Tilocco, Z., Sovis, N., and Powell, C. F., 2015. "Quantification of shot-to-shot variation in single hole diesel injectors". *SAE International Journal of Fuels and Lubricants, 2015-01-0936,* ***8***(1), pp. 160–166.

[7] Kolla, H., Rogerson, J. W., and Swaminathan, N., 2010. "Validation of a turbulent flame speed model across combustion regimes". *Combustion Science and Technology,* ***182***(3), pp. 284–308.

[8] Chaudhuri, S., Wu, F., Zhu, D., and Law, C. K., 2012. "Flame speed and self-similar propagation of expanding

turbulent premixed flames". *Phys. Rev. Lett.,* ***108***, Jan, p. 044503.

[9] Pomraning, E., Richards, K., and Senecal, P. K., 2014. "Modeling turbulent combustion using a rans model, detailed chemistry, and adaptive mesh refinement". In SAE 2014 World Congress and Exhibition, SAE International, 2014-01-1116.

[10] Hottel, H. C., and Broughton, F., 1932. "Determination of true temperature and total radiation from luminous gas flames". *Industrial & Engineering Chemistry Analytical Edition,* ***4***(2), pp. 166–175.

[11] Zhao, H., and Ladommatos, N., 1998. "Optical diagnostics for soot and temperature measurement in diesel engines". *Progress in Energy and Combustion Science,* ***24***(3), pp. 221–255.

[12] Reggeti, S. A., Agrawal, A. K., and Bittle, J. A., 2019. "Two-color pyrometry system to eliminate optical errors for spatially resolved measurements in flames". *Appl. Opt.,* ***58***(32), Nov, pp. 8905–8913.

[13] Wanstall, C. T., Agrawal, A. K., and Bittle, J. A., 2019. "Phase boundary detection in transient, evaporating high-pressure fuel sprays by rainbow schlieren deflectometry". *Appl. Opt.,* ***58***(25), Sep, pp. 6791–6801.

[14] Hiroyasu, H., Kadota, T., and Arai, M., 1983. "Development and use of a spray combustion modeling to predict diesel engine efficiency and pollutant emissions : Part 2 computational procedure and parametric study". *Bulletin of JSME,* ***26***(214), pp. 576–583.

[15] Karlsson, A., Magnusson, I., Balthasar, M., and Mauss, F., 1998. "Simulation of soot formation under diesel engine conditions using a detailed kinetic soot model". *SAE Transactions,* ***107***, pp. 1430–1440.

[16] Vishwanathan, G., and Reitz, R. D., 2010. "Development of a practical soot modeling approach and its application to low-temperature diesel combustion". *Combustion Science and Technology,* ***182***(8), pp. 1050–1082.

[17] Musculus, M. P., and Kattke, K., 2009. "Entrainment waves in diesel jets". *SAE International Journal of Engines, 2009-01-1355,* ***2***(1), pp. 1170–1193.

[18] Hessel, R., Reitz, R., and Musculus, M., 2019. "A visual investigation of cfd-predicted in-cylinder mechanisms that control first- and second-stage ignition in diesel jets". In WCX SAE World Congress Experience, SAE International, 2019-01-0543.

Noname manuscript No.
(will be inserted by the editor)

Quantitative concentration measurements in a turbulent helium jet using rainbow schlieren deflectometry

C. Taber Wanstall · Joshua A. Bittle · Ajay K. Agrawal

Received: date / Accepted: date

Abstract Rainbow schlieren deflectometry (RSD) is applied to acquire quantitative concentration measurements in a turbulent environment for the first time. RSD methodology is developed and validated using Rayleigh scattering data available in the literature. Experiments were performed in an initially laminar, momentum-driven helium jet injected into ambient air. Full-field measurements are acquired that span the laminar, transition, and fully turbulent regions of the jet. The RSD results are shown to provide accurate measurements in each region, and also confirm the self-similar nature of the fully turbulent jet. Analysis shows that the transition from laminar to turbulent flow occurs across an axial span that decreases with increasing Reynolds number. Experiments with a long exposure time were conducted to evaluate the limitations of hardware averaging of the RSD signal in comparison to software averaging.

Keywords Rainbow Schlieren Deflectometry · Turbulent Mixing Measurements · Optical Diagnostics

1 Introduction

Turbulent jets have been the subject of interest from the time of Prandtl's mixing length theory [28] to recent efforts in understanding the entrainment mechanisms along the shear layer [21,36]. Canonical systems, such as binary mixing in an axisymmetric turbulent jet, offer insight into the underlying mixing phenomena without the practical complexities, e.g., the subsequent combustion processes in diesel or gas turbine engines. Several studies of turbulent binary gas jet mixing have been reported in the literature to provide detailed scalar measurements using intrusive techniques (hot-wire anemometry, interference probes, etc.) and non-intrusive optical techniques such as laser induced fluorescence (LIF) and Rayleigh scattering.

Papanicolaou and List [22] obtained a comprehensive set of velocity and concentration measurements in buoyant jets using laser Doppler anemometry and LIF. Dowling and coworkers [11,13,12] used Rayleigh scattering to show that the constant density axisymmetric jets exhibit the self-similar behavior in the fully turbulent region. Pitts *et al.* [25,26,29,27] also used Rayleigh scattering to demonstrate self-similarity in variable density jets. They concluded that the variable density jets reach an asymptotic scaling state regardless of the initial conditions contingent on a fully developed, momentum driven regime. Westerweel *et al.* [38,39] used planar laser induced fluorescence (PLIF) and particle image velocimetry (PIV) to show that the entrainment at the turbulent/non-turbulent interface is dominated by a partially viscous process attributed to irregular small-scale eddy motions, and not to large scale engulfment. More recent PIV/PLIF measurements have been used to evaluate the roles of large scale engulfment versus small scale local entrainment at the interface and have confirmed power-law scaling for the entrained velocity [21].

Path integrated techniques such as interferometry and schlieren deflectometry have also been used in conjunction with a deconvolution procedure to obtain the local scalar measurements in turbulent jets. Watt and coworkers [37,24] applied interferometry coupled with

F. Author
first address
Tel.: +123-45-678910
Fax: +123-45-678910
E-mail: fauthor@example.com

S. Author
second address

computed tomography to obtain the 3-D density field in a turbulent helium jet. Davis [8–10] implemented a single beam laser schlieren system to measure the fluctuation intensity along the shear layer in subsonic and supersonic turbulent jets. Ko and Kihm developed an algebraic tomographic reconstruction technique combined with speckle photography to reconstruct the density field in asymmetric helium jets [15]. Kolhe and Agrawal [17] developed a spectral analysis algorithm and applied it to synthetic deflectometric data to provide local scalar statistics in turbulent flows applicable to any deflectometric line of sight diagnostic, e.g., rainbow schlieren deflectometry (RSD). Schlieren-interferometric systems have also been incorporated in other turbulent flow applications to study vortex shedding behind circular and square cylinders [30].

In the past 25 years, RSD has been used extensively for measurements in laminar flows [3,4,23,40,2, 32]. However, so far RSD has not been validated for quantitative mixing measurements in turbulent flows. Thus, the objective of this study is twofold: 1) validate quantitative RSD for scalar measurements in a turbulent helium jet, and 2) gain insight into the jet mixing behavior including the transition region. This study is an important step towards enabling the use of quantitative RSD for advanced applications such as fuel-air mixing in diesel sprays [34,35]. The study is divided into five sections. First, the experimental details are provided. Next, the theory to apply RSD in a turbulent flow field is developed, followed by the data acquisition and post processing details. Then, RSD results are compared with Rayleigh scattering from Ref. [31], and other supplementary measurements are presented. Lastly, the key findings from this study are summarized.

2 Experimental Setup

Figure 1 illustrates schematic of the test setup and RSD system used in this study. Pressure regulated bottled helium filtered with a 30 µm mesh filter passes through a 200 µm choking orifice to avoid flow oscillations. A GM3 Dakota flow meter measures the mass flow rate to calculate the bulk jet velocity at the tube exit ($\dot{m} = \rho AV$). A ball valve downstream of the flow meter controls the helium supply to the experiment. Once the valve is opened, helium discharges vertically upward into quiescent ambient air at room temperature/pressure conditions through a stainless steel tube with an inner diameter (d), outer diameter (d_o), and length (l) of 4.6 mm, 6.35 mm, and 44d, respectively (chosen to match the dimension from Ref. [31]). The tube is translated by a traverse to vary the field of view (FOV) of the jet flow with respect to the stationary RSD system. Note that Ref. [31] has reported a negligible co-flow, which is not replicated in this work.

Figure 1 also shows the RSD system used in this study. RSD system was optimized following recommendations by Agrawal and Wanstall [3]. An Energetiq EQ-99X continuous laser driven light source emits high intensity broadband light through a 100 µm fiber optic that terminates at a 30 µm wide, 3 mm high rectangular aperture. The emerging light is collimated by a 250 mm focal length 76 mm diameter achromatic doublet lens. Upon collimation, light rays propagate through the test media and refract according to the local density gradients. The refracted light rays are color encoded by a 0.6 mm wide asymmetric rainbow filter mounted on a two-stage traverse. The two stages consist of a motorized stage (ThorLabs KDC101) in the transverse direction to automate calibration and a manual stage in the axial direction to precisely locate the filter at the focal plane of the decollimating lens. A Photron SA5 color camera outfitted with a 50 mm focal length Nikon Nikkor lens (spatial resolution of 100 $^{\mu m}/_{px}$) acquires the color images. RSD images are acquired at sampling rate of 250 Hz for sample duration of 20 s and at an exposure time of 14 µs. This exposure time is the system's lowest reliable exposure time that provides accurate hue measurements.

Table 1 provides the flow conditions for the two test cases performed at room temperature/pressure conditions. The subscript 'o' is used for the helium nozzle exit conditions. Chen and Rodi [7] introduced the non-dimensional axial coordinate, z_{Fr} in Eq. 1 to demarcate the flow regimes.

$$z_{Fr} = Fr^{-1/2}\left(\frac{\rho_\infty}{\rho_0}\right)^{\frac{1}{4}}\frac{z}{d}, \quad Fr = \frac{\rho_0 u_0^2}{gd(\rho_\infty - \rho_0)} \tag{1}$$

where Fr is the Froude number and $\frac{\rho_\infty}{\rho_0}$ is the density ratio. The z/d is the non-dimensional distance downstream. In this study, the maximum downstream location of data collection for each experiment is labeled as z/d_{max}. For $z_{Fr} < 1$, the flow is momentum dominated, buoyancy effects are negligible, and the resulting turbulent flow follows similarity scaling. For $1 < z_{Fr} < 5$, the flow is transitional with both buoyancy and momentum effects present [22]. For $z_{Fr} > 5$, plume-like, buoyant behavior pertains. As shown in Table 1, the $Re_0 = 800$ case includes both buoyant and momentum driven regimes, whereas the $Re_0 = 2500$ case is momentum dominated.

3 Mathematical Background

In this study, RSD is configured to measure the transverse deflection angle of light rays (θ_x) related to the

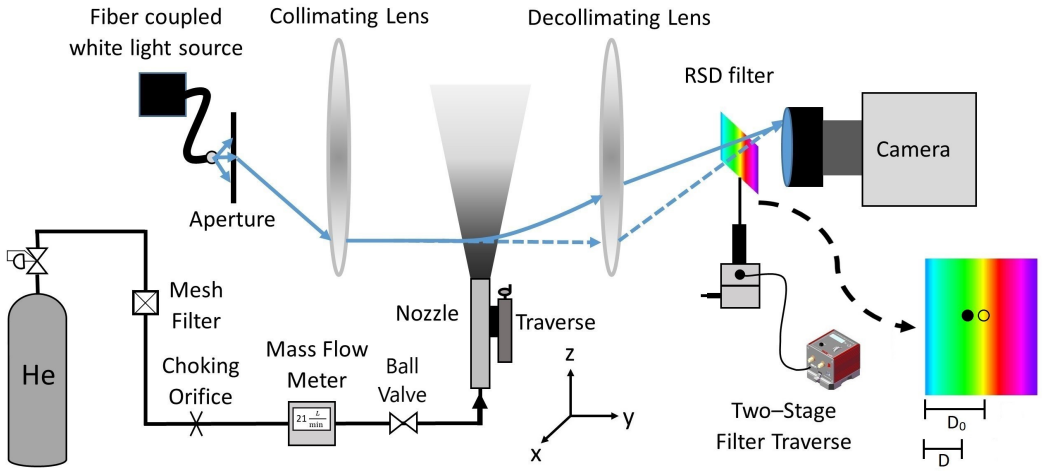

Fig. 1: Schematic of the experimental setup and RSD system.

Table 1: Helium jet flow conditions.

$\dot{V}$ (L/min)	u_0 (m/s)	Re_0	$z_{Fr,max}$	z/d_{max}
21.7	21.7	800	1.31	32
66.5	66.5	2500	0.27	20

normalized refractive index difference (η) according to Eq. 2,

$$\theta_x(x,z,t) = \int_{-\infty}^{\infty} \frac{\partial \eta}{\partial x}\Big|_{x,y,z,t} dy, \quad \eta = \frac{n}{n_0} - 1 \tag{2}$$

where n is the local refractive index and n_0 is the refractive index of the surrounding media [3]. In a turbulent flow, Eq. 2 can be rewritten as Eq. 3 where the overbar and apostrophe represent the mean and fluctuating components, respectively.

$$\overline{\theta_x}(x,z,t)+\theta_x'(x,z,t) = \int_{-\infty}^{\infty} \left(\frac{\partial \overline{\eta}}{\partial x}\Big|_{x,y,z,t} + \frac{\partial \eta'}{\partial x}\Big|_{x,y,z,t} \right) dy \tag{3}$$

For statistically stationary processes, the average of the fluctuating components is zero [19], and thus the average deflection angle field is related to the average refractive index field as developed in Eq. 4.

$$\lim_{T\to\infty} \frac{1}{T} \int_0^T \theta_x(x,z)dt = \overline{\theta}_x(x,z) \tag{4a}$$

$$\lim_{T\to\infty} \frac{1}{T} \int_0^T \int_{-\infty}^{\infty} \frac{\partial \eta}{\partial x}\Big|_{x,y,z} dy dt = \int_{-\infty}^{\infty} \frac{\partial \overline{\eta}}{\partial x}\Big|_{x,y,z} dy \tag{4b}$$

$$\overline{\theta}_x(x,z) = \int_{-\infty}^{\infty} \frac{\partial \overline{\eta}}{\partial x}\Big|_{x,y,z} dy. \tag{4c}$$

Note that the limits of integration remain the same as when swapping the integration order in Eq. 4b.

For a circular jet, the time-averaged turbulent flow is axisymmetric, and thus, Abel transform [5] can be used to invert Eq. 4c to determine the planar refractive index difference field. In this study, the discretized two-point formula to minimize inversion errors in deflectometric measurements given by Eq. 5 is used [16].

$$\overline{\eta}(r_i,t) = \sum_{j=i}^{N+1} D_{ij} \overline{\theta}_x(x_j,t) \tag{5}$$

Thus, the normalized refractive index difference at a point can be expressed as weighted linear combination of the measured total deflection angles along the radial direction.

For ideal gas mixtures, the refractive index is related to thermodynamic properties using Eq. 6,

$$n - 1 = \frac{P}{R_u T} \sum_i M_i \kappa_i x_i \tag{6}$$

where n, P, R_u, T, M, κ, and x are the refractive index, pressure, universal gas constant, temperature, molecular weight, Gladstone-Dale constant, and mole fraction, respectively, and the subscript 'i' refers to each species in the mixture. The Gladstone-Dale constants and refractive index for helium and air are $\kappa_{he} = 1.96 \times 10^{-4}$ $\frac{m^3}{kg}$ and $\kappa_{air} = 2.27 \times 10^{-4}$ $\frac{m^3}{kg}$ and $n_{he} = 1 + 3.6 \times 10^{-5}$ and $n_{air} = 1 + 3 \times 10^{-4}$, respectively. Figure 2 shows the refractive index versus helium mole fraction given by Eq. 6. Because of the linear relationship, the data in Fig. 2 can be used to determine the average helium mole fraction from the average refractive index difference. In summary, the average deflection angle in an axisymmetric turbulent jet can be converted to the average helium mole fraction as long as the process is statistically stationary.

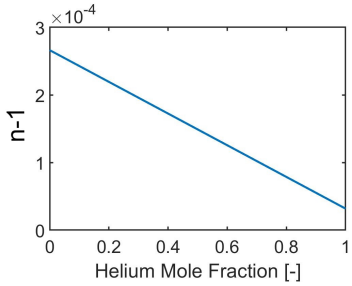

Fig. 2: Refractive index of a helium-air mixture versus helium mole fraction.

4 Data Analysis

4.1 Rainbow Filter

In the present system, RSD uses a rainbow filter to measure the ray deflection angle in the transverse direction (x). The rainbow filter, shown in Fig. 1, is a transparent slide with color gradations to color-code the deflected light rays depending upon the transverse distance (D) on the filter plane. For small deflections, the deflection angle can be calculated from Eq. 7 [33],

$$\theta = \frac{D - D_0}{f} \tag{7}$$

where f is the focal length of the decollimating lens and D_0 is the reference location or distance on the filter plane without ray deflection (see Fig. 1). The error introduced by the small angle approximation for the maximum deflections observed in this study are much less than 1%. Colors in the RSD image provide a quantitative measure of the numerator in Eq. 7, and hence, the ray deflection angle at every time and every pixel location in the FOV.

RSD uses a single parameter, hue (H), to quantify color from the three raw acquired signals Red (R), Green (G) and Blue (B) or RGB acquired by a color camera [14]. However, a filter calibration is required to establish the mapping between the hue in the RSD image and the transverse location on the filter plane. Filter calibration is achieved in the absence of the test media by recording image(s) at each filter location to correlate the background image hue and the transverse location of the filter. Two calibration procedures are possible: an average and a local or pixel-by-pixel calibration. The former computes one calibration curve representative of the average hue in a window of pixels in the FOV, while the latter provides a calibration curve for every pixel in the FOV. The average calibration is easy to implement, albeit at the expense of accuracy and greater uncertainty. In this study, high fidelity measurements are obtained by using a pixel-to-pixel calibration.

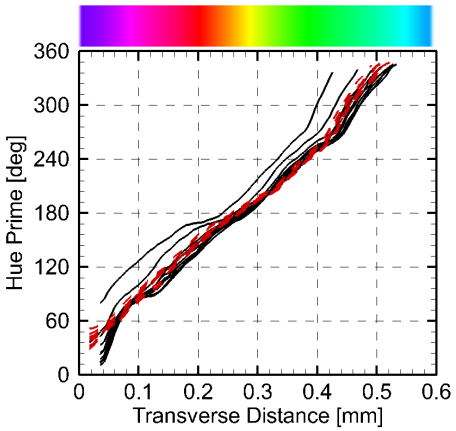

Fig. 3: Hue-to-distance calibration curves at several pixel locations are shown. The solid-black, and red-dashed lines represent horizontal locations along the middle of the FOV image and vertically along the centerline of the image, respectively. The hue prime filter is illustrated above the graph.

The calibration process begins with establishing the appropriate parameters (framing rate, exposure time, etc.) for the experiment. Then, the filter is traversed in small increments (U_X) to acquire the background RSD images. For high accuracy, the step size should be approximately the print resolution of the filter to minimize hue interpolation errors between the filter's printed pixels. In this study, the step size is $Ux = 6\mu m$ - slightly above the print resolution of 4 μm. The filter calibration process is automated with a precision motorized traverse to accommodate such small steps. In this experiment, 25 images were recorded at each location to achieve a converged hue stability of less than 0.5° of variation within the FOV.

The typical hue range is 0 to 2π (0 to 360°) with the filter centered at π (cyan). In this study, the hue varies from $-2\pi/3$ to $10\pi/9$ centered at $2\pi/9$ or 40°. This unorthodox approach is motivated by the high absorptivity of the filter in the dark blue region ($200° - 240°$) that limited the exposure time. Thus, this region was excluded by transforming the hue into hue prime, H', using Eq. 8

$$H' = \begin{cases} H + \frac{10\pi}{9}, & \text{if } H \leq \frac{8\pi}{9} \\ H + \frac{10\pi}{9} - 2\pi, & \text{otherwise} \end{cases} \tag{8}$$

This transformation ensures the continuity of H' at the $0/2\pi$ location. To the author's knowledge, this is the first time a rotated hue coordinate system has been used to overcome the filter linearity issues in RSD applications. Figure 3 shows an image of the hue prime filter and calibration curves at multiple pixel locations. The

solid black curves represent pixels at various radial locations along the dashed region in Fig. 4, whereas the red-dashed curves represent different pixels along the centerline of the image. Both radial and axial variations in the calibration curves arise because of minor optical aberrations, printing imperfections, and pixel variations across the camera sensor. Figure 3 also shows that even though the filter is linearly prescribed, slight nonlinearities manifest from the aforementioned effects. Figure 3 shows that an average calibration curve would introduce unwarranted errors. Thus, a pixel-by-pixel calibration process is highly recommended for turbulent flow applications.

4.2 Uncertainty Analysis

In RSD, hue or hue prime is the primary measurement. In this work, uncertainty propagation begins with uncertainty in hue prime ($U_{H'}$). Note that $U_{H'}$ only contains precision uncertainty caused from fluctuations in the light source, camera, etc. The pixel-by-pixel calibration process provides a new reference for each color effectively driving bias uncertainty from the camera to zero. If an average calibration procedure is implemented, bias uncertainty is not zero and must be included. It is possible to have an uncertainty component from the translation slide; however, the stepper motor used in this study has an uncertainty of $\pm 0.1\,\mu$m which corresponds to approximately 0.05° which is significantly smaller than the precision uncertainty in hue. Equations 9a-9f show all sources of uncertainty considered in this study.

In Eq. 9a, the precision uncertainty at each pixel location is determined from the standard deviation, σ_{cal}, of H' in the 25 background images. Therefore, σ_{cal} is a function of transverse filter location and pixel location in the background image. The degrees of freedom for σ_{cal} is reduced by considering the average transverse deflection distance across the filter at each location in the image during the experiment to provide a unique σ_{cal} for each pixel in the background image. This procedure is performed for all uncertainty variables that are functions of both pixel location and transverse deflection distance, e.g., σ_Θ and $\frac{dD}{dH'}$. The uncertainty in H' ranges from 0.2° to 1.2°.

Equation 9b propagates uncertainty from H' to transverse deflection distance, U_D. A central difference method is used to determine $\frac{dD}{dH'}$ for each pixel in the image. The local derivative corresponding to the average deflection distance during the experiment is used for each pixel. Next, Eq. 9d calculates uncertainty in deflection angle by considering the bias uncertainty from the calibration curve and the lens focal length ($U_f = \pm 2.5\,$mm) (Eq. 9c, and the precision uncertainty from the 5000 images acquired in the experiment. Uncertainty propagation to the refractive index difference is given by Eq. 9e. Note that the Abel inversion causes uncertainty in the center to be the highest. Lastly, Eq. 9f gives the uncertainty in the helium mole fraction. The results from the uncertainty analysis are shown later in Fig. 9.

$$U_{H'} = t\frac{\sigma_{cal}}{\sqrt{N_{I,cal}-1}} \tag{9a}$$

$$U_D = \frac{dD}{dH'}U_{H'} \tag{9b}$$

$$B_\Theta = \sqrt{\left(\frac{U_D}{f}\right)^2 + \left(\frac{D}{f^2}U_f\right)^2} \tag{9c}$$

$$U_\Theta = \sqrt{B_\Theta^2 + P_\Theta^2}, \quad P_\Theta = t\frac{\sigma_\theta}{\sqrt{N_{I,exp}}} \tag{9d}$$

$$U_{\eta i} = \sqrt{\sum_{j=i}^{N}(D_{ij}\cdot U_{\Theta j})^2}, \quad U_\eta = \frac{U_n}{n_0} \tag{9e}$$

$$U_{Xhe} = \frac{U_n}{\frac{P}{RT}(M_{he}\kappa_{he} - M_{air}\kappa_{air})} \tag{9f}$$

5 Results

5.1 Raw RSD Image Analysis

Figure 4 shows instantaneous RSD images for the two test cases stitched together from multiple FOVs; Fig. 4a for $Re_0 = 800$ and Fig. 4b for $Re_0 = 2500$. The black dashed line in the images signifies the middle of each FOV. The yellow color (hue=$\pi/3$) in the background, also observed throughout the center of the jet, corresponds to undeflected light rays, whereas deviations from the background hue indicate ray deflections by the test media. For example, red and green colors indicate large deflections caused by the sharp density gradients in the shear layer of the jet flow. For both cases, the RSD images clearly show the laminar, transition, and fully turbulent regimes. Helium emerges as a laminar jet and then, the turbulent structures in the shear layer lead to breakdown in both cases. For $Re_0 = 800$, the jet flow is laminar for approximately z = 0d to 10d and transitional for z = 10d to 13d. In contrast, for $Re_0 = 2500$, the laminar and transition regions are much shorter, z = 0d to 1d and z = 1d to 2d, respectively. After transition, turbulence engulfs the jet at z = 13d for $Re_0 = 800$ and z = 2d for $Re_0 = 2500$. The RSD images also show stark differences in the sizes of the turbulent structures. The higher Reynolds number case contains much finer structures indicating a higher

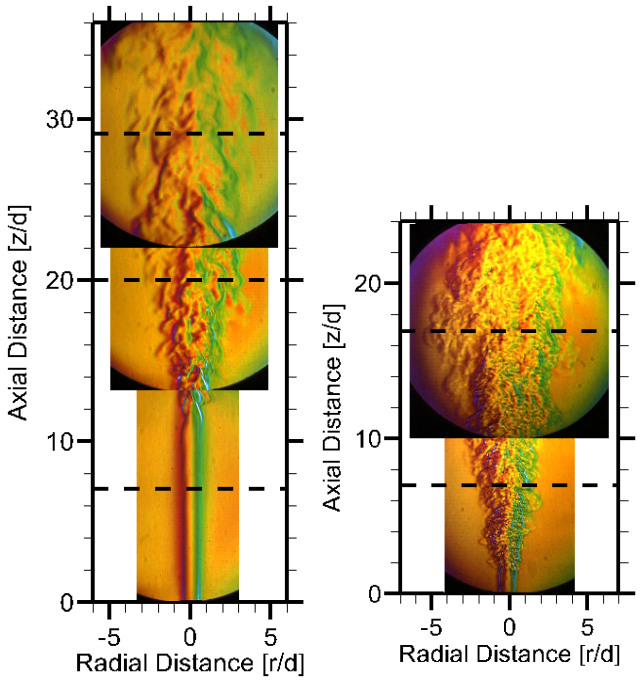

(a) (b)

Fig. 4: Instantaneous RSD images stitched together from multiple FOVs are shown for (a) $Re_0 = 800$ and (b) $Re_0 = 2500$. The black dashed line represents the middle of each FOV.

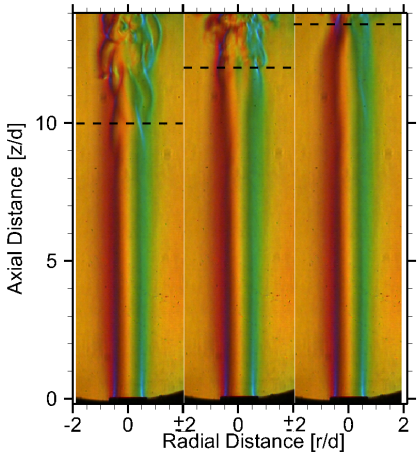

Fig. 5: Selected instantaneous RSD images showing the unsteady transition location for $Re_0 = 800$.

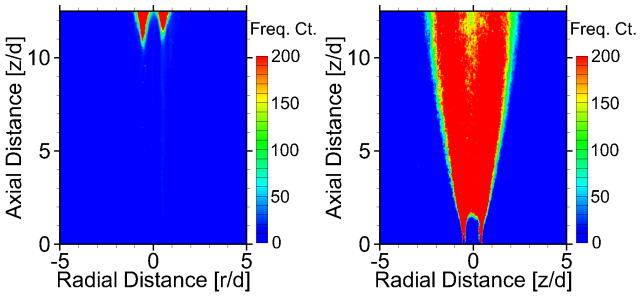

(a) (b)

Fig. 6: Frequency count of hue fluctuation via FFT analysis is shown for (a) $Re = 800$ and (b) $Re = 2500$.

turbulent intensity. Another important contrast illustrated in Fig. 4 is the diffusion of helium in the radial direction. At z=20d, the jet width for $Re_0 = 800$ is 6d and about 8d for $Re_0 = 2500$. In summary, the raw RSD images are useful to identify many distinct features of the jet, and illustrate the ability to acquire images of the turbulent structures at high temporal and spatial resolutions (discussed further in Section 5.2).

The transition region for $Re_0 = 800$ is further analyzed in Fig. 5 showing three different snapshots during the experiment. Figure. 5 illustrates that the transition location varies approximately by 3.5d even though the helium flow rate is nominally constant during the experiment.

Next, the flow regimes are analyzed using a fast Fourier transform (FFT) of hue fluctuations during the experiment. Figure 6 shows the results of the FFT analysis for both cases in terms of a contour plot of the count of frequency components with a detectable signal intensity. In the laminar region, the hue at a pixel is constant (with time), and thus, no frequencies are observed in the contour plot (blue color). In contrast, a higher frequency count indicates the shear layer instabilities (green/yellow color). Once coherent structures overtake the jet, a large continuous frequency count, indicated by the red color, is observed. Thus, Fig. 6 provides a quantitative spatial map of laminar, transition, and turbulent regimes in the jet. In both cases, the mixing layer outlines a wedge shaped potential core - an unmixed region of jet fluid - commonly observed in turbulent plane jets [1]. The wedge begins at the location where the jet starts to diverge. For $Re_0 = 800$, this process begins at around z=10.5d and by z=12.5d the potential core is completely consumed. For $Re_0 = 2500$, the wedge begins at z=1d and end around z=1.5d. Figure 6b shows a reduction in hue fluctuations downstream, suggesting a dissipation of the turbulent intensity.

5.2 Quantitative RSD Image Analysis

Figure 7 shows the contour plots of instantaneous and average deflection angle data for $Re_0 = 2500$. The instantaneous contour shown in Fig. 7a displays larger deflection angles magnitudes than its average counterpart in Fig. 7b. Local eddies create large density gra-

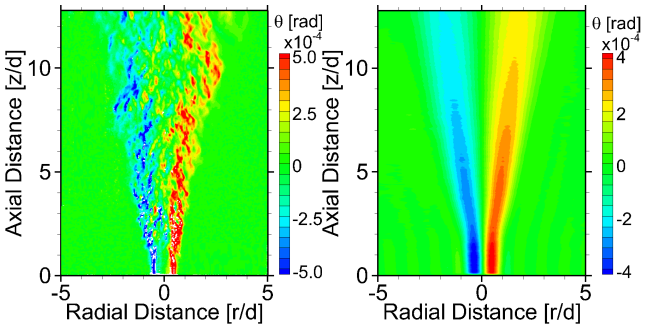

(a) (b)

Fig. 7: Instantaneous (a) and average (b) deflection angle contours for $Re_0 = 2500$.

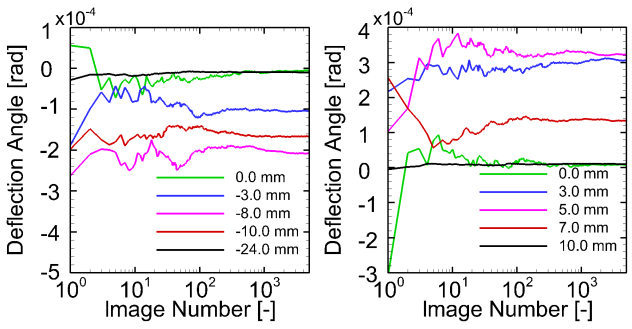

(a) (b)

Fig. 8: Average deflection angle versus number of images for (a) $Re_0 = 800$ and (b) $Re_0 = 2500$. The five different radial locations, indicated in the legend, are at z=20 d for $Re_0 = 800$ and at z=5 d for $Re_0 = 2500$.

dients leading to local regions of large deflections that could exceed the filter range. Figure 7a reveals small eddies of opposite magnitudes in close proximity, e.g., at Z/d=3.25 and r/d=-0.5. Note that the smallest dissipative structures for this case are approximately 200 μm given Eq. 10. [6].

$$\lambda_D = \Lambda \delta Re_\delta^{-3/4} Sc^{-1/2} \tag{10}$$

Here, Λ, $Re_\delta = u_c\delta/\nu_\infty$, and Sc are a mixing layer thickness constant, the outer-scale Reynolds number, and Schmidt number (0.2) respectively. The mean jet centerline velocity (u_c) and the full width of the mean axial velocity profile at 5% (δ) are estimated using the scalings given for pure jets in Chen and Rodi [7] and provided in Eq. 11.

$$u_c = 6.2u_0 \frac{\rho_0}{\rho_\infty}\frac{d}{x}, \qquad \delta = 0.36x \tag{11}$$

Buch and Dahm [6] found the mixing layer thickness constant to vary between 5.6 and 16.8 with a mean of 11.2 (used in this study). The 10px/mm sampling frequency (spatial resolution) used in this study is twice of that for the smallest dissipative eddies (5px/mm). Thus, the Nyquist criterion is satisfied and the instantaneous images are spatially resolved. Figure 7b illustrates that symmetry develops after the averaging process.

Figure 8 plots the average deflection angle versus number of images for both cases to establish statistically stationary flow, which is necessary to apply Eqs. 4a-4c. The $Re_0 = 800$ and $Re_0 = 2500$ cases show the convergence of the deflection angles on the negative (left side of the jet) and positive (right side of the jet) side as the number of images is increased. Plots are shown at multiple radial locations, center (green line), inner shear layer (blue line), middle of the shear layer (orange line), outer shear layer (red line), and the farfield (black line), at z=20d for $Re_0 = 800$ and z=5d for $Re_0 = 2500$. Figure 8 highlights that most fluctuations ($\pm 1 \times 10^-5$) average out for 1000 images for both cases, while the minor fluctuations ($\pm 4 \times 10^-6$) diminish with 3000 images for $Re_0 = 800$ and 4000 images for $Re_0 = 2500$.

Figure 9a shows the radial profile of the average deflection angle and its uncertainty at z=20d for $Re_0 = 800$. The profile exhibits a high level of symmetry, with minor asymmetry likely caused by slight jet tube misalignment and/or ambient flow field circulation. The uncertainty is lowest at the edges where variation is minimal and highest in the shear layer around r=10 mm. Figure 9a shows the corresponding radial profile of the refractive index difference obtained using Eq. 5, independently for each side of the jet. Thus, any asymmetry will manifests itself by a discontinuity at the center. Figure 9a demonstrates symmetric profile of refractive index difference on each side, and only a minor discontinuity at the center. The slight asymmetry can be mitigated by mirroring and averaging the two refractive index difference profiles.

The final result in Fig. 9b shows that the helium mole fraction at the center is 0.54 and it reaches a value of zero at approximately r=20 mm. Figure 9 shows that the uncertainty in both normalized refractive difference and mole fraction is highest at the center. In this study, an uncertainty of less than 1% full scale of hue propagates to an uncertainty of about 3.5% full scale of helium mole fraction. Figure 9b also shows the helium mole fraction profiles for ±10% higher and lower helium flow rates than the nominal flow rate. The ±10% profiles are selected to address possible discrepancies in the helium flow rate measurements between this study and Ref. [31] - where uncertainty in the flow system is not provided. Results show that the measurement uncertainties are far less than those resulting from ±10% change in the flow velocity at the inlet.

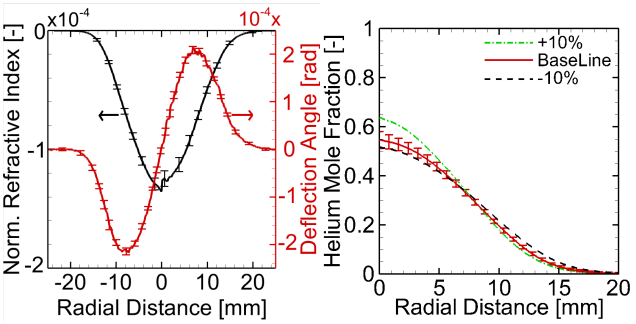

(a) (b)

Fig. 9: Radial profiles of (a) average deflection angle and refractive index difference at z=20d for $Re = 800$, and (b) helium mole fraction at z=20d for $Re_0 = 800$. The uncertainty is shown by the error bars.

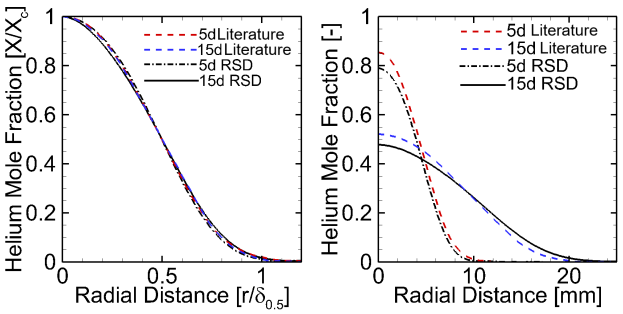

(a) (b)

Fig. 10: (a) Non-dimensional and (b) absolute helium mole fraction from RSD (black lines) and Ref. [31] (colored lines) for $Re_0 = 2500$.

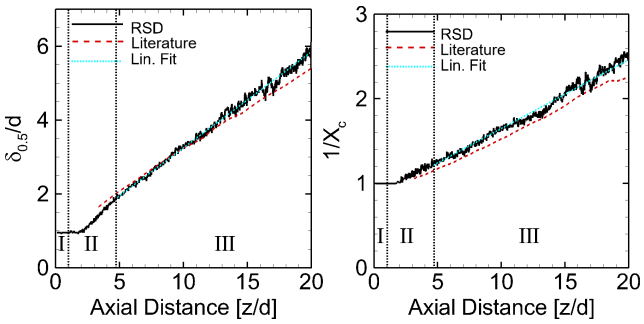

(a) (b)

Fig. 11: (a) Full width at half maximum and (b) centerline helium mole fraction profiles for $Re_0 = 2500$ for RSD (solid black) and Ref. [31] (red dashed).

5.3 Validation with Published Data

Figure 10 compares the radial profiles of mean helium mole fraction for $Re_0 = 2500$ at z= 5d and 15d obtained by RSD in this work and Rayleigh scattering in Ref. [31]. In Fig. 10a, the mole fraction is normalized by the mole fraction at the center (X_c) and the radial distance is normalized by the jet full width at half maximum concentration ($\delta_{0.5}$). This normalization scheme provides self-similarity for the concentration field in momentum dominated ($z_{Fr} < 1$) turbulent free jets [29]. Figure 10a shows good agreement between between the two studies, demonstrating the validity of RSD to provide accurate concentration measurements in a turbulent flow field. The self-similarity observed in Fig. 10a shows that variations in the initial conditions, due to minor experimental differences, do not affect the results. Helium mole fraction profiles in Fig. 10b shows only minor discrepancies likely caused by small differences in initial jet velocity, tube thickness, and/or minor co-flow.

The normalizing parameters,$\delta_{0.5}$ and X_c, across the full-field provide further insight into the jet behavior. These parameters reveal if self-similarity is satisfied by checking the two main assumptions: 1) the constant entrainment hypothesis, and 2) centerline decay is inversely proportional to z [13]. Furthermore, the two parameters show the effect of experimental differences on the jet, e.g., occurrence of jet transition. Both $\delta_{0.5}$ and X_c give context to the radial comparison plots previously shown.

Figure 11 shown axial profiles of $\delta_{0.5}$ and X_c for $Re_0 = 2500$. Three different momentum dominated regions ($z_{Fr} < 1$) are outlined in both plots. Region I indicates the laminar portion of the jet. Although the jet growth rate and centerline decay are constant until about z=2d,the potential core start to diminish at z=1d (see Fig. 6b) - demonstrating that Fig. 11 is not sufficient by itself to identify the end of the laminar region. Region II is the developing turbulent region, where instabilities set in to initiate turbulent mixing. This region shows a slight non-linear behavior in both jet spreading and centerline decay. Beyond z=4.75d, Region III shows a constant entrainment and centerline decay given by a linear fit (blue-dashed line) with an R^2 value of 0.994 and 0.987 for $\delta_{0.5}/d$ and X_c, respectively. The high degree of linearity shows that self-similarity is achieved in Region III, which would also explain the excellent agreement reached between the profiles in Fig. 10a. A linear spreading rate is observed for data from both studies in Region III (Fig. 11a), where the slope from RSD is slightly greater than Ref. [31]. Kwon and Seo [18] showed that an increase in Reynolds number decreases the jet spreading rate for Reynolds numbers greater than 1300. Thus, it is likely that the jet inlet velocity in Ref. [31] was slightly higher than

reported, owing to the uncertainties in the flow measurements.

Next, the normalized and absolute profiles for $Re_0 = 800$ obtained by RSD and Rayleigh scattering [31] are compared in Fig. 12 at z=9d, 20d, and 30d. In this study, z=9d is within the laminar region, and hence, the RSD profile does not follow similarity in Fig. 12a. Conversely, in Ref. [31], the z=9d profile straddles in the transition region, and therefore, shows a centerline mole fraction of less than 1 in Fig. 12b. In spite of these difference, caused by un-quantified minor variations in the inlet conditions from Ref. [31], the two profiles agree with each other for r>3 mm including at the edge of the jet ($r \approx 5$) with sharp gradients. At z=20d, the jet approaches self-similar behavior in Fig. 12a and mostly agrees except at the outer radial positions indicating that the 20d location is still slightly influenced by initial conditions either because the jet is not fully turbulent or because of the minor buoyancy effects ($z_{Fr} = 0.82$). Even the absolute comparison in Fig. 12b for the 20d location shows minor differences which are less than the ±10% velocity discrepancies shown in Fig. 9b. The agreement at z=30d in Fig. 12a is much better indicating negligible influence of experimental discrepancies at this downstream location.

Figure 13 compares $\delta_{0.5}$ and X_c for $Re_0 = 800$ from RSD and Ref. [31]. Region I is the laminar region until z=10.25d (also found in Fig. 6a), Region II is the developing turbulent regime until approximately z=16.2d, Region III is momentum-dominated regime given by a linear fit with an R^2 of 0.990 and 0.983 for $\delta_{0.5}$ and X_c, respectively, from z=16.2d to z=25d, lastly, Region IV governed by combined buoyancy-momentum effects starting at z=25d, where $z_{Fr} = 1$. Profiles in Fig. 13 agree in Region I although Ref. [31] shows an earlier transition. Region III shows similar centerline values but slightly different jet spreading rates. Region IV shows similar slopes in both spreading rate and centerline decay indicating negligible effects of initial experimental conditions at these downstream locations. In both cases, RSD shows full-field spatially resolved data beginning near the tube exit (z>0.1d) to either z=20d ($Re_0 = 2500$) or z=32d ($Re_0 = 800$).

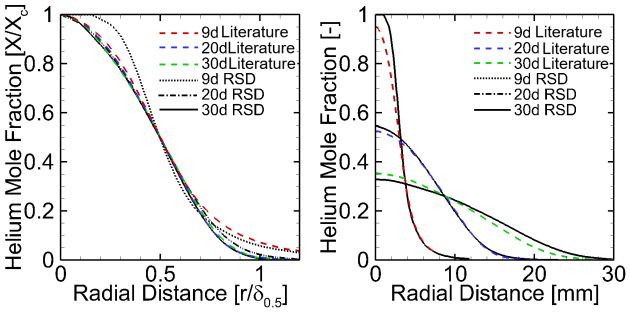

(a) (b)

Fig. 12: (a) Non-dimensional and (b) absolute helium mole fraction from RSD (black lines) and Ref. [31] (colored lines) for $Re_0 = 800$.

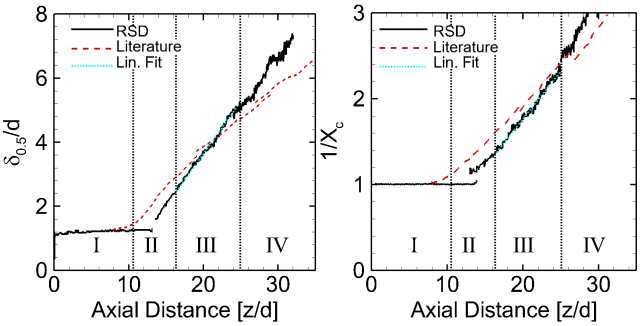

(a) (b)

Fig. 13: (a) Full width at half maximum and (b) centerline helium mole fraction profiles for $Re_0 = 800$ for RSD (solid black) and Ref. [31] (red dashed).

5.4 Full Field Measurements

The RSD technique is extended to quantify the average helium mole fraction across the whole field by stitching together multiple FOVs for both test cases. For $Re_0 = 800$, the jet undergoes slight spreading near the exit, but the mole fraction remains nominally constant until about z=12.5d where the jet width increases suddenly in the transition region. For $Re_0 = 2500$, Fig. 14b shows that the jet spreads at z=1.5d and farther downstream, and the results for each FOV match seamlessly.

Next, radial profiles of helium mole fraction are presented at various flow regimes as useful validation data for computational models and to gain insight into the physical mechanisms of the jet. Five locations for each test case are shown in Fig. 15: tube exit, pre-transition and transition locations, a turbulent location, and at the end of the FOV. In the near field and before transition, self-similarity does not hold, thus experimental data in these regions will be useful to validate the computational models. Both cases show broadening of the jet and decreasing helium mole fraction at the center. Thereafter, a large change occurs in a relatively small axial distance across the transition region. This effect is amplified at the higher Reynolds number, whereby the jet evolves from a potential core with a radius about 0.75 mm to the centerline mole fraction value of 0.9 in just 0.5d as seen in Fig. 14b.

One effect present in the $Re_0 = 2500$ that is not present in $Re_0 = 800$ is the inflection at the two transi-

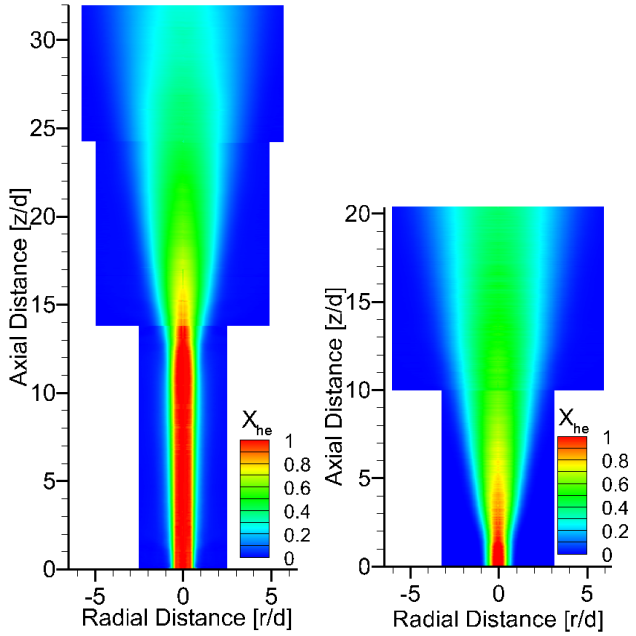

Fig. 14: Full field helium mole fraction for (a) $Re_0 = 800$ (b) and $Re_0 = 2500$.

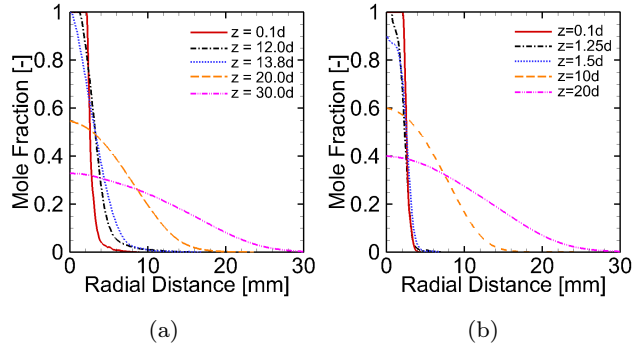

Fig. 15: Radial profiles of helium mole fraction for (a) Re=800 and (b) $Re = 2500$.

tional profiles. This peculiar behavior is postulated to be occurring from a Strouhal number effect enhancing the mixing. It has been observed by Mastorakos *et al.* that forcing at Strouhal numbers around 0.6 enhances the mixing in the developing region of a momentum driven jet and this enhancement increases with increasing amplitude of excitation [20]. Figure 6b clearly shows self excitation frequencies present in the near field prior to turbulent mixing. Post transition- 20d and 30d for $Re_0 = 800$ and 10d and 20d for $Re_0 = 2500$ -the behavior shows the same qualitative shape in Fig. 15 as observed previously.

5.5 Hardware Averaging

The deflection angle required for the RSD analysis can be averaged either in software or in hardware. The former converts the instantaneous hue to the instantaneous deflection angle, and then, the average is obtained in post-processing, as in the methodology described above. However, in hardware averaging, the camera sensor itself effectively averages the RGB signal in a long exposure to obtain an average hue, and thus, the average deflection angle. A higher degree of symmetry can be achieved by a combination of software and hardware averaging rather than the hardware averaging alone. If all the intermediate steps are linear relations then hardware averaging or partial hardware/software is no different than software averaging. Because the RGB to HSV conversion and H to H' conversion are linear relations, the filter calibration process is the only potential source of non-linearity. To further explore this hypothesis, a filter with non-linear calibration on one side and a linear calibration on the other side was designed and used with long exposure experiments.

The optical setup is slightly modified for the long exposure experiments. A neutral density filter is attached to the aperture to reduce the light throughput. The camera's exposure time is changed to 250 ms for hardware averaging. At exposure times longer than 250 ms, the ambient light can interfere with the signal. Thus, 100 long exposure images are used for averaging.

Figure 16a shows sample individual pixel filter calibration curves at r=-20 mm (red line) and r=2.5 mm (green line) and their respective least squared fits (dashed). Considering the R^2 value for each pixel along a radial line, Fig. 16b demonstrates non-linear behavior with R^2 of about 0.91 between r=-14 to -22 mm and a R^2 value of around 0.98 on the positive side ($r > 0$) of the image. Thus, individual pixel calibration curves on the left side of the filter are more non-linear than those on the right-side of the filter.

The sample RSD image in Fig. 17a shows that the long exposure smooths out the turbulent features. As mentioned previously, one hundred such images were acquired and averaged to obtain a converged image used to obtain average deflection angle, average refractive index difference, and finally, average helium mole fraction. Figure 17b shows that the side of the image with linear calibration (right side) provides accurate results, but the results obtained with the non-linear side are highly erroneous. As expected, the results in Fig. 17b demonstrate that hardware averaging can be used only if the filter is linear, e.g., $R^2 > 0.98$. This R^2 target can be a useful guide for future studies where hardware averaging is required because either the light source or

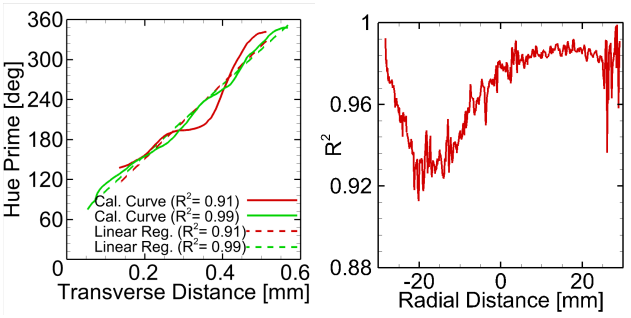

(a) (b)

Fig. 16: (a) Individual pixel calibration curves sampled to show linear (solid green) and non-linear (solid red) behavior and corresponding linear regression lines (dashed). (b) Radial profile of R^2 at z=20d for all pixels in the FOV.

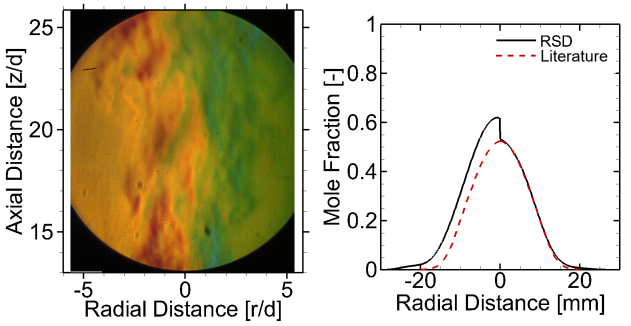

(a) (b)

Fig. 17: (a) Long exposure raw image for the case of $Re_0 = 800$ and (b) corresponding results for mole fraction for RSD (solid black) and Ref. [31] (red dashed).

the data size is limited. However, given a bright light source, it is best to use short exposure times with software averaging. Further for transient events, like initial jet penetration, a high-speed camera is also needed.

6 Conclusions

In this study, RSD was implemented and validated to obtain quantitative mixing measurements in a turbulent environment. Measurements were obtained across the whole field of turbulent helium jets, including laminar, transition, and turbulent regions. Due to instability of transition to turbulence, the average transition region spans a range of axial distances that decreases with increasing Reynolds number. Radial profiles reveal that significant changes occur in the mixing profiles, both in shape and magnitude, across a relatively small transition distance. Self-similarity was observed in the turbulent region of the momentum dominated jet. Results show that RSD can provide high quality quantitative data with low measurement uncertainties, which will be useful to validate computational models, especially in regions where self-similarity may not be satisfied.

Several important considerations are necessary for accurate RSD measurements. First, a pixel-by-pixel calibration process with multiple images acquired at each calibration step is strongly recommended to minimize the uncertainty. Second, an alternative hue coordinate (hue prime) can be utilized to exclude regions of the filter with high absorptivity that limits light throughput. Thus, enabling data acquisition at lower exposure times by eliminating these regions. Third, turbulent RSD measurements require a large dataset (>1000 images) to ensure statistically stationary state. Lastly, the linear relationship between refractive index difference and density can be used to obtain the average thermodynamic properties. The effect of exposure time on the quantitative measurements was also investigated. Partial hardware averaging with long exposure provides the same results as short exposure experiments and software averaging, but a highly linear filter is necessary to avoid spurious measurements. If possible, high-speed, short exposure data acquisition is preferred to provide more details about the transient phenomena that the long exposure cannot provide.

7 Acknowledgements

This work was performed with support by the Department of Energy, Office of Energy Efficiency and Renewable Energy (EERE) and the Department of Defense, Tank and Automotive Research, Development, and Engineering Center (TARDEC), under Award Number DE-EE0007301.

References

1. Abramovich, G.: The theory of turbulent jets,(1963). R411 p. 541 (1963)
2. Agrawal, A., Alammar, K., Gollahalli, S.: Application of rainbow schlieren deflectometry to measure temperature and oxygen concentration in a laminar gas-jet diffusion flame. Experiments in fluids **32**(6), 689–691 (2002)
3. Agrawal, A.K., Wanstall, C.T.: Rainbow schlieren deflectometry for scalar measurements in fluid flows. Journal of Flow Visualization and Image Processing **25**(3-4) (2018)
4. Al-Ammar, K., Agrawal, A., Gollahalli, S., Griffin, D.: Application of rainbow schlieren deflectometry for concentration measurements in an axisymmetric helium jet. Experiments in fluids **25**(2), 89–95 (1998)
5. Bracewell, R.N., Bracewell, R.N.: The Fourier transform and its applications, vol. 31999. McGraw-Hill New York (1986)

6. Buch, K.A., Dahm, W.J.: Experimental study of the fine-scale structure of conserved scalar mixing in turbulent shear flows. part 2. sc≈1. Journal of Fluid Mechanics **364**, 1–29 (1998)
7. Chen, C.J., Rodi, W.: Vertical turbulent buoyant jets: a review of experimental data. Nasa STI/Recon Technical Report A **80** (1980)
8. Davis, M.: Measurements in a subsonic turbulent jet using a quantitative schlieren technique. Journal of Fluid Mechanics **46**(4), 631–656 (1971)
9. Davis, M.: Quantitative schlieren measurements in a supersonic turbulent jet. Journal of Fluid Mechanics **51**(3), 435–447 (1972)
10. Davis, M.: Intensity, scale and convection of turbulent density fluctuations. Journal of Fluid Mechanics **70**(3), 463–479 (1975)
11. Dowling, D., Dimotakis, P.: On mixing and structure of the concentration field of turbulent jets. In: 1st National Fluid Dynamics Conference, p. 3611 (1988)
12. Dowling, D.R.: The estimated scalar dissipation rate in gas-phase turbulent jets. Physics of Fluids A: Fluid Dynamics **3**(9), 2229–2246 (1991)
13. Dowling, D.R., Dimotakis, P.E.: Similarity of the concentration field of gas-phase turbulent jets. Journal of Fluid Mechanics **218**, 109–141 (1990)
14. Greenberg, P.S., Klimek, R.B., Buchele, D.R.: Quantitative rainbow schlieren deflectometry. Applied optics **34**(19), 3810–3825 (1995)
15. Ko, H., Kihm, K.: An extended algebraic reconstruction technique (art) for density-gradient projections: laser speckle photographic tomography. Experiments in fluids **27**(6), 542—550 (1991)
16. Kolhe, P.S., Agrawal, A.K.: Abel inversion of deflectometric data: comparison of accuracy and noise propagation of existing techniques. Applied optics **48**(20), 3894–3902 (2009)
17. Kolhe, P.S., Agrawal, A.K.: A novel spectral analysis algorithm to obtain local scalar field statistics from line-of-sight measurements in turbulent flows. Measurement Science and Technology **20**(11), 115402 (2009)
18. Kwon, S.J., Seo, I.W.: Reynolds number effects on the behavior of a non-buoyant round jet. Experiments in fluids **38**(6), 801–812 (2005)
19. Libby, P.A.: An introduction to turbulence. CRC Press (1996)
20. Mastorakos, E., Shibasaki, M., Hishida, K.: Mixing enhancement in axisymmetric turbulent isothermal and buoyant jets. Experiments in fluids **20**(4), 279–290 (1996)
21. Mistry, D., Philip, J., Dawson, J.R., Marusic, I.: Entrainment at multi-scales across the turbulent/non-turbulent interface in an axisymmetric jet. Journal of Fluid Mechanics **802**, 690–725 (2016)
22. Papanicolaou, P.N., List, E.J.: Investigations of round vertical turbulent buoyant jets. Journal of Fluid Mechanics **195**, 341–391 (1988)
23. Pasumarthi, K.S., Agrawal, A.K.: Schlieren measurements and analysis of concentration field in self-excited helium jets. Physics of Fluids **15**(12), 3683–3692 (2003)
24. Pelliccia-Kraft, B., Watt, D.: Three-dimensional imaging of a turbulent jet using shearing interferometry and optical tomography. Experiments in fluids **29**(6), 573–581 (2000)
25. Pitts, W.M.: Effects of global density ratio on the centerline mixing behavior of axisymmetric turbulent jets. Experiments in Fluids **11**(2-3), 125–134 (1991)
26. Pitts, W.M.: Reynolds number effects on the mixing behavior of axisymmetric turbulent jets. Experiments in fluids **11**(2-3), 135–141 (1991)
27. Pitts, W.M., Kashiwagi, T.: The application of laser-induced rayleigh light scattering to the study of turbulent mixing. Journal of Fluid Mechanics **141**, 391–429 (1984)
28. Prandtl, L.: 7. bericht über untersuchungen zur ausgebildeten turbulenz. ZAMM-Journal of Applied Mathematics and Mechanics/Zeitschrift für Angewandte Mathematik und Mechanik **5**(2), 136–139 (1925)
29. Richards, C.D., Pitts, W.M., et al.: Global density effects on the self-preservation behaviour of turbulent free jets. Journal of Fluid Mechanics **254**, 417–417 (1993)
30. Singh, S., Panigrahi, P., Muralidhar, K.: Effect of buoyancy on the wakes of circular and square cylinders: a schlieren-interferometric study. Experiments in fluids **43**(1), 101–123 (2007)
31. Su, L., Helmer, D., Brownell, C.: Quantitative planar imaging of turbulent buoyant jet mixing. Journal of fluid mechanics **643**, 59–95 (2010)
32. Takano, H., Kamikihara, D., Ono, D., Nakao, S., Yamamoto, H., Miyazato, Y.: Three-dimensional rainbow schlieren measurements in underexpanded sonic jets from axisymmetric convergent nozzles. Journal of Thermal Science **25**(1), 78–83 (2016)
33. Vasil′ev, L.A.: Schlieren methods. Israel Program;[distributed by Keter Inc.] New York (1971)
34. Wanstall, C.T., Agrawal, A.K., Bittle, J.A.: Quantifying liquid boundary and vapor distributions in a fuel spray by rainbow schlieren deflectometry. Applied Optics **56**(30), 8385–8393 (2017)
35. Wanstall, C.T., Agrawal, A.K., Bittle, J.A.: Phase boundary detection in transient, evaporating high-pressure fuel sprays by rainbow schlieren deflectometry. Applied optics **58**(25), 6791–6801 (2019)
36. Watanabe, T., Sakai, Y., Nagata, K., Ito, Y., Hayase, T.: Enstrophy and passive scalar transport near the turbulent/non-turbulent interface in a turbulent planar jet flow. Physics of Fluids **26**(10), 105103 (2014)
37. Watt, D., Vest, C.M.: Turbulent flow visualization by interferometric integral imaging and computed tomography. Experiments in fluids **8**(6), 301–311 (1990)
38. Westerweel, J., Fukushima, C., Pedersen, J., Hunt, J.: Mechanics of the turbulent-nonturbulent interface of a jet. Physical review letters **95**(17), 174501 (2005)
39. Westerweel, J., Hofmann, T., Fukushima, C., Hunt, J.: The turbulent/non-turbulent interface at the outer boundary of a self-similar turbulent jet. Experiments in Fluids **33**(6), 873–878 (2002)
40. Yildirim, B., Agrawal, A.: Full-field measurements of self-excited oscillations in momentum-dominated helium jets. Experiments in fluids **38**(2), 161–173 (2005)

Simultaneous Rainbow Schlieren Deflectometry and OH* Chemiluminescence Imaging of a Diesel Spray Flame in Constant Pressure Flow Rig

Allen Parker[a], C. Taber Wanstall[a], Shawn Reggeti[a], Joshua A. Bittle[a], Ajay K. Agrawal[1]

[a] *University of Alabama, Box 870276, Tuscaloosa AL 35487, USA*

Abstract

The physical and chemical phenomena that take place during fuel injection, entrainment and fuel-air mixing, cool-flame and ignition reaction, and combustion in diesel sprays still require extensive study. Global parameters such as liquid and vapor jet penetration lengths and spreading rates render useful yet still limited information. Understanding of the temporal evolution of the spray as it progresses through various steps is needed to develop advanced clean combustion modes and high-fidelity predictive models with sufficient accuracy. In this study, high-speed rainbow schlieren deflectometry (RSD) and OH* chemiluminescence are used to simultaneously image fuel-air mixing, cool-flame reactions, ignition, flame propagation and stabilization, and combustion in a transient diesel-like flame. A constant pressure flow rig (CPFR) is used to conduct multiple injections in quick succession to obtain a statistically relevant dataset. n-heptane was injected at nominal supply pressure of 1000 bar from a single-hole diesel injector into ambient at pressure of 30 bar and temperature of 800 K. About 500 injections were performed and analyzed to reveal structural features of non-reacting and reacting regions of the spray, quantify jet penetration and spreading rates, and study cool-flame behavior, ignition, flame propagation and stabilization at lift-off length, and combustion at upstream and downstream locations.

Keywords:
Spray diagnostics, rainbow schlieren deflectometry, chemiluminescence imaging, diesel spray flames, constant pressure flow rig

*Corresponding author:
Email address: aagrawal@eng.ua.edu (Ajay K. Agrawal)

1. Introduction

Modern diesel injectors deliver fuel at supply pressures up to 250 MPa through holes from one to a few hundred microns in diameter into the high-pressure, high-temperature ambient environment in pulses often lasting less than 1.0 ms. Processes that follow include liquid fuel penetration, fuel vaporization and mixing with high-temperature ambient gas, cool-flame reactions, autoignition, and premixed and diffusion flame combustion. Fuel-air mixing in the near field and subsequent processes ultimately determine the combustion efficiency and engine-out emissions of soot, carbon monoxides, nitric oxides, etc. Understanding the underlying physics of these turbulent and transient processes is challenging because detailed measurements in a diesel environment are inherently difficult to acquire.

Early studies of diesel sprays focused on the global parameters such as liquid and vapor penetration lengths and spreading angles measured via Mie-scattering [1] and schlieren or shadowgraphy techniques [2]. Simplified analytical models to predict the penetration length [3, 4] and empirical correlations to estimate the flame lift-off length [5] have been used in the literature. Dec's model is widely used to describe the conventional diesel combustion process [4]. Musculus *et al.* [6] presented conceptual models to describe the partially premixed low temperature diesel combustion. These models and approaches tend to approximate the inherently unsteady diesel processes as quasi-steady state. However, detailed information about the temporal evolution of the diesel spray as it progresses through various stages from injection to combustion is needed to develop not only the advanced modes of combustion but also to advance accurate, predictive computational fluid dynamics (CFD) models.

Detailed measurements of transient diesel sprays are difficult because of the complex test environment (high-temperatures and pressures) and diagnostics challenges such as limited optical access, and inadequate spatial and temporal resolutions. Optically accessible constant volume facilities have contributed greatly towards the current understanding, although only a few injections can be realized for a given experiment [7]. Several research groups have used high-speed schlieren imaging and planar laser induced fluorescence (PLIF) or Rayleigh-scattering techniques [7–10]; the former method is qualitative and suffers from poor sensitivity, while the latter method provides spatially resolved results but requires either expensive kHz rate laser systems or multiple experiments with low speed lasers.

In this study, a high-pressure, diesel-like n-heptane spray flame is investigated with two main objectives: (1) perform large number of injections in quick succession to describe the flame evolution both instantaneously and statistically on an average basis, and (2) simultaneously visualize and quantify the relevant physical processes using multiple high-speed diagnostic techniques. An in-house developed constant pressure flow rig (CPFR) will be used for the experiments. Diagnostics include rainbow schlieren deflectometry (RSD), OH* chemiluminescence, and 2-color pyrometry (2CP), although 2CP results will be presented in future work. The RSD uses a continuously graded rainbow filter to quantitatively encode the deflection of light rays in color (or hue) to overcome the limitations of intensity-based, black-and-white schlieren techniques [11].

RSD uses a small source aperture (<100 micron wide) compared to a large pinhole (few mm) in the conventional schlieren technique to achieve high measurement sensitivity. Moreover, the RSD signal is relatively insensitive to light absorption by the test media. These unique features of the RSD are well documented in studies to acquire quantitative measurements in canonical jets and flames [12]. More recently, Wanstall *et al.* have extended the RSD methodology to quantify liquid and vapor boundaries in diesel sprays [13]. RSD is applied for the first time in the harsh environment of the present study, and thus, it has not been fully optimized to obtain the quantitative distributions of the local thermodynamic properties.

2. Experimental Setup

2.1. Constant Pressure Flow Rig (CPFR)

Figure 1a illustrates the CPFR used in this study. It is a vertical continuous flow system designed to provide line-of-sight optical access of fuel injection into a nearly quiescent environment to generate large datasets (~500 injections) in about an hour. The chamber is supplied with pressurized, electrically preheated air at an average speed of about 0.5 m/s (nearly three orders of magnitude less than the fuel injection velocity) in a counter flow arrangement shown in Fig. 1a. The air enters through a flow conditioner consisting of six 0.5 mm thick, 100 micron mesh elements followed by a diffuser section to uniformly distribute the flow across the CPFR. The air exits at the top of the rig through four 3 mm diameter holes placed symmetrically around the injector tip. The air supply pressure is controlled by an upstream dome regulator and the air flow rate is regulated by a downstream control valve. Fuel is injected by a Bosch CRIN3-18 injector modified to have a single 100 μm

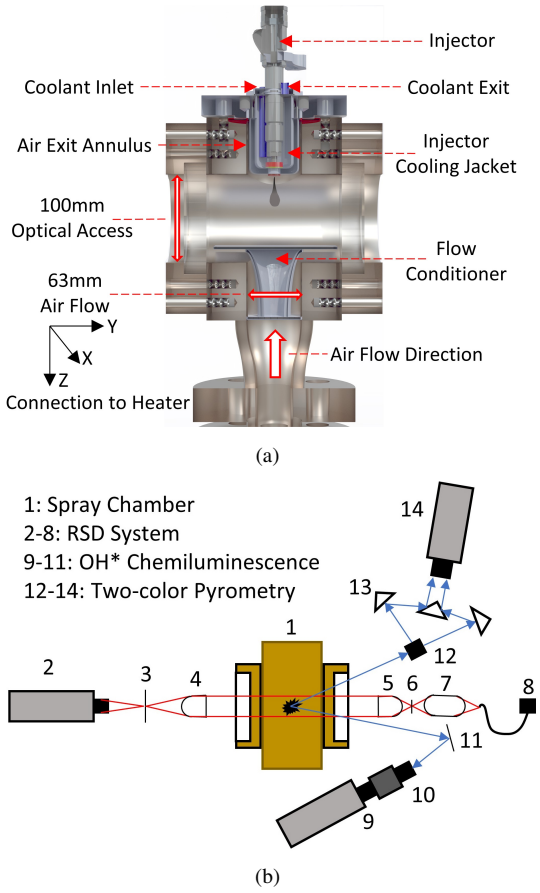

Figure 1: (a) Constant pressure flow rig (CPFR) illustration. (b) Schematic of simultaneous diagnostics where each component is labeled as: CPFR (1), RSD Camera (2), rainbow filter (3), decollimating lense (4), collimating lense (5), focusing aperture (6), focusing lenses (7), laser light source (8), chemiluminescence camera (9), intensifier (10), mirror (11), beam splitter (12), mirrors (13), 2CP camera (14)

Table 1: Air flow and fuel injection conditions in CPFR.

Amb. Temp. (K)	Amb. Pres. (bar)	Fuel Temp. (K)	Fuel Pres. (bar)
803±10	30.1±0.3	89±6	990±8

hole at the tip to create a spray along the axis of the rig. The fuel temperature is maintained at 90 °C by a surrounding cooling jacket circulating coolant. Table 1 shows the test conditions recorded during the experiment. The available facilities limited the maximum operating pressure, which remains below typical compression ignition engine cylinder conditions during injection (as well as ECN Spray A test conditions) at this time.

2.2. *Optical Diagnostics*

Figure 1b shows the layout of the three simultaneous optical diagnostics used for data acquisition, of which only two are utilized in this study (RSD and OH* chemiluminescence, or OH*). RSD is orthogonal to the chamber while OH* chemiluminescence is viewed at an angle. The RSD system uses an Energetiq EQ-99X fiber coupled broadband light source, refocused by two 75 mm focal length, 50 mm diameter lenses onto a 3 mm x 100 μm rectangular aperture located at the focal point of a 75 mm diameter, 250 mm focal length achromatic doublet lens. The collimated light enters the CPFR (Fig. 1b), and after exiting, is decollimated (focused) by a matching achromatic doublet lens onto a digitally printed rainbow filter - a transparent rectangular strip with very fine color (hue) gradations of 4 μm - placed at the focal point. A Photron Nova S9 color camera (1) with 512 x 784 pixel resolution is placed directly behind the filter plane to acquire the RSD images at 20 kHz with 4 μs exposure time. The camera is outfitted with a Nikon Nikkor 50 mm lens to provide a spatial resolution of 90 μm per pixel.

The OH* chemiluminescence emitted in the reacting spray is reflected by a mirror towards the Invisible Vision UV intensifier with gate time of 70 μs, outfitted with a 310 nm band pass filter. The OH* images are acquired by a monochromatic Photron SA5 camera (pixel resolution of 896 x 848). The framing rate and spatial resolution of the camera are 10 kHz and 160 μm, respectively.

3. Data Processing

RSD measures light ray deflection angle, ϵ, related to normalized refractive index difference δ along the line of sight, $\delta = (\eta/\eta_o - 1)$. Here, η is the local refractive index, and η_o is the refractive index of the surroundings. For small deflection angles, the transverse displacement at the filter plane, d, can be obtained as:

$$d = f\ tan\ (\varepsilon) \tag{1}$$

where f is focal length of the decollimating lens. In RSD, the displacement d is coded in color by the rainbow filter, and thus, in the rainbow schlieren image. The color is quantified by hue according to the hue-saturation-intensity (HSI) color model. Hue at a pixel location in the schlieren image is related to the transverse displacement at the filter plane through a filter calibration curve as explained by Al-Ammar *et al.* [12]. In this study, each pixel is calibrated independently for high accuracy. Because both the aperture and filter are

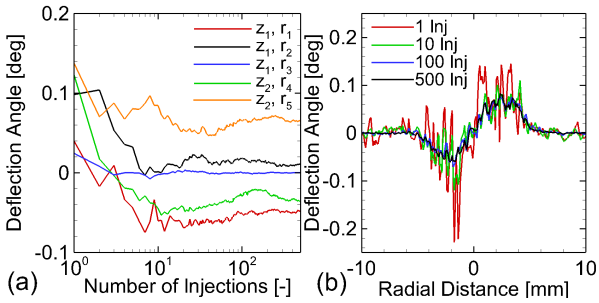

Figure 2: (a) Shown above is an ensemble average of deflection angle versus number of injections at 1.1 ms aSOI at 5 locations in the spray, where $z_1 = 25\,\text{mm}$, $z_2 = 35\,\text{mm}$, $r_1 = -3.7\,\text{mm}$, $r_2 = 0\,\text{mm}$, $r_3 = 8.7\,\text{mm}$, $r_4 = -4.6\,\text{mm}$, and $r_5 = 6.2\,\text{mm}$. Colored symbols corresponding to these locations are overlaid on the RSD images in Fig. 5. (b) Radial profiles of deflection angle are plotted at $z = 25\text{mm}$ downstream for an instantaneous injection (red) along with the ensemble of 10 (green), 100 (blue), and 500 (black) injections.

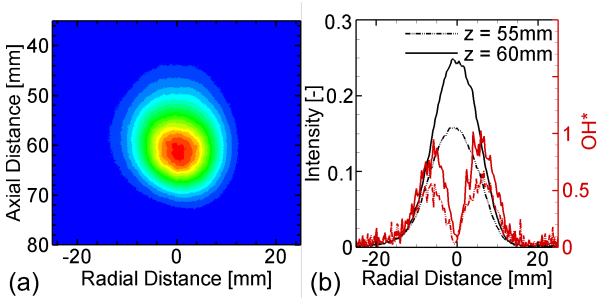

Figure 3: (a) An ensemble averaged false color OH* intensity contour at 1.9 ms aSOI is shown along with (b) the radial profile of raw camera intensity (black lines) and the inverted OH* results (red lines) at two different axial locations.

rectangular, the filter responds only to transverse ray displacement and is insensitive to the axial ray displacement.

Reliable measurements of hue from RSD images require intensity and saturation values above a minimum threshold of 10% and 15%, respectively [13]. Ensemble averaging for turbulent flows requires a large number of realizations to ensure statistical stationarity, i.e., the average of instantaneous fluctuations is zero [14], which is demonstrated in Fig. 2a showing the average deflection angle at specific points versus number of injections at five different locations. In the background (blue line: z_1, r_3), the deflection angle quickly converges to a constant zero deflection angle after only 20 injections. However, over 300 injections were required to reach statistically stationary values at all locations in the jet. In Fig. 2b, the radial profile at z=25 mm shows the outcome of ensemble averaging. Successive averages improve the symmetry and smoothness of the radial profile, which ultimately reaches a well defined symmetric shape for 500 injections.

Both RSD and OH* are line of sight techniques. However, in RSD, the signal (deflection angle) is proportional to the gradient of refractive index difference integrated over the line of sight while, in OH*, the signal detected by the camera is proportional to the OH* chemiluminescence integrated over the line of sight. The two techniques result in different Abel inversion formulas that are complementary to each other, i.e., one is inverse of the other, as noted by Kolhe and Agrawal [15]. Accordingly, for an axisymmetric profile, RSD (ϵ) and OH* data are converted into local measurements (δ and OH* intensity) using Abel transforms expressed in discretized form by Eq. 2.

$$\begin{aligned} \delta(r_j) &= \sum_j D_{i,j}\epsilon_j \\ OH^*(r_j) &= \sum_j D_{i,j}^{-1} I \end{aligned} \tag{2}$$

Here $D_{i,j}$ represents the coefficients matrix given by Kolhe and Agrawal [15]. Figure 3a shows an average false color OH* contour for 200 injections. The symmetric OH* radial profiles in Fig. 3b (black lines) demonstrate that the OH* reaches statistical stationarity and symmetry sooner than RSD. The inverted normalized OH* intensity profiles (red lines) indicate that the OH* intensity peaks away from the jet center where the main reaction zone is located.

4. Results

In this work, a statistically significant dataset of 500 consecutive injections was acquired by utilizing capabilities of the CFPR to obtain transient ensemble averaged behavior of fuel-air mixing and low- and high-temperature ignition via RSD and OH* chemiluminescence imaging. Prior to this work, truly average behavior of diesel spray dynamics and combustion has not been obtained because of the difficulty in acquiring such large datasets required for statistical stationarity. Thus, this work offers a unique perspective of reacting spray dynamics on both instantaneous and average basis. Results in this section are presented in two parts. First, global parameters of the spray and qualitative observations of the instantaneous RSD and OH* chemiluminescence are used to gain insight into the development of the ignition process. Then, instantaneous line of sight RSD and OH* chemiluminescence data are averaged to obtain symmetric profiles that are suitable for the Abel

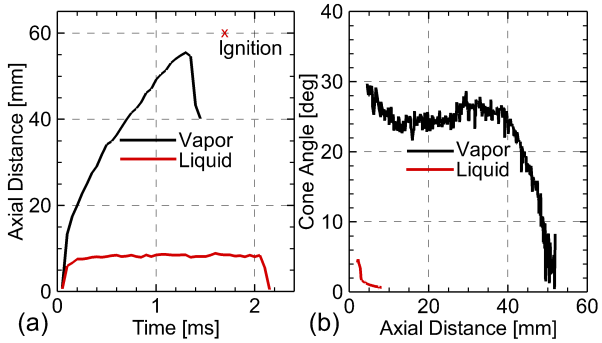

Figure 4: Plots (a) and (b) show the liquid and vapor penetration versus time and the axial development of the liquid and vapor full cone angles at 1.35 ms, respectively. Also shown in (a) is the start of ignition (red 'x') from the OH* signal.

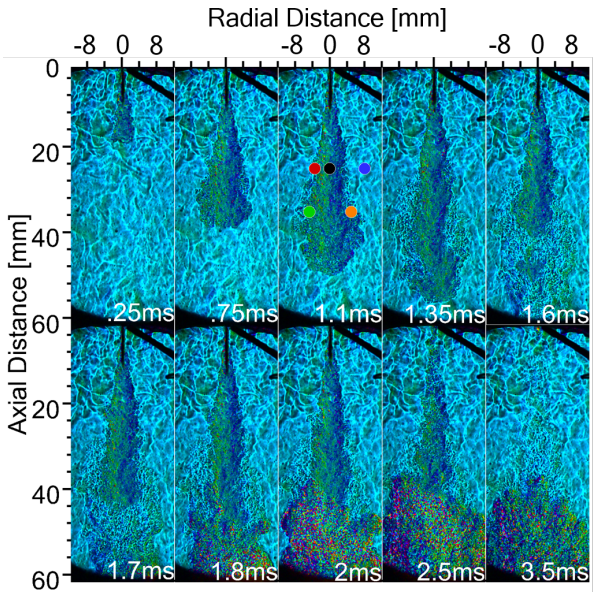

Figure 5: RSD images for a single injection. Two thermocouple sheaths visible in the top-right (black regions) of each frame are used to measure the ambient and injector temperatures. Symbols in top-middle frame correspond to averaging locations in Fig. 2

.

inversion to obtain local ensemble averaged measurements. The qualitative local OH* intensity is determined to track the evolution of the second stage ignition while the local refractive index difference profiles determined by RSD are used to characterize the fuel-air mixing to bridge the first and second stage ignition events.

4.1. RSD Imaging and Global Parameters

Recently, the intensity signal detected by the RSD has been used to obtain liquid and vapor penetration lengths and phase boundaries in high pressure fuel sprays using a novel probabilistic approach [13, 16]. Figure 4a shows the liquid and vapor penetration distances versus time for this experiment. The liquid penetration in Fig. 4 is defined as the region with 95% probability of liquid [13]. The initial jet penetration up to t=0.1 ms, where "t" represents time after start of injection (aSOI), is the same for both liquid and vapor. However, after this time the vapor begins to diverge as the liquid reaches a quasi-steady penetration length of about 8 mm at t=0.2 ms. The vapor penetration continues until t=1.35 ms when the RSD signal shows a retraction caused by a 'softening' of the refractive index gradients indicating that the fuel-air mixture is being heated by the low-temperature chemical reactions such as formaldehyde near the spray head [9]. Thus, by this time the 'cool-flame' or first stage ignition has begun.

Figure 4b shows the axial development of the full cone angle of the liquid and vapor portions of the spray at t=1.35 ms. Half cone angle is defined as $\arctan[r/D]$, where r and D are the spray radius and axial distance, respectively; the sum of left and right half angles is the full cone angle presented. Figure 4 shows a continuously decreasing liquid cone angle until termination around z=8 mm. The vapor cone angle initially decreases until about z=20 mm, where it begins increasing to a value of approximately 27° at around z=35 mm; thereafter, the cone angle decreases signifying the closing of the vapor jet. Note that the vapor jet never reaches a period of a constant cone angle as reported in the literature for non-reacting conditions [13, 17]. The cool-flame softens the refractive index gradients, which affects the detectable vapor boundary (also shown in Fig. 5). The vapor cone angle plot reveals the appearance of cool-flame reactions on the jet periphery earlier than the jet head shown by the vapor penetration length.

These findings are supported by visual inspection of the RSD images in Fig. 5; eight instantaneous RSD images are shown at different times after start of injection (aSOI). In these images, the intensity and saturation values at each pixel location were increased for clarity without affecting the hue (color) detected by the RSD technique. Images in Fig. 5 show a dominantly light blue background corresponding to the undeflected rays passing through the center of the color filter. Injection of the dense fuel (in relation to ambient air) causes density gradients, and thus, color gradations in the jet region. For t=0.25 ms, the first image in Fig. 5 shows the so called quasi-steady liquid region (dark region near

injector tip) and a small surrounding vapor cloud. After this (t=0.75 ms), the vapor penetrates farther downstream, noted by mostly dark blue and green/yellow colors signifying deflections associated with the density gradients in the jet.

At t=1.1 ms, the jet has reached about z=48 mm with no visual signs of ignition. However, at t=1.35 ms the cool-flame is initiated on the jet periphery between z=25 mm and 40 mm. The high sensitivity of the RSD in detecting early stages of the cool-flame is attributed to, and dictated by, the small source aperture (100μm). At t=1.6 ms, the cool-flame spreads downstream to the jet head, resulting in the so-called "softening" observed by other researchers using the conventional schlieren imaging [9]. Interestingly, at this time, the RSD image reveals not only the softening of the jet head but also a reversal in the density gradients in the shear layer region between z=40 mm and 60 mm marked by a switch in color gradations (i.e. green color in top half that is other wise dark-blue), indicating that the local temperatures are higher than those of the surroundings. This process persists and is more clearly observed at t=1.7 ms when nearly all of the jet head (about 20 mm) is consumed by the cool-flame reactions. After this time, density gradients intensify at t=2.0 ms indicating second stage combustion. By 2.5 ms the injection has ended, yet combustion persists consuming the remaining fuel. At 3.5 ms, the fuel jet disappears and the product cloud or end of combustion still remains between z=40 mm and 60 mm. The RSD results are consistent with the findings of Skeen *et al.* [9], based on multiple diagnostics, i.e., schlieren and formaldehyde PLIF. Considering different time steps, two additional observations can be made from Fig. 5: (1) the turbulent structures in the background are stationary proving that the airflow is nearly quiescent, and (2) the spray contains very fine scale turbulent structures in both non-reacting and reacting regions.

OH* images in Fig. 6 spanning z=35 mm to 90 mm support the observations made from the RSD images. The first plot in Fig. 6 pertains to the start of combustion at t=1.8 ms and z = 55 mm, matching with the large deflections (red/purple color) observed in the schlieren image shown in Fig. 5. The OH* first appeared at around t = 1.7 ms signifying first stage ignition (not shown here). Thus, the time between ignition and combustion is only about 0.1 ms or within the framing rate tolerance of the camera system. In contrast, the cool-flame behavior is observed for a much longer period from 1.1 ms to 1.7 ms, in agreement with the findings of [9]. At t = 2.0 ms the combustion zone has expanded (both upstream and downstream) and the OH* signal peaks at z=60 mm.

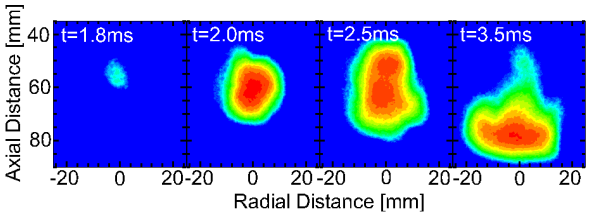

Figure 6: False color images of the instantaneous OH* chemiluminescence are shown for four time steps aSOI.

The RSD images also reveal upstream flame propagation whereby a region of large deflections appears at z=45 mm. At t=2.5 ms (injection ended at 2.2 ms), the combustion zone has elongated and the OH* signal is bimodal signifying reactions in localized upstream and downstream regions. The last frame at t=3.5 ms shows diminishing reactions because of the absence of the incoming fuel in the upstream region while the OH* increases in the downstream combustion zone.

4.2. Local Measurements

In this section, data for multiple injections were ensemble averaged, which resulted in symmetric profiles at each time step. Next, Abel inversion was used to obtain local distributions to gain insight into the combustion processes. Normalized refractive index (δ) profiles from RSD are shown in Fig. 7 followed by OH* intensity contours in Fig.8.

Figure 7 shows the time evolution of δ at z=25 mm, 30 mm, and 35 mm to illustrate the jet arrival, quasi-steady flow, and then softening/retraction by the cool-flame. First note that the quasi-steady period at each axial location is different: at z=25 mm from t=0.75 ms to 1.25 ms, at z=30 mm from 0.75 ms to 1.0 ms, and at z=45 mm from t=1.0 ms to 1.1 ms. These results show that it takes longer to reach the downstream location and that the quasi-steady period decreases with increasing axial distance. The results agree with the RSD image in Fig. 5, where jet head at t=0.75 ms has just passed z=30 mm but it has not yet arrived at z=35 mm. More importantly, agreement between instantaneous RSD images and ensemble averaged refractive index profiles shows that the RSD could be utilized for local quantification once the measurement uncertainties are analyzed in detail for this challenging application. For example, recent work [18] has demonstrated a robust methodology to convert δ to thermodynamic properties such as equivalence ratio.

As discussed, cool-flame reactions affect the RSD signal, visible as softening of the jet periphery in Fig. 5. This effect is also seen in the δ profiles in Fig. 7, again

indicating that the process is repeatable across injections. Each of the three axial locations in Fig. 7a-c show the arrival of the jet (red line), the fuel-air mixing locally (at that axial location) reaching a quasi-steady state (green and blue lines show same profiles), the inception of the cool-flame on the periphery (orange) noted by a narrowing of the profiles, and deepening of the cool-flame into the jet core (purple and black line). Note that the purple/black lines representing later times are nearly identical; this re-stabilization is best seen in Fig. 7c.

Fig. 7d tracks the temporal evolution of the cool flame using radial profiles of normalized refractive index difference for the quasi-steady state at two axial locations, taken from Fig. 7a and 7c. The radial position of the recessed RSD boundary, signifying the inner edge of the cool flame, is shown at three different times, i.e., t = 1.25 ms, 1.50 ms, and 1.75 ms. Fig. 7d shows that the radial location of the cool flame is about the same at both axial locations. It is apparent that the reactions proceed radially inwards into increasingly fuel-rich regions as time progresses. The magnitude of the normalized refractive index difference at the cool flame boundary is greater at the downstream location compared to the upstream location. As shown in [18], a higher value of the normalized refractive index difference denotes a higher mixture fraction or equivalence ratio. Thus, Fig. 7d suggests that the cool flame starts in a fuel-lean region, and subsequently spreads into gradually richer mixtures. These results demonstrate the ability of the RSD diagnostics to quantitatively delineate the spatial and temporal pathways of the cool flame, which eventually leads to the second stage ignition.

The local OH* intensity contours extend the analysis domain into second stage ignition. Figure 8 shows the ensemble averaged planar OH* intensity contours for eight different times aSOI; note that the high degree of similarity between left and right profiles/images in Fig. 7/Fig. 8 supports the axisymmetric assumption of the Abel inversion. Figure 8 quantitatively identifies the time and spatial location (axial and radial) of ignition observed via RSD (Fig. 5). As evidenced in both figures, on average the ignition kernels first appear at t=1.7 ms approximately at z=60 mm. Figure 8 identifies the radial location of main ignition, 4<r<8 mm, which is precisely the region of cool-flame development (Fig. 7). By t=2 ms the ignition region has broadened, with peak OH* intensity at approximately the same location as the previous plot. At t=2.2 ms the flame has stabilized at the lift-off length. After t=2.2 ms, the OH* intensity contour reveals upstream flame propagation consistent with the instantaneous image in Fig. 6 where

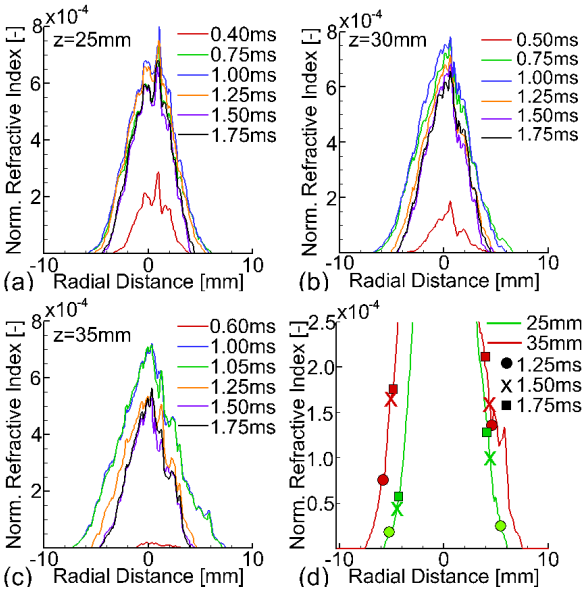

Figure 7: (a,b,c) Radial profiles of normalized refractive index at axial distances of 25, 30, and 35 mm are shown as they develop through time (aSOI). (d) The quasi-steady profiles are shown along with the retraction due to cool-flame progression.

the peak reaction has shifted radially inward. The next time reveals the bimodal shape observed in the instantaneous images where peak OH* concentrations occurs both upstream and downstream. Beyond this time, the upstream radical pool diminishes (t=2.7 ms) and the reactions persist downstream between t=3.1 and 3.5 ms.

5. Summary and Conclusions

This study provides unique insight into the transient fuel-air mixing, cool-flame behavior, ignition, flame stabilization, and combustion in a *n*-heptane spray at diesel-like conditions. The study combined two major experimental advancements: (1) a CPFR allowing for the largest number of fuel injection experiments at high pressure and temperature test conditions to collect statistically significant data, and (2) the first application of combined RSD and OH* imaging to simultaneously measure line of sight ray deflection angle and OH* concentration across the whole field. Both provide insight into fuel-air mixing, cool-flame development, ignition, flame propagation and stabilization, and combustion.

Cool-flame behavior was identified by visual observation of the RSD images and experimental data for liquid/vapor penetration and cone angles. Results supported previous findings showing cool-flames along the jet periphery, much earlier and with a much longer in-

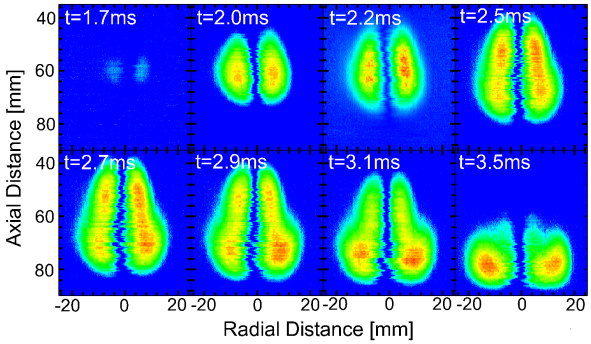

Figure 8: Ensemble average planar OH* relative intensity contours are shown for eight times.

duction time than that between ignition and combustion. Once developed, the cool-flame spreads inwards into the jet core and downwards to the jet head where ignition ultimately occurs. Radial profiles of refractive index difference demonstrate quasi-steady fuel-air mixing conditions, enabling identification of the cool-flame pathway both spatially and temporally. The cool-flame reactions decreased the quasi-steady fuel-air mixing duration at the downstream locations. The planar contours of OH* intensity revealed ignition and combustion occurring close to each other and at nearly the same location. At the end of injection, OH* intensity contours revealed a bimodal distribution indicating distinct upstream (near lift-off length) and downstream reaction zones. At later times, the upstream zone decayed while reactions continued in the downstream zone.

Acknowledgments

Funding for this work was provided by award from US Department of Energy, Office of Energy Efficiency and Renewable Energy (EERE) DE-EE0007980.

References

[1] D. L. Siebers, Liquid-phase fuel penetration in diesel sprays, SAE transactions (1998) 1205–1227.

[2] L. M. Pickett, S. Kook, T. C. Williams, Transient liquid penetration of early-injection diesel sprays, SAE International Journal of Engines 2 (1) (2009) 785–804. doi:https://doi.org/10.4271/2009-01-0839.

[3] D. L. Siebers, Scaling liquid-phase fuel penetration in diesel sprays based on mixing-limited vaporization, SAE transactions (1999) 703–728.

[4] J. E. Dec, A conceptual model of di diesel combustion based on laser-sheet imaging, SAE Transactions - Journal of Engines 106 (SAE Paper No. 970873) (1997) 1319 – 1348.

[5] L. M. Pickett, D. L. Siebers, C. A. Idicheria, Relationship between ignition processes and the lift-off length of diesel fuel jets, SAE transactions (2005) 1714–1731.

[6] M. P. Musculus, P. C. Miles, L. M. Pickett, Conceptual models for partially premixed low-temperature diesel combustion, Progress in energy and combustion science 39 (2-3) (2013) 246–283.

[7] N. Maes, M. Meijer, N. Dam, B. Somers, H. B. Toda, G. Bruneaux, S. A. Skeen, L. M. Pickett, J. Manin, Characterization of spray a flame structure for parametric variations in ecn constant-volume vessels using chemiluminescence and laser-induced fluorescence, Combustion and Flame 174 (2016) 138–151.

[8] J. V. Pastor, J. J. Lopez, J. E. Juliá, J. V. Benajes, Planar laser-induced fluorescence fuel concentration measurements in isothermal diesel sprays, Optics Express 10 (7) (2002) 309–323.

[9] S. A. Skeen, J. Manin, L. M. Pickett, Simultaneous formaldehyde plif and high-speed schlieren imaging for ignition visualization in high-pressure spray flames, Proceedings of the Combustion Institute 35 (3) (2015) 3167–3174.

[10] J. V. Pastor, R. Payri, J. M. Garcia-Oliver, J.-G. Nerva, Schlieren measurements of the ecn-spray a penetration under inert and reacting conditions, Tech. rep., SAE Technical Paper (2012).

[11] P. S. Greenberg, R. B. Klimek, D. R. Buchele, Quantitative rainbow schlieren deflectometry, Appl. Opt. 34 (19) (1995) 3810–3825. doi:http://ao.osa.org/abstract.cfm?URI=ao-34-19-3810.

[12] K. Al-Ammar, A. Agrawal, S. Gollahalli, Quantitative measurements of laminar hydrogen gas-jet diffusion flames in a 2.2 s drop tower, Proceedings of the Combustion Institute 28 (2) (2000) 1997 – 2004. doi:https://doi.org/10.1016/S0082-0784(00)80606-2.

[13] C. T. Wanstall, A. K. Agrawal, J. A. Bittle, Phase boundary detection in transient, evaporating high-pressure fuel sprays by rainbow schlieren deflectometry, Applied optics 58 (25) (2019) 6791–6801.

[14] P. A. Libby, An introduction to turbulence, CRC Press, 1996.

[15] P. S. Kolhe, A. K. Agrawal, Abel inversion of deflectometric data: comparison of accuracy and noise propagation of existing techniques, Applied optics 48 (20) (2009) 3894–3902.

[16] C. T. Wanstall, A. K. Agrawal, J. A. Bittle, Quantifying liquid boundary and vapor distributions in a fuel spray by rainbow schlieren deflectometry, Appl. Opt. 56 (30) (2017) 8385–8393. doi:10.1364/AO.56.008385.

[17] L. M. Pickett, J. Manin, C. L. Genzale, D. L. Siebers, M. P. Musculus, C. A. Idicheria, Relationship between diesel fuel spray vapor penetration/dispersion and local fuel mixture fraction, SAE International Journal of Engines 4 (2011-01-0686) (2011) 764–799.

[18] C. T. Wanstall, A. K. Agrawal, J. A. Bittle, Implications of real-gas behavior on refractive index calculations for optical diagnostics of fuel–air mixing at high pressures, Combustion and Flame 214 (2020) 47–56.

A ROBUST STATISTICAL ALGORITHM FOR BOUNDARY DETECTION IN LIQUID SPRAYS

C. Taber Wanstall,[1] Henning Junne,[2] Joshua A. Bittle,[1] & Ajay K. Agrawal[1,]*

[1]*The University of Alabama, Tuscaloosa, AL, 35487*

[2]*Technische Universität Berlin, Ackerstraße 76, 13355 Berlin, Germany*

*Address all correspondence to: Ajay K. Agrawal, Department of Mechanical Engineering, Tuscaloosa, AL 35487, E-mail: aagrawal@eng.ua.edu

Original Manuscript Submitted: 09/30/2019; Final Draft Received: mm/dd/yyyy

This work presents a statistical algorithm to detect phase boundaries in liquid sprays. Experimental data were obtained in a non-evaporating acetone spray at atmospheric conditions to minimize the refractive index gradients and associated beam steering. Mie-scattering and diffuse background illumination (DBI) diagnostics are implemented to demonstrate the robustness of the approach. The analysis shows that the present algorithm yields similar results for the two different diagnostics, unlike existing threshold-based methodologies providing inconsistent results. The algorithm can be used to identify partial liquid boundaries between single-phase liquid and vapor boundaries. Thus, for each case, liquid boundaries were defined in terms of liquid probability of 100% or less than 100%. Sprays from two different injectors were analyzed to demonstrate the versatility of the methodology. A parametric study was conducted to demonstrate that motion blur can affect an accurate detection of the phase boundaries, and hence, the exposure time in the experiment must be sufficiently small.

KEY WORDS: *DBI, Mie-scattering, Sprays, Exposure Time, Liquid boundary detection*

1. INTRODUCTION

Liquid sprays are important for engineering applications such as drying, cooling, combustion, etc. In particular, clean combustion of liquid fuels in gas turbine and reciprocating engines requires an understanding of the complex physical processes associated with liquid fuel atomization, vaporization, and fuel-oxidizer mixing. These processes occur at harsh conditions of high pressures and temperatures, making it difficult to acquire detailed intrusive measurements. Thus, advanced optical diagnostic techniques and processing tools to study liquid sprays are of continual interest.

Ideally, measurements of droplet size, density, and velocity distributions throughout the spray are desired to fully understand the physical processes and to develop/support models for high-fidelity numerical simulations. Phase-Doppler particle analysis (PDPA) has been used to characterize sprays produced by twin-fluid swirl atomizers (Chong and Hochgreb, 2015), fuel injectors for gas turbines (Behrendt et al., 2006), flow blurring atomizers (Simmons and Agrawal, 2010), etc. Recently, x-ray radiography, an absorption based technique, has been used to measure the fuel mass fraction, fuel velocity, and penetration length (Kastengren et al., 2009; Ramirez et al., 2009; Yue et al., 2001), and to quantify the Sauter mean diameter of fuel droplets in the near injector region (Matusik et al., 2019). The laser absorption-scattering (LAS) technique, employing ultraviolet (UV) and visible wavelengths, has been developed to quantify droplet density and vapor concentration in diesel fuel sprays (Zhang et al., 2000). In LAS, the fuel is replaced with a liquid providing strong absorption of UV light and negligible absorption of visible light at the chosen wavelengths.

The above diagnostics are difficult to apply for the study of diesel-like fuel sprays because of the limited optical access, harsh ambient conditions, intermittent operation, and fast time scales. As such, global parameters such as liquid length, among others, are typically measured. Liquid penetration or liquid length defined as the distance between the injector exit and tip of the liquid jet is a standard measurement acquired by the diesel engine community (Manin et al., 2012; Siebers, 1998). Liquid length provides an indirect measurement of fuel vaporization and fuel-oxidizer mixing, and thus, it is useful to compare different fuel injection systems and/or

operating conditions.

Historically, Mie-scattering has been the standard method to measure liquid length in diesel sprays (Espey and Dec, 1995; Siebers, 1998). In these seminal works, a long exposure Mie-scattered image is acquired during the quasi-steady period of the diesel spray to determine the liquid length. However, Mie-scattering is sensitive to the illumination source, and hence, it is difficult to compare measurements from different test facilities (Manin et al., 2012). In recent years, the Engine Combustion Network (ECN) has recommended diffuse background illumination (DBI) as the new standard because the background light intensity also acts as the reference for calibration (Bardi et al., 2012). DBI is based on attenuation of light directly passing through the liquid spray. DBI provides greater sensitivity compared to Mie-scattering which detects the scattered light only in the direction of the camera, i.e., the light scattered in other directions does not contribute to the signal.

Although DBI and Mie-scattering are based on the same principles, a unifying post processing approach to determine consistent liquid length from different diagnostics can be challenging. For Mie-scattering, the simple approach of an intensity threshold based on sensitivity analysis is well-established (Siebers, 1998). For DBI, first, the optical thickness is determined according to the Beer-Lambert Law in Eq. 1.

$$\tau = -\log\left[\frac{I}{I_{bg}}\right] \tag{1}$$

In Eq. 1, I and I_{bg} are the local intensity and background intensity, respectively. The optical thickness (τ) can be correlated to the liquid length obtained by Mie-scattering (Hamzah et al., 2016; Jung et al., 2015-01-0946; Pickett et al., 2015; Westlye et al., 2016-01-0860). Alternatively, the decay rate of the optical thickness (via a linear tangent approach) is used to estimate the liquid length (Meijer et al., 2013; Nilaphai et al., 2016).

Recently, we presented a statistical approach to detect the liquid boundary in high pressure diesel sprays using rainbow schlieren deflectometry (RSD) (Wanstall et al., 2017, 2019). This probabilistic method was shown to obtain detailed features of the spray by RSD as compared to a single parameter such as the liquid length. The objective of the present work is to extend the statistical approach of (Wanstall et al., 2019) to diagnostics based on scattering and extinction

to describe the probability of liquid existence rather than a fixed parameter, e.g., liquid length. Thus, both Mie-scattering and DBI are used and compared to demonstrate the robustness of the proposed methodology - actually showing that the post-processing algorithm is independent of the diagnostics, and the procedure to find the threshold is built into the algorithm. A non-evaporating acetone spray at atmospheric conditions is used to minimize the refractive index gradients and associated beam steering. The paper is divided into six sections. The first section will discuss the experimental apparatus and hardware. Next, existing methods to detect the liquid boundary and/or length are evaluated. Then, the statistical algorithm is described and used to analyze Mie-scattering and DBI images. Next, the effect of exposure time is investigated in a parametric study. Lastly, the conclusions of the study are summarized.

2. EXPERIMENTAL SETUP

2.1 Spray Apparatus

Figure 1 shows a schematic and photograph of the test stand. A nitrogen supply bottle regulated to 10.5 MPa is used to pressurize the liquid storage tank filled with acetone atomized at atmospheric conditions. A three way valve was installed to fill and vent the pressurized tank. A needle valve located immediately downstream of the tank is used to control liquid injections at a high supply pressure. The acetone is injected continuously through an injector - a capped stainless steel tube with a laser drilled central opening of diameter, D = 75 µm in tube wall of thickness, L = 500 µm - at an estimated velocity and mass flow rate of 160 $^{m}/_{s}$ and 0.56 $^{g}/_{s}$, respectively. A 30 µm mesh filter was installed upstream of the injector to prevent blockage by any impurities in the acetone flow. The spray was contained within a Lexan enclosure with optical cutouts for the optical diagnostics. A ventilation system was installed downstream of the enclosure to safely vent the vaporized acetone.

2.2 Optical Setup

A Phantom v7.3 monochrome camera is used to acquire images for both Mie-scattering and DBI experiments. The camera was outfitted with a Sigma 105mm DG macro lens to obtain a spatial

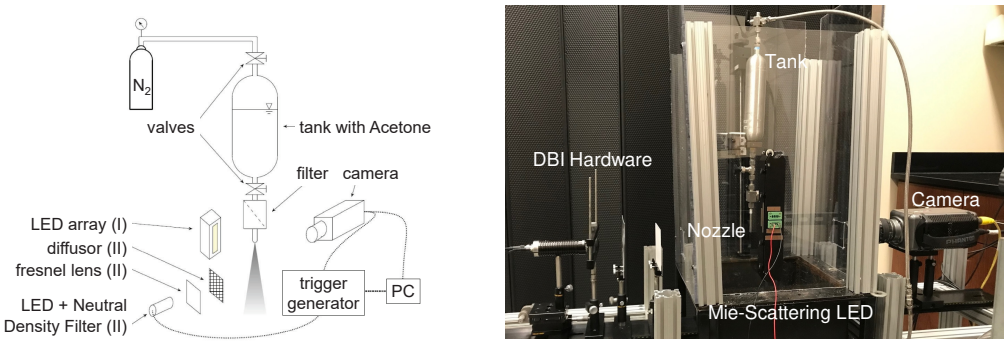

(a) (b)

FIG. 1: Schematic (a) and photograph (b) of the experimental setup. Mie-Scattering and DBI components are labeled, respectively, as I and II in the schematic.

resolution of 50 µm. The camera was operated at 10 kHz to acquire 5000 512 x 128 pixels images. Specific hardware details for each diagnostic are discussed in the following sections.

2.2.1 Mie-Scattering

A customized linear array of 20 individual light emitting diodes or LEDs (OH36-LGME by LightSpeed Technologies, Inc.) packaged in a single housing unit (about 50 mm x 50 mm x 250 mm) mounted on the square Lexan enclosure about 0.15 m away from the injector is used as the illumination source. A sheet generating optic was placed on the LED array and resulted in an approximately 3 mm thick light sheet - with a maximum intensity variation of 20% in the background - to illuminate the spray orthogonal to the camera view. Light scattered by the liquid and directed towards the camera is detected to identify the liquid boundary in an otherwise zero-intensity/black background. The 270 W source used to power the LED array resulted in a minimum exposure time for Mie-scattering of 1 µs; lower exposure times would require higher power light source exceeding the capacity of the LED array.

2.2.2 Diffuse Background-Illumination

The DBI setup is similar to the one described by (Westlye et al., 2017). A single pulsed broad-band LED (450 nm-700 nm) driven by a HPLS-36DD7500 Lightspeed Technologies driver was

installed inline with the camera as shown in Fig. 1. Spatially uniform high-intensity illumination was achieved by using a 125 mm x 125 mm Fresnel lens with an effective diameter of 100 mm and a focal length of 71 mm (Edmund Optics, 32-683) followed by an engineered diffuser (RPC Photonics, EDC-5-06217-A) with a divergence angle of 5 degrees. The small angle diffuser provides uniform illumination while minimizing beam steering (Westlye et al., 2017). The diffuser is outside the Lexan shield with holes cutout for the diffuser and camera. The distance between the diffuser and camera is 500 mm, and the injector is located in-between. The diffuse light attenuated by the liquid is measured by the camera and appears as darker regions in the otherwise bright DBI image. The Phantom v7.3 camera has a minimum exposure time of 1 µs. However, exposure times down to 5 ns were achieved by pulsing the LED driver by a signal generator (Stanford Research System, Model DG 645). Camera saturation at long exposure times was prevented by installing neutral density filters (Thorlabs, NDK01) immediately after the LED.

3. IMAGE PROCESSING

Figure 2 shows the instantaneous Mie-scattering (top) and DBI (bottom) images of the spray rotated 90 degrees counter-clockwise relative to the actual experimental setup, such that the injector tip is on the left. The images were acquired at an exposure time of 1 µs to eliminate the effects of motion blur (see Section 6 for details). Images show an attached bright (Mie-scattering) or dark (DBI) region until an axial distance of approximately x = 6 mm. Farther downstream, the bright/dark regions appear intermittently indicating liquid breakup and dispersion into ligaments and droplets. The jet width at x = 20 mm is approximately 2 mm. Images show a slight asymmetry in the spray likely caused by minor imperfections in the injector opening.

Figure 3 shows the time-averaged Mie-scattering (top) and DBI (bottom) images obtained from 5000 instantaneous images. The time-averaged images shows features similar to the instantaneous images in (Fig. 2), i.e., bright/dark regions representing the liquid core. However, the averaging has smoothed the downstream features as expected.

Next, the liquid length was determined from the time-averaged images in Fig. 3. Following

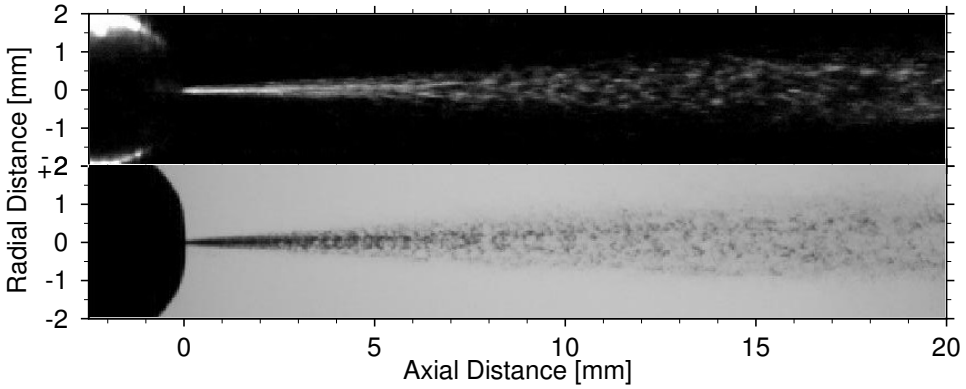

FIG. 2: Instantaneous Mie-scattering (top) and DBI (bottom) images acquired at exposure time of 1 µs. The images have been rotated counterclockwise 90 degrees orienting the injector on the left-hand side.

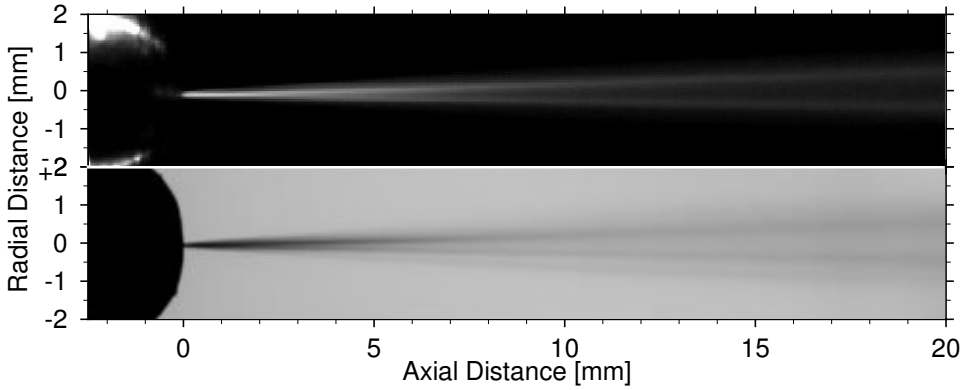

FIG. 3: Time-averaged Mie-scattering (top) and DBI (bottom) images based on 5000 instantaneous images.

(Siebers, 1998), the liquid length from the Mie-scattering image is found using threshold intensity, e.g., 3% of the maximum intensity. The threshold intensity could be greater than 3% if the image is saturated (Pickett et al., 2015) in which case a sensitivity analysis is used to identify the correct threshold. The liquid radius at each axial location is found by searching from the centerline in both directions outwards for the first radial pixel with intensity less than the threshold intensity. The liquid length is then determined from the location of the closed tip of the liquid jet.

For DBI, the linear tangent approach summarized in (Meijer et al., 2013; Nilaphai et al., 2016) is used to determine the liquid length instead of methods that require prior knowledge

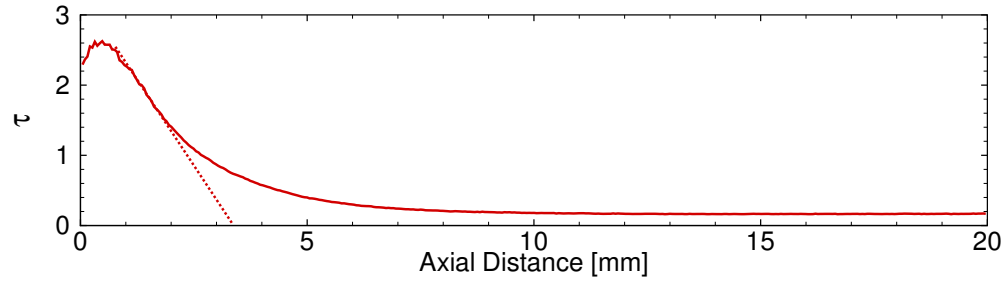

FIG. 4: Axial distribution of the optical thickness τ for the average DBI image in Fig. 3. Liquid length is determined where the tangent to the curve in the near-linear decay region intersects the x-axis.

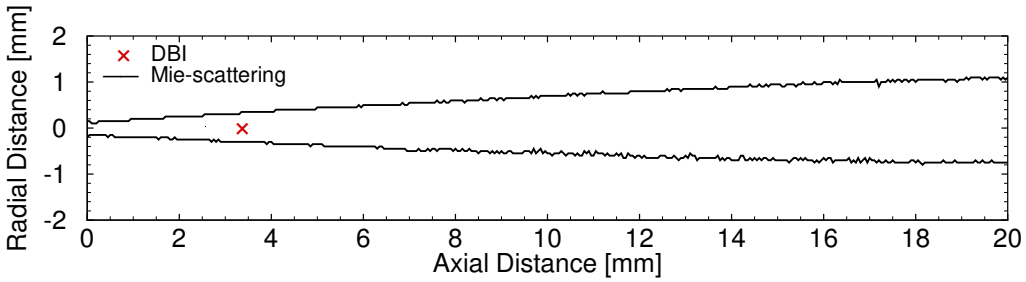

FIG. 5: The liquid boundary determined from Mie-scattering (black solid line) and liquid length (red 'x') measured by DBI.

of the liquid length data obtained by Mie-scattering. First, the average intensity at each pixel location is converted to the optical thickness, τ using Eq. 1. Then, the liquid length is found as the point intersecting tangent to the axial τ distribution in the near-linear decay region and the axial coordinate, i.e. x = 3.3 mm as shown in Fig. 4 (Meijer et al., 2013).

Figure 5 shows the liquid boundary from Mie-scattering images processed with 3% threshold intensity and illustrates that the liquid length is outside the field of view. However, the DBI linear tangent approach yields a liquid length of 3.3 mm shown by a red 'x' in Fig. 5. These results illustrate that the two methods to determine the liquid length are producing inconsistent results demonstrating the need for a robust post-processing methodology. The statistical approach discussed next identifies liquid existence on a probabilistic basis to yield consistent results regardless of the diagnostics.

4. PROPOSED STATISTICAL ALGORITHM

The procedure previously described for RSD (Wanstall et al., 2017, 2019) to determine the liquid boundary on a statistical basis is outlined in Algorithm 1. Thus, instead of analyzing a single time-averaged image, multiple instantaneous images are analyzed to create a probability map of liquid existence. In step 2, the threshold intensity for Mie-scattering is the measured value in the liquid region near the injector, while for DBI, it corresponds to the background intensity, I_{bg}.

Algorithm 1: Algorithm for liquid detection

Step 1 Compile all intensity values at each pixel location of each instantaneous image.
Step 2 Determine a threshold or reference intensity value to compare each intensity value obtained in the first step.
Step 3 Binarize each pixel in each instantaneous image with respect to the threshold such that the regions of liquid are given a value of 1.
Step 4 Add all instantaneous binarized values at each pixel location.
Step 5 Search for the last axial pixel which has a value equal to the maximum number of frames (liquid at every frame).
Step 6 Preform a threshold sensitivity analysis by repeating Steps 3-5.
Step 7 After identifying threshold, generate the final probability map by repeating steps 3-5.

Figure 6 shows a binarized image (step 3) for an arbitrary threshold intensity. The red and blue colors on the contour map signify pixel locations with or without liquid present on an instantaneous basis. As the threshold is changed, more or less pixels will be ”tagged” red or blue. The contour map of probability (or frequency) at each pixel registering liquid (step 4) is shown in Fig. 7. In this case, the farthest axial location with the highest liquid probability (100%) is approximately 5 mm (step 5). An accurate probability map requires a sufficiently large number of instantaneous images to capture the stochastic behavior of the injection event. Figure 8 plots the liquid probability at different locations in the spray versus the number of instantaneous images. In this case, the liquid probability at all locations in the spray converges if over 1000 images are used to calculate the liquid probability.

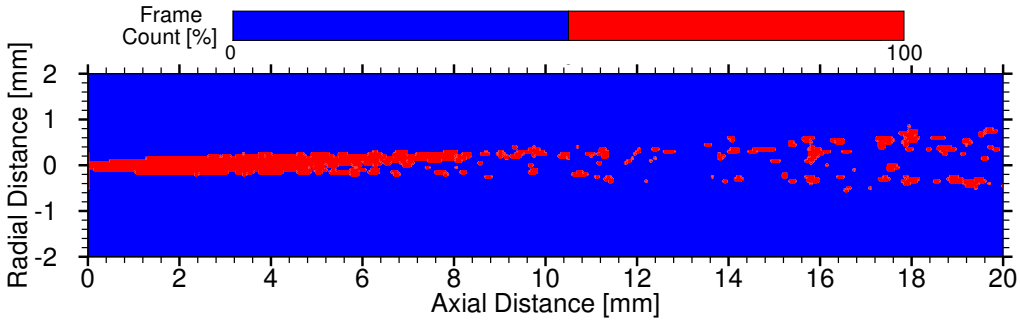

FIG. 6: Instantaneous DBI image binarized using intensity threshold of 80%. Intensity at red pixels is less and at blue pixels is greater than the threshold intensity.

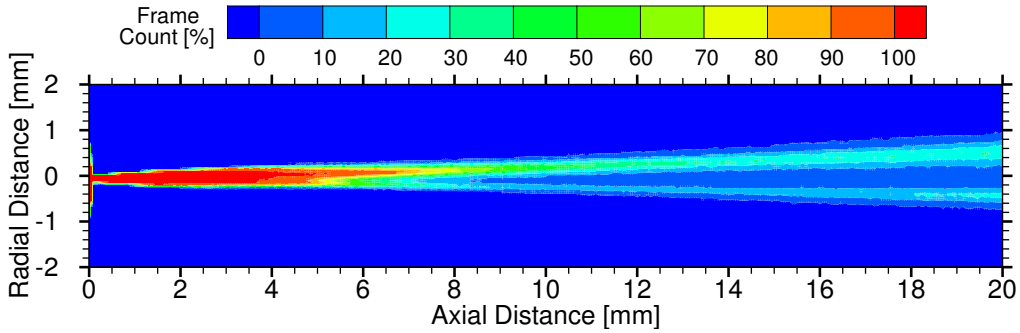

FIG. 7: Liquid probability contour map based on average of all binarized instantaneous (80% threshold) DBI images.

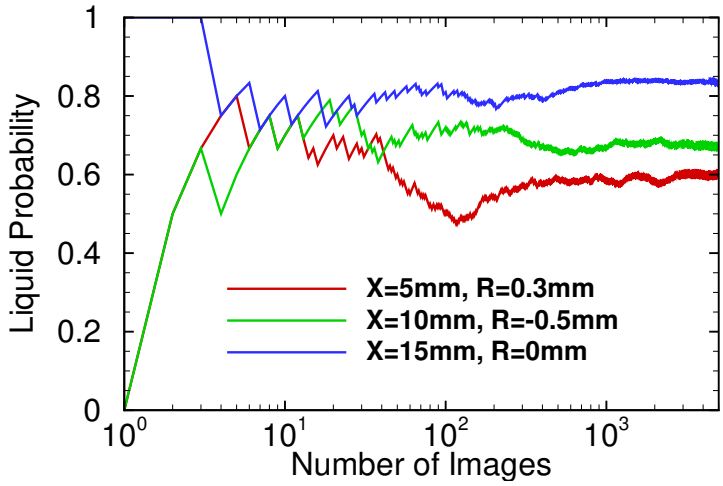

FIG. 8: Effect of the number of images on liquid probability calculation at multiple locations in the spray: two in the shear layer (red and green) and one at center-line (blue).

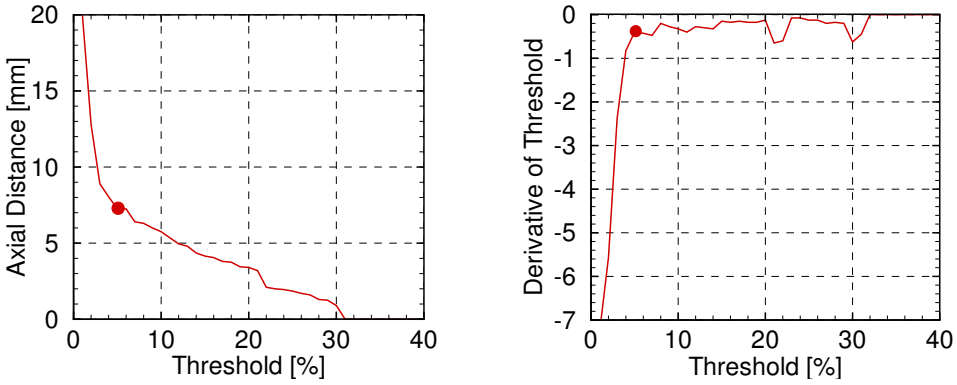

(a) (b)

FIG. 9: (Left) Effect of threshold intensity on the farthest axial distance with 100% liquid determined by Mie-Scattering. (Right) Effect of threshold intensity on derivative of the axial distance determined by Mie-Scattering images.

5. APPLICATION EXAMPLES

In this section, the statistical algorithm is applied to analyze experimental Mie-scattering and DBI images. In each experiment, 5000 frames were recorded at exposure time of 1 µs and the steady portion comprising between 1400 and 5000 image frames was used for post-processing. The results from both diagnostics are compared to demonstrate the efficacy of the approach.

5.1 Mie-scattering

The built-in sensitivity analysis to determine the threshold intensity is similar to the approach used by (Siebers, 1998), i.e., the chosen threshold is based on a distinct change in the output as the threshold changes. Figure 9(a) illustrates the sensitivity analysis, i.e., the farthest axial distance with 100% liquid versus threshold intensity (step 6). In Fig.9(b), the derivative (with respect to the threshold intensity) of the farthest axial distance where 100% liquid appears versus threshold intensity is plotted. These plots show that the axial distance with 100% liquid is insensitive to the threshold intensity for values greater than 5%, which is taken as the threshold intensity to binarize and obtain the final liquid probability map in Fig. 10.

The binarized plot (top) in Fig. 10 shows an instantaneous contour plot with and without liquid regions. The averaged plot (bottom) quantifies the presence of liquid in terms of liquid

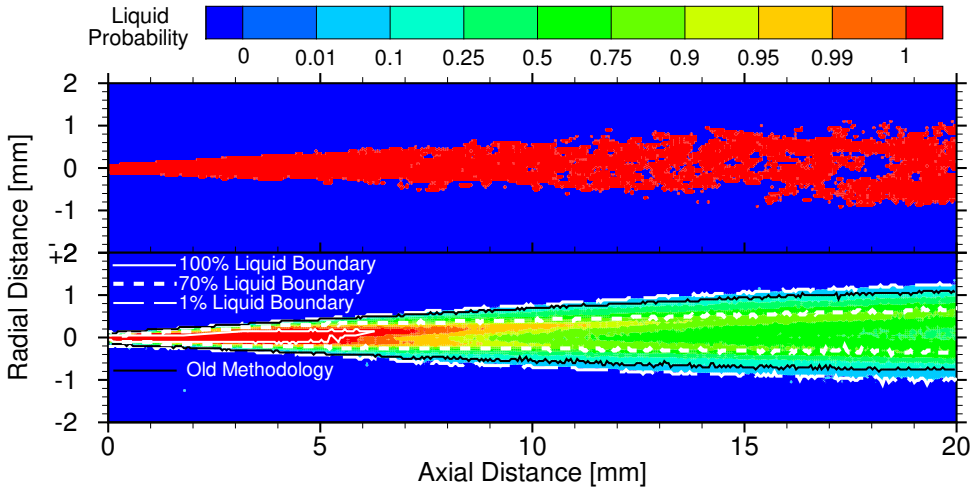

FIG. 10: (Top) Instantaneous Mie-scattering image binarized using intensity threshold of 5%. Intensity at red pixels is less and at blue pixels is more than the threshold intensity. (Bottom) Liquid probability contour map based on average of all binarized instantaneous (5% threshold) Mie-scattering images. The white solid, white dashed-dotted, white dashed, represent respectively the boundaries where the liquid probability is 100%, 70%, and 1%. The black solid line pertains to the existing 3% threshold methodology for Mie-scattering.

probability varying between 0 and 100%. The averaged plot also identifies 100% liquid boundary (solid white line), 70% liquid boundary (white dash-dotted line), and 1% liquid boundary (white line). Note that the 1% liquid boundary matches with the liquid boundary in Fig. 5 determined using the existing threshold-based methodology. However, the 100% liquid boundary represents a smaller region where liquid is present at all times. Similarly, 70% liquid boundary represents the surface with liquid present in only 70% of the instantaneous frames.

5.2 Diffuse Background-Illumination

The sensitivity analysis of the DBI images in Fig. 11 reveals a sudden change in axial distance at threshold intensity of about 90%. Figure 12 shows the corresponding binarized (instantaneous) and liquid probability plots. The instantaneous plot (top) shows randomized regions with no liquid starting at x = 8.5 mm. The jet breakup is illustrated by irregular structures represented by ligaments and droplets at around x = 7 mm. The jet width at x = 20 mm is about 2 mm, which agrees with the visual image in Fig. 2.

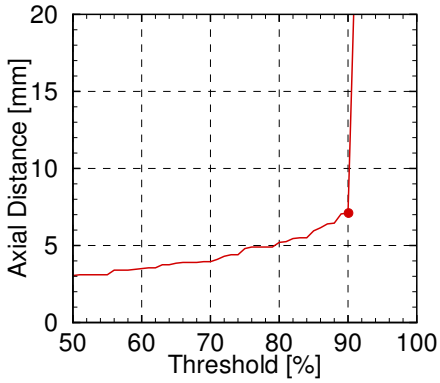

FIG. 11: Effect of threshold intensity on the farthest axial distance with 100% liquid determined from DBI images.

Figure 12 reveals a slightly wider jet (bottom plot) than the jet width on an instantaneous basis (top plot) indicating asymmetric temporal variations in the jet radial boundary. Spray asymmetry is also evident in the contour plot showing greater likelihood of liquid in the top half as compared to that in the bottom half. The probability contour map in Fig. 12 reveals a region where liquid appears 100% of the times (white solid line). The white dashed boundary represents liquid present only 1% of the times - similar to the Mie-scattering boundary presented in Section 3 or the spray boundary. The 70% liquid boundary denoted by white dash-dotted line represents an intermediate region.

5.3 Comparison of Liquid Boundaries

Figure 13 compares the liquid boundary (100% liquid probability) and spray boundary (1% liquid probability) as well as an intermediate boundary (70% liquid probability) for Mie-scattering and DBI. Interestingly, the two different diagnostics provide the same results demonstrating robustness of the proposed algorithms as compared to the inconsistent results obtained by existing methodologies. Figure 13 demonstrates a unique feature of the proposed statistical approach, i.e., different boundaries can be described based on the liquid probability. These results can be further improved by increasing the spatial resolution to achieve higher fidelity in locating the boundary.

Next, a different injector (diameter, D = 200 μm) is used with the same inlet conditions. The

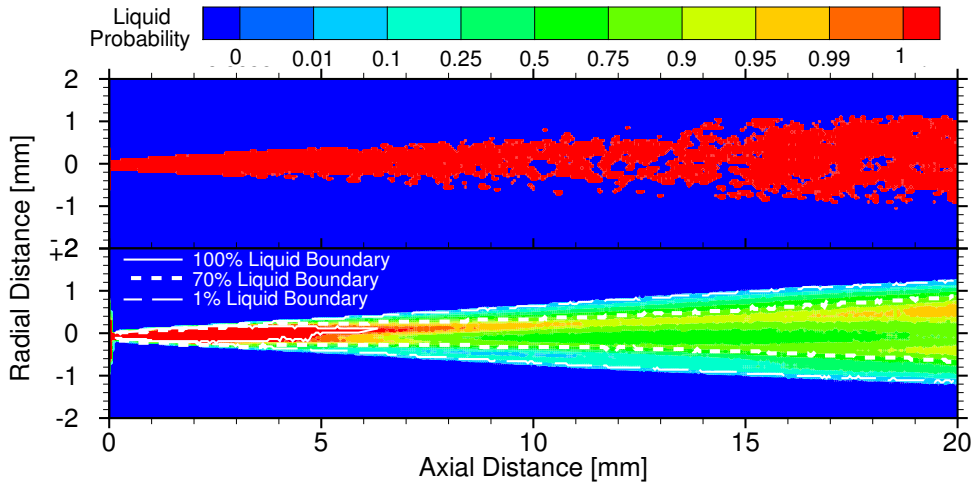

FIG. 12: (Top) Instantaneous DBI image binarized using intensity threshold of 90%. Intensity at red pixels is less and at blue pixels is more than the threshold intensity. Bottom: Liquid probability contour map based on average of all binarized instantaneous (90% threshold) DBI images. The white solid, white dashed-dotted, and white dashed lines represent the boundaries where the probability is 100%, 70% and 1%, respectively.

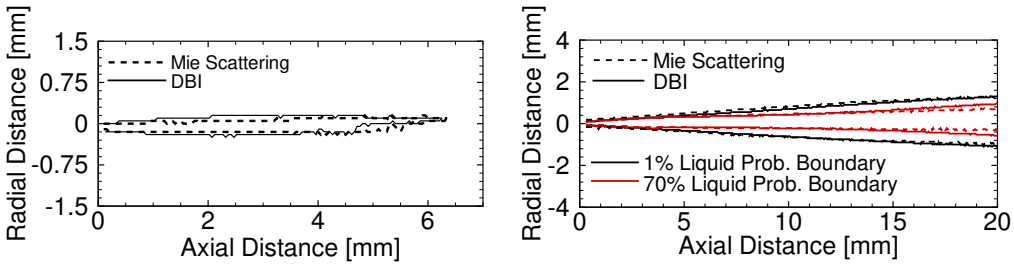

(a) (b)

FIG. 13: Comparison of the liquid boundary measured by Mie-scattering and DBI. The left figure shows the 100% liquid boundary, and the right figure shows the 70% and 1% liquid boundaries.

larger injector increases the spray width and thus, improves the spatial resolution. Figure 14(a) shows a wider 1% liquid boundary compared to that for 75 µm injector indicating that the larger diameter injector produces a wider spray. The measured results show excellent agreement between the two techniques, within 200 µm (one injector diameter) of each other. Figure 14(a). However, Fig. 14(b) shows two distinct 100% liquid boundaries resulting in a hollow cone structure. These results indicate a partially throttled injector as demonstrated in Ref. (Soteriou et al.,

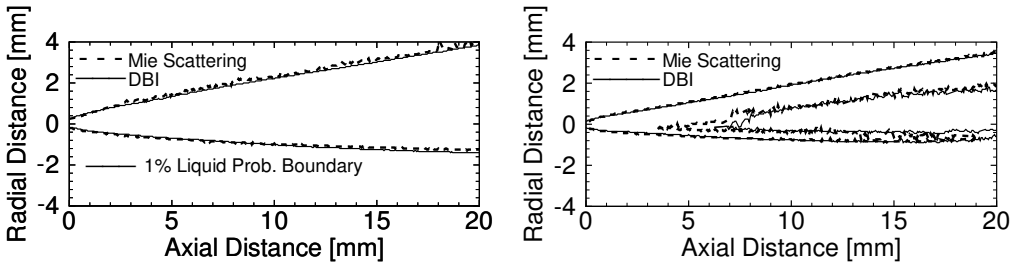

FIG. 14: Results from using a different injector (D = 200 µm) are shown for the 1% liquid boundary (left) the and 100% liquid boundary (right) for Mie-scattering and DBI.

2000). The 100% liquid boundaries measured by Mie-scattering (dashed-black line) and DBI (solid-black line) agree with each other within 200 µm (one injector diameter) at all locations except at the start of the inner boundary at axial distance of 3 to 5 mm. The slight inconsistencies in these regions are attributed to the detection limits of the Mie-scattering system causing very low sensitivities in the core region of the spray.

6. EFFECT OF THE EXPOSURE TIME

As discussed previously, the Mie-scattering image to determine the liquid boundary is typically acquired by long exposure hardware averaging (Siebers, 1998). Long exposure hardware averaged images are also used in DBI to determine the liquid length (Meijer et al., 2013). However, long exposure can introduce motion blur because liquid parcels and droplets would travel longer distances in a given snapshot, thereby, broadening the apparent liquid boundary/length. The intensity measured with motion blur will be different (greater for DBI and lesser for Mie-scattering) from that without the motion blur, which will affect the threshold intensity. However, it is unclear how motion blur affects the threshold intensity and ultimately the measured liquid boundary/length.

Thus, a parametric study was conducted to determine the effect of motion blur on the proposed algorithm. The experiments were repeated for a range of exposure times: 5 ns - 50 µs for DBI and 1 µs - 50 µs for Mie-scattering. Note that the minimum exposure time with DBI was

about 200 times smaller than that with Mie-scattering indicating an attractive feature of the DBI. The sensitivity analysis for DBI in Fig. 15(a) shows that exposure times greater than 1 µs tends to smooth out the step change in the axial distance (farthest 100% liquid location) as the threshold intensity is increased. However, for exposure times less than 1 µs, the axial distance is not affected by the exposure time (or threshold intensity) indicating negligible motion blur.

Similar results for Mie-scattering in Fig. 15(b) show that the measured axial distance with 100% liquid probability increases with increasing exposure time. The threshold intensities for exposure times of 5 and 10 µs were determined using a derivative analysis as shown in Fig. 9(b). For exposure times greater than 10 µs, the camera sensor became at least partially saturated. Camera saturation can produce camera charge blooming to neighboring pixels causing an artificial broadening of the boundary (Pickett et al., 2015). This is one possible reason that an appropriate threshold is not observed at higher exposure times. However, for the non-saturated (5 to 10 µs) cases where motion blur exists, the last predicted axial distance where 100% liquid is registered is consistent between DBI and Mie-scatter measurements. For exposure time of 5 µs, DBI and Mie-scattering predict 100% liquid penetration distances of 10 mm and 10.5 mm, respectively, and exposure time of 10 µs measures 100% liquid penetration distances of 12 mm and 13.5 mm, respectively.

Fig. 15 shows that motion blur can alter the liquid probability maps and thus, artificially lengthen the 100% liquid boundary. However, the 1% liquid (or spray) boundary is not affected by the motion blur since the liquid does not exist outside this boundary. Thus, the existing implementation of Mie-scattering to detect the so-called 1% liquid boundary is likely not affected by the long exposure experiments. The existing DBI methodology seems to detect a region near the 100% liquid boundary, which can be sensitive to the motion blur. However, motion blur in present experiments is eliminated for exposure times at or less than 1 µs since further reduction in exposure time did not change the 100% liquid boundary. Note that exposure times below 1 µs could not be realized with Mie-scattering, indicating that DBI provides better temporal resolution for a given light source.

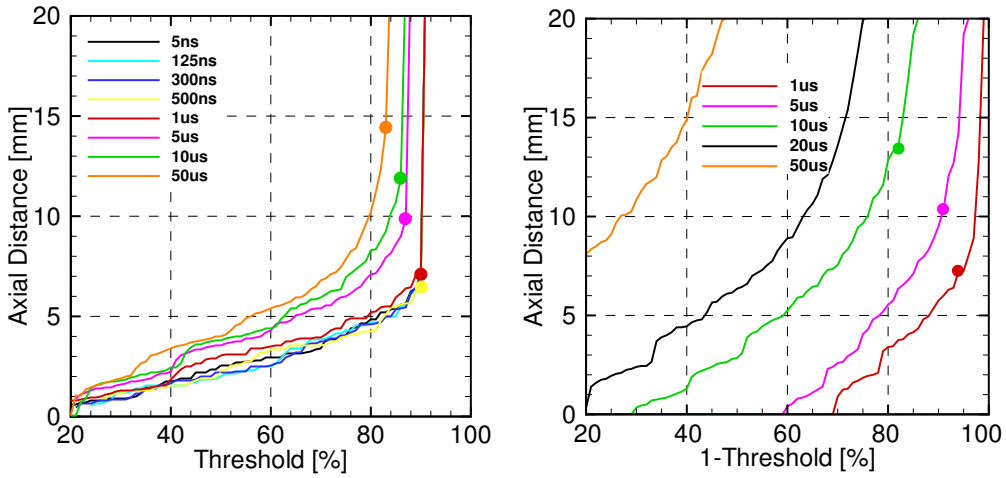

FIG. 15: Effect of exposure time on sensitivity analysis to determine the threshold intensity for DBI (left) and Mie-scattering (right) images.

7. CONCLUSIONS

In this study, a statistical algorithm is presented to identify liquid existence on a probabilistic basis (rather than on deterministic basis) in two-phase liquid sprays. The algorithm was applied to analyze Mie-scattering and DBI images of a quasi-steady non-evaporating acetone spray at atmospheric conditions. A parametric study of the effects of the exposure time was also conducted for both diagnostics. The conclusions of the study are as follows:

- The methodology developed in this work provides a rigorous stand-alone post-processing methodology to obtain the liquid length from both Mie-scattering and DBI.

- The probability map obtained by the present statistical approach describes liquid existence on a probabilistic basis. The approach provides greater details of the spray instead of previous methodologies which provide only a single parameter, i.e., liquid length.

- The liquid boundary was detected consistently regardless of the diagnostics. For example, boundaries representing 100%, 70%, and 1% probability of liquid obtained by Mie-scattering and DBI matched with each other.

- The liquid probability map can be affected by the motion blur, which must be eliminated to prevent artificial thickening of the boundaries. In this regard, DBI is recommended since the minimum exposure time with DBI was 200 times smaller than that with Mie-Scattering using an illumination source of similar power.

This work can be applied to analyze transient sprays such as diesel injections. However, multiple injection events are required to obtain an ensemble dataset at each instant as demonstrated in Ref. (Wanstall et al., 2019). Application of the proposed algorithm to evaporating sprays will require a careful assessment of beam steering introduced by refractive index gradients, which is a task beyond the scope of the present study.

ACKNOWLEDGMENTS

This research was supported in part by the Department of Energy, Office of Energy Efficiency and Renewable Energy (EERE), under Award Number DE-EE0007980. Henning Junne's visit to the University of Alabama was funded by the German Academic Exchange Service (DAAD).

REFERENCES

Bardi, M., Payri, R., Malbec, L.M.C., Bruneaux, G., Pickett, L.M., Manin, J., Bazyn, T., and Genzale, C.L., Engine combustion network: comparison of spray development, vaporization, and combustion in different combustion vessels, *Atomization and Sprays*, vol. **22**, no. 10, pp. 807–842, 2012.

Behrendt, T., Carl, M., Heinze, J., and Hassa, C., Optical measurements of the reacting two-phase flow in a realistic gas turbine combustor at elevated pressures, *Atomization and Sprays*, vol. **16**, no. 5, pp. 475–491, 2006.

Chong, C.T. and Hochgreb, S., Effect of atomizing air flow on spray atomization of an internal-mix twin-fluid atomizer, *Atomization and Sprays*, vol. **25**, no. 8, pp. 657–673, 2015.

Espey, C. and Dec, J.E., The effect of tdc temperature and density on the liquid-phase fuel penetration in a di diesel engine, *SAE transactions*, pp. 1400–1416, 1995.

Hamzah, A., Poursadegh, F., Lacey, J., Petersen, P., Brear, M., and Gordon, R., A comparison of diffuse

back-illumination (dbi) and mie-scattering technique for measuring the liquid length of severely flashing spray, *Proceedings of the 20th Australasian Fluid Mechanics Conference*, pp. 669–672, 2016.

Jung, Y., Manin, J., Skeen, S., and Pickett, L.M., Measurement of liquid and vapor penetration of diesel sprays with a variation in spreading angle, Tech. rep., SAE Technical Paper, 2015-01-0946.

Kastengren, A.L., Powell, C.F., Wang, Y., Im, K.S., and Wang, J., X-ray radiography measurements of diesel spray structure at engine-like ambient density, *Atomization and Sprays*, vol. **19**, no. 11, pp. 1031–1044, 2009.

Manin, J., Bardi, M., and Pickett, L.M., Sp2-4 evaluation of the liquid length via diffused back-illumination imaging in vaporizing diesel sprays (sp: Spray and spray combustion, general session papers), *The Proceedings of the International symposium on diagnostics and modeling of combustion in internal combustion engines 2012.8*, The Japan Society of Mechanical Engineers, pp. 665–673, 2012.

Matusik, K., Sforzo, B., Seong, H.J., Duke, D., Kastengren, A.L., Ilavsky, J., and Powell, C.F., X-ray measurements of fuel spray specific surface area and sauter mean diameter for cavitating and non-cavitating diesel sprays, *Atomization and Sprays*, vol. **29**, no. 3, pp. 199–216, 2019.

Meijer, M., Galle, J., Somers, L., Griensven, J., and Verhelst, S., High-speed characterization of ecn spray a using various diagnostic techniques, *SAE International Journal of Engines*, vol. **6**, no. 2, pp. 1238–1248, 2013.

Nilaphai, O., Hespel, C., Moreau, B., Contino, F., Bourgeois, N., Chanchaona, S., Foucher, F., and Mounaïm-Rousselle, C., New high pressure and high temperature chamber for diesel spray characterization, *27th Annual Conference on Liquid Atomization and Spray Systems ILASS–Europe, Brighton, UK*, pp. –, 2016.

Pickett, L., Genzale, C., and Manin, J., Uncertainty quantification for liquid penetration of evaporating sprays at Diesel-like conditions, *Atomization and Sprays*, vol. **25**, no. 5, pp. 425–452, 2015.

Ramirez, A., Som, S., Aggarwal, S.K., Kastengren, A., El-Hannouny, E., Longman, D., and Powell, C., Quantitative x-ray measurements of high-pressure fuel sprays from a production heavy duty diesel injector, *Experiments in fluids*, vol. **47**, no. 1, pp. 119–134, 2009.

Siebers, D., Liquid-Phase Fuel Penetration in Diesel Sprays, *SAE transactions*, vol. **107**, no. 3, pp. 1205–1227, 1998.

Simmons, B.M. and Agrawal, A.K., Spray characteristics of a flow-blurring atomizer, *Atomization and*

Sprays, vol. **20**, no. 9, pp. 821–835, 2010.

Soteriou, C., Andrews, R., Smith, M., Torres, N., and Sankhalpara, S., The flow patterns and sprays of variable orifice nozzle geometries for diesel injection, *SAE transactions*, pp. 1007–1029, 2000.

Wanstall, C.T., Agrawal, A.K., and Bittle, J.A., Quantifying liquid boundary and vapor distributions in a fuel spray by rainbow schlieren deflectometry, *Applied optics*, vol. **56**, no. 30, pp. 8385–8393, 2017.

Wanstall, C.T., Agrawal, A.K., and Bittle, J.A., Phase boundary detection in transient, evaporating high-pressure fuel sprays by rainbow schlieren deflectometry, *Applied Optics*, vol. **58**, no. 25, pp. 6791–6801, 2019.

Westlye, F., Penney, K., Ivarsson, A., Pickett, L., Manin, J., and Skeen, S., Diffuse back-illumination setup for high temporally resolved extinction imaging, *Applied Optics*, vol. **56**, no. 17, pp. 5028–5038, 2017.

Westlye, F.R., Battistoni, M., Skeen, S.A., Manin, J., Pickett, L.M., and Ivarsson, A., Penetration and combustion characterization of cavitating and non-cavitating fuel injectors under diesel engine conditions, Tech. rep., SAE Technical Paper, 2016-01-0860.

Yue, Y., Powell, C.F., Poola, R., Wang, J.C., and Schaller, J.K., Quantitative measurements of diesel fuel spray characteristics in the near-nozzle region using x-ray absorption, *Atomization and sprays*, vol. **11**, no. 4, pp. 471–490, 2001.

Zhang, Y.y., Yoshizaki, T., and Nishida, K., Imaging of droplets and vapor distributions in a diesel fuel spray by means of a laser absorption–scattering technique, *Applied Optics*, vol. **39**, no. 33, pp. 6221–6229, 2000.

Implications of Real-Gas Behavior on Refractive Index Calculations for Optical Diagnostics of Fuel-Air Mixing at High Pressures

C. Taber Wanstall[b], Ajay K. Agrawal[b,a], Joshua A. Bittle[b]

[a] *corresponding author, aagrawal@eng.ua.edu*
[b] *University of Alabama, Alabama, United States*

Abstract

Three models to compute the refractive index of gaseous mixtures at real gas conditions are presented with the purpose to improve the accuracy of state relationships between refractive index and thermodynamic properties. Models are compared with experimental data to determine one that is applicable to high pressure mixtures with non-ideal thermodynamic behavior near or above a fluids' critical point. The optimal model is applied to analyze adiabatic thermal mixing of fuel and air at typical diesel engine conditions. Results show that the ideal gas mixture law is appropriate in the vapor region, assuming it is known, for example, from experimental measurements. Finally, the model is applied for binary fuel-air mixing at supercritical conditions to demonstrate its full potential.

Keywords: Refractivity, Real-Mixture Thermodynamics, Lorentz-Lorenz Equation, Compression Ignition Engine, Polarizability

1. Introduction

For combustion applications such as diesel engines and gas turbines, fuel is injected into a hot, high pressure oxidizer environment. Ambient air entrainment and turbulent mixing with fuel results in a gaseous phase fuel-air mixing region containing the combustible mixture. Rayleigh scattering can be used to acquire vapor-phase fuel concentration and temperature measurements [1, 2]. In two-phase systems, the Rayleigh scattering signal of the vapor phase must be separated from the Mie scattering signal of the liquid phase. Thus, Mie and Rayleigh scattering diagnostics are often used together, though not simultaneously, to distinguish each phase [3]. Rayleigh scattering is the elastic scattering of light quanta from particles smaller than the wavelength of light, and the measured intensity of the Rayleigh signal (I_R) can be related to the local gaseous mixture properties using Eq. 1 [1].

$$I_R = C I_l N \sum_i X_i \sigma_i \tag{1}$$

Where C, I_l, N, X, and σ are respectively the calibration constant, intensity of the incident light, total number density (molecules per m^3), mole fraction, and Rayleigh scattering cross section. The subscript i represents a species in the gaseous mixture. The Rayleigh scattering cross section is related to the incident light wavelength (λ) and the species refractive index (n) according to Eq. 2 [4].

$$\sigma_i = \frac{24\pi^3}{\lambda^4}\left[\frac{n^2-1}{(n^2+2)N_0}\right]^2 = \frac{24\pi^3}{\lambda^4}\left[\frac{r_e}{N_0}\right]^2 \tag{2}$$

Where N_o is the total molecular number density at standard pressure and temperature (STP), and the refractivity (r_e) is substituted for the refractive

index terms. In the engine community for n $\approx$ 1 , the refractivity (r_e) in Eq. 2 is approximated by Eq. 3:

$$r_e = \frac{n^2 - 1}{(n^2 + 2)} \approx \frac{2}{3}(n - 1) \tag{3}$$

thereby approximating the Rayleigh cross-section as Eq. 4 [1].

$$\sigma_i = \frac{24\pi^3}{\lambda^4} \left[\frac{2(n_i - 1)}{3N_0} \right]^2 \tag{4}$$

For an ideal gas, the number density, N, is determined from the total inlet enthalpy by assuming adiabatic fuel-air mixing [1, 5] as outlined in the ECN [6]. Relating Rayleigh signal to species mole fraction using Eq. 1 and Eq. 4 requires relationships between the refractive index and the thermodynamic properties (i.e., state relationships) for each species as inputs.

In recent years, the line-of-sight rainbow schlieren deflectometry (RSD) technique has been used to obtain the thermodynamic properties in laminar gaseous systems, as outlined in Ref. [7]. However, Wanstall *et al.* have shown the potential of RSD for quantitative measurements in the fuel-air mixing region of diesel sprays [8]. They developed the RSD methodology to simultaneously detect the liquid phase boundary and estimate thermodynamic properties in the surrounding vapor zone to overcome the need for requiring two separate diagnostics for such measurements [8, 9]. RSD directly measures the refractive index which can be related to the thermodynamic properties using the state relationships discussed previously. For an ideal gas with $n \approx 1$, refractive index is related to density using the Dale-Gladstone equation:

$$n - 1 = k\rho = k\frac{PM}{\overline{R}T} \tag{5}$$

Where k is the Dale-Gladstone constant, P is the pressure, M is the molecular weight, $\overline{R}$ is the universal gas constant, and T is the temperature. For an ideal gas mixture,

$$n - 1 = k_{mix}\rho_{mix} = \frac{P}{\overline{R}T}\sum k_i M_i X_i \tag{6}$$

where , X is the species mole fraction, and subscript i refers to species i. The Dale-Gladstone relation uses the same linearized approximation for refractive index ($n \approx 1$) shown in Eq. 3. Thus, both Rayleigh scattering and RSD rely upon the state relationships between refractive index (only the real-part is considered here) and thermodynamic properties, e.g., Eq. 5 for an ideal gas and Eq. 6 for ideal gas mixtures.

Both Rayleigh scattering and RSD have been used to obtain accurate measurements in combustion environments at atmospheric pressures [10, 11]. However, state-of-the-art combustion engines operate at high pressures (e.g., cylinder pressures exceeding 100 bar in diesel engines) and thus ideal gas law and/or ideal mixing laws (e.g., Amagat's Law) may not be applicable.. Recent experimental and theoretical findings have challenged the conventional paradigm by suggesting that the pressure and temperature in modern diesel engines can exceed the thermodynamic supercritical conditions for liquid/gas mixtures in regions of the fuel jet [12, 13, 14, 15, 16, 17, 18, 19]. Thus, the mixing processes and mixture laws in fuel spray could be different than conventionally described. [20, 21]. Oefelein *et al.* have described the evolution of a purely supercritical spray without liquid droplets and surface tension forces where mixing between the fuel jet and the surrounding ambient is dominated by turbulent diffusion [22]. These non-ideal gas conditions require real fluid thermodynamic mixture models. Large eddy simulations

(LES) studies based on real fluid equation of state (EOS) have determined that the fuel-air mixing is profoundly modified by the non-ideal gas thermodynamic properties [23, 24, 25]. Recently, Crua *et al.* showed that the fuel-air mixing at diesel conditions can occur by the classical evaporation of fuel droplets, purely diffusive mixing between supercritical fuel and ambient air, or a combination of both, i.e., transcritical mixing, depending on the pressure and temperature of the ambient environment [18].

The above review raises the following important question, "Are current ideal gas mixture laws relating refractive index to thermodynamic properties valid for applications such as modern diesel environments where the gaseous mixtures can be non-ideal?". Thus, the objective of this study is to develop a robust model to relate optical (e.g, refractive index) and thermodynamic (e.g., density) properties of real-gas mixtures at high pressures. This paper is divided into six more sections. First, the Lorentz-Lorenz equation providing the link between a microscopic quantity (polarizability) and a macroscopic quantity (refractive index) is presented. The next two sections discuss polarizability and thermodynamic models for pure substances and gaseous mixtures. Then, three different models are presented to compute the refractive index of a real gas mixture, and compare them against experimental data available in the literature. Next, the refractive index models are investigated for an extensive range of diesel engine conditions including Spray A, as defined by the ECN community [6]. Then the best model is applied to the problem of fluid mixing at supercritical conditions to demonstrate its full potential. Finally, the conclusions of the paper are summarized.

2. Lorentz-Lorenz Equation

The theoretical basis for relating refractive index to density is embedded in the state equation of electromagnetic polarization established in the late 19^{th} and early 20^{th} century [26, 27]. As the electromagnetic wave travels through a medium, the wave's phase velocity changes proportionally to the refractive index of the substance. At the atomic level, this is caused from disturbances created by the electromagnetic field in the charge of each atom (mostly electrons), and how closely the charges are packed (density). The susceptibility of the substance to these disturbances is called the molecular polarizability, α. The end result is the so called Lorentz-Lorenz equation relating refractive index to molecular polarizability (α) and molar density ($\overline{\rho}$) shown in Eq. 7 from which the Dale-Gladstone equation (Eq. 5) is derived. The Lorentz-Lorenz equation applies to an isotropic system containing non-polar substances with no molecular interactions, e.g., each molecule is treated as an isolated system.

$$r_e = \frac{n^2 - 1}{(n^2 + 2)} = \frac{N_A \alpha}{3} \overline{\rho} = \frac{N_A \alpha}{3M} \rho \tag{7}$$

Where N_A, α, and M are Avogadro's number (constant), mean molecular polarizability, and molecular weight, respectively. Note that Eq. 7 can be written either using molar or mass density (ρ). For $n \approx 1$, the Lorentz-Lorenz equation (Eq. 7) can be simplified to the Dale-Gladstone formulation (Eq. 5) in which the Dale-Gladstone constant is:

$$\kappa = \frac{3}{2} \frac{N_A \alpha}{3M} \tag{8}$$

Figure 1 plots the error in refractivity r_e introduced by the Dale-Gladstone approximation for various hydrocarbons, and highlights regions with errors

greater than 5 and 10 percent. The exponential of r_e is shown on the vertical axis to highlight the difference between Lorentz-Lorenz and Dale-Gladstone equations. Considering the error introduced by the Dale-Gladstone approximation, especially at high refractive index values, it is not recommended for the analysis. The Lorentz-Lorenz Eq. 7 requires virtually no additional effort with today's modern computing power. Thus, moving forward, the Lorentz-Lorenz Eq. 7 will be used and the Dale-Gladstone Eq. 5 will not be considered.

The primary focus of the present study is to extend Eq. 7 for gaseous mixtures at high pressures. This requires accurate models to relate the mixture refractivity (or mixture refractive index) to polarizability and density of the mixture and/or its components. In the next two sections, polarizability and density calculations for pure substances and mixtures are discussed, and then, different refractivity mixture models analyzed in this work will be introduced.

3. Polarizability Models

3.1. Single Component

Polarizability is often reported in the literature at standard temperature and pressure (STP), T = 273 K and P = 1 bar. Gardiner *et al.* provide a detailed data set for polarizability of numerous combustion related substances in [28], and Bosque *et al.* provide one of the largest experimental data sets for polarizability with over 400 compounds including many diesel surrogate fuels [29] such as *n*-heptane and *n*-dodecane. However, the validity of using polarizability data at STP for applications at high pressures or temperatures

is not immediately clear. Thus, existing literature was searched to identify experimental studies that report polarizability of several gases as functions of pressure and temperature [30, 31, 32]. Figure 2 shows the percent change in polarizability with pressure for seven species relevant to this study at a constant temperature of 305 K except for heptane at 550 K, i.e., close to its critical temperature.

Figure 2 shows a slight increase and then decrease in polarizability with increasing pressure for all seven species. However, the change in polarizability with pressure is small, less than 1 percent, except for CO_2 at around its critical point of 304 K and 73.9 bar where the difference from the STP value is about 4.5%. Polarizability also has a slight linear temperature dependence [32], especially for propane among the seven species considered in this study. However, at some pressures/temperatures the temperature effect counteracts the pressure effect, e.g., the temperature effect can cause a decrease in polarizability while the pressure can cause an increase [32]. Still, the effect of pressure and temperature on polarizability is quite small for combustion relevant species, less than 5% of the value at the reference conditions. Thus, following the Lorentz-Lorenz formulation of Eq. 7, polarizability at STP is used to rewrite Eq. 7 as Eq. 9

$$r_e = \frac{n^2 - 1}{n^2 + 2} = \overline{A}\overline{\rho} = A\rho \tag{9}$$

where $\overline{A} = \frac{N_A \alpha}{3}$ and $A = \frac{N_A \alpha}{3M}$ are, respectively, mole and mass based constants. More advanced forms of the Lorentz-Lorenz Eq. 7 have been developed by Buckingham [33, 34, 35] where the refractivity (or refractive index) is calculated from a higher order virial expansion as shown in Eq. 10. Equation 10 accounts for pressure and temperature effects on polarizability as

shown in Fig. 2.

$$r_e = \frac{n^2 - 1}{n^2 + 2} = [\overline{A} + \overline{B}\overline{\rho} + \overline{C}\overline{\rho}^2 + ...]\overline{\rho} \tag{10}$$

3.2. Mixtures

For mixtures, Buckingham *et al.* [36] derived a theoretical basis for Eq. 10 as shown in Eq. 11.

$$\overline{A}_{mix} = \sum_i \overline{A_i} X_i \tag{11a}$$

$$\overline{B}_{mix} = \sum_{i,j} \overline{B}_{i,j} X_i X_j \tag{11b}$$

The constant $\overline{A}$ is the same as in Eq. 9. However, the coefficient $\overline{B}$ requires an interaction term (B_{ij}) which is generally unknown. Since the higher order virial coefficients are negligible (as shown in the last section), the first term alone (i.e., $\overline{A}$) is a good approximation to compute the mixture polarizability, and will be used in this study. Nearly linear behavior of mixture polarizability ($\overline{A}_{mix} = \sum_i \overline{A_i} X_i$) has been observed in supercritical environments for methanol-carbon dioxide and ethanol-carbon dioxide mixtures [37, 38].

4. Thermodynamic Models

4.1. Single Component

Real fluid EOS are well-developed for determining thermodynamic properties at non-ideal gas conditions. The most useful EOS are semi-empirical or empirical in nature. Once reasonable computing power became available in 1960s, empirical multiparameter EOS became the new standard [39].

The most recent and accurate multiparameter EOS are formulated in terms of reduced Helmholtz energy, a. Equation 12 shows the form of the reduced Helmholtz EOS [40]

$$\begin{aligned} \frac{a(T,\rho)}{RT} &= \frac{a^{IG}(T,\rho) + a^{R}(T,\rho)}{RT} \\ &= f^{IG}(\tau,\delta) + f^{R}(\tau,\delta). \end{aligned} \tag{12}$$

where T is temperature, R is the ideal gas constant, the parameters δ and τ are the reduced density and temperature based on the critical values (ρ/ρ_c and T_c/T). The superscripts IG and R stand for the ideal gas and residual, respectively. The ideal gas Helmholtz energy is generally obtained from the isobaric ideal gas heat capacity correlation shown in Eq. 13

$$\begin{aligned} a^{IG} = a_o + \int_{T_o}^{T} (c_P^{IG} - R)dT - \\ T\int_{T_o}^{T} \frac{c_P^{IG} - R}{T} dT + RT\ln(\frac{\rho}{\rho_o}). \end{aligned} \tag{13}$$

where c_p is the specific heat and the subscript o refers to a chosen reference state. Often empirical calorimetric data (c_p) are correlated with polynomial functions [40].

The residual part, loosely supported by theoretical considerations, is given by a general empirical function:

$$f^{R}(\tau,\delta) = \sum_{k=1}^{k=n} N_k \delta^{d_k} \tau^{t_k} + N_k \delta^{d_k} \tau^{t_k} \exp(-\delta^{l_k}). \tag{14}$$

Where N, d, t, and l are substance specific coefficients determined by a complex multivariable fitting procedure; in which the summation contains between 4-20 terms [41]. Often vapor-liquid equilibrium of a substance is utilized to optimize these EOS parameters. Once the EOS is determined,

consistency can be checked by ensuring that pressure (P), temperature (T), and Gibbs function ($\overline{g}$) values follow vapor-liquid (V and L) equilibrium conditions, respectively.

$$\begin{aligned} P^L &= P^V \\ T^L &= T^V \\ \overline{g}^L &= \overline{g}^V. \end{aligned} \tag{15}$$

Figure 3 shows the effect of pressure on density in terms of percent difference between real gas and ideal gas models. Figure 3 shows that computing density from ideal gas law leads to large errors at high pressures, as expected. The sharp peaks for methane, heptane, and carbon dioxide in Fig. 3 are a consequence of phase change not accounted for by the ideal gas law. At temperatures farther away (higher) from the critical point, the errors would decrease because the density decreases at high temperatures (for a given pressure), and hence, the substance approaches towards the ideal gas conditions, i.e., compressibility factor closer to unity. Comparing Fig. 2 and Fig. 3, one can observe that the pressure has a negligible effect on polarizability but a much greater effect on the density of the pure substance. Thus, accurate density calculations will require a real gas equation of state at high pressures.

4.2. Mixtures

The Helmholtz energy equation can be extended to fluid mixtures. Each component of the mixture is linearly combined and weighted by mole fraction to obtain the mixture EOS. For fluid mixtures with negligible intermolecular interactions between the species, mole weighted additive principle is sufficient. However, a comprehensive treatment of fluid mixtures requires a

departure function to account for the intermolecular mixture dynamics. The departure function is determined through regression analysis of available experimental data [42, 43] and is shown in Eq. 16 where $\vec{X}$ represents the mole fraction of all species as a vector.

$$f(\tau, \delta, \vec{X}) = \sum_i X_i f_i^{IG}(\tau, \delta) + X_i f_i^R(\tau, \delta) + \Delta f(\tau, \delta, \vec{X}) \tag{16}$$

This approach was further improved for binary mixtures in Ref. [44] where the reducing functions, $\tau(x)$ and $\delta(x)$, are determined for the mixture to produce a reduced mixture Helmholtz EOS. The mixture's reduced temperature and density are determined by applying weighting functions to each component's reduced temperature and density and the general functional form is shown in Eq. 17

$$Y_r(\boldsymbol{X}) = \sum_{i=1}^{N} x_i^2 Y_{c,i} + \sum_{i=1}^{N-1} \sum_{j=i+1}^{N} 2 x_i x_j \frac{x_i + x_j}{\beta_{Y,ij} x_i + x_j} Y_{ij}. \tag{17}$$

Where Y is a function of either density or temperature, β is one of the fitting parameters, and the subscripts r and c refer to the reduced and critical property parameters, respectively. The fitting parameters e.g. β in Eq. 17 are obtained by matching the numerical thermodynamic surface to experimental data points for the mixture, namely the bubble and dew points. The binary interaction parameters, and thus, the mixture EOS obtained are only as good as the experimental data upon which they are based [44]. In this study, the software package REFPROP by NIST incorporating the above methodology with features such as a python library for thermodynamic mixture property calculations [45] for a limited number of substances and even a smaller set of binary mixtures has been used.

5. Refractive Index Models

5.1. Model Development

The Lorentz-Lorenz Eq. 7 was formulated for pure substances, and unfortunately, little research exits to extend it to real gas mixture at high pressures. Nevertheless, Liu et al.provide a detailed summary of different first order mixture laws for refractivity (r_e) neglecting the higher order terms in Eq. 10 and the subtleties associated with each one [46]. Mixture laws can be divided into two categories - additive refractivity and additive polarizability. Both are an extension of the Amagat's law whereby the mixture property is calculated as the mole-weighted summation of the component property, i.e., refractivity or polarizability. The general form of the additive refractivity formulation is given in Eq. 18.

$$r_{e,mix} = \sum_i r_{e,i} X_i = \sum_i \overline{A}_i \overline{\rho}_i X_i \tag{18}$$

In the additive polarizability formulation, the mixture polarizability, $\overline{A}_{mix}$, is calculated from Eq. 11a to obtain the mixture refractivity, $r_{e,mix}$, from Eq. 19.

$$r_{e,mix} = \overline{\rho}_{mix} \overline{A}_{mix} = \overline{\rho}_{mix} \sum_i \overline{A}_i X_i \tag{19}$$

Here, $\overline{\rho}_{mix}$ is the mixture density. These formulations have been used for mixtures of gases and liquids, though with no particular attention to real gas mixtures. In this study, three different models are formulated to calculate the refractivity of gaseous mixture. The first is an ideal gas model while the last two are real-gas models. For the ideal gas model, the two formulations in Eq. 18 and Eq. 19 are identical.

Ideal Gas (IG) Model

$$\frac{n^2-1}{n^2+2} = \sum_i \overline{A}_i \overline{\rho}_{i,IG} X_i = \overline{\rho}_{IG,mix} \sum_i \overline{A}_i X_i \tag{20a}$$

Real Gas Model 1 - Additive Refractivity (AR)

$$\frac{n^2-1}{n^2+2} = \sum_i \overline{A}_i \overline{\rho}_{i,RG} X_i \tag{20b}$$

Real Gas Model 2 - Additive Polarizability (AP)

$$\frac{n^2-1}{n^2+2} = \overline{\rho}_{mix,RG} \sum_i \overline{A}_i X_i \tag{20c}$$

In this work, Eqs. 20a-c are referred to as the IG, AR, and AP models, respectively. Note that additive refractivity and additive polarizability formulations are different for real gas mixtures. The AR model uses species polarizability at STP and the density of each species is computed from real-fluid EOS as discussed in Section 4.1. For AP model, the mixture polarizability is mole-weighted sum of species polarizability at STP, and the mixture density is obtained from real-fluid mixture EOS as discussed in Section 4.2.

5.2. Model Validation

The above mixture models are compared against experimental refractive index data at high pressures relevant to compression ignition engines. Unfortunately, very limited experimental data exist [37, 38, 47, 48, 49] of which [49] provides the most extensive measurements of refractive index of mixtures for a large range of high pressures. Thus, Ref. [49] will be used to compare the three refractive index mixture models presented above.

In Ref. [49], the refractive index was measured by a Michelson interferometer with a maximum relative uncertainty of 0.03%. The refractive index

was measured for binary mixtures of methane and carbon dioxide at pressures ranging from 0.5 to 20 MPa, and a fixed temperature of 303 K. Six different mole fractions of CO_2 were studied: 0%, 50%, 78.2%, 80.2%, 82.2%, and 100%. In our study, the molar polarizability for methane and carbon dioxide is taken from [28]. For each test condition in Ref. [49], the density is calculated by the ideal gas law for the IG model, reduced Helmholtz EOS for each component for the AR model, and reduced Helmholtz EOS for the mixture for the AP model.

Figure 4 shows the computed refractive index difference (n-1) for each model compared with experimental data for a binary mixture of 78.2% CO_2 and 21.8% CH_4 at pressures of 1 to 200 bar. For pressures below about 30 bar, all models predict nearly the same linear increase in the refractive index difference with an increase in the pressure. In this regime, the mixture behaves as an ideal gas, thus, the IG model is a valid approximation. Additionally, the AR and AP models are equivalent, and same as the IG model, indicating that each species also behaves as an ideal gas. However, at pressures above 30 bar, the refractive index difference is increasingly under-predicted by the IG model.

The two real gas models provide very different results at pressures above 50 bar: AR model grossly overpredicts while AP model shows excellent agreement with experimental data for the entire pressure range. At high pressures, the compressibility (or real-gas behavior) affects the density significantly but polarizability is nearly constant as shown in Figs. 2 and Fig. 3. However, the AR model combines both density and polarizability as one "lumped" parameter weighted linearly with the mole fraction. The net effect is a higher

(and erroneous) weighting for components with higher density. The non-linear behavior of density is most significant near the critical point and phase boundaries. The experimental data in Fig. 4 were obtained at 300 K. The density of carbon dioxide will exhibit highly non-linear behavior near its critical point of 304.4 K and 73.8 bar, which explains the large errors introduced by the AR model at around 70 bar. The error decreases at higher pressures as conditions depart away from the critical point. Note that the test conditions are far above the critical point of methane (190 K and 46.5 bar), i.e., methane would behave close to an ideal gas, and thus, would contribute little to the errors in the AR model. The molecular interactions between species also change the phase transition space of mixtures compared to that of the component species. Thus, the AR model will introduce large errors if any of the component species are near the two-phase region. However, if all of the mixture species are sufficiently far away from the phase boundary and critical point, e.g., in the compressed liquid region or ideal gas region, then the AR model and AP model will give equivalent results. For example, AR type models have been successfully used in liquid mixtures of biodiesel-diesel fuels blends [50].

Based on the above results and discussion, it is clear that if the pressures and/or temperatures of the experiment are near one or more of the constituent fluids phase transition point or critical point, the AP model is the only reliable option among the three models. The AP model uses mixture EOS to compute the mixture density but retains the so-called ideal gas behavior to compute the mixture polarizability to yield accurate results. Figure 4 illustrates that (1) computing mixture refractivity as the summation of

mole-weighted refractivity of its components or AR model is grossly inaccurate at high pressures, regardless of the method used to compute the density (ideal gas or real gas), and (2) AP model can accurately predict the refractive index for non-polar binary real gas mixtures. Thus, the higher order terms in Eq. 11b (B_1, B_2, and B_{12}) are indeed negligible, especially for the CO_2-CH_4 mixture. Considering that CO_2 exhibited the strongest pressure dependence on pure component polarizability in Fig. 2 (though still <5% error), the fact that the AP model accurately captures its mixture behavior with CH_4, it is expected that the AP model will work for the other combinations of these non-polar substances. The error could be much smaller if the temperature/pressure are farther away from the critical point of one of the components.

Next, Fig. 5 shows comparison of refractive index data for all of the mixtures in Ref [49] with predictions from the AP model. The maximum error is less than 0.6% indicating robustness of the model. The corresponding maximum error in the computed mole fraction is less than 3.5%. In summary, the AP model has been demonstrated to accurately predict the refractive index at high pressures with non-ideal gas behavior. A detailed investigation of the possible sources of errors is beyond the scope of this work. However, minor errors observed in Fig. 5 are likely caused by the small effect of pressure on polarizability (see Fig. 2) which are ignored in this study.

6. Application Examples

In this section, the models developed above will be applied to investigate fuel-air mixing at compression ignition engine conditions assuming adiabatic

mixing. First, models will be compared against each other for Spray A condition. Next, AP model will be applied for a wide range of engine conditions.

6.1. Adiabatic mixing and phase space

Spray A condition is designed to represent low temperature combustion with moderate exhaust gas recirculation. The fuel for Spray A is n-dodecane - a diesel fuel surrogate - injected at a pressure of 1500 bar. The fuel (pre-injection) temperature is 363 K, and the ambient pressure and temperature at the test point are 60 bar and 900 K, respectively. Nitrogen is used as the ambient fluid to limit the discussion to binary mixtures. The fuel temperature changes across the injector, and isenthalpic and isothermal conditions across the injector provide the two limiting bounds for the fuel injection temperature. In this study, the fuel injection temperature is obtained by assuming constant enthalpy across the injector, though this choice only affects specific numbers and not any of the trends or conclusions.

Thermodynamic properties of the mixture are determined by assuming adiabatic fuel-air mixing supported by Siebers and others [51, 52, 53, 54]. Adiabatic mixing assumes: (1) local thermodynamic equilibrium with heat transfer occurring only via mass transfer, i.e., no radiation or exothermic reactions, and (2) non-differential transport of all mass, momentum, and energy, i.e., all Schmidt numbers and Lewis numbers are unity. In turbulent flows, the mixing is dominated by turbulent viscosity transport, which is the basis for most CFD simulations. For example, Ref [53] investigated the effect of a realizable Schmidt number in the near nozzle region and found the results were independent of the Schmidt number. CFD studies have found good agreement with experimental centerline mixing measurements

using adiabatic mixing assumption [54]. Adiabatic mixing assumption will not work in the sooty flame region or even in cool-flame and ignition regimes associated with exothermic reactions.

The time scale for thermodynamic equilibrium are typically much shorter than heat transfer time scales, and mixing assumption is applied locally (each pixel or grid in CFD) to determine the non-uniform mixing behavior. For adiabatic mixing at a constant chamber pressure, fuel enters as liquid at the fuel injection temperature, the ambient gas is at the chamber temperature, and the exiting fluid can be gaseous, liquid, or two-phase mixture. For a given chamber pressure and temperature, the mixture enthalpy and hence, the thermodynamic state of the mixture including its temperature, quality (if two-phase), mixture fraction, and equivalence ratio can be calculated as a function of the fuel mole fraction.

Figure 6 shows mixture temperature versus fuel mole fraction for real gas and ideal gas mixtures. The saturated liquid/vapor lines, two-phase region, and the critical point determined from real-gas EOS for the mixture are also shown. For Spray A fuel injection and ambient conditions, the two-phase mixture occurs at fuel mole fraction of 0.1 (saturated vapor) to 0.9 (saturated liquid). Figure 6 shows that the mixture temperature for ideal and real gas assumptions agree with each other for fuel mole fraction of up to 0.15, but depart significantly at higher fuel mole fractions, i.e., for mixtures in the two-phase region. This result is expected since the ideal gas model assumes a vapor phase for the entire fuel mole fraction (or mixture fraction) space. In the two-phase region, the ideal gas model severely underpredicts the mixture temperature as the fuel mole fraction is increased. The dashed

green line in the two phase region is a spline fit where REFPROP fails to return a valid solution. Note that the two-phase region cannot be quantified by Rayleigh scattering or RSD diagnostics. Thus, reliable measurements can only be obtained in the vapor region, i.e., for fuel mole fraction of up to 0.10 for this test case. Fortunately, this is not a serious drawback for compression ignition engine applications since fuel mole fraction (or equivalence ratio) measurements are needed mainly in the combustible vapor region.

6.2. Model Comparison

In this section, the three models (IG, AR, and AP) will be compared at Spray A condition. Model Eqs. 20 will be used to compute the refractive index as a function of fuel mole fraction, which can be related to density, temperature, equivalence ratio, etc. of the mixture. In practice, a look-up table is generated with refractive index as input to determine thermodynamic properties outputs. Figure 7 shows the equivalence ratio and mixture temperature for different models as function of the normalized refractive index difference defined as $\delta{=}n/n_0 - 1$ where n_0 is the refractive index of the surrounding ambient - pure nitrogen in this case. The vapor zone (left side, $\delta < 0.012$) and two-phase zone (right side, $\delta > 0.012$) are identified in the figure.

Figure 7 shows that the AR model performs poorly in both vapor and two-phase zones in comparison to the validated AP model. The AR model overpredicts the mixture temperature and slightly underpredicts equivalence ratio even though it uses real-gas properties, again indicating that the additive principle incorporated in the model is grossly inaccurate. This is explained by the chamber conditions being close to the critical point of *n*-

dodecane. The IG model performs well in the vapor zone, but it increasingly deviates from the AP model in the two-phase zone. The large deviation in the two-phase region is easy to explain since the IG model treats the two-phase zone as ideal gas as discussed previously. Results show that the IG and AP models are equivalent in the vapor zone, indicating that Spray A can be approximated by the ideal gas assumption. However, one should be aware that the phase boundary must be determined either experimentally or from the real-gas analysis. While a detailed uncertainty analysis is outside the scope of this work, uncertainty in δ will propagate to uncertainty in calculated thermodynamic quantities. For example, at Spray A conditions a 1% error in δ corresponds to a maximum of a 1% error in ϕ in the vapor region; where the percent error in ϕ decreases as ϕ increases.

6.3. Parametric Study

Next, the IG and AR models are compared with the AP model for a wide range of compression ignition engine conditions: Ambient conditions are varied from an assumed engine intake at P_{intake} =2 bar and T_{intake} =360 K to top dead center (TDC) at P_{TDC} =200 bar and T_{TDC} =1250 K, and the inlet fuel temperature in the chamber is 419 K (after isenthalpically expanding from T_{inj}=363 K and P_{inj}=1500 bar). These conditions represent a typical engine with 2 bar boost at the intake and isentropic compression at compression ratio of 6 to 29 to span the range in compression ignition engines. Figures 8 and 9 show, respectively, the absolute error in mixture temperature and equivalence ratio introduced by the IG model when compared to the validated AP model.

The y-axes in Figs. 8,9 represent pairs of chamber (cylinder) pressure

and temperature reached via isentropic compression from the initial state. In Fig. 8, the right edge of the colored region represents $\phi = 0$ and the left edge is terminated at $\phi = 50$. The dashed white line denotes the phase boundary with vapor on the right and two-phase region on the left side. Figure 8 shows that the IG model does quite well in the vapor zone (<5% error). i.e., the IG model is adequate in the vapor zone for most diesel applications. However, one could inadvertently apply the IG model in the two-phase region causing large errors (≈20% error). If the IG model is used, the two-phase boundary must be identified from either real-gas analysis or diagnostics for liquid boundary detection. Such errors can be avoided by applying the AP model throughout the operational regime.

Figure 9 shows the error in the equivalence ratio introduced by the IG model. The right side of the colored region represents the phase boundary. Figure 9 shows that the IG model introduces larger errors at higher compression ratios (or high chamber temperatures and pressures). Figure 9 identifies region with errors above 5% (solid white line) and 10 % (dashed white line). However, for pressures below 100 bar, the error in equivalence ratio is small indicating that the IG model is adequate.

Next, Fig. 10 shows the error in mixture temperature and equivalence ratio introduced by the AR model as compared to the validated AP model. Even in the vapor zone, the temperature is overpredicted or underpredicted by as much as 150 C. At low chamber pressures (or temperatures), the error is greater near the phase boundary, but at high pressures, it is confined to fuel-lean conditions with significant compressibility effects. Figure 11 further supports the poor performance of the AR model. Even in the vapor zone,

the errors in equivalence ratio could be up to 80%. As such, the AR model should not be used in optical diagnostics of gas mixtures at high pressures.

6.4. Supercritical Fuel-Oxidizer Mixing

The AP model will reach its full potential at conditions departing from the ideal gas behavior, e.g., transcritical and supercritical mixing regimes. Recent experimental and theoretical findings have stimulated interest in supercritical fuel-oxidizer mixing at diesel conditions. [12, 13, 14, 15, 16, 17, 18]. Thus, the ability to acquire quantitative thermodynamic measurements in the supercritical regime is of great interest. However, purely supercritical mixing in diesel engines requires either much higher ambient pressures (and thus, temperatures) or fuel modifications, e.g., high injection temperature or fuels with low critical temperature. In this study, propane at Spray A conditions is used to simulate supercritical mixing. Figure 12 shows that the mixture temperature for propane at supply temperature of 395 K (after isenthalpically expanding from T_{inj} =363 K and P_{inj} =1500 bar), i.e., slightly above its critical temperature of 370 K, injected into an ambient at Spray A conditions (60 bar and 900 K) never enters the two-phase regime and thus completely diffusive mixing without surface tension (or no droplets) is likely to occur. Absence of droplets could potentially allow RSD or Rayleigh scattering measurements across the entire mixture fraction space.

Figure 13 shows equivalence ratio and mixture temperature versus refractive index difference (or fuel mole fraction) for the three models presented in this study. For refractive index difference, δ, less than 0.01, all three models provide similar results indicating that the mixture is close to an ideal gas. For refractive index difference of 0.02 or fuel mole fraction of 0.5, the mixture

temperature is underpredicted by about 25°C by the IG model and overpredicted by about 25°C by the AR model. For fuel mole fraction greater than 0.5 ($\delta > 0.02$), the IG model is no longer useful since it deviates exponentially from the accurate AP model. The AR model is also inaccurate for fuel mole fractions between 0.5 and 0.96. The poor performance of the IG model can be attributed to the significant compressibility effects in this fully supercritical mixing regime. The AR model approaches the AP model at fuel mole fraction close to unity when the mixture approaches a pure substance. However, the AP model would be the method of choice to accurately calculate both mixture temperature and equivalence ratio across the entirety of the mixture fraction space for mixing at purely supercritical conditions.

7. Conclusions

This study investigated the effect of pressure on polarizability and density to extend the Lorentz-Lorenz equation to real-gas mixtures at high pressure. Three different formulations of the Lorentz-Lorenz equation for gaseous mixtures were compared against experimental data in the literature. The Additive Polarizability (AP) model was identified as the robust model for applications at the harshest conditions. The AP model was validated using published experimental data on refractive index and then used to estimate errors in the other two models (IG and AR models) for a wide range of compression ignition engine operating conditions. Finally, the AP model was applied to study supercritical mixing of propane and nitrogen. Following is a summary of the conclusions from this study:

- The original Lorentz-Lorenz equation should be used instead of the sim-

plified Dale-Gladstone equation to eliminate unwarranted errors that can affect the thermophysical property calculations.

- For liquids, both polarizability and density are nearly constant. However, for non-polar gases, the polarizability is nearly constant while density varies significantly with pressure. In contrast, density variation with pressure is linear in the ideal-gas regime, but highly non-linear near the critical point and phase change boundaries of component species and mixture.

- Following the additive principle (e.g., Amagat law), the mixture laws for Lorentz-Loretz equation can be expressed as mole weighted sum of component refractivity (product of polarizability and density) or polarizability. For incompressible liquids (constant density) or ideal gases (linear variation in density with pressure), both formulations yield the same result. However, they are different when density varies non-linearly with pressure, for example, near the critical point and/or phase boundaries of components or mixture.

- In the ideal-gas regime, the IG, AR, and AP models are equivalent. In the compressed liquid region where density is linear with mixture fraction, the AR and AP models are equivalent.

- In the non-linear density regime, the IG and AR models can be highly inaccurate. The AR model performs poorly across the entire range of compression ignition conditions, yielding errors in equivalence ratio of up to 80%.

- The AP model works well across the entire compression ignition engine regimes including conditions near the critical point and phase boundaries. The IG model is valid in the vapor region (assuming it is known) at the typical compression ignition engine operating conditions. However, IG model could introduce large errors if inadvertently applied to the two-phase region, for example, in CFD analysis.

8. Acknowledgements

This work was performed with support by the Department of Energy, Office of Energy Efficiency and Renewable Energy (EERE) and the Department of Defense, Tank and Automotive Research, Development, and Engineering Center (TARDEC), under Award Number DE-EE0007301.

9. References

References

[1] C. Espey, J. E. Dec, T. A. Litzinger, D. A. Santavicca, Planar laser rayleigh scattering for quantitative vapor-fuel imaging in a diesel jet, Combustion and flame 109 (1997) 65–86.

[2] C. A. Idicheria, L. M. Pickett, Quantitative mixing measurements in a vaporizing diesel spray by Rayleigh imaging, Technical Report, SAE Technical Paper, 2007.

[3] A. Adam, P. Leick, G. Bittlinger, C. Schulz, Visualization of the evaporation of a diesel spray using combined mie and rayleigh scattering techniques, Experiments in fluids 47 (2009) 439–449.

[4] R. B. Miles, W. R. Lempert, J. N. Forkey, Laser rayleigh scattering, Measurement Science and Technology 12 (2001) R33.

[5] F.-Q. Zhao, H. Hiroyasu, The applications of laser rayleigh scattering to combustion diagnostics, Progress in energy and combustion science 19 (1993) 447–485.

[6] L. Pickett, G. Bruneaux, R. Payri, Engine combustion network, Sandia National Laboratories, Livermore, CA, http://www. ca. sandia. gov/ecn (2014).

[7] A. K. Agrawal, C. T. Wanstall, Rainbow schlieren deflectometry for scalar measurements in fluid flows, Journal of Flow Visualization and Image Processing 25 (2018).

[8] C. T. Wanstall, A. K. Agrawal, J. A. Bittle, Quantifying liquid boundary and vapor distributions in a fuel spray by rainbow schlieren deflectometry, Applied optics 56 (2017) 8385–8393.

[9] C. T. Wanstall, A. K. Agrawal, J. A. Bittle, Phase boundary detection in transient, evaporating high-pressure fuel sprays by rainbow schlieren deflectometry, Applied Optics (2019).

[10] B. W. Albers, A. K. Agrawal, Schlieren analysis of an oscillating gas-jet diffusion flame, Combustion and flame 119 (1999) 84–94.

[11] W. Meier, R. S. Barlow, Y.-L. Chen, J.-Y. Chen, Raman/rayleigh/lif measurements in a turbulent ch4/h2/n2 jet diffusion flame: experimental techniques and turbulence–chemistry interaction, Combustion and Flame 123 (2000) 326–343.

[12] R. N. Dahms, J. Manin, L. M. Pickett, J. C. Oefelein, Understanding high-pressure gas-liquid interface phenomena in diesel engines, Proceedings of the Combustion Institute 34 (2013) 1667–1675.

[13] R. N. Dahms, J. C. Oefelein, On the transition between two-phase and single-phase interface dynamics in multicomponent fluids at supercritical pressures, Physics of Fluids 25 (2013) 092103.

[14] R. N. Dahms, J. C. Oefelein, Non-equilibrium gas–liquid interface dynamics in high-pressure liquid injection systems, Proceedings of the Combustion Institute 35 (2015) 1587–1594.

[15] R. N. Dahms, Understanding the breakdown of classic two-phase theory and spray atomization at engine-relevant conditions, Physics of Fluids 28 (2016) 042108.

[16] Z. Falgout, M. Rahm, Z. Wang, M. Linne, Evidence for supercritical mixing layers in the ecn spray a, Proceedings of the Combustion Institute 35 (2015) 1579–1586.

[17] Z. Falgout, M. Rahm, D. Sedarsky, M. Linne, Gas/fuel jet interfaces under high pressures and temperatures, Fuel 168 (2016) 14–21.

[18] C. Crua, J. Manin, L. M. Pickett, On the transcritical mixing of fuels at diesel engine conditions, Fuel 208 (2017) 535–548.

[19] R. N. Dahms, J. C. Oefelein, Liquid jet breakup regimes at supercritical pressures, Combustion and Flame 162 (2015) 3648–3657.

[20] H. Lee, A. Fernandez-Pello, G. Corcos, A. Oppenheim, A mixing and deformation mechanism for a supercritical fuel droplet, Combustion and Flame 81 (1990) 50–58.

[21] J. Shuen, V. Yang, C. Hsiao, Combustion of liquid-fuel droplets in supercritical conditions, Combustion and Flame 89 (1992) 299–319.

[22] J. Oefelein, R. Dahms, G. Lacaze, Detailed modeling and simulation of high-pressure fuel injection processes in diesel engines, SAE International Journal of Engines 5 (2012) 1410–1419.

[23] J. Oefelein, G. Lacaze, R. Dahms, A. Ruiz, A. Misdariis, Effects of real-fluid thermodynamics on high-pressure fuel injection processes, SAE International Journal of Engines 7 (2014) 1125–1136.

[24] G. Lacaze, A. Misdariis, A. Ruiz, J. C. Oefelein, Analysis of high-pressure diesel fuel injection processes using les with real-fluid thermodynamics and transport, Proceedings of the Combustion Institute 35 (2015) 1603–1611.

[25] X. Wang, H. Huo, U. Unnikrishnan, V. Yang, A systematic approach to high-fidelity modeling and efficient simulation of supercritical fluid mixing and combustion, Combustion and Flame 195 (2018) 203–215.

[26] D. Aspnes, Local-field effects and effective-medium theory: a microscopic perspective, American Journal of Physics 50 (1982) 704–709.

[27] H. A. Lorentz, The Theory of Electrons and Its Applications to the Phenomena of Light and Radiant Heart: A Course of Lectures Delivered

in Columbia University, New York in March and April, 1906, volume 29, Teubner, 1916.

[28] W. Gardiner Jr, Y. Hidaka, T. Tanzawa, Refractivity of combustion gases, Combustion and Flame 40 (1981) 213–219.

[29] R. Bosque, J. Sales, Polarizabilities of solvents from the chemical composition, Journal of chemical information and computer sciences 42 (2002) 1154–1163.

[30] H. Achtermann, G. Magnus, T. Bose, Refractivity virial coefficients of gaseous ch4, c2h4, c2h6, co2, sf6, h2, n2, he, and ar, The Journal of chemical physics 94 (1991) 5669–5684.

[31] J. W. Schmidt, M. R. Moldover, Dielectric permittivity of eight gases measured with cross capacitors, International Journal of Thermophysics 24 (2003) 375–403.

[32] A. H. Harvey, E. W. Lemmon, Method for estimating the dielectric constant of natural gas mixtures, International journal of thermophysics 26 (2005) 31–46.

[33] A. Buckingham, J. Pople, The dielectric constant of an imperfect nonpolar gas, Transactions of the Faraday Society 51 (1955) 1029–1035.

[34] A. Buckingham, The molecular refraction of an imperfect gas, Transactions of the Faraday Society 52 (1956) 747–753.

[35] A. Buckingham, J. Pople, Electromagnetic properties of compressed gases, Discussions of the Faraday Society 22 (1956) 17–21.

[36] A. Buckingham, R. Raab, The dielectric constant of a compressed gas mixture, Transactions of the Faraday Society 54 (1958) 623–628.

[37] D. L. Goldfarb, D. P. Fernández, H. R. Corti, Dielectric and volumetric properties of supercritical carbon dioxide (1)+ methanol (2) mixtures at 323.15 k, Fluid phase equilibria 158 (1999) 1011–1019.

[38] Y. Sun, B. Y. Shekunov, P. York, Refractive index of supercritical co 2-ethanol solvents, Chemical Engineering Communications 190 (2003) 1–14.

[39] R. Span, Multiparameter equations of state: an accurate source of thermodynamic property data, Springer Science & Business Media, 2013.

[40] W. C. Reynolds, P. Colonna, Thermodynamics, Cambridge University Press, 2018.

[41] E. W. Lemmon, R. T. Jacobsen, A new functional form and new fitting techniques for equations of state with application to pentafluoroethane (hfc-125), Journal of Physical and Chemical Reference Data 34 (2005) 69–108.

[42] E. W. Lemmon, R. Jacobsen, A generalized model for the thermodynamic properties of mixtures, International journal of thermophysics 20 (1999) 825–835.

[43] E. W. Lemmon, R. Tillner-Roth, A helmholtz energy equation of state for calculating the thermodynamic properties of fluid mixtures, Fluid phase equilibria 165 (1999) 1–21.

[44] I. H. Bell, E. W. Lemmon, Automatic fitting of binary interaction parameters for multi-fluid helmholtz-energy-explicit mixture models, Journal of Chemical & Engineering Data 61 (2016) 3752–3760.

[45] E. Lemmon, M. Huber, M. McLinden, Refprop 9.1, NIST standard reference database 23 (2013).

[46] Y. Liu, P. H. Daum, Relationship of refractive index to mass density and self-consistency of mixing rules for multicomponent mixtures like ambient aerosols, Journal of Aerosol Science 39 (2008) 974–986.

[47] F. Croccolo, M.-A. Arnaud, D. Bégué, H. Bataller, Concentration dependent refractive index of a binary mixture at high pressure, The Journal of chemical physics 135 (2011) 034901.

[48] M. V. Avdeev, A. N. Konovalov, V. N. Bagratashvili, V. K. Popov, S. I. Tsypina, M. Sokolova, J. Ke, M. Poliakoff, The fibre optic reflectometer: A new and simple probe for refractive index and phase separation measurements in gases, liquids and supercritical fluids, Physical Chemistry Chemical Physics 6 (2004) 1258–1263.

[49] C. Giraudet, L. Marlin, D. Bégué, F. Croccolo, H. Bataller, Concentration dependent refractive index of co2/ch4 mixture in gaseous and supercritical phase, The Journal of Chemical Physics 144 (2016) 134304.

[50] S. Geacai, I. Nita, O. Iulian, E. Geacai, Refractive indices for biodiesel mixtures, UPB Sci. Bull. Ser. B 74 (2012) 149–160.

[51] D. L. Siebers, Liquid-phase fuel penetration in diesel sprays, SAE transactions (1998) 1205–1227.

[52] D. L. Siebers, Scaling liquid-phase fuel penetration in diesel sprays based on mixing-limited vaporization, Technical Report, SAE technical paper, 1999.

[53] J. Desantes, J. M. García-Oliver, J. Pastor, A. Pandal, E. Baldwin, D. Schmidt, Coupled/decoupled spray simulation comparison of the ecn spray a condition with the σ-y eulerian atomization model, International Journal of Multiphase Flow 80 (2016) 89–99.

[54] J. M. Garcia-Oliver, J. M. Pastor, A. Pandal, N. Trask, E. Baldwin, D. P. Schmidt, Diesel spray cfd simulations based on the σ-y eulerian atomization model, Atomization and Sprays 23 (2013) 71–95.

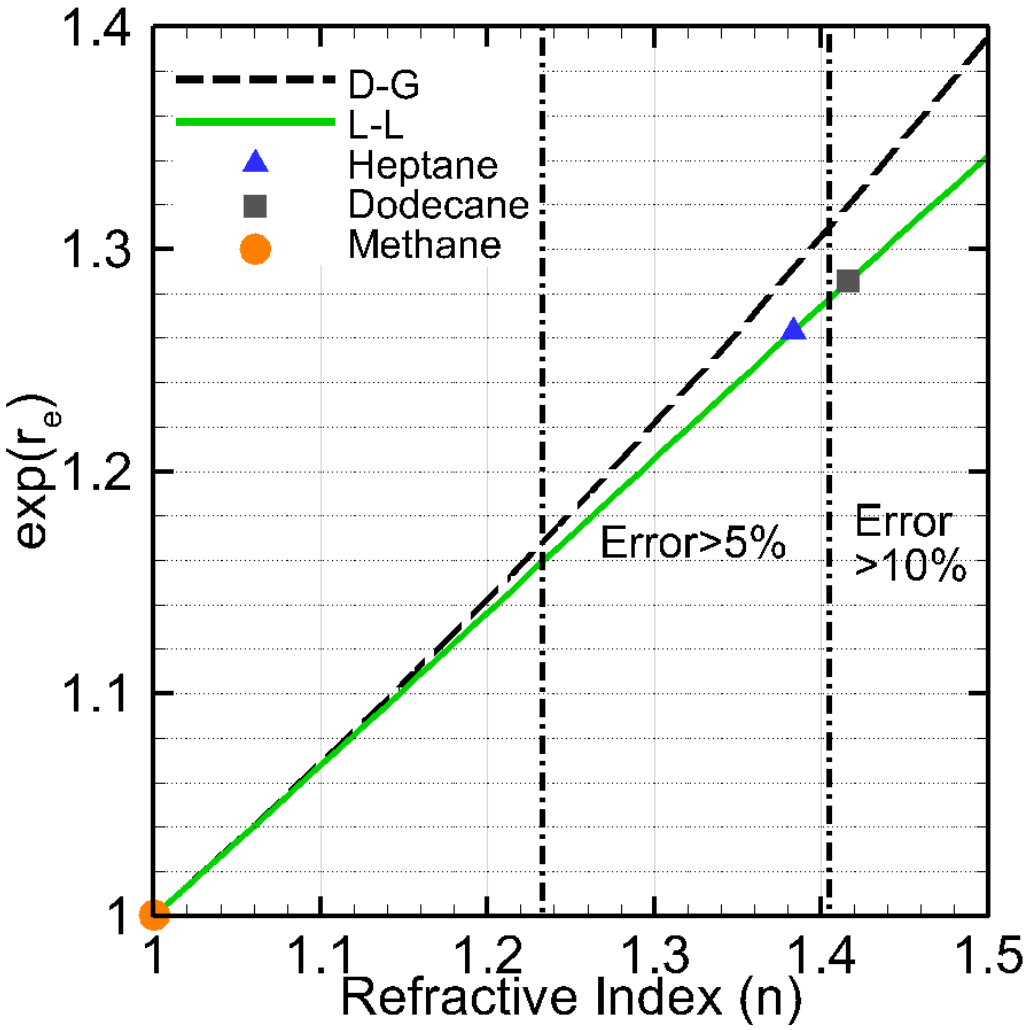

Figure 1: A plot showing the exponential of refractivity (r_e) based on the Lorentz-Lorenz (L-L) equation and the Dale-Gladstone (D-G) approximation for three different fuels.

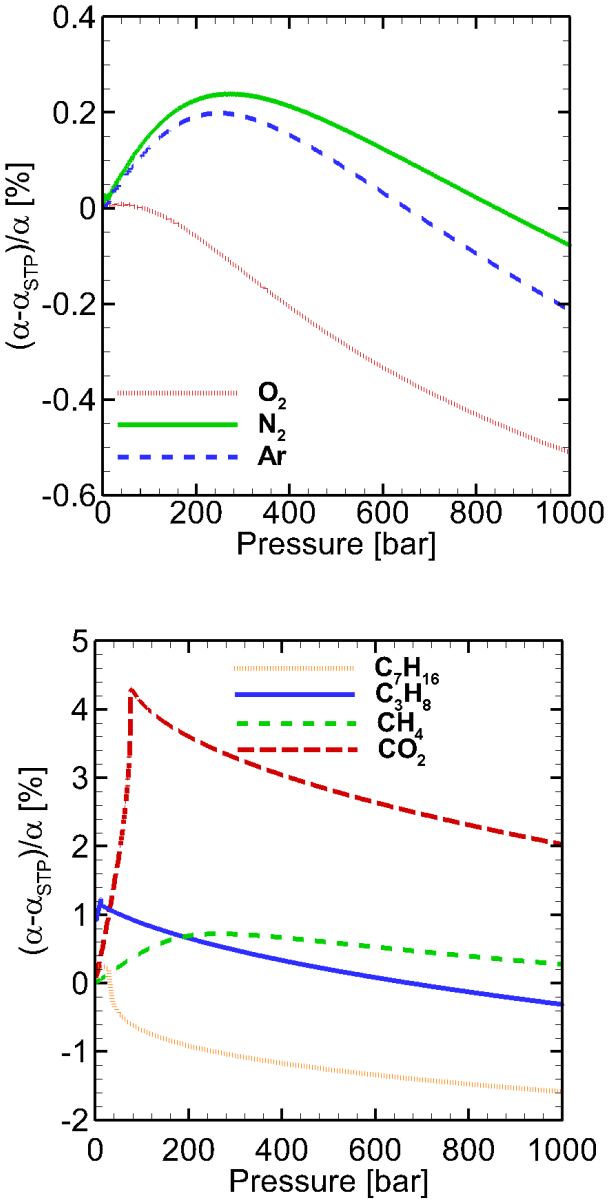

Figure 2: Effect of pressure on polarizability of constituents of air (top) and hydrocarbons and carbon dioxide (bottom). The vertical axis shows the percent change in polarizability with respect to the value at STP (273 K and 1 bar) except 550 K and 1 bar for n-heptane.

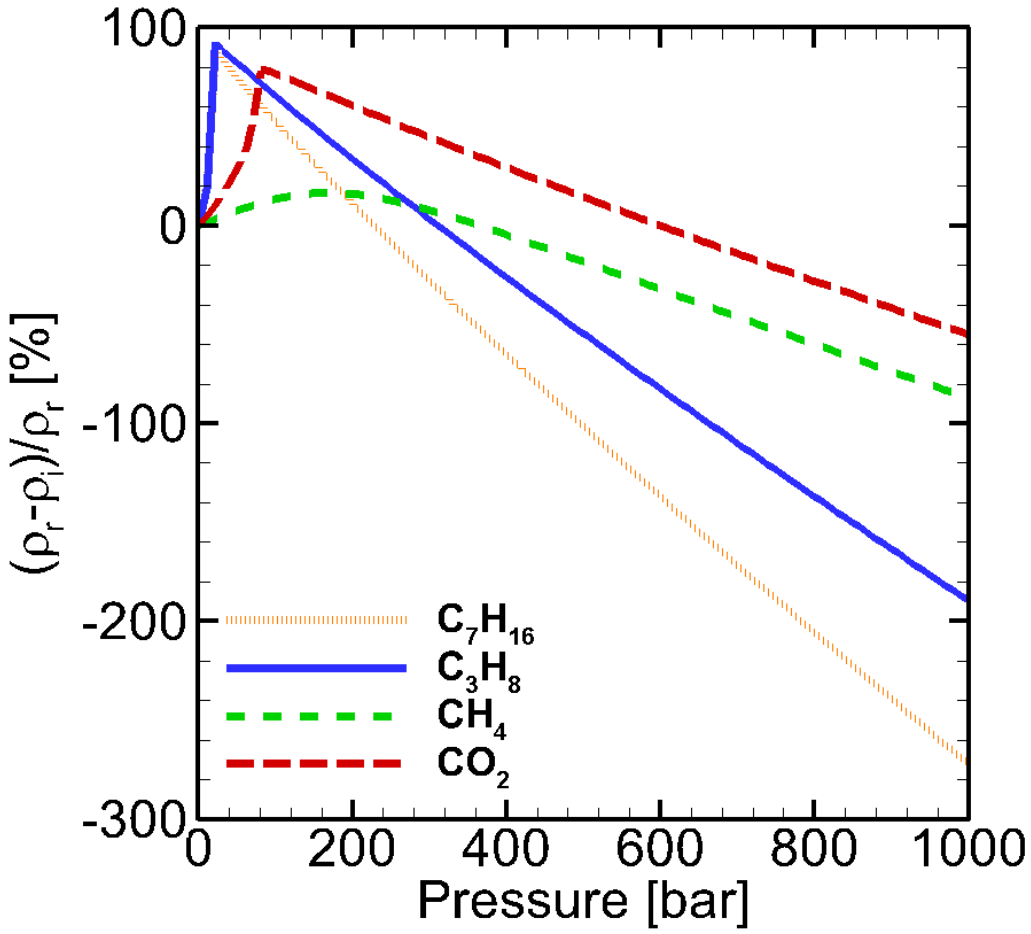

Figure 3: Effect of pressure on density for hydrocarbons and carbon dioxide. The vertical axis shows the percent difference in density computed by real-gas and ideal gas models. Reference conditions are STP (273 K and 1 bar) except 550 K and 1 bar for n-heptane.

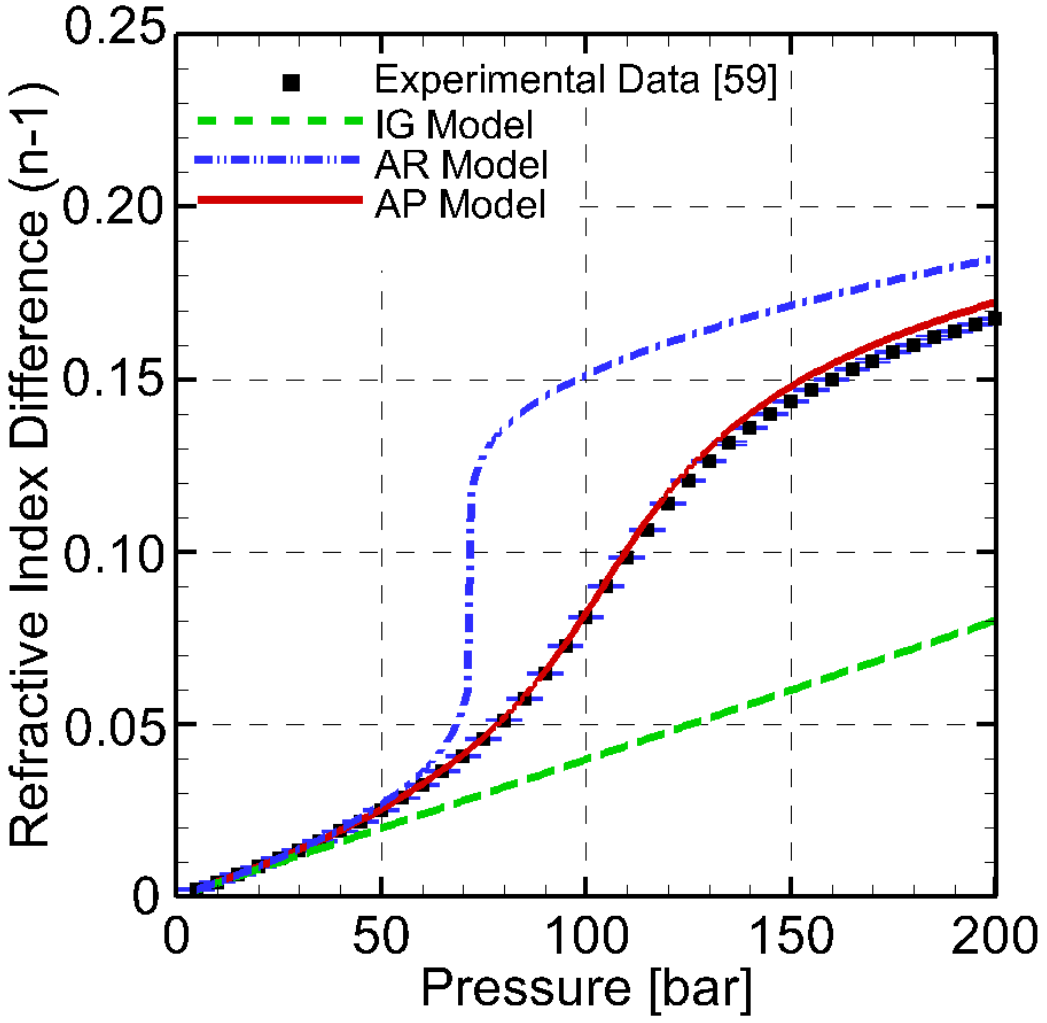

Figure 4: Refractive index difference versus pressure for a binary mixture of 78.2% CO_2 21.8% CH_4 at a temperature of 303 K.

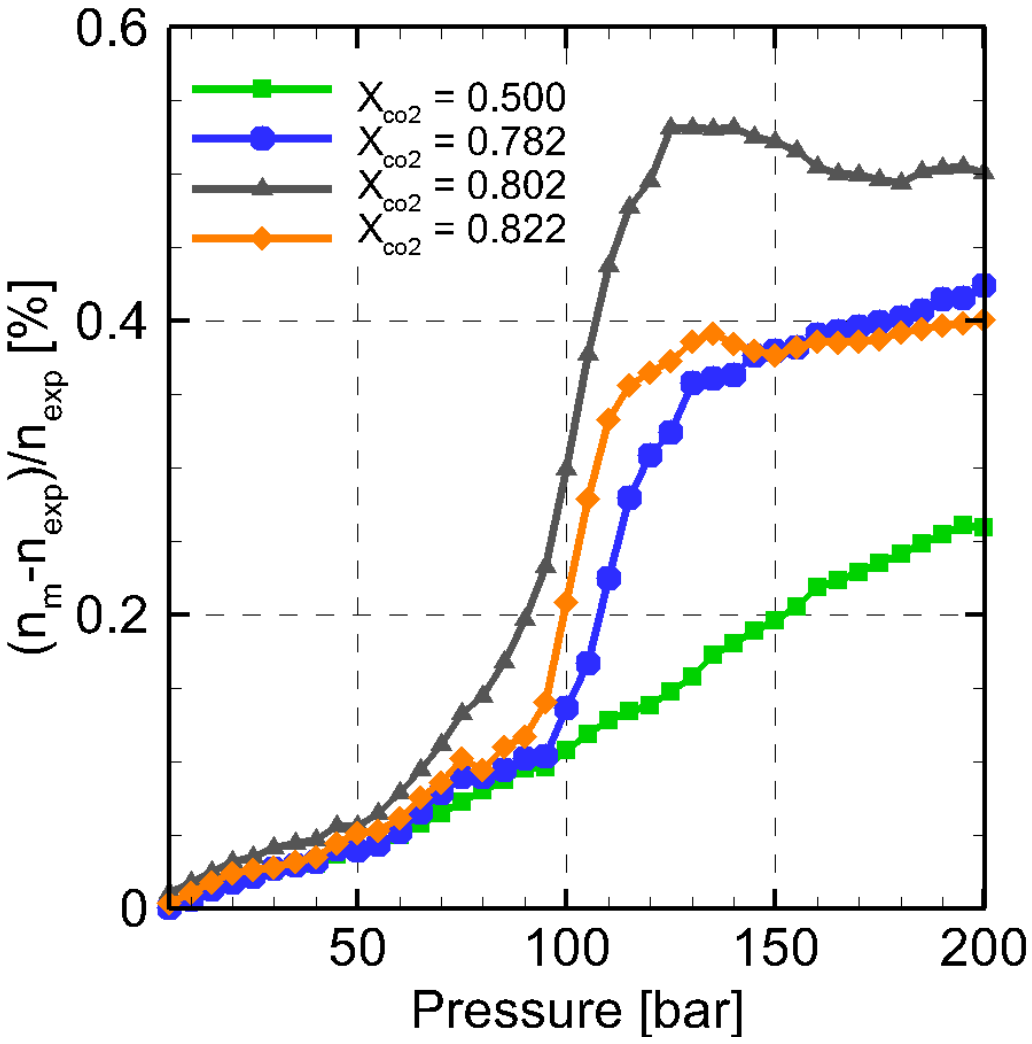

Figure 5: Percent difference in predicted (by the AP model) and experimental refractive index data of Ref. [49] at a temperature of 303 [K].

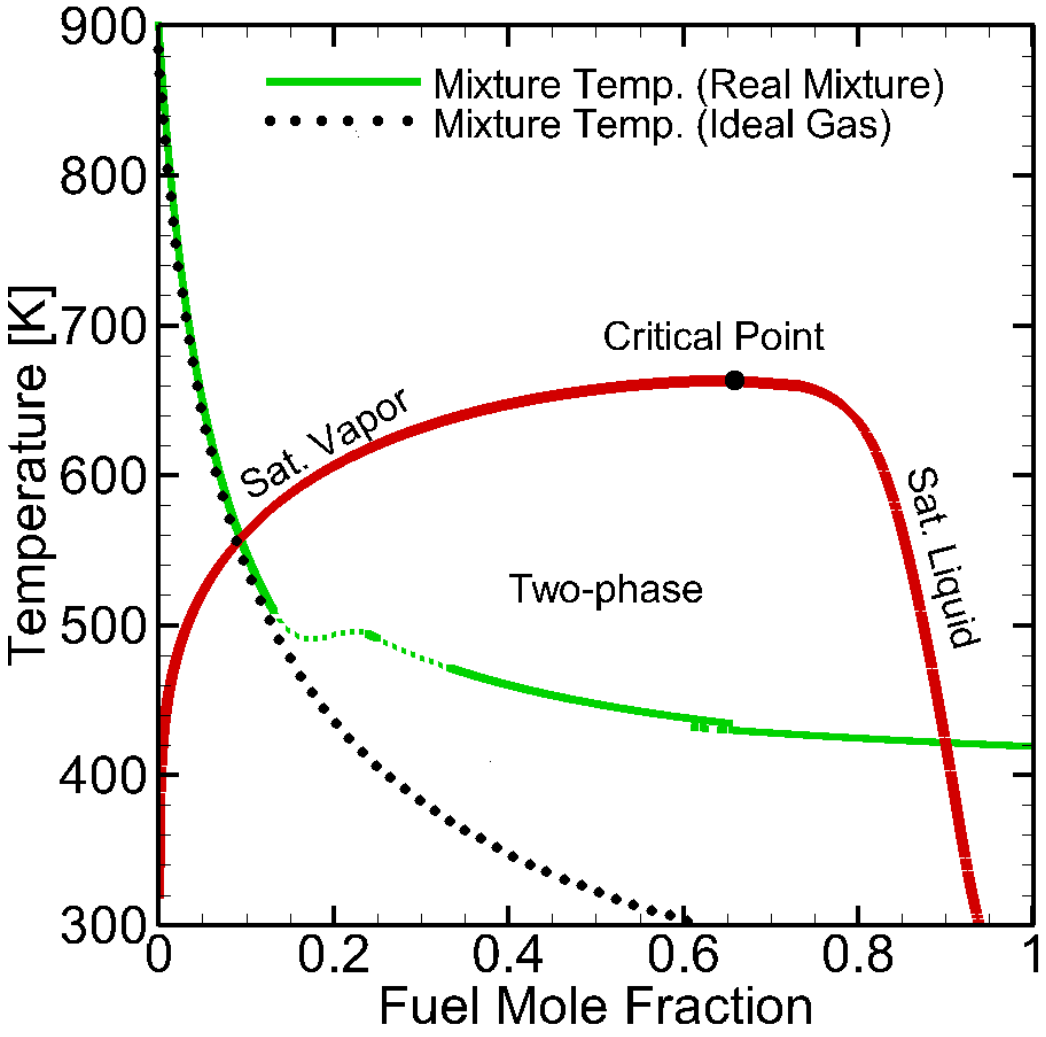

Figure 6: Temperature vs fuel mole fraction binary mixture of n-dodecane and nitrogen at Spray A conditions. The phase boundaries and vapor-liquid equilibrium region are also shown.

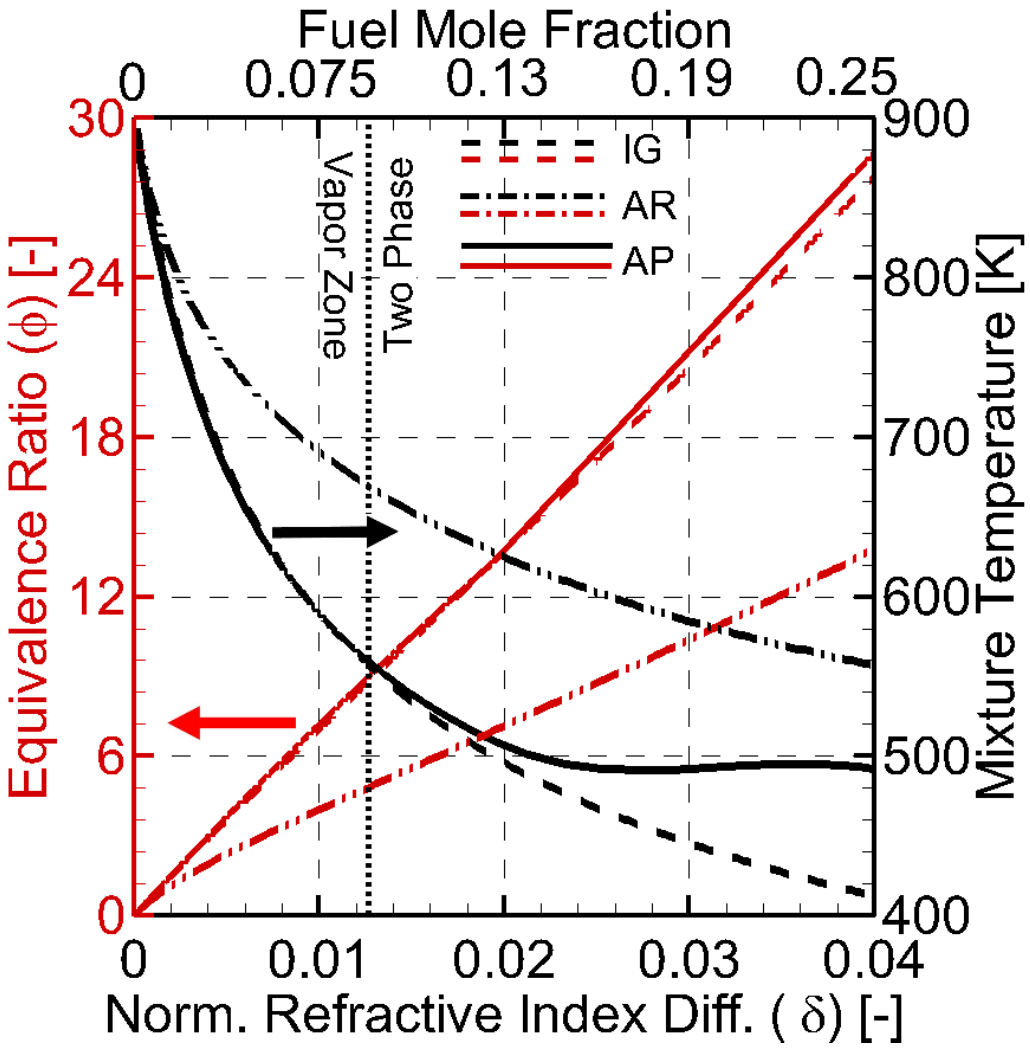

Figure 7: Equivalence ratio and mixture temperature as function of normalized refractive index difference for the IG, AR, and AP models.

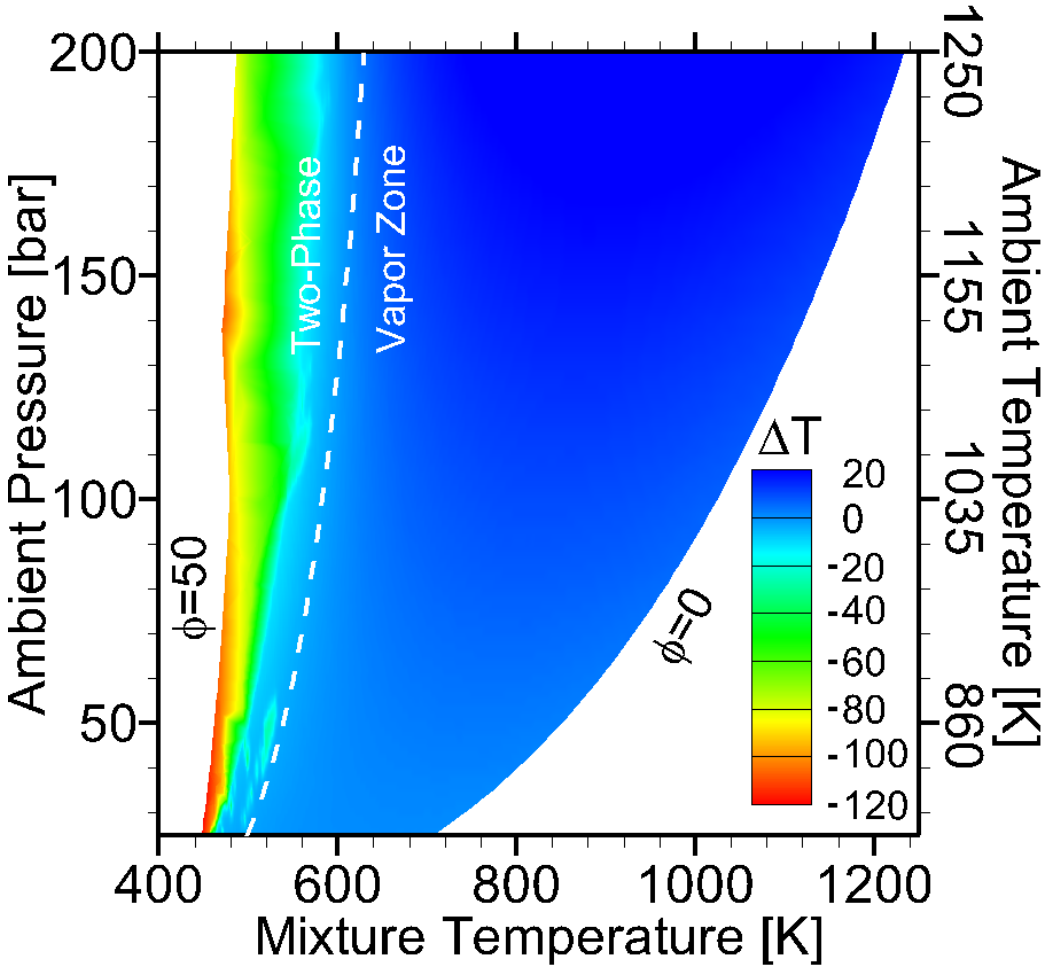

Figure 8: Absolute error in the mixture temperature calculated using the IG model (ΔT=T$_{IG}$-T$_{AP}$) for n-dodecane and nitrogen as a function of ambient conditions (pairs for pressure and temperature assuming isentropic compression from P_i=2 bar T_i=360 K). The dashed white line represents the two-phase boundary.

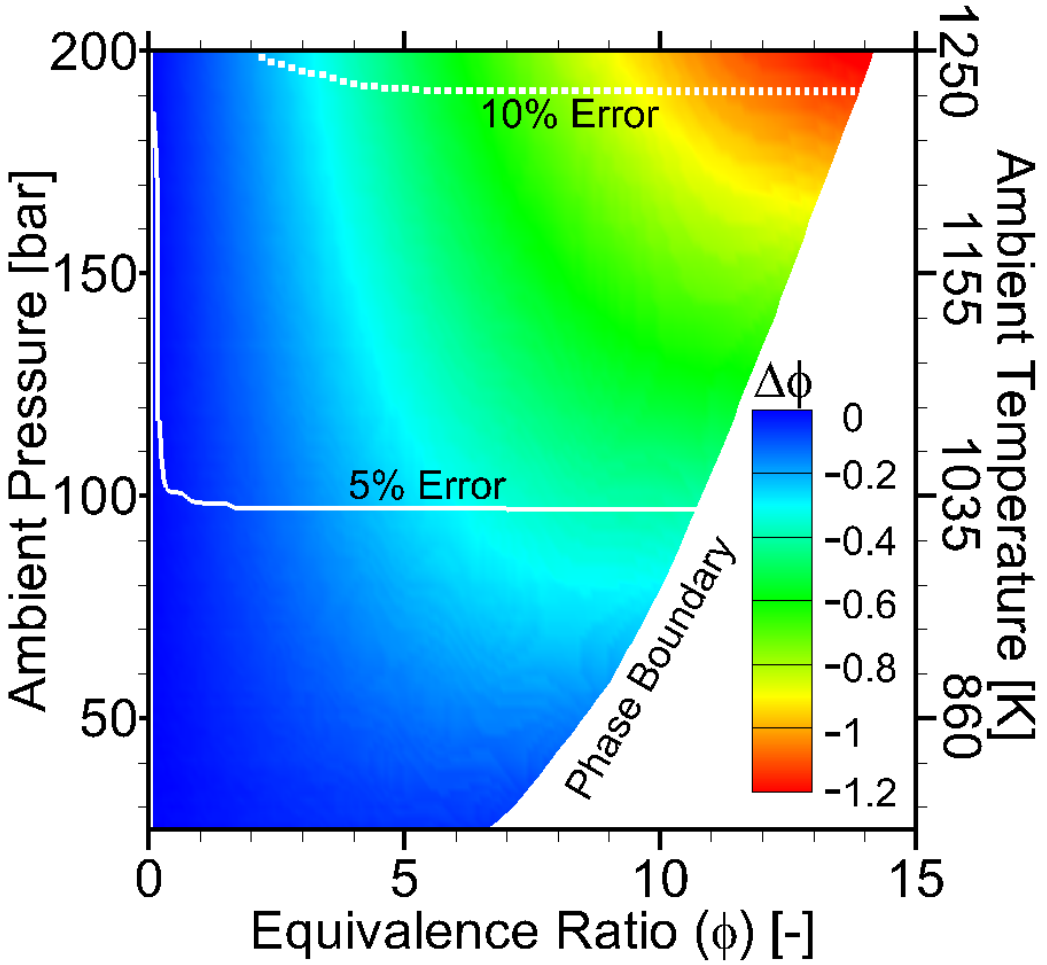

Figure 9: Absolute error in the equivalence ratio calculated using the IG model ($\Delta\phi$=ϕ_{IG}-ϕ_{AP}) for n-dodecane and nitrogen as a function of ambient conditions (pairs for pressure and temperature assuming isentropic compression from P_i=2 bar T_i=360K) for gas phase mixtures. The solid and dashed white lines are error isolines of 5% and 10%, respectively.

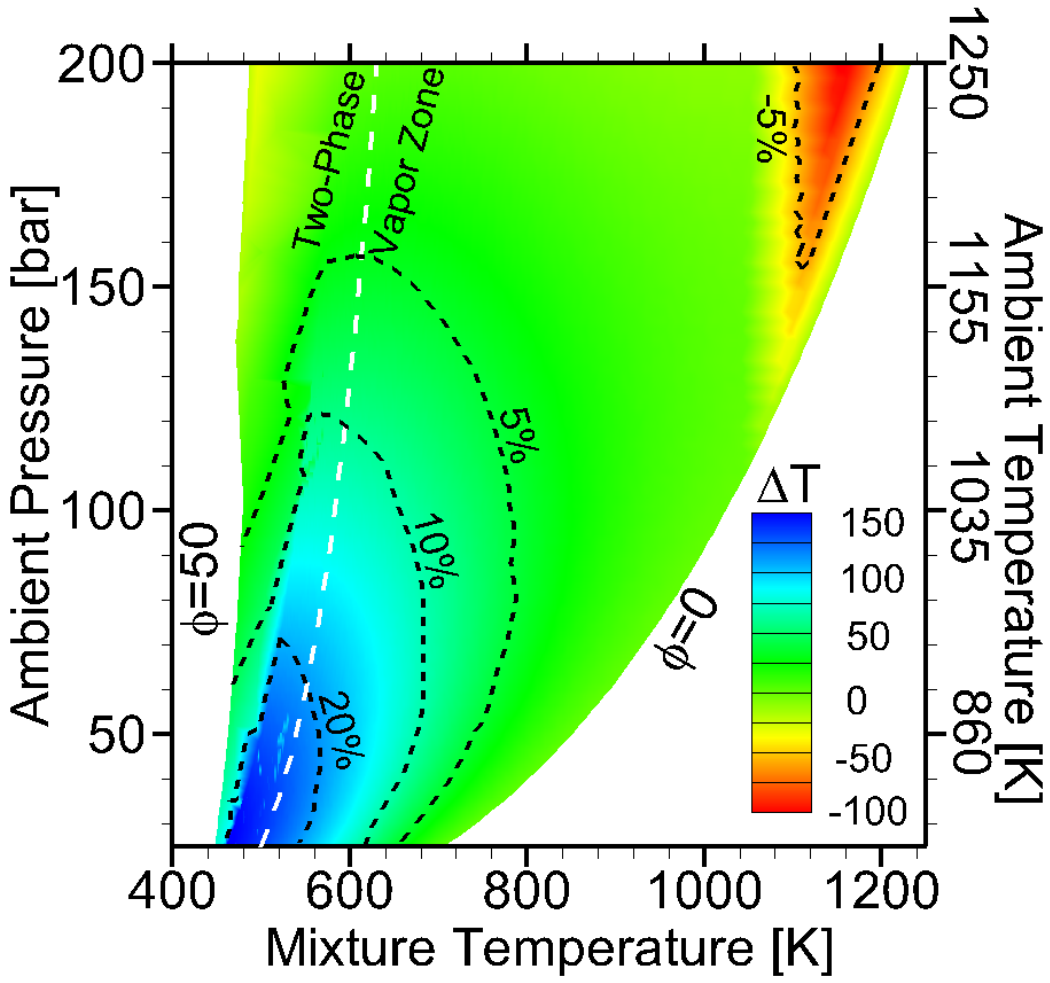

Figure 10: Absolute error in the mixture temperature calculated using the AR model (ΔT=T$_{AR}$-T$_{AP}$) for n-dodecane and nitrogen as a function of ambient conditions (pairs for pressure and temperature assuming isentropic compression from P_i=2 bar T_i=360K). The dashed white line represents the two-phase boundary and the black dashed lines represent percent error isolines.

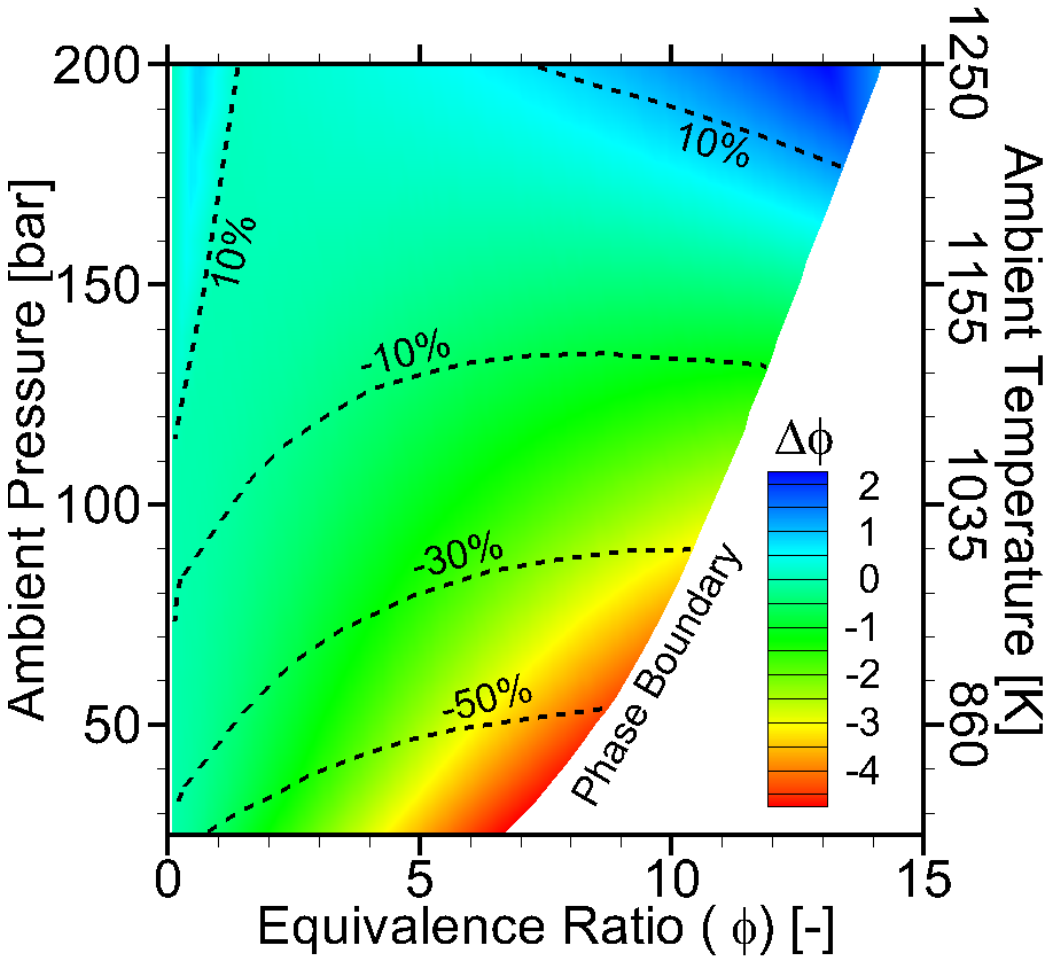

Figure 11: Absolute error in equivalence ratio is calculated using the AP and AR model ($\Delta\phi$=ϕ_{AR}-ϕ_{AP}) for n-dodecane and nitrogen as a function of ambient conditions (pairs for pressure and temperature assuming isentropic compression from P_i=2 bar T_i=360K) for gas phase mixtures. The right edge of the contour represents the phase boundary. Percent error isolines are overlaid as black dashed lines.

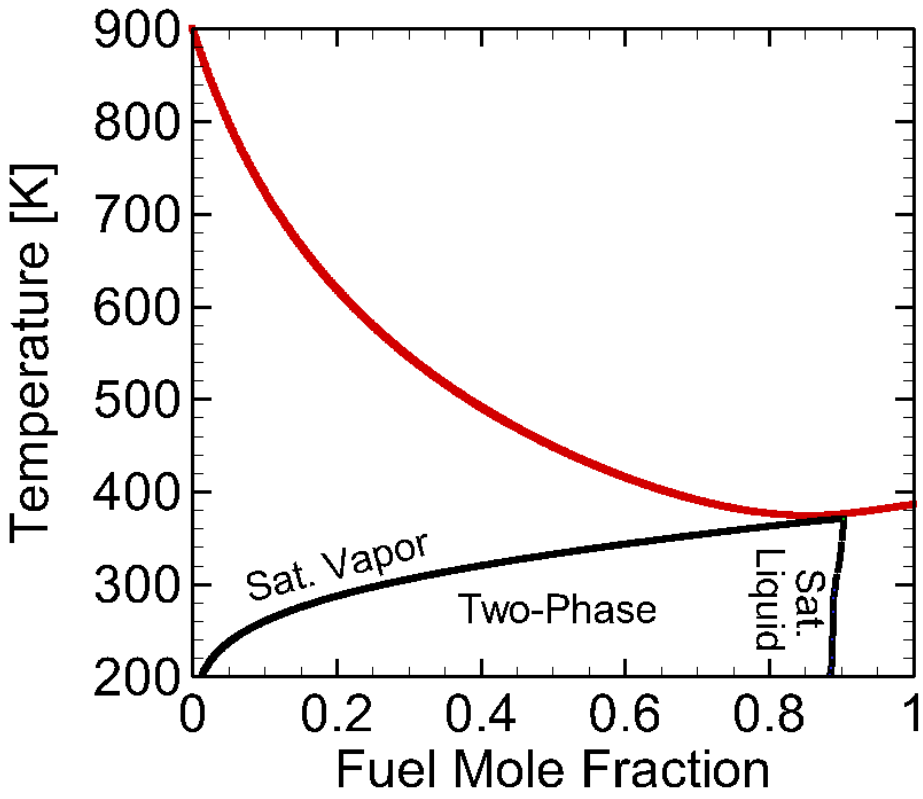

Figure 12: Calculated temperature versus fuel mole fraction for binary propane-nitrogen mixture at Spray A conditions using the IG, AR, and AP models.

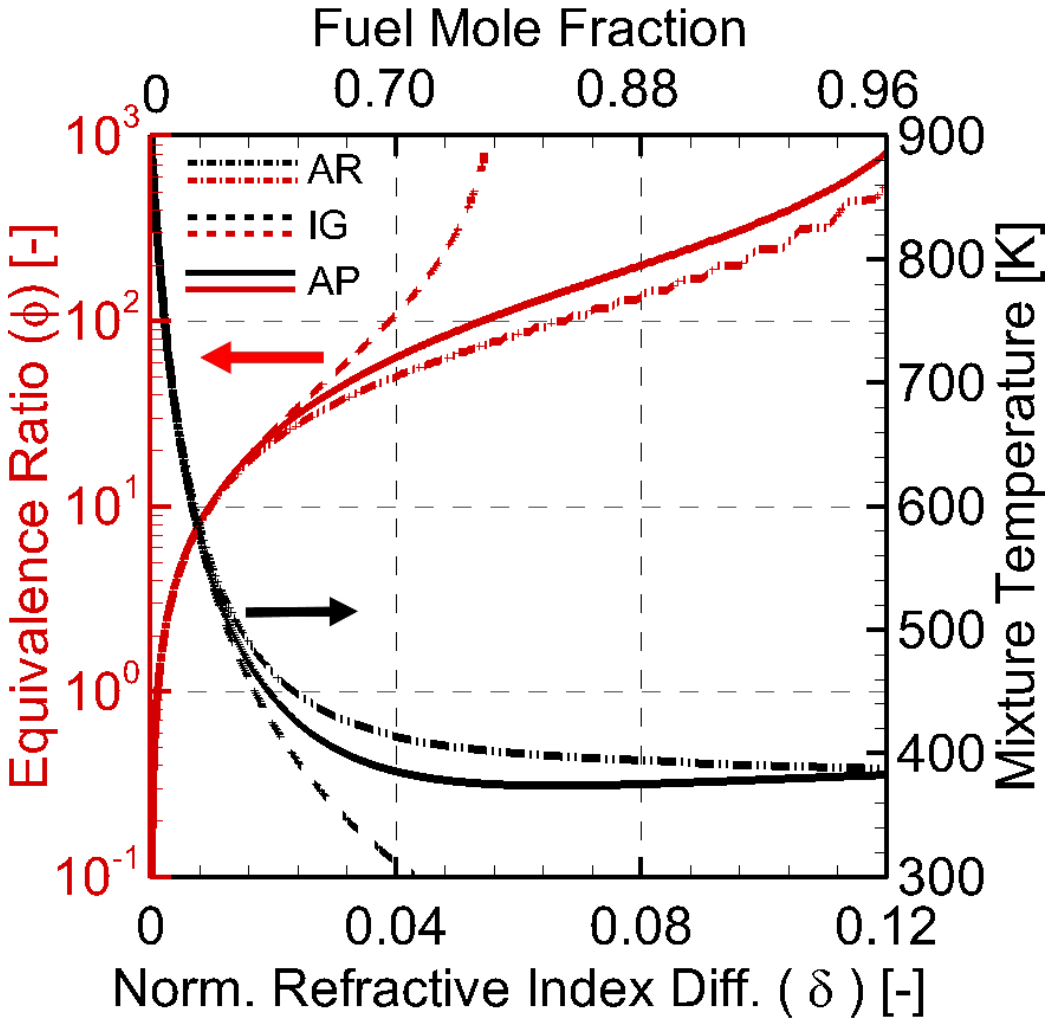

Figure 13: Equivalence ratio and mixture temperature as function of normalized refractive index difference for binary propane-nitrogen mixture at Spray A conditions calculated using the IG, AR, and AP models.

A Two-Color Pyrometry System to Eliminate Optical Errors for Spatially Resolved Measurements in Flames

SHAWN A. REGGETI, AJAY K. AGRAWAL* AND JOSHUA A. BITTLE

Department of Mechanical Engineering, University of Alabama, Tuscaloosa, AL, USA
**aagrawal@eng.ua.edu*

Abstract:

Two color (2C) pyrometry has long been used to measure flame temperature and soot concentration from radiative emission in flames. While 2C pyrometry is not an absolute measurement in non-axisymmetric flames (such as diesel spray combustion) it is a desirable diagnostic for semi-quantitative or qualitative measurements since it requires minimal optical access and can utilize high-speed imaging to attain exceptional temporal and spatial resolution. In this work, an improved optical configuration of 2C pyrometry is presented that 1) eliminates optical errors inherent in other designs, and 2) uses off-the-shelf optics and a single camera . In particular, this work analyzes the impact of parallax and path length differences on the 2C pyrometry measurement and exemplifies how the present design eliminates associated errors by design rather than in post-processing. The theoretical range of measurements were generated *a priori* and overlaid with experimental data to illustrate the dynamic range over which 2C pyrometry can determine the soot concentration and temperature in theory and in practice.

1. Introduction

Particulate Matter (PM) or soot emissions from combustion have long been recognized for their harmful effects on human health and the environment. Exposure to PM can cause respiratory irritation, asthma-like symptoms, and increased risk of cancer [1]. PM emission is second only to carbon dioxide in its impact on climate forcing [2]. Unfortuately, combustion strategies that improve fuel efficiency such as gasoline direct injection (GDI) or diesel engines tend to increase PM emissions [3]. However, advanced engine combustion control strategies and new fuel blendstocks have continued to enable cleaner combustion [4]. Two-Color (2C) pyrometry (also called the 2-Color method or 2-Color thermometry) has been used since the 1930s to characterize the sooting tendency of flames in a variety of studies for diesel engines [5]. The 2C pyrometry is based on the detection of radiative emissions from soot along the line-of-sight at two distinct wavelengths in the visible light spectra to calculate the soot concentration and temperature. Numerous optical system designs of 2C pyrometry to suit different test scenarios have been developed.

Early versions of the 2C Pyrometer utilized a pair of photodiodes equipped with bandpass filters to measure the spectral signals from the test media [6]. As a result, the photodiodes "averaged" the radiative emissions over the field of view (FOV) of the optics and thus, lacked spatial resolution. Singh et al. and Musculus utilized a hybrid system with photodiodes and a high-speed camera [7, 8], whereby the camera detected the natural luminosity of the flame to yield qualitative information about the sooting regions. Most current systems utilize high-speed digital cameras to acquire temporally and spatially resolved 2C pyrometry measurements. However, spatially resolved measurements require accurate pixel-by-pixel mapping of the two images at different wavelengths. Thus, Densmore et al. applied a beamsplitter and bandpass

filters to image the spectral images to two separate cameras [9, 10]. Other researchers have used an image doubler equipped with bandpass filters to project the spectral images on a single camera sensor [11-13]. Some works have circumvented the need for splitting the image by using a color camera and demosaicing the image from the built-in color filter of the camera to extract two spectral signals in post processing [14-19].

Existing optical designs of 2C pyrometry can introduce errors of parallax [11-13], path length difference [20], or demosaicing [14-18], which degrade the measurement accuracy and/or spatial resolution. Image processing techniques to account for these errors can be helpful, but they depend upon the application and don't completely eliminate the problems. This work presents a novel hardware design for 2C pyrometry that eliminates the above errors completely, i.e., it does not produce them. Limitations of existing design, present design, 2C pyrometry theory, and results demonstrating the capabilities of the new optical configuration are discussed in the following sections.

2. Limitations of existing optical designs

The widely used 2C pyrometry configuration with an image doubler and single monochrome camera [11-13] is represented schematically in Fig. 1a. This design offers simplicity since the image doubler is mounted on the camera like a lens and the system is ready for calibration and data collection. There is no need to select, configure, and align optical components. However, this system introduces parallax since the point of view to image the test media is different for each wavelength. As can be inferred from Fig. 1a, placing the 2C pyrometer too close to the test media will increase the parallax angle (θ) or the parallax error. Placing the 2C pyrometer far away from the test media will reduce the parallax angle (θ) but at the expense of the overall signal strength and/or spatial resolution.

Khosravi and Kirchen [13] sought to address parallax by modifying the images in post-processing before solving for temperature and soot concentration. Thus, a spatial calibration was performed by placing a two-dimensional target in the combustion chamber and recording it with the image doubler. Then, a matrix transformation of the two images was performed to correlate the images on a pixel-by-pixel basis; the same transformation matrix was applied to the experimental images recorded by the 2C pyrometer. While this methodology yielded a converged solution at more pixels (more on the solution method in Section 4.1), the pixel-to-pixel mapping is not assured since the two-dimensional target for calibration does not represent the turbulent three-dimensonal flame. The hardware solution presented in this work overcomes the limitations of the post-processing techniques by accurately mapping the line-of-sight emissions at two wave lengths on a pixel to pixel basis.

Payri et al. [20] devised a hardware solution to eliminate parallax (see Fig. 2b) by adding a beamsplitter. However, this modification resulted in different optical path lengths upstream of the camera sensor for each wavelength. Thus, the images recorded by the camera would be of different sizes and one or both will be slightly out of focus. Poor focus would cause more of an averaging effect of turbulent flame structures across the FOV as the light is essentially diffused across multiple pixels in one of the two images on the camera. The different size of the images can be resolved by resizing one of the images in post-processing, which introduces uncertainty. Furthermore, the pixel resolution of the image is limited by the smaller of the two images.

Other works have opted to use color cameras [14-19], which do not encounter parallax or path length differences, but produce an error in the demosaicing process. Each pixel in the color camera image sensor corresponds to a single color (wavelength) on the Bayer filter mosaic, therefore the two spectral signals will always be off by one pixel. This implies that the two spectral signals measured by a color camera will not correspond to the same line of sight. Naturally, the pixel resolution determines the distance between the two lines of sight. In [14]

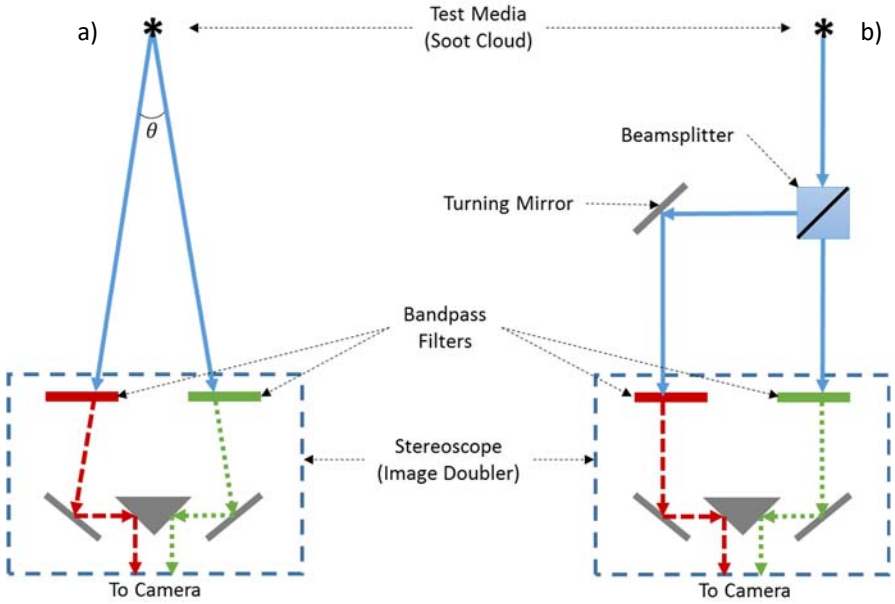

Figure 1: Schematic showing image doubler with a) separate viewpoints causing parallax, and b) single viewpoint enabled with addition of a beamsplitter that eliminates parallax error but introduces difference in the optical path length [20].

the pixel resolution of the color camera was 35 μm/pixel whereas the soot particle size for an acetylene diffusion flame, for example, ranges from 2.5 nm to 40 nm [21], i.e., the soot particle size is three orders of magnitude smaller than this exceptional pixel resolution. Thus, without significant down sampling (binning) to spatially average the measurements, even a single pixel discrepancy could result in different values of soot emissions, rendering 2C pyrometry measurement without physical meaning. Additionally, a disadvantage with this configuration is that the wavelength selection, and therefore the measurement range, is limited to the built in Bayer filter of the camera.

3. Present optical design

The 2C pyrometer design presented in Fig. 2 provides a cost-effective solution using off-the-shelf optics and a single camera to resolve issues associated with previous designs. The setup uses a beamsplitter for light collection and it is oriented at 45° angle with respect to the camera sensor, thereby dividing the image symmetrically about the axis of the camera lens. Bandpass filters are attached to the beamsplitter to pass the light at the desired wavelengths. Filters with 550 nm and 650 nm central wavelengths and bandwidths of 10 nm FWHM are used as in [11]. A pair of turning mirrors reflect the two signals towards a right-angle prism mirror which directs the signals toward the high-speed camera (Phantom v7.3) for imaging on the same but separate portions of the sensor.

4. 2C pyrometry principle and impact on optical design

Thermal radiation from soot particles dominates flame luminosity – this is the basis of 2C pyrometry. The detection of thermal radiation at two distinct wavelengths allows for the calculation of soot concentration and temperature in the flame [22]. It has been demonstrated that the soot concentration and flame thickness (combined as the product KL) is related to the apparent emissivity of the imaged soot cloud and is independent of the wavelength [5, 6, 11, 20]. Combining these theoretical concepts results in Eq. 1 which relates the apparent blackbody

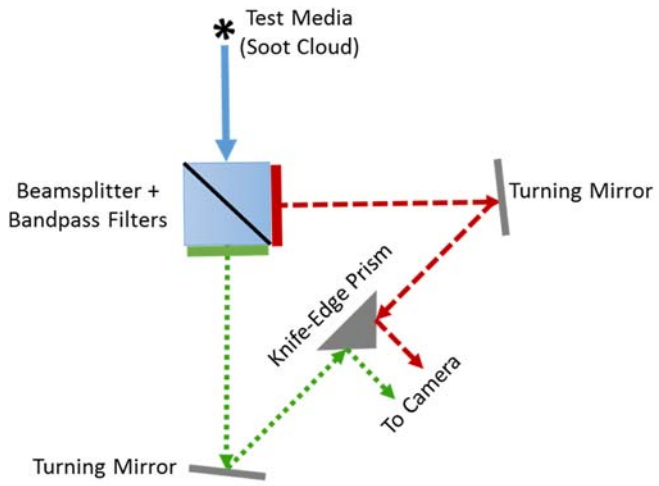

Figure 2: Schematic of Optical Configuration for the new 2C pyrometer

soot temperature, T_a at the two wavelengths to the wavelength indepependent product, KL and the actual teperature, T.

$$(KL)_{\lambda_1} = (KL)_{\lambda_2} = \left[1 - \left(\frac{e^{(C_2/\lambda_1 T)} - 1}{e^{(C_2/\lambda_1 T_{a_1})} - 1}\right)\right]^{\lambda_1{}^{\alpha}} = \left[1 - \left(\frac{e^{(C_2/\lambda_2 T)} - 1}{e^{(C_2/\lambda_2 T_{a_2})} - 1}\right)\right]^{\lambda_2{}^{\alpha}} \quad (1)$$

The 2C pyrometer enables measurement of the apparent temperatures (T_{a_1}, T_{a_2}) via a calibrated detector, typically a digital camera. Then, the soot temperature, T, and product KL are calculated from Eq. 1 by an iterative method. Khosravi and Kirchen [13] studied several different solution algorithms to evaluate the calculation time and accuracy. For spatially resolved 2C pyrometry, Eq. 1 must be solved at each pixel for each frame in the data set. Thus, the algorithms speed has a significant impact on the overall computation time [13]. In this work, a look-up table relating T and KL to a range of apparent temperatures was created using the bisection method, which dramatically decreased the computational effort. Alternatively, a coarse table could be created to "look up" an initial guess for an iterative solver such as the Newton-Raphson method to more precisely calculate T and KL.

Figure 3 exhibits the viable solutions to Eq. 1 in a graphical form. This style of plot was inspired by Hottel and Broughtons' work on 2C pyrometry in 1932 [5] although similar computations and predicitons of measurement ranges have been performed in recent studies [23, 24]. In Fig. 3, experimental data from a diesel wick flame are superimposed to show the range of values actually observed in the measurements. The actual measured flame temperature varied from around 1450 K to 2400 K, yet the apparent temperature for the 650 nm wavelength ranged between 1300 K and 1500 K showing a significant variation in the effective emissivity throughout the flame. The clear left edge of the experimental data in Fig. 3 results from the camera noise threshold utilized to process the images, i.e., data to the left of the experimental points in the plot were filtered out. Conversely, if the flame brightness were to saturate the camera sensor, a similar cut-off would need to be implemented on the right side of the experimental data. Therefore, while the isolines in Fig. 3 represents all possible measurement conditions, the actual range is constrained by the dynamic range of the camera.

More details of the specific experiment are given in the results section, however in the context of optical design considerations for 2C pyrometry systems it is important to note that Fig. 3 could be quite useful to design and construct the 2C pyrometer for a particular application. For a given process, an approximate range of temperatures and soot can be predicted to select the appropriate wavelengths for the bandpass filters to optimize the

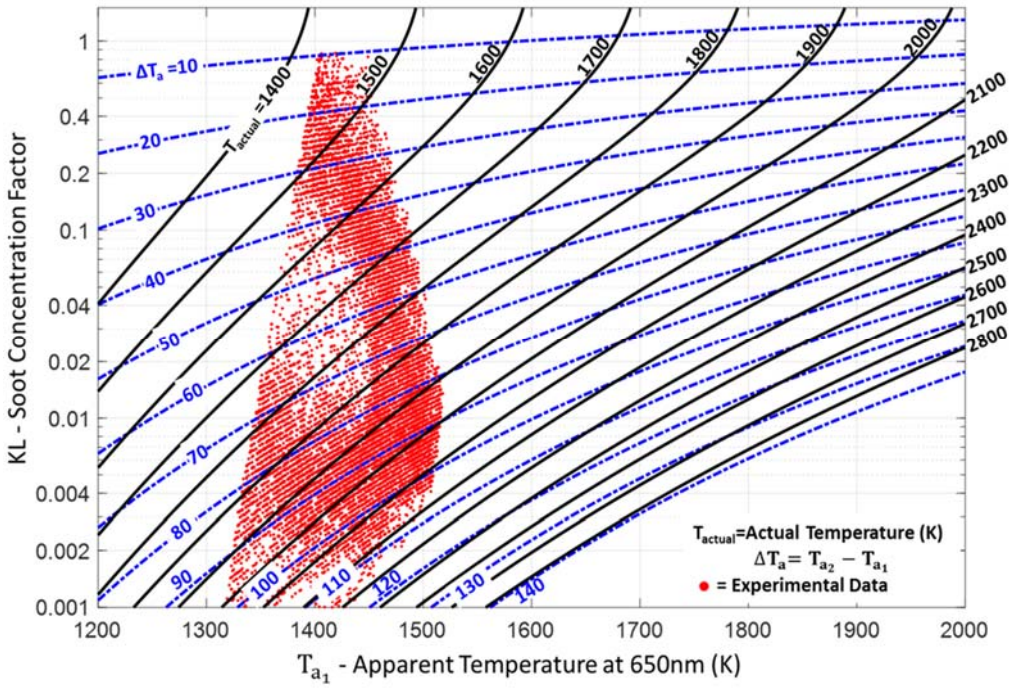

Figure 3: Relationship between apparent temperatures measured at 650nm and 550nm and temperature and product KL or soot concentration. Experimental data for the diesel wick flame are overlaid on the plot.

measurement range given by Fig. 3. Additionally, camera settings such as exposure time and f-stop could be modified to optimize the collection range of the camera for the process of interest.

4.1. 2C pyrometer calibration

Each 2C pyrometer is unique in design and application and thus, it requires calibration to relate the measured spectral signals to their respective apparent temperatures. Ideally, a blackbody emitter at a known temperature is used as the source to deliver known emissions to the 2C pyrometer, which can then be correlated to the intensity measured by the camera with specific settings (lens, f-stop, exposure time, and camera distance from the emitter). This process is then repeated at different blackbody temperatures to develop the calibration curve between camera intensity and blackbody emission at various temperatures. Thereafter, when collecting data in an experiment, the measured camera intensity can be correlated to the apparent blackbody temperature of the incandescent soot at each wavelength (T_{a_1}, T_{a_2}) to solve Eq. 1.

However, the use of a blackbody calibration source is often impractical because of the high cost. As a result, many studies report calibrations carried out with a tungsten filament lamp [7, 8, 13, 20]. The lamp emulates blackbody behavior by passing an electrical current to heat the filament invoking thermal radiation. Although such lamps do not exactly follow a blackbody emission spectrum, their radiance across the visible spectrum is known from manufacturers' calibration; radiance is spectral emissive power divided by π. Certainly, as has been pointed out in the literature [15], the calibrated tungsten lamp method is less accurate than a true blackbody. However, this calibration approach is often sufficient since a properly calibrated lamp has NIST traceable calibration.

The 2C pyrometer in this study was calibrated using a tungsten uniform illumination sphere (UIS) as in [13] from StellarNet which employs a tungsten halogen bulb inside of a sphere with

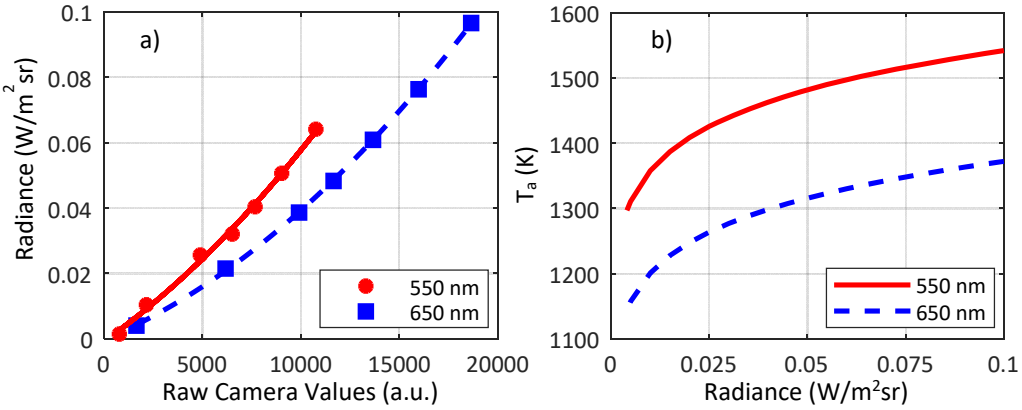

Figure 4: a) Calibration curves for the two wavelengths (exposure time: 98 µs, f-strop: 1.4, distance from source: 0.61 m, b) Apparent blackbody temperature versus radiance for each wavelength.

reflective interior coating to produce uniform and diffuse light output across a 50 mm diameter opening in the sphere. The UIS had three calibration points based on a variable power setting to yield three corresponding radiance spectra. To create a more continuous calibration curve, neutral density (ND) filters were used to decrease the radiance at a known power setting by a fraction (given by the optical density of the ND filter) which yields additional data points to relate intensity measured by the camera to radiance values [11]. With this method, a series of images were recorded by the camera using the various power settings and ND filters; intensity values measured across the UIS emission port were averaged to build the calibration curve in Fig. 4a. Radiance values are then converted to apparent temperatures according to Planck's law. When processing flame data, the intensity measured at a given pixel location of the camera is related to the radiance using the calibration curve for the particular wavelength in Fig. 4a and then the apparent temperature is obtained from Fig. 4b. The camera signal will of course vary depending upon the exposure time, f-stop, and distance from the source; therefore, calibration is performed for the settings used for actual data acquisition.

5. Results and discussion

The capability of the new 2C pyrometer design was demonstrated by collecting data on a simple diesel wick flame. A beaker was partially filled with diesel fuel and a cotton wick was inserted into the fuel to draw it up for burning. Flame images were recorded at 10,000 frames per second with an exposure time of 98 µs and pixel resolution of 345 µm/pixel. For this experiment, a 50 mm camera lens with an f-stop of 1.4 was used; however, the FOV and spatial resolution could be altered by using a different lens.

5.1. Optical distortion inherent in previous designs

The optical hardware used to build the final design was configured to emulate the two designs in Fig. 1 and associated optical distortions. An image doubler is created with two turning mirrors and a knife-edge mirror as in Fig. 1a. The diesel burning wick flame was placed at distances of 0.61 m and 1.22 m away from the pyrometer setup, yielding θ = 9.9° and 5.6°, respectively. Two natural luminosity images (without bandpass filters) were recorded simultaneously with a high speed camera and are shown in Fig. 5a for the 9.9° case. This setup demonstrates noticeable differences in the images due to the parallax indicating asymmetric flame structure. Upon close observation of Fig. 5a, it is apparent that the image on the left is wider than the one on the right and the features in the right image are more pronounced and grouped within a smaller radial extent. These differences are further exemplified in Fig. 5b,

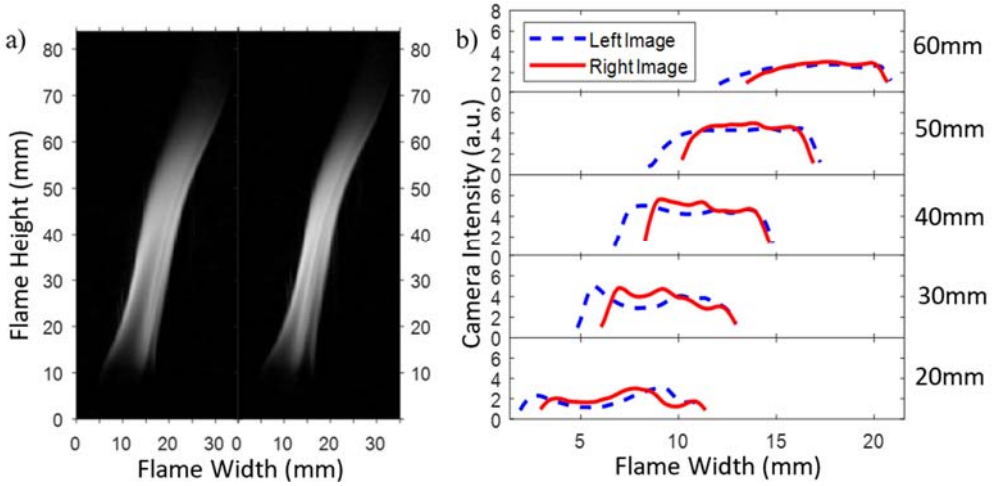

Figure 5: a) Flame images for parallax angle of 9.9°, and b) Transverse profiles of intensity at varying axial locations

which shows the transverse profiles of intensity at different axial locations. For example, the crests and troughs of intensity profiles for the two images appear out of phase in Fig. 5b. With the flame placed further from the camera, resulting in a smaller parallax angle of 5.6°, the transverse profiles more closley match but are still clearly different and therefore are not shown.

The misalignment of flame images is a result of the parallax and indicates that the individual pixels in the two images cannot be mapped precisely with each other which would result in non-physical solutions for T and KL values. For example, consider a hypothetical case in which the red light (650 nm) of one soot particle and the green light (550 nm) of another soot particle are measured and used to solve for the temperature. If a numerical solution is even possible, it will not represent the temperature of either of the two soot particle, i.e., the result is effectively meaningless. This problem is completely avoided by incorporating a beamsplitter in the 2C pyrometer design as each pixel will image the same line of sight.

To simulate the effect of different path lengths, the right-angle prism mirror in Fig. 2 was moved towards one of the turning mirrors to increase the length of one path by 1.25 cm and decrease the length of the other path by 1.25 cm causing a path length difference of 2.5 cm. In this case, Fig. 6a shows that one of the recorded flame images is smaller than the other. In Fig. 6a, the data from the smaller image is on the left was manually scaled to best match the larger image size and then the intensity profiles for both flames were plotted in Fig. 6b. Contrary to Fig. 5b, Fig. 6b shows matching intensity profiles for the two images albeit after resizing in post-processing. The scaled intensity profile shapes are similar since the beamsplitter ensures a single viewpoint for both wavelengths. While this setup is a viable option, the image resizing represents a potential source of error. Resizing can be difficult or impractical in turbulent flames containing structures with multiple length and time scales. Additionally, it is impossible to focus both images due to the difference in the focal lengths. Lack of focus is manifested as bluring of the image(s) that would make it difficult to identify the turbulent structures in the soot cloud yielding a more spatially averaged measurement, rather than precise pixel mapping at all physical locations in the flame. Again, the present system eliminates these problems by design to ensure equal path lengths for the two signals.

5.2. Error free performance of current design

The beamsplitter in the new 2C pyrometer design presented here records the flame emissions from the same point of view for both wavelengths with equal path lengths, and therefore the

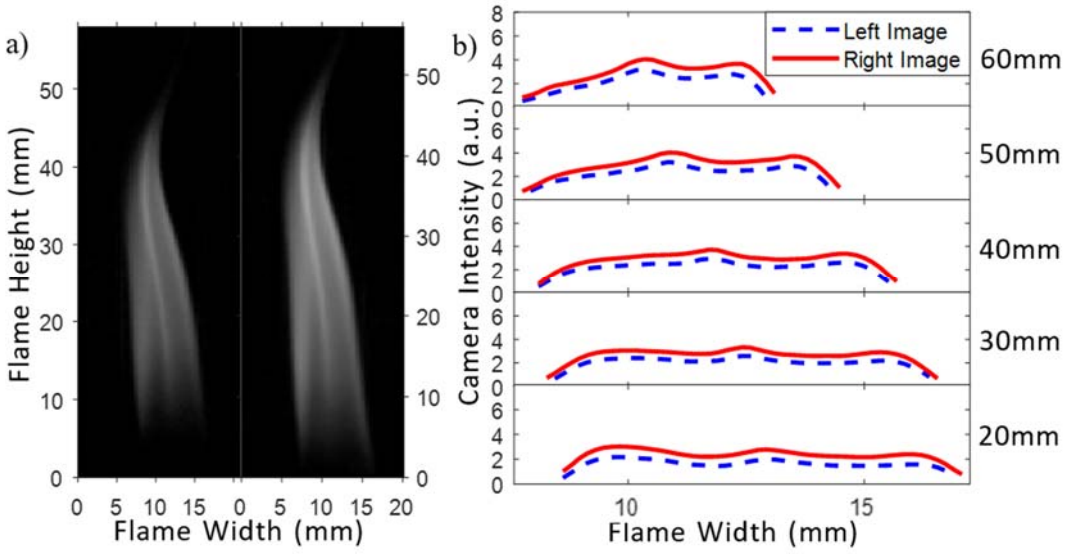

Figure 6: a) Flame images for path length difference of 2.5 cm, b) Transverse profiles of intensity at varying axial locations; the small image was scaled up to the size of the larger image at each axial location.

intensity characteristics of the two images can be precisely correlated at each pixel location, which is crucial to achieve accurate pixel-to-pixel mapping with high spatial resolution. Indeed, flame images acquired with the bandpass filters showed that the intensity distributions in the two images are proportional to one another and Fig. 7 demonstrates the ability of the present 2C pyrometer to map the features of the flame in the two images recorded by the single camera. In effect, the intensity level in the two images is different only because of the different spectral emissions at the two wavelengths and camera spectral response (the calibration in Fig. 4 eliminates the spectral response differences). Figure 7b shows transverse intensity profiles at various axial locations demonstrating matching profile shapes at all axial locations for the two images. The difference in intensities of the two images is much smaller at the bottom compared to that at the top of the flame, which is indicative of the 2C pyrometry processing as can be interpreted from the graphical solution in Fig. 3 and is discussed in the following sections.

5.3. Application example and discussion

Figure 8 shows results using the present setup for three timesteps at 10 ms intervals to depict the flickering of the flame. For each instant and pixel location, the intensity measured by the camera is converted into radiance using the calibration curve for the corresponding wavelength (Fig. 4a). The radiance values for the two wavelengths are converted to a pair of apparent temperatures (Fig. 4b) which accounts for differences in the camreas spectral response, and then Eq. 1 is used to solve for the actual temperature (T) and the product KL. Detailed analysis of the specific features of the flame is beyond the scope of this work, but as expected, the soot concentration is highest at the flame tip where the temperature is the lowest because of rich, sooty combustion.

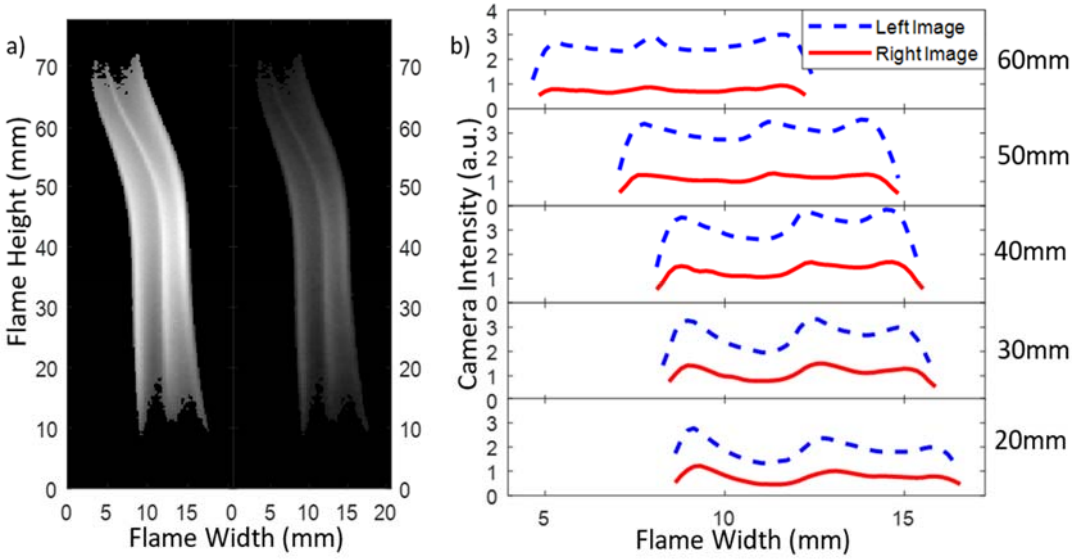

Figure 7: a) Flame images obtained by the present 2C pyrometer design, left and right images were obtained with 650 nm and 550 nm band-pass filters respectively, b) Transverse profiles of intensity profiles at varying axial locations.

According to the relationship between soot concentration and apparent emissivity in [5], $\epsilon_\lambda = 1 - e^{-KL/\lambda^\alpha}$, an increase in KL will also increase ϵ_λ. Thus, increasing soot concentration causes soot emission to behave more like a blackbody. Indeed, for very high soot concentration or KL, the two apparent temperatures would be close to each other and approach the blackbody temperature. The top portion of Fig. 3 depicts these conditions when the measured apparent temperatures are close to each other ($\Delta T_a \approx 10$ K); the soot concentration or KL is large and the temperature, T, is only slightly greater than the apparent temperatures. For the diesel wick flame in this study, the smallest difference in apparent temperatures was 9.2 K, resulting in KL of approximately 1.0 and monochromatic emissivity of 0.84 and 0.90 respectively for wavelengths of 650 nm and 550 nm. Only a few experimental data points resided in this region. Conversely, low soot concentration implies low emissivity or a significant departure from the blackbody behavior. Experimental results in Figs. 3 and 8 show that the flame temperature is lower in regions of high soot concetration. This result can be explained by recognizing that the soot tends to form at fuel-rich conditions where temperatures are far below the stoichiometric flame temperature. The bottom of Fig. 3 and also the bottom of the flame in Fig. 8 represent conditions near stoichiometric where soot is burned off at high flame temperatures, and is therefore characterized by low KL and high temperature. Once again, considering results in the context of Fig. 3 can provide useful guidance to the specific 2C pyrometry and camera setup. While not performed in this work, the knowledge gained from this preliminary experiment could be directly used to optimize the bandpass filter selection for subsequent tests. Using the 2C pyrometry theory, the expected intensity at alternative wavelengths could be predicted and used to ensure optimal use of the dynamic range of the camera.

6. Summary

In this study, a new optical design for 2C pyrometry is presented to eliminate errors associated with parallax (perspective), optical path length difference, and demosaicing. These errors have been discussed to varying extents in past studies with some attempts to compensate in post-processing [13, 20]. The design presented here is unique in that it eliminates each type

simultaneously using a novel optical hardware configuration.The present system consists of off-the-shelf hardware components to develop a highly flexible and cost effective device utilizing a single imaging camera.

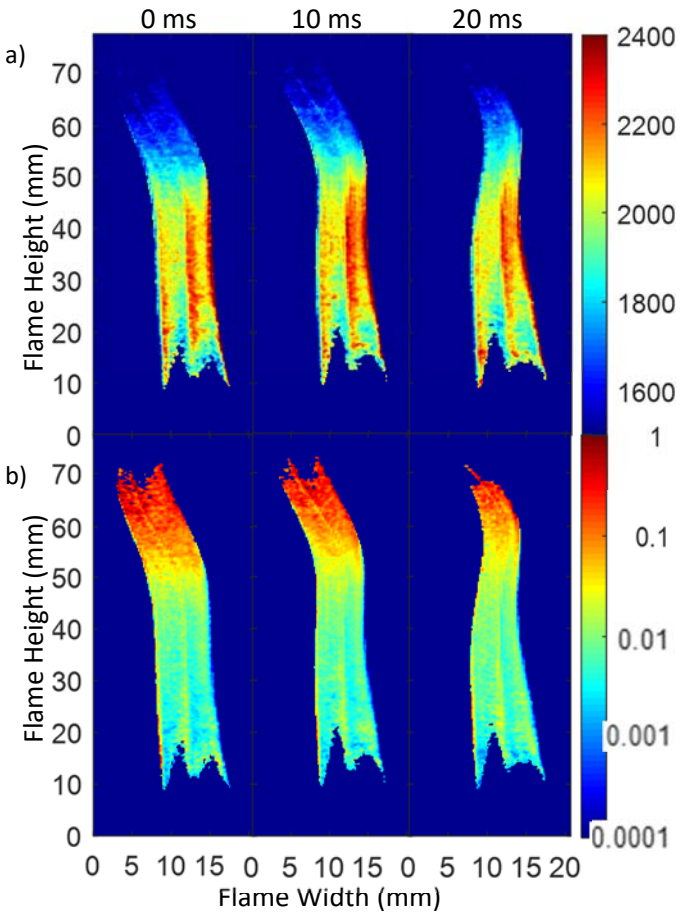

Figure 8: Time evolution of a) temperature (K) and b) product KL in a diesel wick flame.

The measurement capability of the new 2C pyrometer was demonstrated relative to two alternative designs common in literature, and then the system was used to obtain contours of temperature and soot concentration in a flickering diesel wick flame. Results are considered spatially resolved since matching pixels in both images are captured from the same line-of-sight, and thus same set of soot particles in the flame. However, 2C pyrometry is a line-of-sight technique, and thus, multiple views and tomography techniques are required to obtain the true local measurements in asymmetric turbulent flames. Still, the present spatially resolved single view measurements can be effective to compare different portions of the flame and/or flames at different operating conditions such as varying fuel type, ambient temperature, fuel injection strategies, etc.

For researchers developing new 2C pyrometry systems the design presented in this work is encouraged for its inherent elimination of the common optical distortions of alternative designs.

Acknowledgements

This research was supported in part by US Department of Energy award DE-EE0007980.

References

1. H. E. Wichmann, "Diesel exhaust particles," Inhalation Toxicology **19**(1), 241-244 (2007).
2. T. C. Bond, et al. "Bounding the role of black carbon in the climate system: A scientific assessment," Journal of Geophysical Research: Atmospheric **118**(11), 5380-5552 (2013).
3. T. W. Chan, E. Meloche, J. Kubsh, and R. Brezny, "Black carbon emissions in gasoline exhaust and a reduction alternative with a gasoline particulate filter," Environmental Science & Technology **48**(10), 6027-6034 (2014).
4. US Department of Energy, "Co-Optimizations of Fuels and Engines: FY17 Year in Review," (2017). www.energy.gov/sites/prod/files/2018/04/f50/Co-Optima_YIR2017_FINAL_Web_180417_0.pdf.
5. H. C. Hottel, and F. P. Broughton, "Determination of true temperature and total radiation from luminous gas flames," Industrial & Engineering Chemistry Analytical Edition **4.2**, 166-175 (1932).
6. H. Zhao, and N. Ladommatos, "Optical diagnostics for soot and temperature measurement in diesel engines," Progress in Energy and Combustion Science **24**(3), 221-255 (1998).
7. S. Singh, R. D. Reitz, and M. P. B. Musculus, "2-color thermometry experiments and high-speed imaging of multi-mode diesel engine combustion," SAE Transactions **114**(4), 1605-1621 (2005).
8. M. P. B. Musculus, "Measurements of the influence of soot radiation on in-cylinder temperatures and exhaust NOx in a heavy-duty DI diesel engine," SAE Transactions, **114**(3), 845-866 (2005).
9. J. M. Densmore, B. E. Homan, M. M. Biss, and K. L. McNesby, "High-speed two-camera imaging pyrometer for mapping fireball temperatures," Applied Optics **50**(33), 6267-6271 (2011).
10. K. L. McNesby, B. E. Homan, R. A. Benjamin, V. M. Boyle, J. M. Densmore, and M. M. Biss, "Quantitative imaging of explosions with high-speed cameras," Review of Scientific Instruments, **87**, 051301 (2016).
11. J. Zhang, W. Jing, W. L. Roberts, and T. Fang, "Soot temperature and KL factor for biodiesel and diesel spray combustion in a constant volume combustion chamber," Applied Energy **107**, 52-65 (2013).
12. W. Jing, Z. Wu, W. Zhang, and T. Fang, "Measurements of soot temperature and KL factor for spray combustion of biomass derived renewable fuels," Energy **91**, 758-771 (2015).
13. M. Khosravi, and P. Kirchen, "Refinement of the two-color pyrometry method for application in a direct injection diesel and natural gas compression-ignition engine." Proceedings of the Institution of Mechanical Engineers, Part D: Journal of Automobile Engineering (0954407019832774), (2019).
14. D. D. Das, et al, "Sooting tendencies of diesel fuels, jet fuels, and their surrogates in diffusion flames," Fuel **197**, 445-458 (2017).
15. Q. Shi, T. Li, X. Zhang, B. Wang, and M. Zheng, "Measurement of Temperature and Soot (KL) Distributions in Spray Flames of Diesel-Butanol Blends by Two-Color Method Using High-Speed RGB Video Camera," SAE International (2016-01-2190), (2016).
16. J. M. Densmore, M. M. Biss, K. L. McNesby, and B. E. Homan, "High-speed digital color imaging pyrometry," Applied Optics **50**(17), 2659-2665 (2011).
17. H. Guo, J. A. Castillo, and P. B. Sunderland, "Digital camera measurements of soot temperature and soot volume fraction in axisymmetric flames," Applied Optics **52**(33), 8040-8047 (2013).
18. F. Cignoli, S. De luliis, V. Manta, and G. Zizak, "Two-dimensional two-wavelength emission technique for soot diagnostics," Applied Optics **40**(30), 5370-5378 (2001).
19. C. Toro, L. Arias, S. Torres, and D. Sbarbaro, "Flame spectra-temperature estimation based on a color imaging camera and a spectral reconstruction technique," Applied Optics **53**(28), 6351-6361 (2014).
20. F. Payri, J. V. Pastor, J. M. García, and J. M. Pastor, "Contribution to the application of two-colour imaging to diesel combustion," Measurement Science and Technology **18**(8), 2579-2598 (2007).
21. S. di Stasio, and P. Massoli, "Influence of the soot property uncertainties in temperature and volume-fraction measurements by two-colour pyrometry," Measurement Science and Technology **5**(12), 1453-1465 (1994).
22. T. L. Bergman, F. P. Incropera, D. P. DeWitt, and A. S. Lavine, *Fundamentals of Heat and Mass Transfer*, (John Wiley & Sons, 2011).
23. T. Fu, X. Cheng, M. Zhong, and T. Liu, "The theoretical prediction analyses of the measurement range for multi-band pyrometry," Measurement Science and Technology **17**(10), 2751-2756 (2006).
24. T. Fu, X. Cheng, B. Wu, M. Zhong, C. Shi, and T. Liu, "The measurement coordinates for multi-band pyrometry," Measurement Science and Technology **17**(2), 379-383 (2006).